# Insulating magnetic oxides for spintronic applications

Dissertation
zur Erlangung des Grades
"Doktor der Naturwissenschaften" (Dr. rer. nat.)
am Institut für Physik der
Johannes Gutenberg-Universität Mainz

**Sven Becker**
geb. in Traben-Trarbach
Mainz, 2021

JOHANNES GUTENBERG UNIVERSITÄT MAINZ

JG|U

Sven Becker
*Insulating magnetic oxides for spintronic applications*
Dissertation, Datum der mündlichen Prüfung 27.06.2022
1. Berichterstatter: Gerhard Jakob
2. Berichterstatter: Aus Datenschutzgründen entfernt / Removed due to data privacy

Johannes Gutenberg-Universität Mainz
AG Kläui
Institut für Physik
Staudingerweg 7
55128 Mainz

# Contents

# Abstract

Current technologies for data storage and information processing are heavily reliant on metallic, ferromagnetic materials. This hinders further improvement of devices due to a sensitivity to external perturbations, limits of processing speeds and excessive Joule heating from the passing charge currents. In this thesis, several promising material composites are explored for implementing magnonic logic operations. On a more fundamental side, interfacial effects are employed for probing the magnetic anisotropies and phase changes of a novel material system.

Spin currents are discussed as an information carrier and for information processing. In magnetically ordered insulators, these spin currents are carried by magnons, the quanta of spin waves. The ferrimagnetic insulator $Y_3Fe_5O_{12}$ (YIG) has shown to be able to transport magnons over large distances. However, for building devices based on magnons to implement key logic operations, one needs the possibility to actively manipulate the spin current. To this end, this thesis considers the experimental implementation of a magnon valve using bilayers of YIG and another magnetic garnet, $Gd_3Fe_5O_{12}$.

An alternative approach to implement improvements to spintronic devices is to replace the ferromagnetic material with an antiferromagnet, enabling writing speeds in the terahertz range. However, determining the state of an antiferromagnet is a major challenge necessitating the development of new techniques. One of these is spin Hall magnetoresistance (SMR), a surface-sensitive all-electrical measurement that probes the magnetic order of a material. In this thesis, SMR is utilized to probe the magnetic properties of the antiferromagnetically ordered compound $TmFeO_3$ (TFO). First, a single crystal of TFO is investigated and its structural and magnetic properties are determined using bulk measurements. Using then only surface-sensitive SMR, we can attribute the electrical signals to the magnetic properties of the TFO.

However, for device applications, bulk materials are not suitable. This motivates us to grow TFO as thin films, using pulsed laser deposition. The dependence of the magnetic properties on the choice of substrate is demonstrated. These thin films possess similar properties to single crystals, as probed with volume-sensitive measurements. Performing then surface sensitive SMR measurements on these samples allows us to probe the magnetic properties of the TFO thin film in a more device relevant setting.

# Zusammenfassung

Heutige Technologien zur Datenspeicherung und Informationsverarbeitung sind stark auf metallische, ferromagnetische Materialien angewiesen. Dies verhindert eine weitere Verbesserung der Geräte wegen der Sensitivität bezüglich externen Störungen, Grenzen von Verarbeitungsgeschwindigkeiten und frei werdender Joulsche Wärme durch Ladungsströme. In dieser Doktorarbeit werden einige vielversprechende Materialkompositionen für die Implementierung von Magnonenlogik untersucht. Auf einer fundamentalen Seite beschäftigt sich die Arbeit mit Grenzschichteffekten, um magnetische Anisotropie und Phasenänderungen von neuen Materialsystemen zu messen.
Spinströme werden als Informationsträger und zur Informationsverarbeitung diskutiert. In magnetisch geordneten Isolatoren werden diese Spinströme von Magnonen getragen, den Quanten von Spinwellen. Im ferrimagnetischen Isolator $Y_3Fe_5O_{12}$ (YIG) können Magnonen über weite Strecken transportiert werden. Doch um Geräte zu bauen, die auf Magnonen for logische Operationen basieren, braucht es die Möglichkeit die Spinströme zu manipulieren. Dahingehend prüft diese Arbeit die experimentelle Implementierung von Magnonenventilen, wozu Bilagen aus YIG und einem anderen magnetischen Granat, $Gd_3Fe_5O_{12}$ (GIG), genutzt werden.
Ein zweiter Ansatz um spintronische Bauteile zu verbessern zielt auf die Ersetzung der ferromagnetischen Materialien durch Antiferromagneten, die Schreibgeschwindigkeiten im Gigahertzbereich ermöglichen. Jedoch ist die Bestimmung des magnetischen Zustand eines Antiferromagneten eine große Herausforderung, die der Entwicklung neuer Techniken bedarf. Eine von diesen ist der Spin Hall Magnetwiderstand (SMR), eine oberflächensensitive rein elektrische Messung, die die magnetische Ordnung des Materials prüft. In dieser Arbeit wird SMR genutzt um das antiferromagnetisch geordnete Oxid $TmFeO_3$ (TFO) zu untersuchen.
Zuerst wird ein TFO Einkristall erforscht und seine Struktur und seine magnetischen Eigenschaften werden bestimmt, wozu das ganze Volumen des Materials untersucht wird. Indem anschließend die oberflächensensitiven SMR Messungen genutzt werden, können wir die elektrischen Signale den magnetischen Eigenschaften des TFO zuordnen.
Im Hinblick auf Anwendungen sind Volumenkristalle jedoch ungeeignet. Dies motiviert uns TFO als dünne Schicht mithilfe gepulster Laserdeposition zu wachsen. Die Abhängigkeit der magnetischen Eigenschaften der TFO Dünnschichten von dem verwendeten Substrat wird hier gezeigt. Diese Proben besitzen ähnliche Eigenschaften wie Einkristalle, was mit volumensensitiven Techniken überprüft wird. Indem dann die oberflächensensitiven SMR Messungen durchgeführt werden, kann gezeigt werden, dass wir damit auch die magnetischen Eigenschaften dieser Dünnschichten in einer für Applikationen relevanten Umgebung bestimmen können.

# Introduction

Information technology has always aimed for faster and more compact devices [1, 2]. However, the smaller the structures become, the larger the current densities employed, leading to an increase of Joule heating of the electrical conductors. There are two problematic consequences of this: the efficiency is limited due to the generation of waste heat, which can also cause damage to the circuitry. Secondly, there is a lower size limit of magnetic bits since thermal demagnetization could lead to memory loss. A way out of this would be to replace electrical charge currents by pure spin currents in magnetically ordered insulators, which can also carry information and do not generate Joule heating [3].

Magnons can travel large distances in magnetically ordered insulators such as $Y_3Fe_5O_{12}$ (YIG) [4], which is necessary to utilize magnons in spintronic devices. This makes YIG an ideal candidate for investigating such novel concepts. With regard to device applications, one not only needs to transport information, but also to manipulate it. In current electronic devices, there are for example magnetoresistive elements using the concept of giant magnetoresistance (GMR) effect [5–7], where there are two defined electrical resistance states. An analog for magnons would be a magnon valve [8], where there are two 'magnon resistance' states. There have been attempts to realize such a device by different material stacks like YIG/CoO/Co [8], YIG/Au/YIG [9] and YIG/NiO/YIG [10]. The effect reported in these studies relies on a magnetic configuration that depends on the history of the sample since the magnetic layers are decoupled from each other.

An alternative, more resilient approach would be to couple the magnetic layers. The magnetic coupling leads to the cancellation of hysteretic behavior when switching between parallel and antiparallel magnetization alignment. Here, magnetically interface-coupled heterostructures of YIG with the another magnetic garnet $Gd_3Fe_5O_{12}$ (GIG) are grown. The magnetic configuration is determined by the relative thickness of the heterostructure as well as the external magnetic field and temperature. This allows us to precisely tune the magnetic properties of the heterostructures making them interesting for device applications.

Using ferromagnetic materials in spintronic devices limits the writing speed to the gigahertz range [11] due to the intrinsic switching speeds of the ferromagnetic ordering. The field of spintronics has recently shifted focus towards utilizing antiferromagnetic materials due to intrinsic high frequency spin dynamics in the terahertz range and stability against external perturbations [12–14]. These benefits over ferromagnetic materials place antiferromagnets (AFs) at the forefront for future low power, high frequency spintronic devices. However, these advantages come at a cost. Information storage devices rely on manipulating and reading the magnetic state. The high

stability and the lack of stray fields complicate the replacement of current standard ferromagnetic materials for antiferromagnets, and their integration into current technologies. Current read-out techniques for ferromagnetic data storage rely on effects like tunneling magnetoresistance and giant magnetoresistance. These cannot be simply applied for AFs, so to access the AF state, new techniques are necessary. One is the surface-sensitive spin Hall magnetoresistance (SMR), with roots in the so called spin Hall effect (SHE) and its inverse effect. A heavy metal is placed in contact with the AF. Depending on the orientation of the magnetic order parameter of the AF, the resistance of the heavy metal is altered [15, 16].
In terms of new materials, $TmFeO_3$ (TFO) has recently gathered a lot of attention, mostly due to the ultra-fast spin control by light [17–20]. In 2019, Schlauderer *et al.* showed that the magnetic state of TFO single crystals can be rotated coherently by 90° using a terahertz electromagnetic pulse [21]. In their work, the Faraday effect has been utilized to probe the long-lived final spin state. The manipulation and probing of the antiferromagnetic state marks an important point on the way to antiferromagnetic spintronic applications. However, with respect to actual applications, single crystal materials as well as terahertz lasers and transmission-geometry probing are difficult to integrate in devices.
Here, we aim to use the all-electrical SMR to investigate TFO. First, a TFO single crystal is employed and we show that the surface-sensitive SMR is a suitable tool for probing the bulk magnetic properties of a sample. We further investigate the possibility to grow TFO as thin films. The properties of these samples and the influence of the underlying substrate is demonstrated, before SMR measurements are used to determine the magnetic configuration of TFO thin film samples. There exist another crystallographic phase of TFO else than the bulk orthorhombic one. On substrates with the appropriate symmetry, the hexagonal, multiferroic phase can be stabilized [22]. This makes TFO also interesting for possible applications in magnetoelectric devices [23]. We demonstrate the growth of hexagonal TFO (h-TFO) on a variety of different substrates. We show that functional devices can only be fabricated when improving the stability of the conducting bottom electrode on which the h-TFO grows.
In **chapter 1**, we briefly summarize aspects of the theoretical understanding of the principles of magnetic ordering. Additionally, a choice of electronic transport effects that are essential for understanding the experimental results of this thesis are introduced.
**Chapter 2** focuses on the materials investigated in this thesis. We present the structural and magnetic properties of the family of garnets and rare earth ferrites. A focus is maintained on the behavior of the magnetic properties in the presence of a magnetic field and a changing temperature. The two magnetic garnets GIG and YIG used in part of this thesis are well-known materials to the spintronics community, so they will only be briefly introduced. We will discuss in more detail TFO, which plays a major role in two results chapters. The concept of spin reorientation transitions and spin flops in rare earth orthoferrites will be discussed.
In **chapter 3**, the methods employed in the course of this thesis for sample preparation as well as for probing the structural and magnetic properties of materials are

introduced. We further demonstrate how electrical measurements are employed.
Coming then to the key results of this thesis, **chapter 4** will discuss YIG-GIG heterostructures with magnetic interlayer coupling. The growth process is presented in detail. The presence of coupling is determined using a variety of methods. A first attempt of measuring the magnon valve effect via spin Seebeck effect is presented.
**Chapter 5** contains the investigation of TFO single crystals. The bulk properties like the structure and the magnetic behavior of the sample as a function of the temperature and external magnetic field are determined. We then conduct electrical transport measurements and show that SMR is an effective probe of the bulk magnetic properties of antiferromagnets. An additional contribution to the SMR signal likely stemming from TFO/PT interface effects is discussed.
In **chapter 6**, an in-depth analysis of thin film, orthorhombic TFO is presented. We investigate the structural and magnetic properties, before then moving to surface-sensitive electrical measurements. Again, SMR proves to be the suiting tool to determine the magnetic properties of these kind of samples, allowing for electrical access to the antiferromagnetic state. We further show that the quality of the orthorhombic thin films can be improved by the choice of the substrate. If the substrate has special symmetry, it even allows for stabilization of the meta-stable hexagonal phase of TFO. These samples are investigated with regard to their multiferroic properties.
Finally, **chapter 7** summarizes the core results of this thesis and discusses the current understanding afforded by the work performed and shown here. Future steps and new research avenues are suggested.
In the **appendix** chapter, additional background on rare earth ferrites is given, exceeding the scope of the main text. A complete set of trajectories of the magnetization and the Néel vector for field-induced spin reorientations in TFO is given. Furthermore, continuative measurements on TFO bulk single crystals and STO/TFO thin films are summarized. The last section deals with the investigation of $RuO_2$ thin films, which are candidates for measuring novel transport effects. Since key experiments are yet to be performed, here, only basic properties of $RuO_2$ thin films are presented.

Sven Becker wrote the first author publications [S3], [S7] and [S6] with suggestions from all authors. A fourth publication is currently under preparation [S10]. Concerning the results presented in this thesis, in the following, the contributions are sorted according the results chapters.

**YIG-GIG heterostructures**

- Growth optimization: Sven Becker, Andrew Ross (JGU) and Sally Lord (Manchester)
- Fabrication of exchange coupled YIG-GIG samples: Sven Becker, Zengyao Ren (University of Science and Technology Beijing)
- Structural characterization by XRD: Sven Becker, Zengyao Ren

*Introduction*

- Magnetic characterization by SQUID: Sven Becker, Zengyao Ren
- SHE measurements: Sven Becker
- Spin Seebeck effect measurements: Felix Fuhrmann (JGU)

**Bulk TFO**

- Single crystal growth: Ekaterina Pomjakushina (PSI)
- Structural characterization and determination of crystal orientation by XRD: Sven Becker
- Measurement of magnetic domains using MOKE: Felix Schreiber (JGU)
- Patterning of Pt Hall bars and non-local devices: Andrew Ross (JGU)
- Electrical measurements at Hall bars and non-local structures: Sven Becker and Andrew Ross (JGU)

**TFO thin films**

- Target fabrication and growth optimization: Sven Becker
- Structural and topographic characterization: Sven Becker
- SQUID measurements: Sven Becker
- XMLD and XMCD measurements: Lorenzo Baldrati, Andrew Ross, Shilei Ding and Felix Schreiber (JGU) with support from Francesco Maccerozzi and Dirk Backes (DIAMOND)
- Patterning of Pt Hall bars: Andrew Ross (JGU)
- Electrical measurements at Hall bars and non-local structures: Sven Becker and Andrew Ross (JGU)

# 1. Theory

## 1.1. Magnetic free energy

The magnetic properties of a solid depend on several intrinsic and extrinsic parameters. To describe the contributions, one can write down Hamiltonians $\mathcal{H}$ for each energy term that influences the magnetization. This may look like

$$\mathcal{H} = \mathcal{H}_e + \mathcal{H}_d + \mathcal{H}_{ani} + \mathcal{H}_{Zee} + ..., \tag{1.1}$$

where $\mathcal{H}_e$ describes the symmetric exchange energy, $\mathcal{H}_d$ describes the antisymmetric exchange energy, $\mathcal{H}_{ani}$ represents the anisotropy energies and $\mathcal{H}_{Zee}$ is the Zeeman energy. This list can be continued depending on the specific system. We will now focus on the individual energy terms above, which are most important for the samples investigated in this work.

#### Exchange energy

The exchange energy originates from the Coulomb interaction and the Pauli exclusion principle. The Hamiltonian for two single spins $\mathbf{S}_1$ and $\mathbf{S}_2$ can be written in the Heisenberg model as

$$\mathcal{H}_e = -2\mathcal{J}\mathbf{S}_1 \cdot \mathbf{S}_2. \tag{1.2}$$

From this formula one can already realize that the exchange energy is isotropic and that a parallel alignment of spins is favorable if $\mathcal{J} > 0$ (ferromagnet, FM) and an antiparallel alignment for $\mathcal{J} < 0$ and equally large magnetic moments (antiferromagnet AFM). If the magnetic moments of the respective sublattices have different magnitude one obtains ferrimagnetic order for $\mathcal{J} < 0$. For a macroscopic solid one often assumes $\mathcal{J}$ is a finite constant for neighboring spins and zero otherwise since nearest neighbour interaction is usually dominating. Summing over all pairs of spins one gets

$$\mathcal{H}_e = -\sum_{i,j} \mathcal{J}_{ij}\mathbf{S}_i \cdot \mathbf{S}_j \tag{1.3}$$

#### Superexchange energy

In many crystalline oxides, the nearest neighbors of magnetic ions are nonmagnetic oxygen ions. Despite the lack of direct exchange, antiferromagnetic ordering is still observed. For direct exchange, the distance between next-neighbored magnetic ions is too large. However, one can model a strong coupling using the concept of superexchange interaction [24]. For this, the oxygen ion in between two magnetic ions plays

an important role. The d-orbitals of the magnetic ion hybridize with the 2p orbitals of the oxygen ion. Due to the Pauli principle, the delocalization of electrons is only achieved if the spins from the magnetic ion couples antiferromagnetically to the oxygen 2p electron spins. This leads to an overall antiferromagnetic alignment of the spins of the magnetic ions. Despite the more complicated process compared to the direct exchange interaction, the superexchange interaction can still be modeled using the same Hamiltonian given in equation 1.3, where $\mathcal{J}$ becomes $\mathcal{J} \approx -t^2/U$, with the hopping integral $t$ and the Coulomb energy $U$ [25].

### Antisymmetric exchange energy

Antisymmetric exchange energy is found to play an important role in some antiferromagnets. This energy term favors the orthogonal alignment of the spins and leads to a canting of the spins away from the perfect antiparallel alignment. The result is a finite magnetic moment that can be found e.g. in orthoferrites (see 2.2). The family of canted antiferromagnets is sometimes referred to as weak ferromagnets. Valuable contributions to the understanding of this was provided by Dzyaloshinskii [26] and Moriya [27] so that the asymmetric exchange interaction is often called Dzyaloshinskii-Moriya interaction (DMI). The Hamiltonian for this interaction is given as

$$\mathcal{H}_D = \mathcal{D} \cdot (\mathbf{S}_1 \times \mathbf{S}_2)\,, \tag{1.4}$$

where $\mathcal{D}$ is a vector that lies perpendicular to $\mathbf{S}_1$ and $\mathbf{S}_2$.

### Zeeman energy

The Zeeman energy describes the influence of an external magnetic field on the magnetic moments. For a single spin the the Hamiltonian can be written as

$$\mathcal{H}_{Zee} = \mu_0 \mathbf{HS}. \tag{1.5}$$

This equation can be extended for a macroscopic solid by performing the sum over all spin moments. The term is minimum when the magnetization of the sample aligns with the magnetic field. In case of a collinear AFM, the Zeeman energy influences the magnetic order only weakly because of the small net magnetization and large exchange energy. However, in contrast to ferromagnets, the Zeeman energy is minimized when the spins of the AFM order lie perpendicular to the external magnetic field. The field, applied in the direction of the spins leading to the perpendicular spin reorientation is called spin-flop field, where the field required to induce this transition is set by the anisotropy energy. In the case of magnetic fields larger than the spin-flop, the sublattices of the AFM will cant away from the perfectly collinear arrangement, leading to a field-induced net magnetic moment parallel with $\mathbf{H}$.

### Anisotropy energy

The energy terms described above are isotropic. However, in macroscopic samples one observes ‘easy’ and ‘hard’ magnetic directions. The origin of the anisotropy can come

from many places such as the shape of the sample (shape anisotropy), the crystal structure (magnetocrystalline anisotropy) or a neighboring magnetic structure (exchange bias anisotropy).
The shape anisotropy is closely linked to the dipolar interaction [25]. Roughly speaking, when the spins are pointing in direction of a large interface, there are many uncompensated dipole moments at the interface, which increases the overall energy. This is, however, not relevant for antiferromagnetically ordered solids, which make up a large portion of the results in this work. In the case of the magnetic garnets in chapter 4, the shape anisotropy is a lot smaller than other energy terms so can be ignored. For the work presented in this thesis, we will focus more on the magnetocrystalline anisotropy rather than the shape anisotropy. Its origin lies in spin-orbit coupling. The orientation of the orbital momenta are influenced by the crystal structure due to the overlap of neighboring orbitals. Usually, a phenomenological energy term is given as a power series. For uniaxial anisotropy (only one preferred magnetic direction) this can be written up to the second order anisotropy as

$$\mathcal{H}_{ani} = K_1 \sin^2(\theta) + K_2 \sin^4(\theta) + ..., \tag{1.6}$$

where $K_1$ and $K_2$ are anisotropy constants and $\theta$ the angle of the spins and the easy magnetic direction. $K_1$ and $K_2$ are, in general, temperature-dependent [25].

## 1.2. Landau theory of magnetism

To simplify the description of the magnetic properties around a phase transition Landau developed a formalism based on very general considerations, assuming that every spins is exposed to an identical average field [25]. The free energy is expressed as a power series in the order parameter. For ferromagnetic ordering, the order parameter is the magnetization $M$, for antiferromagnetic ordering it is the Néel vector $N$, for a spin reorientation transition it is the angle of the magnetic order parameter with the crystallographic axis, and for ferroelectric materials it is the polarization $P$. The order parameter has to be zero above the transition that is to be described and finite below. The free energy term then has the form of

$$\mathcal{F} = \mathcal{F}_0 + a(T)M^2 + bM^4 - HM + ... \tag{1.7}$$

$M$ can be one of the above mentioned order parameters, $\mathcal{F}_0$ and $b$ are constants and $a(T)$ is a temperature-dependent factor that changes sign at the critical temperature. The free energy can also be extended to higher order terms if required. This critical temperature is called Curie temperature for ferromagnets (and ferroelectrics) ($T_C$) and Néel temperature for antiferromagnets ($T_N$). Close to this temperature $a(T)$ can be written as $a(T) = a_0(T - T_C)$ with a positive constant $a_0$.

## 1.3. Ferroelectricity

Ferroelectricity describes the property of some materials which possess a net dipole moment (spontaneous polarization) [28]. The orientation of the dipole moment is sensitive to an external electric field. As an order parameter one defines the polarization vector $\mathbf{P}$, pointing in the direction of the charge gradient. The magnitude of the polarization is given in units of $\mathrm{As/m^2}$, while in publication mostly $\mu\mathrm{C/cm^2}$ is used. A sufficiently large electric field applied in the opposite direction leads to the replacement of charges and a resulting switch of the polarization vector. This field-induced polarization switching can be described as a first-order phase transition. Similarly to the ordering temperature of (anti-)ferromagnets, there exists also a ferroelectric ordering temperature at which a second-order phase transition takes place. Due to the similarities with ferromagnets this temperature is also called Curie temperature $T_C$. Above $T_C$, no spontaneous polarization is detectable and the material is identified as paraelectric.

## 1.4. Multiferroicity

We have seen in the previous sections how the phenomena of ferromagnetism can be described and that there are many similarities between ferroelectric and ferromagnetic ordering. Taking also into account a further effect, namely ferroelasticity, these properties are grouped and labeled ferroic properties. If a material possesses more than one ferroic order parameter, it is called multiferroic. Especially those materials are deeply investigated, which show coupling between their order parameters [29, 30]. Mainly the magnetoelectric coupling, the coupling of magnetic and ferroelectric order parameter, is interesting for future information technology applications [31, 32]. In these materials, the polarization can be altered using a magnetic field and vice versa, the magnetic ordering can be manipulated using an electric field.

## 1.5. Magnons

An insulating magnetically ordered material can be excited by external stimuli such that the spins are canted from their equilibrium positions. This displacement is shared among the neighboring spins with a finite phase difference, leading to a periodic oscillation of the spins. This spin wave has, similar to phonons in thermal excitations of the lattice, a quasi-particle character. The smallest quantum of a spin wave is called a magnon. It can be described by a wavelength $\lambda$ and a frequency $\omega$, and follows a Bose-Einstein distribution. At a finite temperature, the thermal energy leads to the excitation of thermal magnons possessing a frequency of the order of THz ($\hbar\omega = k_B T$) for $T > 50\,\mathrm{K}$. One can describe magnons in momentum space using a band structure which visualizes which combinations of frequency (i.e. energy) and momentum are possible in the magnetically ordered crystal. The magnon spectrum is a handy tool e.g. for the interpretation of spin Seebeck effect measurements [33]. Magnons can

carry angular momentum over large distances making them interesting candidates for future spintronic applications. They could be used to transfer information in magnetic insulators in the absence of Joule heating, which is the major source of inefficiency of current electron-based technology.
Not every magnetically ordered material is a good magnon conductor. Long-distance magnon transport has been shown to occur in few materials, like ferromagnetic $Y_3Fe_5O_{12}$ [4] and antiferromagnetic $\alpha-Fe_2O_3$ [34], and very recently $YFeO_3$ [S8]. These materials share a common property that they possess low magnetic damping. In TFO, which has been investigated in this work, no long-distant magnon transport was observed (see A.6), likely due to the larger Gilbert damping parameter, however, the exact mechanisms of magnon transport in antiferromagnetic materials are still unclear. In YIG-GIG heterostructures, we have investigated the possibility to manipulate magnon currents by changing the magnetic state of the heterostructure. These results are presented in chapter 4.

## 1.6. Magnetoresistive and Hall effects

Numerous effects lead to the deflection of electrons within a conductor away from the straight path given by the electric field gradient. The first of these effects was discovered in 1879 by Edwin Hall [35], who became the namesake for a whole family of effects, which all describe the occurrence of a voltage perpendicular to the current direction. Magnetoresistive effects on the other hand describe the modification of the longitudinal resistance, parallel to the applied charge current. In this section, the specific effects which are relevant for our measurement geometries used will be briefly discussed. We note that the list of transport effects is incomplete. Even recently, novel transport phenomena like the crystal Hall effect (CHE) have been discovered and are yet to be experimentally demonstrated. The appendix section A.8 deals with an attempt to measure the CHE in $RuO_2$ thin films, however, key experiments are yet to be performed. While all the transport effects effects can in principle be observed in samples of any shape, we will use a defined shape to facilitate experiments and

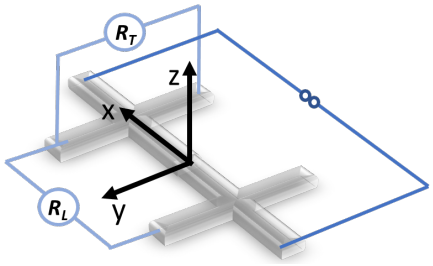


Figure 1.1.: Hall bar geometry with its relative directions $x$, $y$ and $z$ indicated, where $x$ is the current direction. The longitudinal resistance $R_L$ and transverse resistance $R_T$ are being measured as indicated.

interpretation of the data. We therefore utilize the structure known as a Hall bar. To describe directions relative to the Hall bar, a coordinate system is introduced as shown in Fig. 1.1, where $x$ is the direction of the current, $y$ is the in-plane direction perpendicular to the current and $z$ is the out-of-plane direction.

### 1.6.1. Ordinary Hall effect (OHE)

One of the very fundamental equations of electromagnetism describes the Lorentz force $\mathbf{F} = q\,(\mathbf{E} + \mathbf{v} \times \mu_0\mathbf{H})$, which is the force $\mathbf{F}$ on a particle with charge $q$ moving with velocity $\mathbf{v}$ in an electric field $\mathbf{E}$ and magnetic field $\mathbf{H}$. For a 2-dimensional nonmagnetic conducting system confined in the $xy$-plane, a charge current, generated by an electric field applied in the $x$ direction, and a magnetic field applied perpendicular to the plane in the $z$-direction will lead to a force on the charge carriers in the $y$-direction. This results in the separation of charge carriers and a resulting $\mathbf{E}$-field in the $y$-direction. The separation of charge carriers continues until the force of the resulting electrostatic field and the Lorentz force compensate one another. In the case of normal metals, where electrons are the only charge carriers, one observes an accumulation of electrons at one side. This can be measured as a Hall voltage $V_H$ which depends linearly on the magnetic field. Normalizing $V_H$ to the current flowing, we express the OHE as a transverse resistance,

$$R_{OHE} = R_H \mu_0 H_z. \tag{1.8}$$

Here, $\mu_0$ is the vacuum permeability and $R_H$ is the material dependent Hall coefficient. Applying the field perpendicular to the $z$-direction leads to no effect, when the current is confined in a 2-dimensional plane. Rotation of the magnetic field in the three planes shown in Fig. 1.2 lead to the following dependencies:

$$\begin{aligned} xy &: R_{OHE} = 0 \\ xz &: R_{OHE} = R_H \mu_0 H \cos(\gamma) \\ yz &: R_{OHE} = R_H \mu_0 H \cos(\beta) \end{aligned}$$

Here, $H = |\mathbf{H}|$, $\gamma$ is the angle $\mathbf{H}$ makes with the $z$-axis in the $xz$-plane and $\beta$ is the angle $\mathbf{H}$ makes with the $z$-axis in the $yz$-plane (see Fig. 1.2).

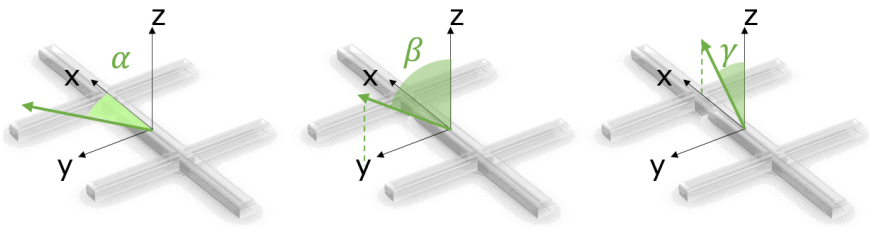


Figure 1.2.: Definition of angles: $\alpha$ is the angle with the $x$-axis in the $xy$-plane, $\beta$ is the angle with the $z$-axis in the $yz$-plane and $\gamma$ is the angle with the $z$-axis in the $xz$-plane.

The ordinary Hall effect also influences the longitudinal resistance of the conductor, leading to ordinary magnetoresistance (OMR) in addition to the normal resistance of the conductor $R_0$. The change of resistance due to an external magnetic field can be described by Kohlers rule [36] as $\Delta R/R_0 = F\left(\frac{B}{R_0}\right)$, where $F$ depends on the properties of the material under investigation and $B$ is the magnetic flux density. For a two-dimensional charge carrier, the resistance increases when the magnetic field is applied along the $z$-direction. This effect appears along side others of more interest, for example it has been observed in $Pt/Y_3O_5O_{12}$ bilayers as a parabolic increase of $\Delta R$ [37], independent of the magnetic state of the YIG. Similar to the Hall effect, we expect the longitudinal resistance change in a 2D system to follow:

$$\begin{aligned} xy &: R_{OMR} \propto 0 \\ xz &: R_{OMR} \propto \Delta R \mu_0 H \sin^2(\gamma) \\ yz &: R_{OMR} \propto \Delta R \mu_0 H \sin^2(\beta) \end{aligned}$$

However, real conducting structures generally posses a finite thickness in $z$-direction. Both OHE and OMR can thereby also give a contribution to the longitudinal resistivity, when the field is applied in the $y$-direction [15]. This leads to a finite effect also, when the field is rotated in the $xy$-plane.

### 1.6.2. Spin Hall effect (SHE)

The mechanisms of SHE are very similar to the well understood AHE [38] (Skew scattering, side jumps and intrinsic mechanisms). However, the SHE effect can be observed in non-magnetic metals with large spin-orbit coupling [39]. The heavy metal (HM) Pt is commonly used due to its reproducible properties. In the absence of a magnetic field, charge carriers are scattered asymmetrically and spin-dependently leading to a pure spin current perpendicular to the charge current and a resulting spin accumulation at the interface of the conductor. Likewise, the reverse process called the inverse spin Hall effect (ISHE) exists: a pure spin current generates a transverse charge current. A sketch of each process is shown in Fig. 1.3. The SHE and ISHE become even more interesting if one considers a bilayer system of a magnetically ordered insulator (MI) and a HM. The spin current then interacts with the order parameter of the MI. The order parameter can be either the magnetization $\mathbf{M}$ [39, 40] or the Néel vector $\mathbf{N}$ [41, 42] depending on the MI. For now, we will focus on ferromagnetic insulator (FMI) with $\mathbf{M}$ as an order parameter and will later point out the differences in the case of sensitivity to $\mathbf{N}$.
In a ballistic picture, the spin current $\mathbf{J_S}$ perpendicular to the interface leads to a spin accumulation with spin polarization $\boldsymbol{\mu}$ parallel to the interface ($y$-direction) as depicted in Fig. 1.3 (a). The spin current can interact with the magnetic ions at the interface to the FMI. If the magnetization $\mathbf{M}$ of the FMI is parallel to the spin polarization $\boldsymbol{\mu}$ at the interface, the spin current into the FMI is zero. The spins at the interface are reflected back into the HM generating an opposing spin current to $J_S$.

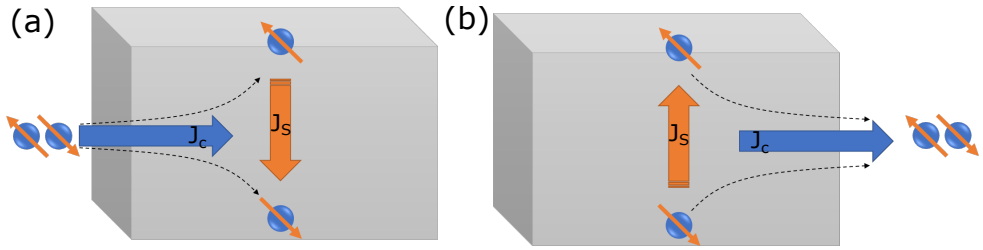


Figure 1.3.: (a) Sketch of the spin Hall effect. A charge current $\mathbf{J_C}$ (blue arrow shows the technical current direction) leads to a transverse spin current $\mathbf{J_S}$ and a spin accumulation at the interface. (b) Sketch of the inverse spin Hall effect. A spin current $\mathbf{J_S}$ leads to a transverse charge current $\mathbf{J_C}$.

By the ISHE, a parallel contribution to $J_C$ is generated leading to an effective low-resistance state. If $\mathbf{M}$ is perpendicular to $\boldsymbol{\mu}$, a spin current is absorbed by the FMI, acting as a spin-transfer torque [39, 43]. Therefore, the reflection of spins is suppressed, decreasing the additional contribution to $J_C$ and leading to an effective high-resistance state. The absorption of spin current by the FMI depends on the material and surface quality, which collectively is dictated by the spin-mixing conductance $G^{\uparrow\downarrow}$ [44]. $G^{\uparrow\downarrow}$ is a complex number that can be expressed as $G^{\uparrow\downarrow} = G_r^{\uparrow\downarrow} + iG_i^{\uparrow\downarrow}$ and represents the spin-transparency of an interface. The transfer of spin through the HM/FMI interface is given by

$$J_S = \frac{G_r^{\uparrow\downarrow}}{4\pi}\mathbf{M} \times \mu \times \mathbf{M} + \frac{G_i^{\uparrow\downarrow}}{4\pi}\mu \times \mathbf{M}.$$

The transverse resistance is modulated as [43]

$$\Delta R_T \propto \Delta R_{1,m}\mathbf{M}_x\mathbf{M}_y + \Delta R_2\mathbf{M}_z. \tag{1.9}$$

and the longitudinal resistance as

$$\Delta R_L \propto \Delta R_{1,m}(1 - \mathbf{M}_y^2) \tag{1.10}$$

$\Delta R_{1,m}$ depends on the properties of the HM layer and the real part of the spin mixing conductance $G_r^{\uparrow\downarrow}$, while $\Delta R_2$ is connected with the imaginary part of the spin mixing conductance $G_i^{\uparrow\downarrow}$. The change of resistance due to SHE is referred to as spin Hall magnetoresistance (SMR). The change of transverse resistance due to the $M_z$ component is often referred to as spin Hall anomalous Hall effect (SHAHE) [43]. Using a magnetic field to manipulate the magnetization direction of the FMI, the magnetic state of the FMI can be traced by measuring this effect. If one assumes that the magnetization $\mathbf{M}$ follows the external magnetic field $\mathbf{H}$, uniaxial measurements in the $x$- and $z$-directions lead to an increase of the resistance, because the magnetization rotates away from the $y$-direction. Likewise, measurements with an external field applied in $y$-direction will lead to a decrease of the longitudinal resistance. For rotation

measurements, the following dependencies can be concluded for $R_T$:

$$\begin{aligned} xy &: R_T = \Delta R_{1,m} M \cos(\alpha) \sin(\alpha) \\ xz &: R_T = \Delta R_2 M \cos(\gamma) \\ yz &: R_T = \Delta R2 M \cos(\beta) \end{aligned}$$

and for $R_L$:

$$\begin{aligned} xy &: R_L \propto \Delta R_{1,m} M \cos^2(\alpha) \\ xz &: R_L \propto 0 \\ yz &: R_L \propto \Delta R_{1,m} M \cos^2(\beta) \end{aligned}$$

Here, we adapt the notation from Fig. 1.2.
In contrast to FMIs, in AFMs, there are two magnetic sublattices present. One can perform the summation over both sublattices and find that the change of $\Delta R_{1,n}$ is then associated with the Néel vector instead of the magnetization [45]. While the magnetization direction directly follows the magnetic field direction, the Néel vector tends to orientate 90° to **H**. This manifests itself in a 90° shift in rotation measurements. Equations 1.10 and 1.9 are then rewritten as

$$\Delta R_L \propto \Delta R_{1,n}(1 - \mathbf{N}_y^2) \tag{1.11}$$

and

$$\Delta R_T \propto \Delta R_{1,n} \mathbf{N}_x \mathbf{N}_y + \Delta R_2 \mathbf{M}_z. \tag{1.12}$$

Note that the second term in equation 1.12 is dependent on **M**, not on **N**. A finite moment acts as a field-like torque and is expected to be zero in a compensated AFM, but as will be discussed in later chapters, a full interpretation of the SMR in antiferromagnets requires consideration of this additional term. Ignoring anisotropy, the Néel vector **N** tends to align perpendicular to **H**. This gives a plane of possibilities where the Néel vector could lie. The actual orientation of the **N** depends on the material properties. The angular dependencies of easy-plane AFMs NiO [15, 46] and $\alpha$-$Fe_2O_3$ (hematite) [41] have shown complicated behavior for $R_T$, depending on the relative angle of the easy magnetic plane and the $xy$-plane. If the $xy$-plane coincides with the easy plane, one observes a 90° phase shift compared to if $R_T$ depend on **M**:

$$xy : R_T = -\Delta R_{1,n} N \cos(\alpha) \sin(\alpha)$$

and for $R_L$:

$$xy : R_L \propto \Delta R_{1,n} N \sin^2(\alpha)$$

This resistive behavior is referred to as 'negative SMR'. We mention that the above equations are not necessarily valid for every AFM/HM bilayer. While for e.g. for NiO and hematite SMR data can be explained using these formulas, other experiments at AFM/HM bilayers show a SMR dependence on the canted moment **M** and not on **N**, like for the AFM $SrMnO_3$ [47] and $SmFeO_3$ [40].
Not only rotational, but also uniaxial measurements will experience a change in resistivity if the structure is chosen correctly so that the spin flop under a field changes the

$y$-component or $xy$-component of $R_L$ and $R_T$. The SHE can not only be used to determine the magnetic state of a MI. The pure spin current generated in the HM can be absorbed by the MI, leading to the excitation of magnons that can propagate within the material and be read out at a spatially separated position. The long-distance spin transport has been shown in several ferromagnetic compounds like $Y_3Fe_5O_{12}$, as well as recently in antiferromagnetic $Fe_2O_3$ bulk [34] and thin film [S2] samples, and recently in the bulk antiferromagnetic orthoferrite $YFeO_3$ [S8], opening new pathways towards spin- and wave-based computing. Another application for the SHE is utilization of spin orbit torque by the spin accumulation on the MI making efficient electrical switching of the magnetization possible [S1, S4, S5].

### 1.6.3. Hanle effect

The Hanle effect describes the dephasing of spins due to precession and diffusion in an external magnetic field [48]. This can lead to a magnetoresistive effect [49] named Hanle magnetoresistance (HMR) [50, 51]. The HMR has the same symmetry as SMR for a FM/HM bilayer, but the signal depends on the magnitude of the applied field. This manifests itself in an increase of the signal in $R(H)$ measurements with increasing field strength despite the magnetization of the FM being already saturated. The change of longitudinal resistance can be expressed as [50]:

$$\Delta R_L = \Delta R_1'(1 - H_y^2) \tag{1.13}$$

and the change of transverse resistance as

$$\Delta R_T = \Delta R_1' H_x H_y + \Delta R_2' H_z. \tag{1.14}$$

$H_i$ are the components of the magnetic field in $x$ (along the Hall bar), $y$ (perpendicular to the Hall bar in plane) and $z$ (out of plane) direction. The HMR is independent of the adjacent MI layer and can be observed in a free standing HM layer. In an experiment with an AFM/HM bilayer, where the SMR can be sensitive to a field-induced, canted moment, the HMR and SMR will be difficult to disentangle, because the magnitude of the net moment will continuously increase without saturating up to very high magnetic fields.

## 1.7. Spin caloric effects

In the previous section, we have discussed magnetoresistance and Hall effects. In a wider perspective, the ordinary Hall effect is a electrical response to an electrical current as an input. The spin Hall effect on the other hand is gives a spin current as a response to a charge current. One can extend this list of effects by allowing for heat currents and the inter-conversion between these and spin- and/or charge currents. In 1821, T.J. Seebeck discovered that in metals and semiconductors, a heat current can be converted into a charge current, after whom this effect, the Seebeck effect, is named. Due to its similar geometry, the spin Seebeck effect is named in a similar

fashion, describing the inter-conversion between heat and spin currents. This effect is used in this thesis to investigate garnet heterostructures (chapter 4).

### 1.7.1. Spin Seebeck effect

The spin Seebeck effect (SSE) describes the generation of a spin current (magnons in the case of insulators, see section 1.5) as a response to a heat gradient $\nabla \mathbf{T}$ [52, 53]. The established method to measure the SSE in insulators is via the longitudinal spin Seebeck effect. In this geometry, the heat gradient is applied perpendicular to the surface. The spin current is detected via the ISHE in an adjacent heavy metal layer. The electric field in the Pt layer due to the SSE can be described as [53]:

$$\mathbf{E} = (\theta\rho)\mathbf{J}_s \times \sigma. \tag{1.15}$$

Here, $\theta$ and $\rho$ are the spin Hall angle and the resistivity of the Pt, respectively, $\mathbf{J}_s$ the spin current perpendicular to the surface and $\sigma$ is the spin-polarization vector, which is parallel to the magnetization $\mathbf{M}$ of the insulator. A whole spectrum of magnons is excited by the thermal gradient, which can contribute differently to the SSE signal. The contribution of a magnon branch to the ISHE signal depends on the coupling strength of the magnons to the heavy metal, i.e. the spin mixing conductance and defines the amplitude of the SSE signal. Different magnons may carry different angular momentum leading to a different sign in the SSE signal. Since the occupation of magnon modes can vary with temperature, this can lead to a complex behavior of the SSE signal [33, 54]. In this work, SSE measurements have been performed at YIG-GIG heterostructures presented in chapter 4.

# 2. Materials

This chapter focuses on the materials that have been investigated in the course of this thesis. There is $TmFeO_3$, a representative of rare earth ferrites, belonging to the large family of perovskites. Secondly, we employ $Y_3Fe_5O_{12}$ and $Gd_3Fe_5O_{12}$, famous representatives of the garnet family. All of these materials are magnetically ordered oxides and promising candidates for novel spintronic devices. In this thesis, we will employ the effects described in the previous chapter to access the properties of these materials.

## 2.1. Perovskites

Originally, perovskites described oxygen-based materials with the chemical formula $ABO_3$ like the first known representative, naturally occurring $CaTiO_3$ [55]. Nowadays, the term perovskites describes material composition with the general formula $ABX_3$ with the arrangement shown in Fig. 2.1, and can be found in diverse applications including solar cells [56, 57], superconductors [58] and multiferroics [S3, 59, 60]. Here, we focus on the 'classical' $ABO_3$ perovskite, modeled by assuming that the oxygen forms $O^{2-}$ ions while $A$ and $B$ are positively charged ions, where the $A$ ion has the larger atomic radius. Depending on the size of the $A$ and $B$ ions, the unit cell has different symmetry. How 'cubic' a perovskite is can roughly be determined by the Goldschmidt tolerance factor [61]. The structure of a perfectly cubic perovskite material is shown in Fig. 2.1. The figure represents the unit cell of $SrTiO_3$ (STO).

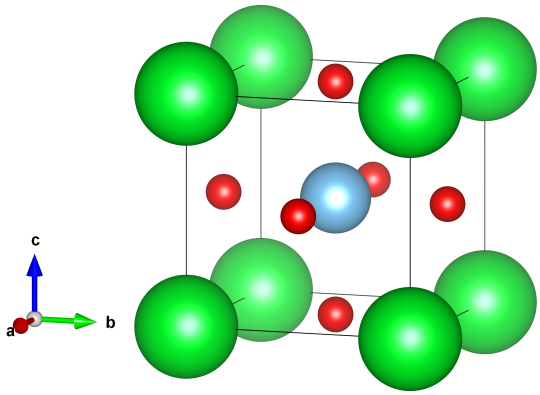


Figure 2.1.: Cubic perovskite structure for $SrTiO_3$. Green: $Sr^{2+}$, blue: $Ti^{4+}$, red: $O^{2-}$. Drawn in Vesta [62].

It is characterized by its cubic symmetry ($a = 3.905\,\text{Å}$), insulating and diamagnetic properties. In this work, STO has been used as substrate material for thin film deposition of $TmFeO_3$, which will be introduced below. The investigation of perovskite oxides continues the tradition of our group in this research area [S3, 63–68].

## 2.2. Rare earth orthoferrites

Research into rare earth (RE) orthoferrites, $REFeO_3$, began in the 1950s with analyzing the magnetic and structural properties of $GdFeO_3$ [69, 70]. The structure is similar to that of perovskites but, due to distortions, the symmetry is lowered. The unit cell consists of four perovskite 'units' building up an orthorhombic unit cell with lattice constants being roughly $\sqrt{2}a_p \times \sqrt{2}a_p \times 2a_p$, with $a_p$ being the pseudocubic lattice constant of a perovskite unit. The magnetic ordering temperature $T_N$ of this class of materials is around 600 K to 750 K depending on the RE ion [71]. Due to super-exchange coupling via the oxygen ions (see 1.1), the iron magnetic moments of the $Fe^{3+}$ ions couple antiferromagnetically, leading to a $G$-type antiferromagnetic structure [72]. The super-exchange coupling is attributed to virtual hopping of electrons between the $d$-electrons of the iron ion and the $p$ shell of the oxygen ion [24]. However, the perfect antiparallel alignment of the iron spins in orthoferrites is prohibited by the antisymmetric Dzyaloshinskii-Moriya interaction (DMI) [26, 27, 73]. A significant canting [74] between the irons spins creates a weak ferromagnetic moment $\mathbf{M}$ perpendicular to both the Néel vector $\mathbf{N}$ and DMI vector. For all orthoferrites just below the Néel temperature, $\mathbf{M}$ is along the $c$-axis and $\mathbf{N}$ along the $a$-axis. In Bertaut's notation [75] this can be expressed as $G_xA_yF_z$, also called the $\Gamma_4$ state. Translating this to the nomenclature used here, this corresponds to $N_aA_bM_c$ since $a$ ($x$), $b$ ($y$) and $c$ ($z$) are the crystallographic axes, $N$ ($G$) is the Néel vector, $M$ ($F$) is the ferromagnetic vector and $A$ is another linear combination of the four iron spins in each unit cell. The behavior of a rare earth crystal under magnetic fields and temperature changes can be calculated using the model introduced in section 1.1. This is presented in the appendix section A.1.

#### $TmFeO_3$

$TmFeO_3$ belongs to the family of orthoferrites. The lattice parameters for this material are $a = 5.251\,\text{Å}$, $b = 5.576\,\text{Å}$ and $c = 7.584\,\text{Å}$ [76]. The magnetic ordering temperature for Fe ions is 632 K [74]. Regarding the Tm ions, they possess 12 4f electrons in the outer shell. Thus, according to Hund's rules, we have $S = 1$ and $L = 5$, leaving us with $J = 6$. So the $Tm^{3+}$ ion is magnetic, but the interaction between the ions is weak so that they do not show ferromagnetic coupling at any given temperature [72, 77]. However, the Fe sublattices generate an effective field at the Tm site, which leads to the polarization of the Tm moment contributing to the overall magnetization. Also, the RE-Fe interaction leads to a strong temperature-dependence of the magnetic anisotropy and the SRT from the $\Gamma_4$ state to the $\Gamma_2$ ($G_zC_yF_x$ [75]) state. The SRT happens in the temperature region between $T_2 = 92\,\text{K}$ and $T_1 = 84\,\text{K}$ [72]. Within

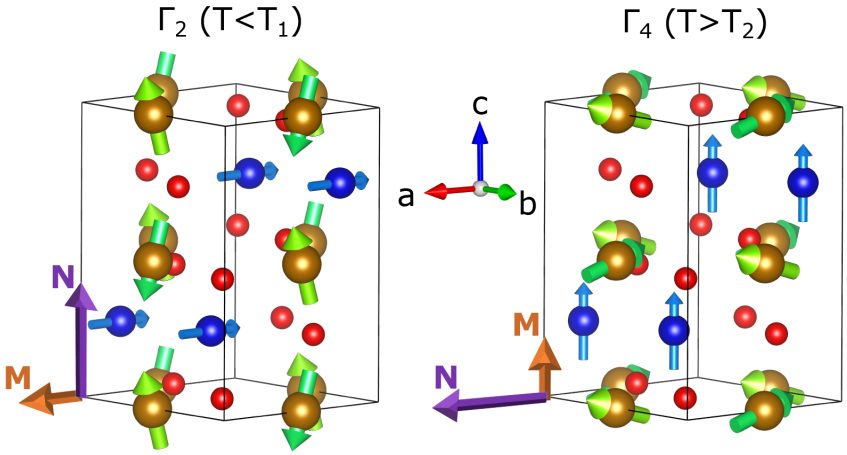


Figure 2.2.: Orthorhombic structure of TFO. Fe ions are orange, Tm ions are blue, O ions are red. Green arrows indicate the spins of the Fe ions pointing along the $a$-axis above the spin reorientation transition (right, $\Gamma_4$ phase) and along the $c$-axis below the spin reorientation transition (left, $\Gamma_2$ phase). The arrow **N** indicates the direction of the Néel vector, **M** indicates the direction of the canted moment. The blue arrows indicate the polarized Tm moments. The dimensions of arrows are not to scale. Vesta [62] has been used to draw the figure.

the transition **N** and **M** rotate smoothly in the $ac$-plane. Above the SRT, the Tm moments are parallel to the canted moment while below the SRT, the Tm moments are antiparallel to the canted moment [71].
We can describe the magnetic states of TFO mathematically as done for a general orthoferrite in the appendix section A.1. Key result of this calculation is that the canting angle of the Fe sublattices is determined by the relative magnitude of the asymmetric and symmetric exchange fields (see equation A.7). Applying a magnetic field parallel to the magnetization leads to an increase of the canting angle, which scales about linear with external magnetic field (equation A.8). If a magnetic field is applied parallel to **N**, this leads to a 90° rotation of all spins and thereby a simultaneous rotation of both **M** and **N**. This corresponds to a field-induced SRT from $\Gamma_4 \rightarrow \Gamma_2$ for $\mathbf{H} \parallel a$ and $T > T2$ and $\Gamma_2 \rightarrow \Gamma_4$ for $\mathbf{H} \parallel c$ and $T < T_1$. At the spin flop field $H_{sf}$ (also called spin reorientation field), the rotation is complete. The magnitude of $H_{sf}$ depends on the anisotropy of the sample (see equation A.9). The spin reorientation does not appear as an abrupt transition as for example seen e.g. in hematite [78] or $MnF_2$ [79], but happens gradually. This means that already small magnetic fields can lead to a reorientation within the $ac$-plane of **N** and **M** by a few degrees. Experiments have shown that the spin-flop field in TFO is of the order of $H_{sf} \approx 11\,\mathrm{T}$ for TFO [80] at room temperature. Due to the decrease of magnetic anisotropy towards the SRT, $H_{sf}$ is also decreased and goes to zero at the borders of the SRT [81].
The properties of TFO have been analyzed mostly at bulk samples. There are few re-

ports on TFO thin films, which exhibit polycrystalline growth [82, 83] or a hexagonal structure [22, 84]. This motivates the growth and characterization of orthorhombic TFO thin films. The hexagonal phase exists only in thin films and has different properties compared to the orthorhombic bulk structure. It is reported that the hexagonal structure of TFO possesses multiferroic properties. They are in focus of photovoltaic research due to their high stability, environmental safety and high photovoltages [85]. The properties of the hexagonal TFO phase are in more detail discussed in section 2.3.

## 2.3. Hexagonal rare earth ferrites

A material class closely related to orthoferrites are the rare earth *manganites* $REMnO_3$. The atomic radii of $Fe^{3+}$ and $Mn^{3+}$ are very similar [86], so one would expect an identical structures from the Goldschmidt tolerance factor [61]. However, one observes that $REMnO_3$ crystallize with a hexagonal structure (Fig. 2.3) rather than the orthorhombic phase of $REFeO_3$, likely due to the different electronic structures [87].
The hexagonal structure of RE manganites in their bulk form is known already since

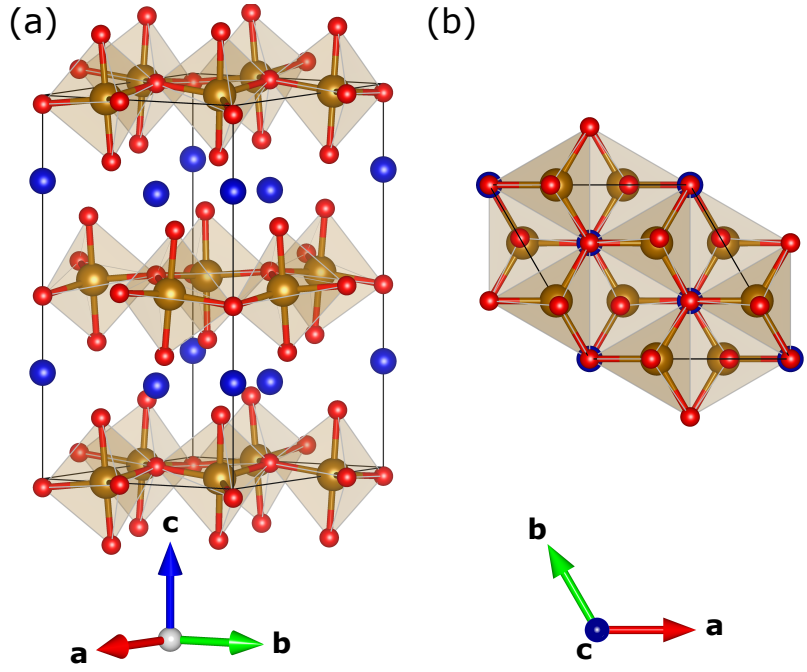


Figure 2.3.: Unit cell of a hexagonal rare earth ferrite drawn in VESTA [62]. Rare earth ions are drawn in blue, oxygen ions in red and iron ions in brown. The polyhedral coordination of the iron ion is indicated. (a) depicts the side view and (b) the top view.

the sixties [88]. The hexagonal phase of rare earth ferrites is metastable, but could recently be stabilized in special systems, like e.g. by chemical routes [89] or in thin films grown on substrates with special symmetry [22, 84, 90]. These hexagonal show several interesting properties, but the one attracting the most attention in recent years, is multiferroism [91–93], which means that ferroelectric and ferromagnetic ordering exist simultaneously in the material. This is especially interesting if the order parameters are coupled to each other so that the magnetization can be manipulated by an electric field or the polarization can be manipulated by a magnetic field. In the course of this thesis, thin films of hexagonal $TmFeO_3$ (h-TFO) were realized in order to investigate the manipulation of the magnetic state by an electric field. The magnetic response is then determined by magnetic measurements. Moreover, we propose a device concept where the magnetic state of the h-TFO is read-out by all-electrical spin Hall magnetoresistance. This magnetoelectric coupling is of great interest for magnetoelectric data storage devices and other spintronic device concepts [94].

## 2.4. Garnets

Rare earth iron garnets $RE_3Fe_5O_{12}$ belong to the family of garnets with the generalized sum formula $\{c_3\}[a_2](d_3)O_{12}$. They possess a complex cubic lattice structure with 160 atoms per unit cell as depicted in Fig. 2.4 (a) [95]. There are in total 24 d-sites in the

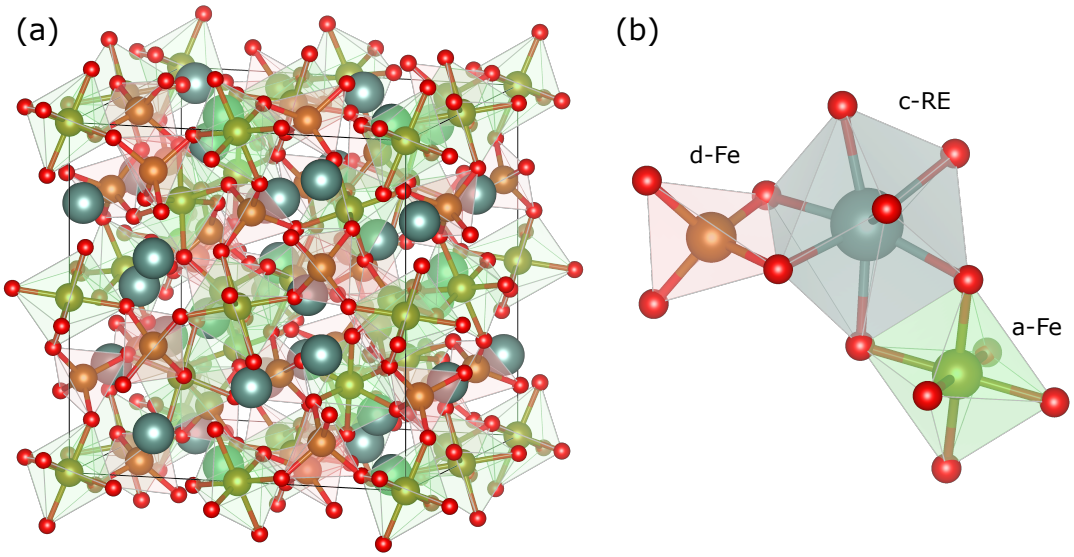


Figure 2.4.: (a) Unit cell of a rare earth garnet with oxygen atoms in red, iron atoms in orange and green and rare earth ions in turquoise. (b) Reduced garnet crystal structure with the relative alignment of the tetrahedrally coordinated d-Fe, the octahedrally coordinated a-Fe and the dodecahedrally coordinated c-RE site.

garnet unit cell, which are tetrahedrally coordinated by oxygen ions, 16 octahedrally coordinated a-sites and 24 dodecahedrally coordinated c-sites. The a- and d-sites are occupied by $Fe^{3+}$ ions, the c-sites by $RE^{3+}$ ions. This is depicted in the simplified structure in Fig. 2.4 (b). The $Fe^{3+}$ ions possess a total spin angular momentum of $5\,\mu_B$. The spins on the a-sites couple ferromagnetically to each other forming a magnetic a-Fe sublattice and similarly, the spins on the d-sites form a ferromagnetic d-Fe sublattice. The coupling between these two sublattices is antiferromagnetic. In the following, two garnets which have been used in this thesis, are presented. The lattice parameters of these are given in table 2.1. The small difference between these parameters makes them ideal candidates for heteroepitaxial growth. Due to the good lattice matching, the paramagnetic insulator gadolinium gallium garnet ($Gd_3Ga_5O_{12}$, GGG) has been used as substrate to grow iron garnet thin films.

| Garnet | Lattice Parameter (Å) |
|---|---|
| $Gd_3Ga_5O_{12}$ | 12.383 [96] |
| $Y_3Fe_5O_{12}$ | 12.376 [95] |
| $Gd_3Fe_5O_{12}$ | 12.472 [97] |

Table 2.1.: Lattice parameters of iron garnet structures used in this thesis in comparison with GGG lattice parameter used as a substrate.

### $\mathbf{Y_3Fe_5O_{12}}$

Yttrium iron garnet ($Y_3Fe_5O_{12}$, YIG) is the 'fruitfly of magnetism' [98]. Due to its desired properties like low magnetic anisotropy, low magnetic damping and high chemical stability, it is the material of choice for many projects in the spintronic research community [99]. The c-site is occupied by nonmagnetic $Y^{3+}$. The magnetic properties are thereby defined by the a-Fe and d-Fe sublattices. Due to the different number of a- and d- sites, YIG is a ferrimagnet with one excess Fe spin ($5\ \mu_B$) per formula unit, corresponding to a magnetization of around $140\,kAm^{-1}$ at 300 K [100]. Magnetic ordering of YIG persists until the Curie temperature of $T_C = 560\,K$ [100]. The Fe sublattices are strongly antiferromagnetically coupled so that the inter-lattice coupling cannot be broken with magnetic fields available in our labs. Applying a magnetic field to a YIG sample leads to a coincident movement of both sublattices. For the investigations described in this thesis, we can therefore simplify the magnetic properties of YIG by introducing one effective magnetic lattice.
Concerning electrical properties, YIG possesses an electron gap of $\Delta E \approx 2.6\,eV$ [101], making it a good insulator. This is beneficial when performing magnon transport or spin Hall effect experiments since no current flow in the YIG layer has to be taken into account.

### $\mathbf{Gd_3Fe_5O_{12}}$

In Gadolinium iron garnet ($Gd_3Fe_5O_{12}$, GIG), the c-site is occupied by paramagnetic $Gd^{3+}$ ions. These have 7 electrons in the 4f shell and according to Hund's rules, the ion has a spin angular momentum of $S = 0$ and an orbital angular momentum of $L = 7$. The direct exchange interaction between the Gd moments is weak, however, the effective field created at the c-site by the Fe sublattices leads to a polarized moment which aligns antiparallel to the net Fe moment. Due to the temperature-dependence of the Gd moment, GIG possesses a magnetic compensation point $T_{comp,G}$ at which the the Gd moment is as large as the net Fe moment [102]. Applying a magnetic field to a GIG sample when cooling through $T_{comp,G}$, all magnetic sublattices reverse. The complex magnetic behavior has been the target of research in the Kläui group in the recent past. In particular, spin Seebeck effect (SSE) measurements has been measured across a large temperature rage revealing a so-called second compensation point, where the SSE signal reflects changes to the magnon mode occupation [33, 103].

# 3. Methods

The work presented in this thesis covers the growth of heteroepitaxial thin films using the materials introduced in the previous chapter. The techniques for fabricating these samples as well as the key methods to investigate the crystallographic properties are presented in this chapter. The methods for measuring bulk magnetic properties of the samples are presented. We further present a setup for magnetoelectric measurements together with a proof of concept. Finally, we describe the techniques for surface-sensitive electrical transport measurements.

## 3.1. Pulsed laser deposition

Pulsed laser deposition (PLD) belongs to the category of physical vapor deposition, like sputtering. It is a powerful technique to grow high quality thin films of effectively any material composition and is the main technique for the thin films developed in the course of this thesis. The key advantages compared to sputtering, are that the target can be relatively small in size and thereby cheaper, and that the material transfer from the target to the substrate is stoichiometric. Furthermore, PLD can be performed in a broad range of gas pressures down to ultra high vacuum. During the deposition, in-situ diagnostics with RHEED (reflection high energy electron diffraction) is possible due to the absence of magnetic and electric fields [104].
The principle of PLD is as follows; a high-energy ultra violet (UV) laser pulse is guided on a target, a block of material with the composition of interest. The UV light breaks the bonds of the material at the surface of the target. The atoms become ionized and accelerate perpendicular to the target surface. Some distance away from the target, a substrate, where the thin film of the material is aimed to be grown on, is positioned. In our case the substrate is heated in order to transfer kinetic energy to the incoming target material, so it can form crystallites on the surface. In this work, we focus on oxide compositions. Therefore, an oxygen background pressure is generated to assist the growth of the material in the desired stoichiometry. The source of UV light is a KrF laser with 248 nm wavelength. The laser, a Coherent COMPex Pro 205, emits laser pulses of 20 ns duration at a frequency between 1 and 50 Hz. The typical energy of one pulse is around 200 mJ when created in the laser. The light is guided through an optical system of mirrors and lenses, and projected at an angle of 45° on the target surface as suggested by the manufacturer [105]. The energy density at the target is around 860 $mJ/cm^2$, which is spread homogeneously over the area of the laser spot. In order not to shoot a hole in the material, the target is moved back and forth and simultaneously rotated during the deposition. Details of the setup can be found in [106]. During this PhD, the PLD setup was constantly maintained and improved by

the author, enabling further successful projects like the investigation of $Tm_3Fe_5O_{12}$ [S1, S4, S5, S9]. In this work, PLD has been used for the deposition of YIG-GIG heterostructures (see chapter 4) and TFO thin films (see chapter 6).

## 3.2. DC magnetron sputtering

The second physical vapor deposition technique used in this work is DC magnetron sputtering (short: sputtering). This method is based on the ionization of gas ions in a large electric field close to the target. The ions are accelerated towards the target, where they transfer kinetic energy to the material. These atoms diffuse to the substrate placed above the target. Simultaneously, more gas atoms are ionized due to the creation of ions and free electrons. The plasma is confined close to the target by strong magnetic fields stemming from permanent magnets inside the cathode. This technique works well for noble metals as used in this work. It is employed for deposition of noble metals given that PLD is not suited to their deposition due to the creation of droplets in the sample caused by local melting of the metal [107]. Additionally, from a manufacturing perspective, magnetron sputtering is easily scalable and therefore used in industrial thin film processing. When depositing compound materials, one has to be aware of the fact that sputtering process itself does not lead to a stoichiometric transfer from the target to the substrate, since the momentum transfer from the ionized gas to the target atom leads to different sputtering rates of the atoms, depending on their mass. However, a pre-sputtering process can reduce this effect [108]. Like for PLD, the substrate can be heated to enable the creation of a crystal structure of the deposited material. In this work, sputtering was preliminary used to deposit Pt at room temperature for spin Hall effect measurements and Gold for conducting bonding pads on YIG-GIG heterostructures (Ch. 4), as well as TFO bulk crystals (Ch. 5 and thin films (Ch. 6.1). The Pt deposited at room temperature is not long-range ordered. However, we also used sputtering also to deposit an ordered Pt layer as a bottom electrode for a material (Sec. 6.3). In this case, the crystallographic order of the Pt is important and therefore, it is deposited at elevated temperatures.

## 3.3. X-ray diffraction

X-ray diffraction is a technique that relies on the scattering of electromagnetic waves in the nm-range from lattice planes of the crystal. It allows one to investigate the structural properties of a sample. The essential formula is $\mathbf{Q} = \mathbf{G}$, indicating that one detects a signal when the scattering vector $\mathbf{Q}$ is equal to a reciprocal lattice vector $\mathbf{G}$. A detailed explanation can be found in [109]. Here, we focus on the specific types of measurements which have been performed in the course of this work.
The instrument used to perform the x-ray measurements in this thesis is a Bruker D8 Discover 4-circle diffractometer equipped with a Cu anode. In this setup, the measurements are performed in the Bragg-Brentano geometry. The x-rays exit the Cu anode in line-focus and are then reflected from a Göbel mirror collimating the x-ray

beam and monochromizing it to a certain degree. The beam is then guided through a slit to confine it. To further suppresses contributions to the x-ray spectrum other than the Cu $K_\alpha$ radiation, a 2-bounce Ge channel-cut monochromator is used. The beam then hits the sample, which can be rotated around three perpendicular axes, so that every lattice plane can be accessed. The reflected beam then passes through a set of motorized slits before being absorbed in the point detector. Different axes of the diffractometer can be moved independently from each other, yielding different information. In the following, the different scans used in this work are described.

### $2\Theta/\omega$ scans

In this measurement geometry the angle of incoming and outgoing x-ray beam are simultaneously increased so that $\omega = \Theta$. This corresponds to the increase of scattering vector $\mathbf{Q}$ in one direction. If a reciprocal lattice vector of the sample is parallel to $\mathbf{Q}$, one finds a peak in the spectrum, when $\mathbf{Q} = \mathbf{G}$. Since the modulus $\mathbf{G}$ is closely related to the lattice plane spacing $d_{hkl}$ by $\frac{|\mathbf{G}|}{d_{hkl}}$, one can determine the dimensions of the unit cell of the material when scanning in different directions of the crystal. From this expression the well known Bragg formula can be derived: $n\lambda = 2d \sin\Theta$, where $n$ is the order of the reflection, $\lambda$ the wavelength of the x-rays, $d$ the spacing of the lattice planes and $\Theta$ the angle of the incoming x-ray beam with the lattice planes. These reflexes provide essential information about the thin film sample under investigation. Comparing the values of a thin film with those from bulk samples, one can determine the type of growth, whether strained or relaxed. The relative intensity of the peaks can also give information about the atomic order of the material [106, 110].

From the width of the peak one can learn about the size of the crystallites that causes the reflex. The Scherrer formula is often used for powder samples, but also gives some idea of crystallite size $L$ in thin films: $L = \frac{L\lambda}{\Delta\Theta \cos\Theta}$, where $K$ is a correction factor that we put here as 1, $\lambda$ is the wavelength of the x-rays, $\Delta\Theta$ is the width of the peak and $\Theta$ the angle at which the reflex occurs [111]. Here we use the Scherrer formula as a rough estimate for the crystallinity of the sample. For quantitative analysis, more care has to be taken of the $K$ factor. For a single crystalline sample measured in the out-of-plane geometry, the value of $L$ gives the thickness of the thin film.

One more feature we focus on when analyzing $2\Theta/\omega$ scans is the occurrence of finite size oscillations, which are also called Laue oscillations. They are visible only when the lattice planes are very parallel to each other. The periodicity of the oscillation is linked with the thickness of the scattering volume [112].

A third method to determine the thickness of a thin film is to perform a $2\Theta/\omega$ scan at grazing incidence. Close to total reflection, x-ray photons are not scattered at the lattice planes as discussed above, but by gradients in the electron density, so in other words, at interfaces. Multiple reflections within the layers lead to constructive interference of the outgoing x-rays, depending on the angle. This results in a spectrum containing so-called Kiessig fringes, which are linked to the thickness of the layer [113].

### Rocking curves

A rocking curve is a measurement where the detector is fixed at the $2\Theta$ position of a specific reflex. The sample is then rotated around the angle $\omega$. In a perfect crystal this would be a sharp peak at $\omega = \Theta$. However, if the sample consists of several crystallites which are tilted with respect to each other, this peak is broadened. The full width at half maximum (FWHM) is a measure for the broadness of the peak. In general, we fit the rocking curve with a Gaussian distribution. However, sometimes one observes more than one contribution to the rocking curve [106]. In practice, the rocking curve is performed after the $2\Theta/\omega$ scan. To perform the first scan, we align the crystal using the substrate reflex, which should be well known and possess strong intensity. In rocking curves, it can then be found that the peak is not centered at $\Theta$, which indicates that the axis of the thin film is not aligned with those of the substrate [S2].

### $\Phi$ scans

$\Phi$ describes the rotation of the sample around the out-of-plane-axis. To perform this measurement, the sample is tilted by the angle $\Psi$ to obtain an in-plane contribution of the scattering vector. $\Phi$-scans can tell us about the symmetry of the crystal and the relative growth orientation with respect to the substrate. Twinning, the occurrence of differently ordered crystallographic domains can also be easily detected using this method.

## 3.4. SQUID magnetometry

To investigate the magnetic properties of samples, a superconducting quantum interference device (SQUID) magnetometer is used. Using a Quantum Design MPMS XL the field- and temperature- dependent magnetic moment of the samples can be determined. As measurement mode, the reciprocal space option (RSO) has been chosen, where the sample is passed at a rate of 1 Hz through a second order gradiometer pick-up coil. Details on the working principle are given in detail in Ref. [114]. The SQUID has an internal fitting procedure to calculate the magnetic moment for every data point. The fitting routine assumes a point dipole so that every data point has to be corrected depending on the shape of the sample [115]. The magnetic moment of the sample can be measured at different temperatures and external magnetic fields. The SQUID can apply up to $\pm 5$ T in a temperature range of 2 to 400 K.

### Field-dependent measurements

In field-dependent magnetization measurements ($M(H)$), the temperature is kept constant and the field is ramped from a positive magnetic field to a negative magnetic field back to a positive magnetic field to be able to record a full hysteresis. Care has to be taken with regard to the substrate, which also contributes to the signal given

the bulk nature of SQUID measurements. In this work mostly diamagnetic substrates have been utilized. They contribute linearly with magnetic field. To determine the magnetic properties of the thin film grown on diamagnetic substrate, we subtract a linear fit from the raw $M(H)$ data. We are thereby left with only the nonlinear magnetic contribution. Possible additional linear contributions from the thin film are thereby omitted due to this background subtraction.

#### Temperature-dependent measurements

Performing temperature-dependent measurements ($M(T)$), the magnetization is fixed while the temperature gradually changes. During the temperature sweep, magnetization measurements are performed. During the measurements, the temperature is not fixed, however due to the relatively slow temperature sweep and the relatively quick nature of each measurement point, the small error due to the temperature drift is neglected. When performing $M(T)$ measurements, we will focus on the qualitative change of the magnetic moment of the sample and therefore not perform further corrections. We are aware that diamagnetic substrates lead to a constant offset in the $M(T)$ curve while paramagnetic components contribute by $1/T$.

## 3.5. Magnetoelectric measurement setup

To perform magnetoelectric measurements in the SQUID a rod was designed and constructed by the author to measure the in-plane magnetic response to an electric field. This could for example measure the magnetoelectric coupling in multiferroic bilayers. The setup was tested at the sample stack Pt (50 nm)/PNM-PT(110)/Pt(50 nm)/Ti(5 nm)/Ni(35 nm) of which the magnetoelectric properties have previously been described [116]. Given difficulties in the fabrication of magnetoelectric samples, as described in section 6.3, this setup has not been used in this work for new experiments. It might still be useful for future work, so the setup is described in this section. Therefore, we demonstrate here, that the rod works as intended.
The rod consists out of two aluminum stripes, where the the sample is being attached to. The two stripes are connected to the bottom and top electrode of the sample, respectively, so that there can be a voltage applied to it. The rod was tested using a sample grown by sputtering on piezoelectric PMN-PT (011) substrate ($[Pb(Mg_{0.33}Nb_{0.66})O_3]_{0.68}$-$[PbTiO_3]_{0.32}$). On each side, 50 nm Pt has been deposited to guarantee a homogeneous voltage distribution across the substrate. On the top side, 5 nm Ti and 35 nm Ni have been deposited. The Ti layer acts as an adhesion layer, while Ni is a magnetoelastic material. When a voltage is applied at the substrate, an in-plane strain is generated in the $x$- and $y$-directions. The strain is transferred to the Ni layer which alters its uniaxial magnetic anisotropy. The strain-induced change in anisotropy leads to a displacement of domain walls and a growing (shrinking) of energetically favored (unfavored) domains [116]. In the SQUID, this is visible by measuring the overall magnetization of the sample.

The sample is mounted with $y$ ($[01\bar{1}]$) along the sensitive direction of the SQUID. Initially, the sample is unpoled, meaning that it consists of domains with all possible polarization directions. The virgin curve has been measured as shown in Fig. 3.1 (a). For this measurement, a magnetic field of 50 mT has been applied to the sample. At this field, the background curve was measured and subtracted for the measurements with a voltage applied. Therefore, the signal at low voltages is zero and it only suddenly increases at an applied voltage of 160 V (equivalent to 160 kV/m across the 1 mm thick substrate). This is the voltage at which the PMN-PT substrate is poled, creating a single piezoelectric domain and abruptly changes strain in both the $x$- and especially in the $y$-direction. When first poling, the $y$ axis shrinks by an average of around 0.15%. As shown in ref. [117], when going from the unpoled to the poled state, the hysteresis loop in the $y$-direction becomes harder i.e. reducing the magnetization if $H$ is between 0 mT and 100 mT in line with the decrease of magnetization after the application of the poling voltage shown in Fig. 3.1. Once poled positively, the PMN-PT substrate changes its strain linearly in $x$- and $y$-direction when applying a positive voltage. This linear change of strain is converted to a linear change of the uniaxial anisotropy in the Ni layer, which changes its magnetization also linearly. This is shown in Fig. 3.1.

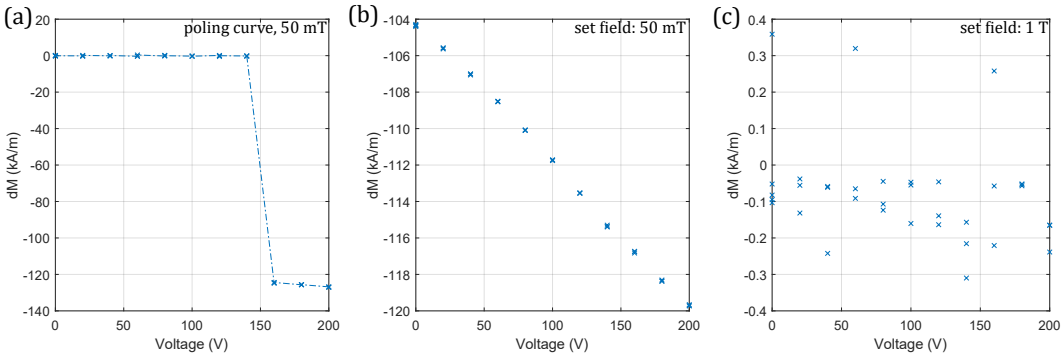


Figure 3.1.: Change of magnetization upon application of an electric field at a Pt/PNM-PT/Pt/Ti/Ni sample. (a) virgin curve at 50 mT (b) after poling at 50 mT subtracting the same background data (c) after poling at an applied magnetic field of 1 T subtracting another background file.

The magnetization decreases linearly with a slope of -0.079 kA/m/V. Taking into account the magneto-elastic coupling coefficient $\alpha = \mu_0 \frac{\Delta M}{\Delta E}$ one estimates $\alpha \approx 1 \cdot 10^{-7}$ s/m. This value has the same order of magnitude like the one determined by XMCD-PEEM [116] for patterned samples of a similar material stack. The fact that the $\alpha$ is lower in the presented experiment might stem from the different sample geometry. Here, we analyzed the behavior of a continuous film, while in [116] a patterned sample has been investigated. Therefore, a different shape anisotropy is present. Secondly, we measure the overall magnetization of the sample. We are therefore sensitive not only for the direction of the ferromagnetic vector, but also

to its length. In [116], the magnetization is determined using PEEM-XMCD, being sensitive to the direction of the magnetization, but not for the magnitude. One can also see that, once poled, the magnetic configuration of the Ni layer does not go back to the virgin state due to the permanent changes in strain along the $y$ direction [118]. To confirm that the signal stems only from the change of magnetization and not for example from the change of paramagnetic properties of the system, the measurement has been repeated under an applied field of 1 T, where the Ni layer is completely saturated, independent from the relative orientation of uniaxial anisotropy and magnetic field. As one can see in Fig. 3.1 (c), the magnetization does not change upon application of an electric field in the given range. This confirms that the signal measured is purely magnetic.
We have demonstrated that magnetoelectric measurements are indeed possible using this ME rod. It might be of use when determining the strain-dependent magnetization of $Mn_3NiN$ [119] or when investigating the voltage coupling at $Tm_3Fe_5O_{12}$/Pt interface [120] and remains the focus of future work.

## 3.6. Electrical measurements

Electrical transport measurements are performed in this work for insulator/Pt samples. Each sample is prepared in a way that the conducting Pt is defined as Hall structures (see 1.6.1. To do so, electron beam lithography is utilized. A positive mask is defined on the surface of the insulator. In a second step Pt is deposited on top and a lift-off technique is used to result in defined Pt Hall bars. To facilitate contacting individual devices, Au contacts are deposited, again using the lift-off technique. Due to Au being known for bad adhesion properties, a thin Cr or Ti layer of a few nanometers is deposited below the Au. The dimensions of the main channel of each Hall bar are 10 $\mu$m width and 100 $\mu$m length. The two set of arms of the Hall bar have a width of 3 $\mu$m and are separated by a distance of 55 $\mu$m along the Hall bar. The standard Pt thickness of the structure is 7 nm.
The structured sample is glued on a printed circuit board (PCB). Depending on the measurement, different PCB boards are available for in- and out-of-plane measurements as shown in Fig. 3.2. The PCB board is attached to a rotating element that is capable of rotating the sample in a magnetic field directed along the sample rod at fixed temperature. The rotator in use is the ANRv51RES from Attocube, which is based on piezoelectric elements. This allows us to apply the field in any arbitrary direction with respect to the sample. This then means that, not only can uniaxial measurements be performed, but also angular dependent measurements are possible. We can rotate over an angle range of 200°. To measure over a full rotation, the magnetic field has to be reversed.
The measurements are performed inside a cryostat that can access temperatures between 4 K and 300 K by He cooling. A superconducting magnet able to generate a magnetic field of up to 12 T during the measurements is used. We have used fields of up to 11 T in order not to go to the limits of the cryostat to prevent quenching

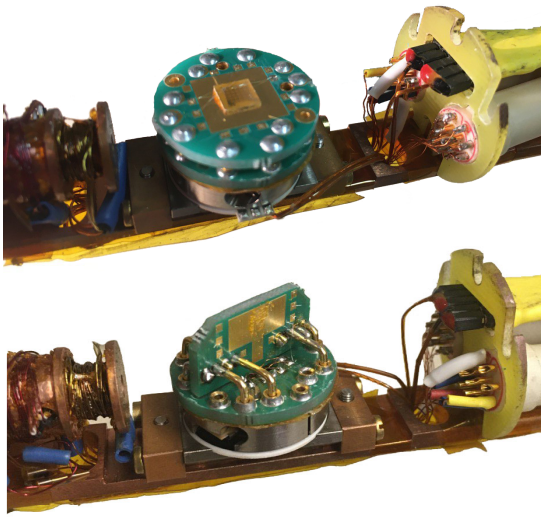

Figure 3.2.: Measurement rod equipped with an in-plane (top) and out-of-plane (bottom) sample holder.

of the magnet. Several measurement procedures are possible. One can measure the transverse and longitudinal resistivity as a function of temperature, magnetic field and rotation angle. If not stated otherwise, a charge current of $10^{-4}$ A has been passed through the Hall bar, which corresponds to a current density of around $1.4 \cdot 10^9$ A/m$^2$ for the above mentioned design. Every measurement is repeated 15 times to gather sufficient statistics. To compensate for an asymmetric Hall structure, the current $J$ is reversed and the 15 measurements are repeated. The transverse and longitudinal resistances $R_T$ and $R_L$ are the average of these 30 resistivity measurements for each data point. Since $R_L$ is sensitive to temperature fluctuations, some measurements allow for drift corrections assuming that the temperature fluctuates on a relatively large timescale.
For all of theses measurements we use a Keithley 2400 as a current source. To read the voltages two Keithley 2182A nanovoltmeters are utilized in order to simultaneously capture the longitudinal and transverse resistivites.

# 4. Magnetic coupling in YIG-GIG heterostructures

In this chapter, we investigate the material stack $Y_3Fe_5O_{12}$ (YIG) - $Gd_3Fe_5O_{12}$ (GIG) grown by PLD on $Gd_3Ga_5O_{12}$ (GGG) substrates. In the presence of interlayer exchange coupling between YIG and GIG, this heterostructure could act as a magnon valve. The idea is summarized in Fig. 4.1. The central element of such a device is a thin layer of YIG, which is well-known for being a good magnon conductor [4]. In the presence of domain walls, propagating magnons can scatter, leading to a reduction of the propagation length [121]. This effect could be used to manipulate the magnon current by the generation or annihilation of domain walls. In this geometry shown in Fig. 4.1 (a), the domain walls occur perpendicular to the spin current direction.
We can imagine a second design, where the domain walls are parallel to the spin current such as shown in Fig. 4.1 (b). In this proposed concept, the domain walls are realized by introducing a layer of a different garnet between two YIG layers. The garnet of choice here is GIG, which has a similar structure and properties to YIG, but possesses an additional magnetic sublattice formed by the Gd moments. If there is interfacial coupling present in this heterostructure, the Fe sublattices might couple ferromagnetically so that there is a coherent magnetic structure across the interface

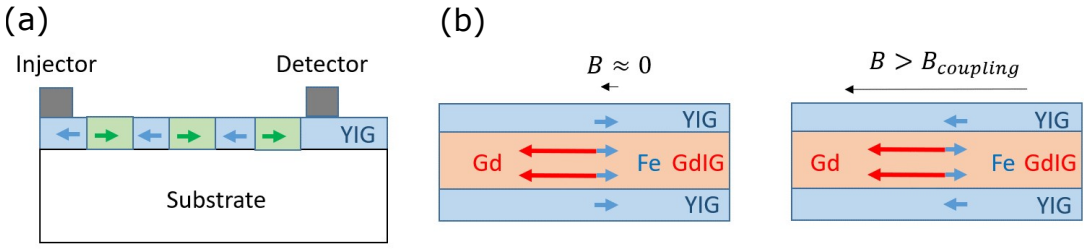


Figure 4.1.: Two concepts of a magnon valve. (a) Thin film YIG with a number of oppositely oriented magnetic domains (blue and green). The magnon current is perpendicular to the domain walls in the YIG. (b) YIG-GIG multilayer system with interlayer exchange coupling. At low magnetic field (indicated by the small black arrow), the net iron moments are coupled ferromagnetically (left) since the interlayer exchange coupling is larger than the Zeeman energy. When a large magnetic field is applied (right), the YIG magnetization rotates and the interlayer coupling breaks. In this geometry, the magnon current is parallel to the domain walls, similar to GMR devices.

as depicted in the left sketch of Fig. 4.1 (b). Due to the large magnitude of the magnetic moment from the Gd sublattice below the GIG compensation point, the ferromagnetic coupling of the iron sublattices leads to an effective antiferromagnetic orientation of the net magnetizations of each layer. An external magnetic field may align the Gd moments in the direction of the field to reduce the Zeeman energy, which then leads to the antiparallel alignment of the Fe moments of GIG with the field. In contrast to that, the net YIG magnetic moment always aligns in field direction. This leads to the breaking of the coherent magnetic structure as shown in Fig. 4.1 (b), if the external magnetic field is sufficiently large that the Zeeman energy overcomes the interfacial coupling energy. This creates domain walls with respect to the Fe sublattices within the plane parallel to the spin current direction. Like for electrons in giant magnetoresistance (GMR) devices, we thereby expect different magnitudes of the net spin current that traverses the device. A device like this could be used to realize magnon logic operations.
The fabrication of an all-insulating magnon valve requires the capability to grow high quality heteroepitaxial thin films to have a good matching of the unit cells at the YIG-GIG interface. The method of choice to grow these samples is PLD. The YIG and GIG targets used here have been fabricated in earlier projects [33, 103, 122, 123]. While high-quality thin films of the individual materials have been fabricated already, the fabrication of heteroepitaxial heterostructures is not straight forward as will be seen in the present chapter. The optimization of YIG-GIG heterostructures growth was performed by the author and Sally Lord, who worked as an exchange student for three months in the lab under the supervision of the author and Andrew Ross. Once the ideal technique has been found to grow high-quality YIG-GIG samples, Zengyao Ren fabricated a series of samples with different relative thicknesses and performed SQUID measurements. Spin Hall magnetoresistance measurements have been carried out by the auther and Felix Fuhrmann conducted spin Seebeck effect measurements. The results have been published in Ref. [S6], where Z. Ren and the author contributed equally. A full breakdown of contributions to the results of this chapter can be found in the introduction chapter.

## 4.1. Thin film growth

In order to realize the proposed magnon-valve heterostructure, the two individual garnets need to be grown to a high quality. In this section, the growth of the individual layers will be discussed by depositing YIG and GIG samples separately on bare GGG (001) substrates. Following this, the combined heterostructure will be developed. To find the best growth conditions for the individual materials, the oxygen background pressure and the substrate temperature have been varied around the established deposition parameters of YIG [124] and GIG [33].
Fig. 4.2 shows the $2\Theta/\omega$ scans around the (004) reflex of GIG (left) and GGG (right) for sample series where the temperature (a) and pressure (b) have been varied. High deposition temperatures lead to relaxation of the GIG unit cells after a certain number

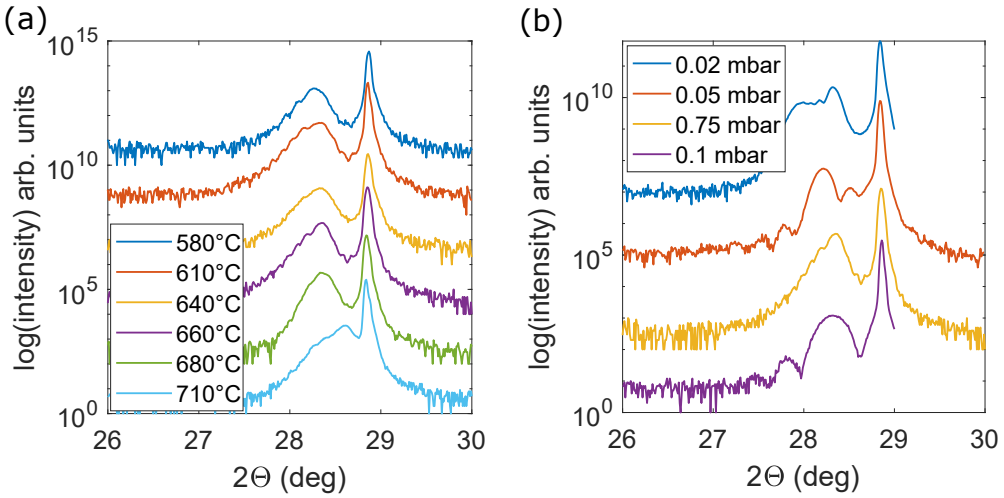


Figure 4.2.: $2\Theta/\omega$-scans around the (004) reflex of GIG (left peak) and GGG (right peak). (a) influence of the deposition temperature on the sample properties for a fixed oxygen pressure of 0.075 mbar. (b) influence of the oxygen background pressure during deposition for a fixed temperature of 660°C.

of strained layers, as indicated by the split peak, where the dominating contribution is found at higher angles. This indicates a decrease of the lattice parameter in the out-of-plane direction, which is accompanied by an in-plane relaxation, which can be determined by separate measurements along in-plane axes. We aim to avoid any relaxation in our system in order to have homogeneous magnetic properties across the entire thickness of the sample. By reducing the deposition temperature below 700°C, the GIG peak becomes more symmetric, indicating the absence of a relaxed phase. At 660°C [purple in Fig. 4.2 (a)], Laue oscillations are visible to the left of the GIG reflex. These indicate coherent structure of the sample perpendicular to the surface and smooth interfaces [112]. The asymmetry of the Laue oscillation might stem from a slight strain relaxation at the GGG/GIG interface while coherent strain is maintained in the rest of the sample [125]. Since the GIG reflex for the sample grown at 660°C appears to be the sharpest, this temperature is chosen for the variation of the oxygen pressure.

As one can see in Fig. 4.2, a low oxygen pressure leads to the formation of multiple phases. Oxygen pressures $p(O_2)$ >= 0.05 mbar lead to the occurrence of Laue oscillations indicating good crystal quality. For further experiments we choose $p(O_2) = 0.05$ mbar for the deposition of GIG. The samples grown at these conditions possess tetragonal distortion due to strained growth. The c-axis is elongated from the relaxed value of 12.472 Å in bulk [97] to 12.58 Å in our thin films.

Having established good growth conditions for GIG, we turn our attention to the second garnet in the proposed magnon-valve device, YIG. YIG can not only be grown by PLD, but also by liquid phase epitaxy (LPE), which is the method of choice to achieve thick films with reproducible properties while reducing the preparation time

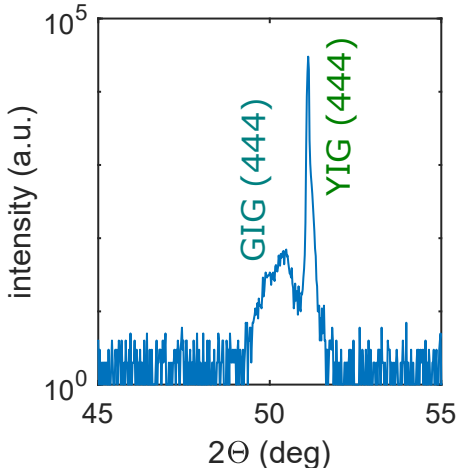


Figure 4.3.: $2\Theta/\omega$-scan (111) reflex of LPE-grown YIG with GIG deposited at ideal deposition conditions as a top layer.

compared to PLD and sputtering. Making use of (111)-oriented LPE-YIG substrates, utilized in former projects in the lab [8, 122, 123, 126], we initially aim to grow heteroepitaxial GIG layers directly on these high-quality YIG samples. To do so, we proceed as with regular substrates, depositing GIG on the LPE-YIG, making use of the deposition conditions determined before. It should be noted that, the growth orientation is different [(111) as compared to (001)], but given the cubic nature of garnets, the deposition conditions should not be drastically different. As one can see in Fig. 4.3, the (444) reflex of the GIG grown on (111)-oriented LPE-YIG does not have a well-defined Lorenzian shape, but consists of two or more superimposed peaks. This indicates that the GIG film does not grow coherently on the LPE-YIG, but consists of multiple crystallites with different crystallographic properties, yielding inhomogeneous magnetic properties. From this, we further assume that the GIG-YIG interface in these samples is not homogeneous across the sample, which is disadvantageous for the investigation of interlayer coupling. The growth on LPE-YIG has been repeated for several samples and the deposition parameters have been varied away from the ideal parameters defined before to account for the difference between the interfaces of GGG (001) and YIG (111). However, for all GIG samples grown on LPE-YIG, no high quality GIG layer was achieved.

We therefore turn away from using LPE-YIG for coupled YIG-GIG heterostructures but instead focus on investigating samples where both YIG and GIG are deposited in-situ by PLD on GGG (001) substrates. As for GIG, the growth of YIG has been optimized concerning the crystallographic properties by varying the substrate temperature and oxygen background pressure during the deposition. Fig. 4.4 (a) shows the influence of the oxygen background pressure on the crystallographic properties of YIG while keeping the substrate temperature at 570°C for each sample. We note that none of these samples shows prominent Laue oscillations. Only for growth at the lowest

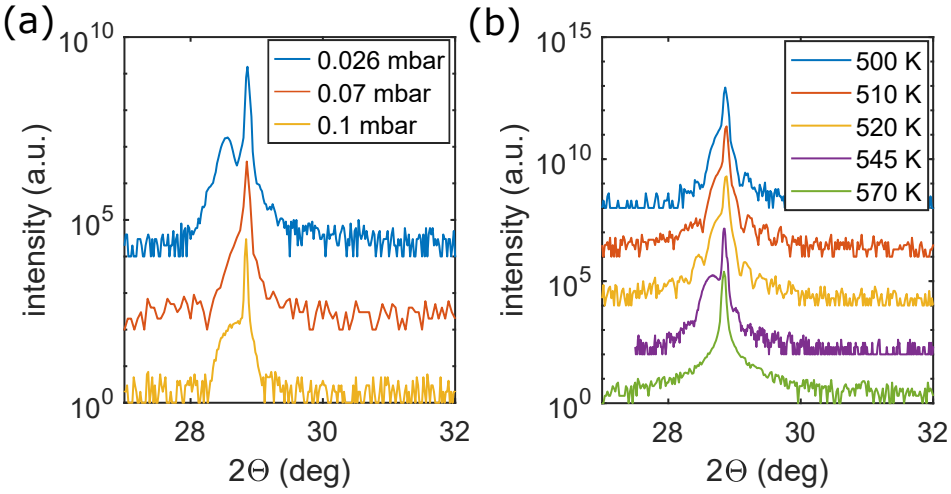


Figure 4.4.: $2\Theta/\omega$-scans around the (004) reflex of YIG and GGG. (a) influence of the oxygen background pressure during deposition at a fixed temperature of 570°C. (b) Influence of the deposition temperature on the sample properties at a fixed pressure of 0.026 mbar.

pressure are some indications of Laue oscillations seen to the right to the GGG (004) reflex. We therefore keep the deposition pressure at 0.026 mbar and vary the substrate temperature. The $2\Theta/\omega$ of these samples are shown in Fig. 4.4 (b). We find symmetric Laue oscillations for the sample grown at a substrate temperature at 520°C. The YIG reflex is superimposed by the dominating GGG (004) substrate reflex. We find the out-of-plane lattice constant of the YIG films deposited at ideal condition to reproduce the bulk value of 12.376 Å [95]. Ferromagnetic resonance (FMR) measurements have been employed to determine the Gilbert damping parameter $\alpha$ of these samples. This experiment has been performed by Sally Lord and Romain Lebrun. Besides the crystallographic properties, $\alpha$ is an indicator for the quality of the crystal. It has been determined to be around $\alpha = 7 \pm 5 \cdot 10^{-4}$, which is similar to other PLD-grown YIG films [124], but higher than for bulk samples, which can posses a damping parameter of down to $\alpha = 3 \cdot 10^{-5}$ [127]. There are reports on low-damping YIG grown by PLD on GGG (111) substrates with a consecutive annealing process [128]. Therefore, we performed annealing processes of the YIG samples in order to improve the crystallinity of the samples. It is suggested that this process reduces the defect density, which leads to a reduction of the Gilbert damping parameter. However, heating the sample to temperatures up to 800°C for 20 min did not have a significant impact on the sample properties. Therefore, no annealing process was performed for successive samples.

Having established growth parameters for YIG and GIG to fabricate high quality thin films, we now turn to the production of multilayer systems. A series of double layers have been prepared where the YIG and GIG layers have been deposited at the respective ideal conditions without breaking the vacuum between the individual

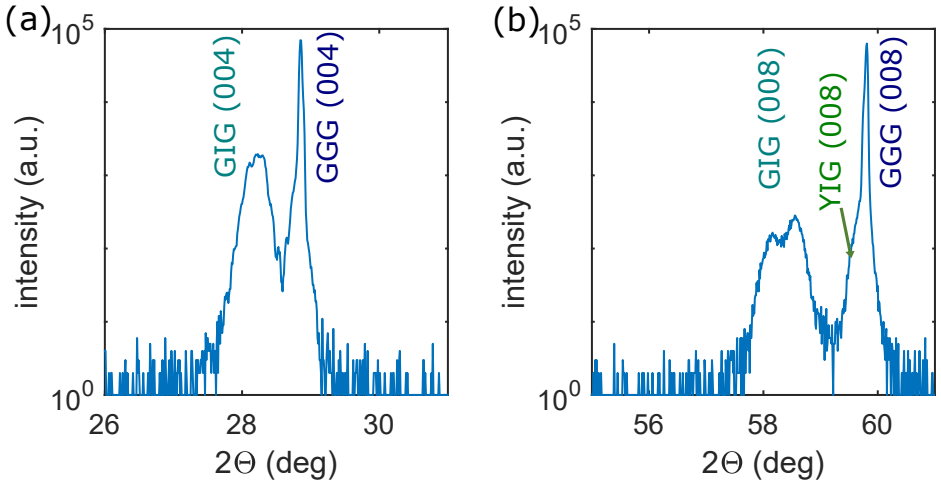


Figure 4.5.: (a) $2\Theta/\omega$-scan around the (004) reflex of GGG of a GGG/YIG(30 nm)/GIG(95 nm) sample, with each layer grown at the ideal deposition conditions shown previously. (b) shows the (008) reflex of the same sample.

deposition steps. Fig. 4.5 (a) shows the $2\Theta/\omega$ scan around the (004) reflexes of a bilayer of GGG/YIG(30 nm)/GIG(95 nm). As for the single layers, the YIG reflex is hidden below the strong GGG reflex from the substrate. The GIG (004) reflex at around $2\Theta = 28°$ shows splitting, indicating the presence of differently strained GIG phases. This splitting is even more pronounced when looking at the (008) reflex shown in Fig. 4.5 (b) due to the relationship between the reflection angle and lattice spacing (see section 3.3). The YIG reflex is also visible here as a shoulder of the GGG peak as indicated by the green arrow.

There might be several reasons why the growth of the GIG layer on top of the GGG/YIG and LPE-YIG samples does not work by the methods presented so far. First, the YIG surface is different from the GGG surface, for which the growth parameters of GIG have been optimized. The difference in stoichiometry and a possible difference in the topography may lead to differences in the kinetics of the atoms arriving at the surface of the sample. Second, a time delay between the deposition of the YIG and the deposition of the GIG as the temperature and oxygen pressure are changed likely leads to the incorporation of impurities in the surface, which are nucleation centers of crystallographic defects.

Given that the aim is to grow multilayers of the two garnets, we compromise the deposition conditions of the YIG and GIG films from the ideal conditions to optimize the total multilayer. We achieve this by changing not only the kinetics during the deposition, but also reducing the time delay between the two deposition steps, which likely reduces the defect density at the YIG-GIG interface. Several different samples have been grown where the YIG and GIG layer have been deposited at the same pressure and temperature, respectively. We find best results for the deposition conditions

| | |
|---|---|
| $O_2$ background pressure | 0.026 mbar |
| Substrate temperature | 480°C |

Table 4.1.: Ideal deposition conditions for YIG-GIG heterostructures grown on GGG (001) substrates.

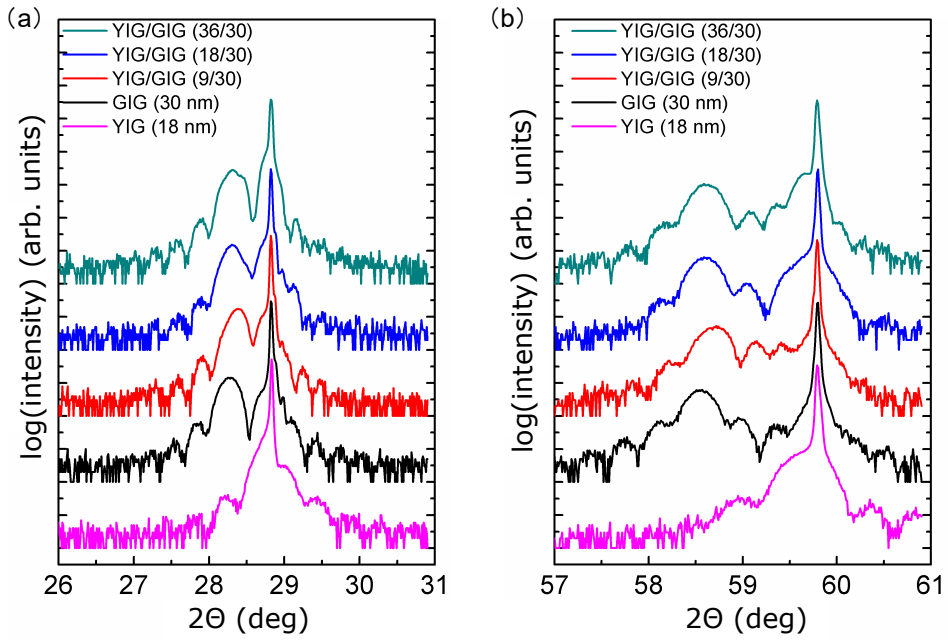


Figure 4.6.: (a) $2\Theta/\omega$-scan around the (004) reflex of GGG of GGG/YIG/GIG samples with different relative thicknesses grown at the compromised deposition conditions given in Tab. 4.1. (b) shows the (008) reflex of the same sample. [S6]

given in table 4.1. The growth rates are around 1.80 nm/min and 1.08 nm/min for GIG and YIG, respectively.

$2\Theta/\omega$ scans of GGG/YIG/GIG samples with different relative thicknesses of the two layers are shown in Fig. 4.6. While the YIG reflex is hidden behind the GGG reflex and only visible as a shoulder to the left of the substrate peak, we observe prominent and symmetric GIG reflexes, GIG (004) at around $2\Theta = 28.4°$ and GIG (008) at around $2\Theta = 58.5°$, which both possess symmetric Laue oscillations. From the peak position we find a lattice parameter of $c_{GIG} = 1.26$ nm, which is independent from the thickness of the underlying YIG. We measure the rocking curve of the GIG (004) as a measure for the relative orientation of the unit cells. We find a remarkable narrow width of $\Delta\omega = 0.04°$, giving an additional measure for the heteroepitaxy of the samples. Although the YIG peak is not clearly visible in the $2\Theta/\omega$ scans, we can conclude from the presence of the symmetric GIG reflex, as well as the Laue oscillations to

the right of the GGG peak, that the YIG layer must possess high crystalline quality, enabling the GIG layer to grow heteroepitaxially. Fig. 4.6 also shows a comparison to a single GIG film, highlighting that the YIG under-layer does not influence the crystallographic properties of the GIG.
In summary, the presented XRD measurements demonstrate the high-quality growth of GGG/YIG/GIG heterostructures, grown by PLD. These samples are ideal candidates to test whether interlayer exchange coupling in YIG/GIG heterostructures is present with the aim to realise the proposed magnon-value concept. In the next section, the magnetic coupling will be probed through magnetic measurements before the impact of this coupling on electrical measurements is discussed.

## 4.2. Determination of the magnetic coupling

To determine the magnetic properties of the samples, we perform SQUID measurements (see section 3.4), which detect the magnetic moment $m$ of the entire sample. In order to disentangle the relative contributions of the different films, we start with investigating the bare films of GGG/YIG(18 nm) and GGG/GIG(30 nm) to use as a reference. Note that the GGG substrate is strongly paramagnetic. Since in SQUID measurements, the whole volume of the sample is probed, the GGG gives a strong field-dependent background. We therefore start with sweeping the field up to $\pm 0.05$ T, to limit this background contribution. We note that both YIG and GIG are known to be soft magnetic materials so that their properties can be measured in this field range. A linear fit is then subtracted from each data set, which is the expected behavior of a paramagnet.
Fig. 4.7 shows an example for a field-dependent SQUID measurement of both films at a temperature of 120 K. The curves show small coercive fields for both YIG and GIG, indicating the soft magnetic character of these materials. Since the antiferromagnetic coupling between the a-Fe and the d-Fe sublattice cannot be broken by the magnetic fields we apply to the materials, the magnetic sublattices (2 for YIG and 3 for GIG) switch coherently (see section 2.4). This means that we can introduce a simple model with effective sublattices to describe our samples. We introduce an effective Fe sublattice for YIG, which is sufficient to describe the magnetic properties observed in SQUID. We do the same for the two iron sublattices in GIG and describe the material by an effective Fe sublattice and a magnetic Gd sublattice. This is indicated in Fig. 4.7 (b), where the temperature-dependent magnetic moment of YIG and GIG is presented. The values are determined by repeated field-dependent measurements at different temperatures, to limit the $1/T$ contribution of the paramagnetic substrate. One can see the strong temperature-dependence of the GIG due to the Gd moment increasing towards lower temperatures. At around 280 K, we observe a minimum of zero magnetic moment marking the magnetic compensation point of GIG, $T_{comp,G}$, where the magnitude of the net Gd moments equals the magnitude of the net Fe moments. This is close to the value reported for bulk GIG samples of 295 K [102]. Above $T_{comp,G}$, the effective Fe moment aligns with the external magnetic field while

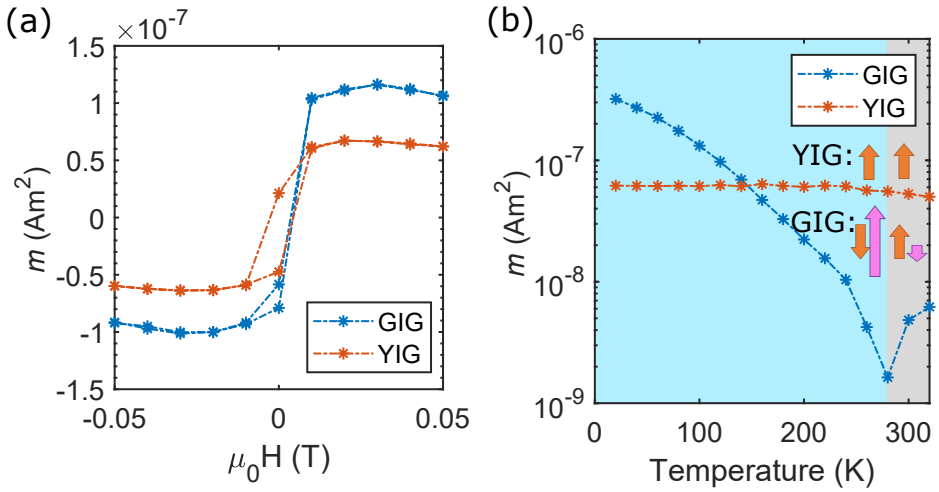


Figure 4.7.: (a) Field-dependent magnetic moment $m$ of a GGG/YIG (18 nm) and a GGG/GIG (30 nm) sample, respectively. The magnetic field is applied within the sample plane at a temperature of 120 K. (b) Temperature-dependent magnetic moment measured by multiple field-dependent measurements as in (a). The blue area marks the temperature region where the GIG magnetization is dominated by the Gd moment (purple arrow) and the grey area the region where the GIG magnetization is dominated by the Fe moment (orange arrow). The YIG magnetic properties do not change fundamentally in this temperature window.

the coupled Gd moment aligns antiparallel. Below $T_{comp,G}$, the Gd moment is larger and the Fe moment aligns antiparallel to the field in order to reduce the Zeeman energy. The magnetic moment of YIG on the other hand, is almost constant in this temperature range, which is to be expected since we measure far from the magnetic ordering temperature of 560 K.

We have seen in the previous section that we are able to grow high-quality, heteroepitaxial YIG/GIG bilayer samples, where the crystallographic properties of the top GIG layer is independent of the underlying YIG layer. From the close correlation between the crystallographic and magnetic properties of garnets [129], we can estimate that the magnetic properties of each GIG layer is the same, independent of the layout of the heterostructure. As a consequence, the compensation point of GIG is assumed to be $T_{comp,G}$=280 K for each sample. The same holds for the YIG layers, for which we can also safely assume the same magnetization for all samples.

When measuring YIG-GIG heterostructures, the first observation we make is that at temperatures below $T_{comp,G}$, the overall magnetic moment is reduced compared to a single GIG layer. An example of this is shown in Fig. 4.8 (a), where we measure the field-dependent magnetic moment of a GGG/YIG(18 nm)/GIG(30 nm) sample at a temperature of 120 K and compare it with a GGG/GIG(30 nm) sample. The reduction of the overall magnetic moment indicates an antiparallel alignment of the net magnetic

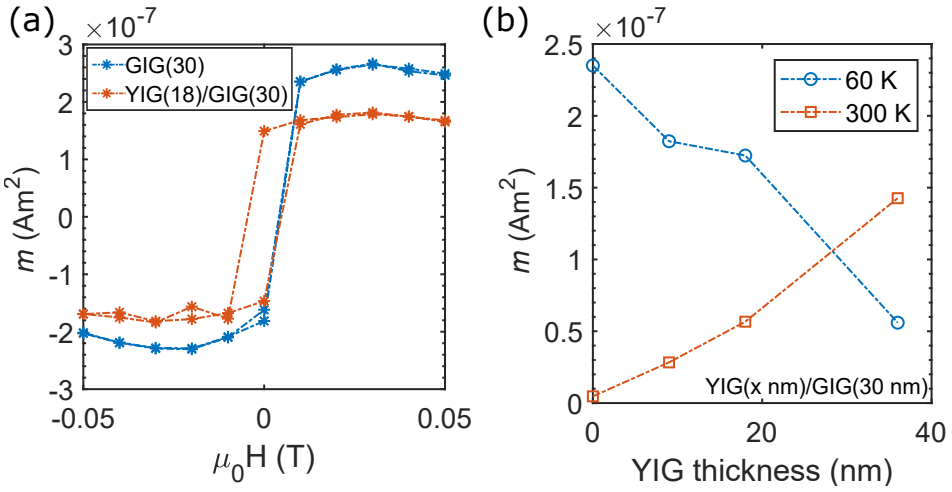


Figure 4.8.: (a) Field-dependent SQUID measurement performed at a temperature of 120 K for a GGG/GIG (30 nm) sample and a GGG/YIG (18 nm)/GIG (30 nm) sample. (b) Magnetic moment of GGG/YIG (x nm)/GIG(30 nm) samples at 60 and 300 K.

moments of YIG and GIG. Given that the magnetization of GIG is larger than YIG at this temperature (see Fig. 4.7), this indicates that not only is the relative alignment antiparallel, but also that the YIG moment is antiparallel to the external field. Since in GIG, the magnetization direction is determined by the orientation of the Gd moment, this reduction would indicate a parallel alignment of the iron sublattices across the interface. To test this hypothesis, we investigate the magnetic moments of YIG/GIG samples for a variety of YIG thicknesses at different temperatures. As one can see in Fig. 4.8 (b), the net magnetic moment decreases monotonically with increasing YIG thickness at a temperature of 60 K. We repeat these measurements at 300 K, which is above $T_{comp,G}$. Here, the Fe moments in GIG align with the external magnetic field. The increase of the overall magnetic moment with YIG thickness confirms that the Fe moments are indeed coupled parallel across the YIG-GIG interface at low magnetic fields.

The observed interfacial exchange coupling impacts the magnetic properties of the whole sample. In the presence of such coupling, the sample will have a minimum of the total magnetic moment at some temperature, which is different from the GIG compensation point. We call it therefore the bilayer compensation point $T_{comp,B}$. At this temperature, the sum of the net iron moments in the YIG and GIG equal the Gd moment causing the external magnetic moment to be zero. As a result, $T_{comp,B}$ shifts to lower temperatures as the thickness of the YIG increases. This is demonstrated in Fig. 4.9 (a), where the temperature-dependent moment, measured via small amplitude field sweeps, is shown for samples with different relative thicknesses of the YIG and GIG layer.

The decrease of $T_{comp,B}$ with increasing YIG thickness is evident from this figure.

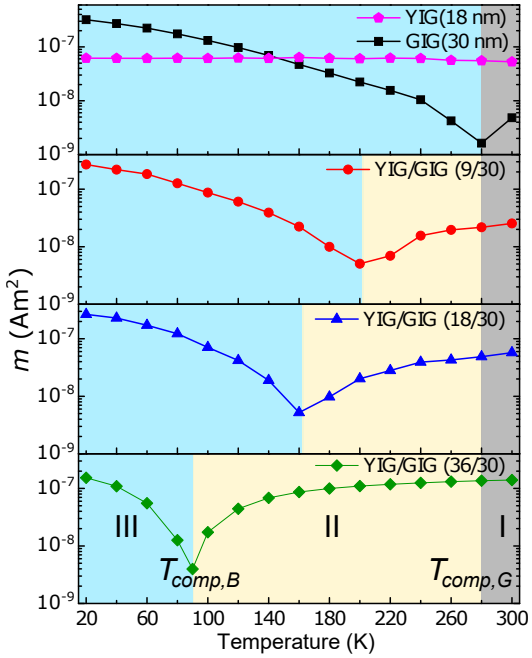


Figure 4.9.: Temperature-dependent magnetic moment of GGG/YIG($x$ nm)/GIG(30 nm) with $x$=0, 9, 18, 36 measured in SQUID by field-sweeps at each temperature. The colored areas mark regions, separated by the two compensation points. [S6]

We can further confirm the ferromagnetic coupling across the YIG-GIG interface by modeling the other possible cases: antiferromagnetic coupling and absence of coupling. The model shows fundamentally different features compared with the experimental data and therefore excludes these coupling cases and confirms the ferromagnetic Fe-Fe coupling [S6].

### 4.2.1. Probing the magnetic coupling at high magnetic fields

From small amplitude magnetic field sweeps in SQUID we demonstrated strong evidence for the presence of ferromagnetic Fe-Fe across the YIG-GIG interface. We now turn to measurements at higher magnetic fields given that it is expected that at sufficiently large fields, the Zeeman energy will become larger than the exchange coupling energy at the interface. As a result, the interlayer coupling will break and the net magnetic moments of both layers are expected to rotate parallel to the applied field. From these consideration we draw a general picture of the behavior of exchange coupled YIG-GIG samples. Fig. 4.10 indicates how the net Fe and Gd moments in the layers orient relative to a magnetic field in a given temperature range. In the grey region (I) above $T_{comp,G}$, the Gd moment is smaller than the net Fe moment in the GIG layer itself. Therefore, the Fe moments of both layers always align with the external

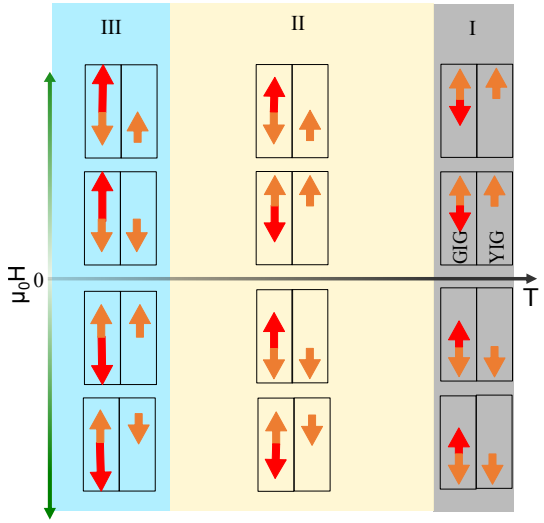


Figure 4.10.: Generalized model of the relative alignment of the magnetic moments in a YIG-GIG heterostructure depending on external magnetic field $\mu_0 H$ and temperature $T$. [S6]

field, independent of its amplitude. The situation is different in the yellow region (II) between the two compensation points. Here, the Gd moment is larger than the Fe moment in the GIG layer, but smaller than the sum of the Fe moments in YIG and GIG. Therefore, the Fe moments align with a small external magnetic field. However, if the Zeeman energy of the GIG layer, which can be given as $\Delta E = 2 \cdot H \cdot (m_{Gd} - m_{Fe,GIG})$, becomes larger than the interlayer exchange coupling, the magnetic sublattices of the GIG layer rotate while the Fe moments in YIG remain oriented as in the presence of a small field. This then means that, at low magnetic fields, the interfacial coupling between the layer Fe sublattices is ferromagnetic but, at higher magnetic fields, this coupling becomes antiferromagnetic. Finally, in the blue region (III) below $T_{comp,B}$, the Gd moment is larger than the sum of the net iron moments of YIG and GIG. In a small magnetic field, the Gd moment will align with the external field while the net Fe moments will both align antiparallel. In a sufficiently large field, the magnetic moments in YIG will coherently rotate.

To measure these features, we perform SQUID measurements at larger magnetic fields. Our experience tells us that the strong paramagnetic background of the GGG substrate makes the analysis of large magnetic field measurements difficult. We therefore make a reference measurement of a bare GGG substrate in SQUID and subtract this data from the measurements of the thin films samples. To account for slight differences in the volume of the GGG, mounting equipment and incorporated impurities from the sample handling, we additionally subtract a linear fit.

Fig. 4.11 shows two examples for field-dependent SQUID measurements performed at 60 K (region III) and 160 K (region II), below and above the $T_{comp,B}$ of that sample. One can identify an 'inner hysteresis'. The magnetic moment plateaus at small

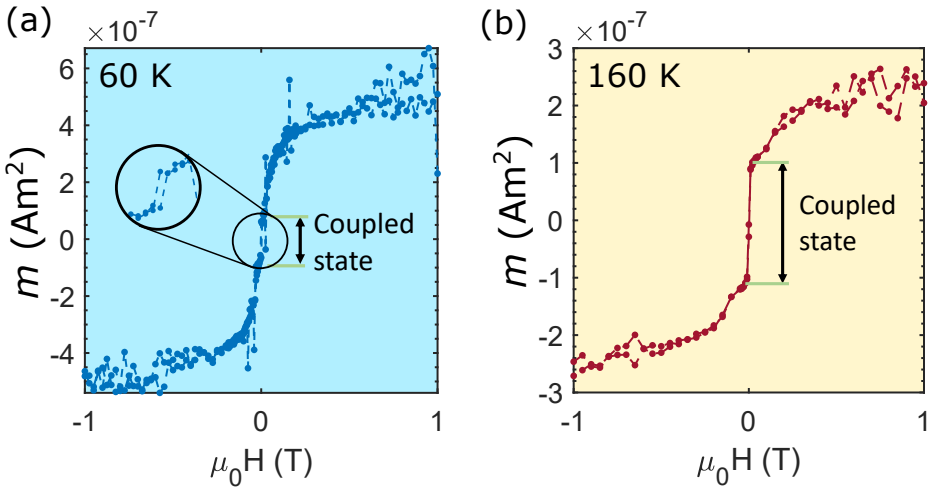


Figure 4.11.: Field dependent magnetic moment of a GGG/YIG(36 nm)/GIG(30 nm) sample measured up to 1 T (a) at 60 K and (b) at 160 K.

magnetic fields. Here, the coupling energy is larger than the Zeeman energy and the ferromagnetic Fe-Fe coupling is maintained ('coupled state'). This leads to the antiparallel alignment of the net magnetic moment of YIG (GIG) with the field in region III (II). Going to larger magnetic fields, the magnetic moment increases before it finally saturates. This represents the transition from the from the coupled state to the field-aligned state as described in the model in Fig. 4.10. The double switching in both temperature regions indicates that the interlayer coupling is indeed broken by sufficiently large fields and that both net magnetizations point in the direction of the large magnetic fields.
However, by virtue of being a bulk measurement technique, SQUID is insensitive to which of the layers actually switches in each case. To demonstrate that in region III the YIG magnetization rotates and in region II the GIG magnetization rotates, one needs to use a surface-sensitive method from which one can conclude the magnetization direction of the top layer.

### 4.2.2. Probing the magnetic coupling via transport measurements

In order to identify which layer switches under larger magnetic fields, we choose spin Hall magnetoresistance (SMR) measurements which is a surface sensitive, electrical measurement with a symmetry that reflects the magnetic state of a magnetic insulator [15, 39] (see section 1.6.2). Indeed, the SMR is sensitive to depths on the order of the exchange length, in other words, reflects the magnetic state of the top few nanometers and allows us to probe the GIG magnetic ordering. To perform these measurements, a Pt Hall bar is defined on the surface, aligned along the crystallographic axes. Pt is deposited by magnetron sputtering though a shadow mask, resulting in a Pt bar of 4 nm thickness and 0.3 mm width across the whole length of the sample.

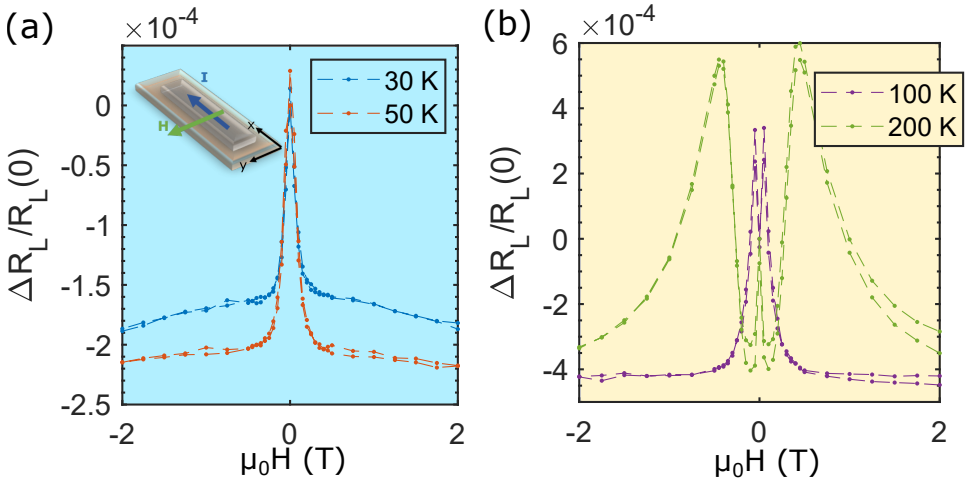


Figure 4.12.: (a) Uniaxial SMR measurement performed at a GGG/YIG(36 nm)/GIG(30 nm) sample in the temperature region III. The inset sketches the geometry of the measurement. (b) SMR measurement performed at the same sample in the temperature region II. [S6]

For the measurement, the resistance of the Pt bar is determined by four-probe method. The magnetic field is applied within the sample plane perpendicular to the current as sketched in the inset of Fig. 4.12 (a). The magnetic-field dependent resistivity $R_L(H)$ is measured and we plot the SMR ratio $\Delta R_L/R_L(0) = \frac{R_L(H)-R_L(0)}{R_L(0)}$ in Fig. 4.12 for temperatures within the different regions of interest. In Fig. (a), two measurements in temperature region III below $T_{comp,B}$ are shown. Both have the same characteristics. At small magnetic fields, the resistance sharply drops to a constant level, where upon further increase of the magnetic field, the resistance does not significantly change. In contrast to this, in temperature region II between the two compensation temperatures, the resistivity of the Hall bar describes a more complex trajectory as can be seen in Fig. 4.12 (b). In the presence of SMR, the longitudinal resistivity is varied according to $\Delta R_L \propto \Delta R_{1,m}(1-\mathbf{M}_y^2)$ (see section 1.6.2). Note that we do not expect a difference between the alignment of the top layer magnetization parallel or antiparallel to the field due to the dependence on $M_y^2$. However, if the surface magnetization changes between collinear and non-collinear with the field, this is visible via SMR. This is the case during the rotation of the magnetization between the coupled state and the field-aligned state. In the temperature region (III), the sharp drop can likely be explained by a transition from multidomain state to monodomain state. Due to the quadratic anisotropy within the plane (tetragonal symmetry of the unit cells), both domains with $\mathbf{M}$ aligned along $x$ and $y$ are expected. A small field in $y$-direction annihilates domains with a $M_x$ contribution. This increases the overall $M_y$ and leads to a reduction of $R_L$ caused by SMR.
Since further increase of the magnetic field leads to no significant variation of $R_L$, this

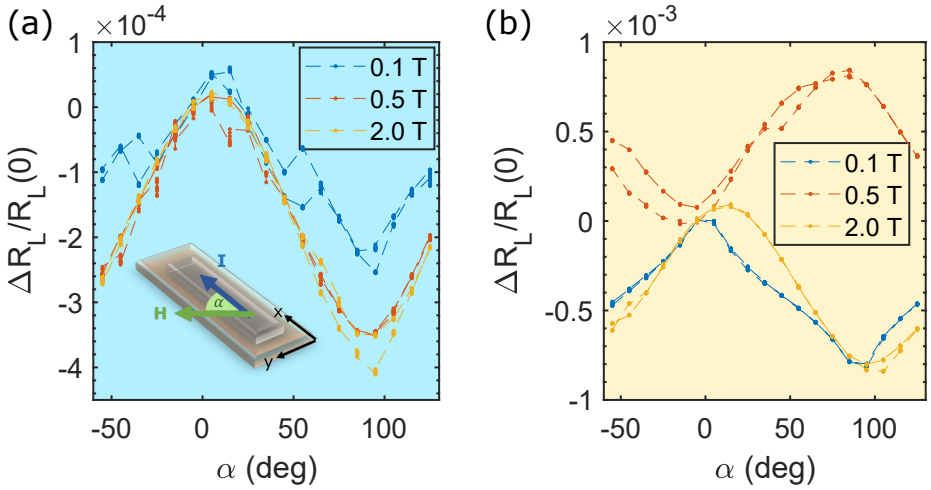


Figure 4.13.: (a) Angle-dependent SMR measurement performed at a GGG/YIG(36 nm)/GIG(30 nm) sample in the temperature region III at different magnetic fields rotated in the sample plane. The inset sketches the geometry of the measurement. (b) angle-dependent SMR measurement performed at the same sample in the temperature region II. [S6]

allows us to conclude that the surface magnetic layer stays aligned with the external magnetic field. However, since we see a double switching in SQUID, this shows that in fact the buried YIG layer changes magnetization direction as we expect from our previous considerations. Likewise, in temperature region II, the complex trajectory of $\Delta R_L$ is due to the continuous rotation of the magnetization of the top GIG layer in the reorientation region between coupled state and field-aligned state.

The uniaxial SMR measurements confirm the model we have suggested for the bilayer system given in Fig. 4.10. However, they also show that there is a large transition regime between the coupled state and the field-aligned state in which the layers rotate. We find further proof of this by performing rotation measurements at fixed temperature and external magnetic field. In Fig. 4.13 (a), the relative angle-dependent longitudinal resistivity change is plotted for three different magnetic fields at a temperature of 30 K, which is in temperature region III. The resistivity change is relative to the 0°-value, which describes $\mathbf{M} \parallel \mathbf{I}$ as indicated in the inset of Fig. 4.13 (a). The magnetic field is rotated by 200 ° back and forth. The two rotations are then plotted over one another. The $\Delta R_L(\alpha)$ describes a $\cos^2(\alpha)$-dependence for every magnetic field as one expects for a ferromagnet that aligns its magnetization with the external magnetic field (see Sec. 1.6.2). This again confirms that the top magnetic layer does not change its magnetization alignment relative to the magnetic field, given that this is the layer the SMR is sensitive to. Instead, the changes we see in SQUID stems from the rotation of the magnetization of the buried magnetic layer. The hysteresis seen around $\alpha = -40°$ and 50° for $\mathbf{H}$=0.1 T in Fig. 4.13 is due to the four-fold anisotropy

present in-plane for the tetragonal-strained garnet crystal structure. The magnetic field only then causes a rotation of **M** towards the hard direction, which is at 45° to the in-plane axes, if the external field overcomes the anisotropy field. This is not the case for 0.1 T, so the magnetization flips abruptly when the projection of **M** is larger along one crystallographic axis than along the other (the crystallographic axes are the magnetic easy axes).
The rotation measurements performed at the same magnetic fields in temperature region II can be seen in Fig. 4.13 (b). Here, a $\cos^2(\alpha)$-function can similarly be fitted to the data, indicating that the SMR model can be applied to the data. In contrast to the measurements performed in region III, here, at intermediate fields, there is a significant phase shift to the data measured at 0.5 T. This shows that the magnetization of the top layer is not collinear with the external magnetic field at intermediate field strengths, confirming our interpretation given for the complex behavior of the field-dependent change of the longitudinal resistivity in temperature region II, as shown in Fig. 4.12 (b). At small magnetic fields, the coupled iron magnetic moments align with the field. Increasing **H** leads to a continuous rotation of the GIG magnetization until, at large magnetic fields, the Gd moment aligns with field and the ferromagnetic Fe-Fe coupling at the interface is broken.
The measurements presented so far have confirmed the simple model we suggested in Fig. 4.10. However, there are still open questions that cannot be answered with the measurements thus presented. It is, for example, not expected that the magnetization of the layers behave like a single spin. Outside the coupled state we rather expect a continuous rotation of the magnetization in the rotating layer with increasing distance to the interface since an abrupt change of magnetization direction at the very interface is energetically not favourable. There is likely a Bloch-type domain wall of a certain width at the YIG-GIG interface. The domain wall's dimensions are expected to depend on the sample layout, temperature and magnetic field. This type of magnetic configuration is for example seen in exchange-springs between a soft and a hard ferromagnet at intermediate fields [130, 131].

### 4.2.3. Quantifying the Magnetic Coupling

We now want to quantify the exchange coupling in the YIG-GIG bilayer system. Despite being aware of a possible extended domain wall at the YIG-GIG interface, we maintain our simple model of uniformly magnetized layers which we will see is sufficient to gain reasonable insight into the exchange coupling present in the system. We assume that in the field-aligned state, there is a sharp transition at the YIG-GIG interface and the neighboring Fe sublattices align 180° to one another. We need to return to the SQUID measurements which show the double switching, Fig. 4.11. We introduce two amplitudes for our field-dependent SQUID measurements. We describe the magnetic moment of the whole bilayer in the coupled state as $Amp1$ and the magnetic moment at high magnetic fields as $Amp2$. According to our switching model in Fig. 4.10, in region III, we can ascertain the gain in magnetic moment between the coupled and aligned state to the rotation of the YIG layer. Therefore, we can calculate

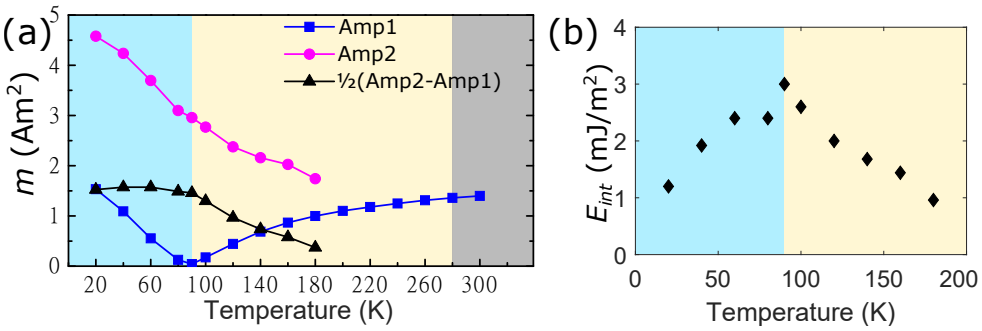


Figure 4.14.: (a) Field-dependent magnetic moment of a GGG/YIG(36 nm)/GIG(30 nm) for small magnetic fields, where the ferromagnetic Fe-Fe coupling is undisturbed ($Amp1$), and large magnetic fields, where the coupling is broken ($Amp2$). (b) Interfacial coupling energy ($E_{int}$) estimated from switching fields and magnetic moments of the layers. [S6]

the total magnetic moment of the YIG layer by $m_{YIG} = \frac{1}{2}(Amp2 - Amp1)$. In region II, the difference in the amplitude gives us the total net magnetic moment of the GIG layer $m_{GIG}$.

The evolution of these parameters with temperature is shown in Fig. 4.14 (a) for a GGG/YIG(36 nm)/GIG(30 nm) bilayer. In region III, the difference in the amplitudes (black curve in Fig. 4.14) is constant as expected given that $m_{YIG}$ does not change significantly in this temperature range. In region II, it decreases and describes the temperature-dependent $m_{GIG}$. Note that above 180 K, a value for $Amp2$ cannot be given due to the poor signal-to-noise ratio in the SQUID measurements at the magnetic fields required to overcome the exchange coupling. From these measurements, we can estimate the interlayer coupling strength in our samples. To do so, we determine the Zeeman energy at the magnetic field, at which $Amp2$ is just reached. In our model, this is the field at which the rotating layer reaches the final orientation in the field-aligned state. At this point, the Zeeman energy and interfacial exchange coupling are equal to one another.

In region III, the gain in Zeeman energy, and therefore the interfacial coupling energy, is given by $2\mu_0 H m_{YIG}$, while in region II it is $2\mu_0 H m_{GIG}$, where $\mu_0$ is the magnetic permeability of free space. We divide these values by the interface area, which is equal to the substrate dimensions, i.e. $5 \times 5\,\mathrm{mm}^2$. The interfacial coupling energy per surface area is given for each temperature in Fig. 4.14 (b), where one finds that it peaks at the transition temperature $T_{comp,B}$. Considering that the origins of the observed exchange coupling lie in the overlap of the electron orbitals, we can state that the the exchange energy should be only weakly temperature dependent. Changes in the orbital overlap only occur due to lattice expansion/contraction, and are expected to show a monotonic trend with temperature. One can safely assume that this holds also for the interlayer exchange coupling. The temperature-dependence we see in

our calculation is likely due to our rather inexact method of determining the critical values and our simple model rather than the coupling strength varies across this temperature range. We therefore assume a constant coupling energy of $2.3\,\mathrm{mJ/m^2}$ for the whole temperature range, which is the mean value. To calculate the energy at the surface of one unit cell, we multiply by the area of the (001) plane, which is determined by the GGG lattice parameter (1.2377 nm). We further take into account 8 iron atoms at the face of a unit cell. Assuming that the coupling is only between nearest neighbours, we find the coupling energy per iron atom equals $J_{int} = 2.8\,\mathrm{meV}$. We compare this value with the established coupling constants in YIG and GIG, which are $J_{1,YIG} = 6.8\,\mathrm{meV}$ [54] and $J_{1,GIG} = 4.0\,\mathrm{meV}$ [132]. These values describe the theoretical maximum of interlayer exchange coupling. The fact that we are in the same order of magnitude and only a factor 2 smaller than the Fe-Fe exchange coupling in GIG, demonstrates the exceptional strength of the interlayer exchange coupling in our high quality bilayer samples. We note that the exchange coupling between YIG and a thin GIG layer stemming from the inter-diffusion of YIG and GGG was calculated based on the antiferromagnetic interaction between c-Gd and d-Fe [132]. By this method, a coupling energy of 0.14 meV is determined, which is significantly lower than the value determined for our bilayers. The strong coupling in our samples is beneficial with regard to device applications due to the robustness of the coupling the resulting reproducibility of the magnetic states.

## 4.3. Measurement of thermal spin currents

In the introduction of this chapter, we proposed a magnon valve based on exchange-coupled YIG-GIG heterostructures. Having demonstrated a strong exchange coupling in our heterostructures, we now turn to probing the possibility for the implementation as a magnon-valve. One method to test these properties is by using longitudinal spin Seebeck effect (SSE). A temperature gradient is applied perpendicular to the sample surface and the inverse spin Hall voltage ($V_{ISHE}$) is measured in a continuous platinum layer while a magnetic field is swept withing the sample plane, perpendicular to the voltage measurement axis. Before we investigate our bilayer system, we need to quickly recapitulate results from previous investigations on pure GIG samples [33, 103]. Those are crucial in order to understand our new measurements.

There exist different magnon modes excited by the thermal gradient contributing to the SSE signal, where the measured voltage is the sum of these different contributions. Fig. 4.15 (a) indicates the calculated magnon spectrum of GIG at different temperatures. In the low THz range, there is the $\alpha$-mode, corresponding to the ferromagnetic resonance. This mode increases with frequency as one moves through the Brillouin zone. Just above this mode at around 1 THz lie the optical modes associated with Gd moments precessing in the Fe exchange field and are constant in frequency when traversing away from the $\Gamma$ point. There is then an energy gap where no modes are populated before reaching the parabolic $\beta$-mode at around 2 THz at 20 K, which has opposite sense of precession compared to the $\alpha$-mode. The opposing sense of rotation

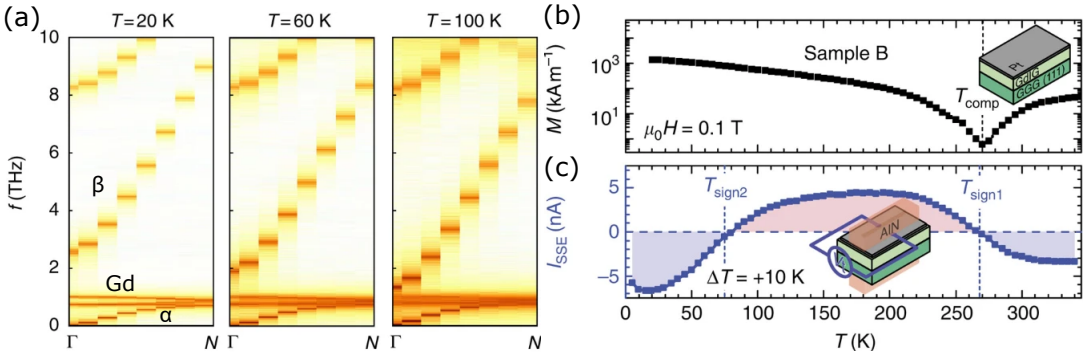


Figure 4.15.: (a) Calculated magnon spectra for different temperatures. (b) Temperature-dependent magnetization of a GGG/GIG sample recorded at a magnetic field of 0.1 T. (c) Corresponding SSE signal $I_{SSE}$ obtained from the difference in $I_{ISHE}$ at the positive and negative saturation fields of the magnetization taking the temperature dependence of the Pt resistance R(T) into account. The inset shows the longitudinal SSE measurement geometry. Figure from [33].

of the $\beta$-mode leads to the generation of an opposite charge current via ISHE in the Pt layer. At 20 K, the $\beta$-mode is gapped and has a low population, and thus a weak contribution to the $I_{SSE}$. With increasing temperature, the branch shifts continuously to lower frequencies. The decrease in frequency is associated with an increase of magnon population in the $\beta$ branch. At $T = T_{sign,2}$, there is an inversion of the magnon population between the $\alpha$- and $\beta$-modes, which then leads to a change of sign in the SSE signal as can be seen in Fig. 4.15 (c) at around 70 K. In Fig. 4.15 (b), the temperature-dependent magnetization is determined by SQUID measurements, indicating a magnetic compensation point at around 270 K. Going through the compensation point, all magnetic sublattices reverse which leads to the sign change of the spin current leading to the other sign change $T = T_{sign,1}$ in the SSE signal.
Knowing the behavior of the SSE signal measured at a pure GIG sample, we can investigate the thermal magnon transport in a GGG/YIG(36 nm)/GIG(30 nm) heterostructure. The SSE measurements at different temperatures, which where performed by Felix Fuhrmann, are shown in Fig. 4.16. Using the same arrangement of electrical contacts and thermal gradient as in [33], we observe a negative amplitude of the SSE signal at a temperature of 35 K as can be seen in Fig. 4.16 (a). Increasing the temperature to 60 K [see Fig. 4.16 (b)], the SSE amplitude reverses. Note that both these temperatures are in region III, below $T_{comp,B}$, so that no inversion of the magnetization direction of the GIG layer is expected. The change of sign is therefore associated with the inversion of magnon population such as observed for pure GIG samples [33]. At 110 K, in region II, a negative SSE amplitude is observed at small magnetic fields. Upon increasing the field further, the amplitude changes sign again, to positive as illustrated in Fig. 4.16 (c). We can attribute these features to the properties of the top GIG layer. The negative SSE signal at small fields is due to

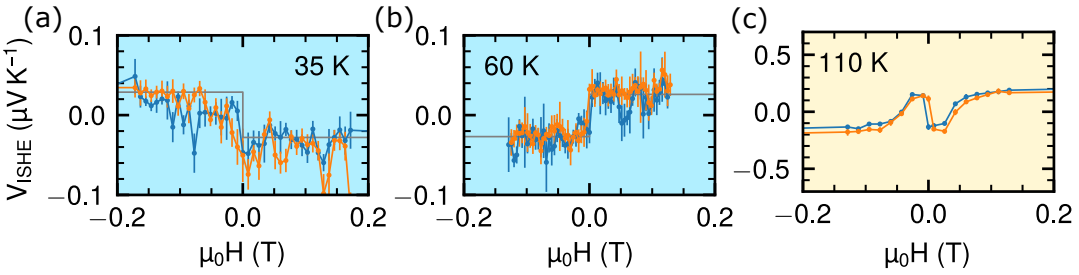


Figure 4.16.: Magnetic field-dependent spin Seebeck effect measurement performed at different temperatures at a GGG/YIG(36 nm)/GIG(30 nm) sample. (a) At $T < T_{sign,2}$, (b) $T_{sign,2} < T < T_{comp,B}$, (c) $T_{comp,B} < T < T_{comp,G}$. [S6]

the antiparallel alignment of the net GIG magnetization with respect to the external magnetic field. At larger fields, the GIG layer continuously rotates in field direction, which leads to a positive SSE signal at large fields. The SSE measurements thereby confirm our previous results from SQUID and SMR.
However, we do not observe clear evidence of a contribution from the bottom YIG layer. Intuitively, we expected a change in the signal upon the rotation of the YIG magnetization. With rotation of the YIG magnetization, the polarization of the YIG-magnons (which are generated in the YIG layer) rotates, leading to a continuous change in the spin accumulation at the Pt/GIG interface, if the YIG-magnons travelled through the GIG layer. This would result in a linear change of the $V_{ISHE}$. This is not visible in the curves measured at 35 K and 60 K shown in Fig. 4.16. Here, the SSE signal remains constant during the continuous rotation of the YIG layer, indicating that the YIG-magnons are not contributing to the signal, independent of the relative magnetization direction of YIG with respect to GIG. We have to conclude that the first attempt of the realization of a YIG-GIG magnon valve does not show the necessary GMR-type features as proposed in the introduction.
The question why the YIG-magnons are not detected by the Pt electrode is yet to be solved. One possibility is that the Gilbert damping parameter in the GIG top layer is so high that magnons from underlying regions of the sample do not reach the surface. This will be tested in future experiments by measuring the SSE signal as a function of the GIG layer thickness in single layer samples as previously done for YIG [122]. Besides the magnetic damping, the possibly complex magnetic structure at the YIG-GIG interface could lead to magnon scattering at the YIG-GIG interface, drastically reducing the magnon transmission at the interface. The magnetic structure at the YIG-GIG interface will also be the target of future studies.
In parallel, theoretical support will be needed to understand whether the concept given in the introduction can work as proposed. The magnon valve with a spin current parallel to the domain walls relies on the assumption that magnons from YIG can propagate through the GIG layer without being excessively scattered. This can only be possible if the same magnonic states in both GIG and YIG exist. The magnon

bands of a magnetically coupled YIG (7.4 nm) - GIG (2.5 nm) heterostructure has been calculated by Li et al. [133] for the case of ferromagnetic Fe-Fe across the interface, as observed in our samples. According to this publication, the fundamental modes in YIG and GIG have opposite chiralities ($\beta$ and $\alpha$, respectively) and thereby carry opposite spin angular momentum. Therefore, these modes cannot propagate in the respective other layer without spin-flip scattering. At higher frequencies, there is an overlap of $\beta$ modes of YIG and GIG leading to a hybridization of modes. As discussed at the beginning of this chapter, the SSE signal is dominated by the $\alpha$ modes at low temperatures. Therefore, the contribution from the hybridized $\beta$ modes might be insufficient to observe the switching of the YIG layer around the second compensation point at $T_{comp,B}$. One might find clearer evidence for a contribution to the SSE signal by hybridized YIG modes by shifting the bilayer compensation point to higher temperatures, where the $\beta$ modes are more occupied in GIG. To keep the GIG below the Pt layer as in the sample already measured, one could grow a trilayer as: GGG/GIG($x$)/YIG(36 nm)/GIG(30 nm) with different bottom layer GIG thicknesses $x$. Whether the switching of the YIG layer is visible in these samples will depend on the magnon spectrum and contribution to the SSE signal in the field-aligned state, which is not known to date.
Despite the missing evidence of magnon hybridization in the field-dependent SSE measurements, there might be an indication in the temperature-dependent SSE amplitude. According to [133], the second compensation temperature in SSE measurements shifts to lower temperatures in YIG/GIG samples with increasing YIG thickness. In our measurements, the second compensation point in a GGG/YIG(36 nm)/GIG(30 nm) is found at around 50 K, which is significantly lower compared to pure GIG samples (around 70-80 K [33]). While this could depend also on the ratio of the interface coupling of the different magnon modes to the Pt layer [33, 103], a series of measurements at different GGG/YIG($x$ nm)/GIG(30 nm) samples with a top Pt layer deposited at exactly the same conditions, could lead to a better understanding of the second compensation point in bilayer samples. This could then indicate the presence of hybridized YIG/GIG magnon modes.

## 4.4. Further usage of exchange coupled YIG-GIG heterostructures

Despite the missing demonstration of a functioning YIG-GIG magnon valve, the heterostructures could be used for different applications. These samples represent devices with defined magnetic properties depending on the relative thickness of the different garnet layers. At low magnetic fields, the YIG and GIG net magnetic moments are always aligned antiparallel below $T_{comp,G}$. This could be for example also used in tunneling magnetoresistance threshold sensors. Magnetic tunnel junctions consist of two conducting ferromagnetic layers (FM), separated by a thin insulating layer (I). The resistivity perpendicular to I depends on the relative magnetization alignment of the FM layers. In a sample, where a MTJ is deposited on a YIG/GIG structure, the

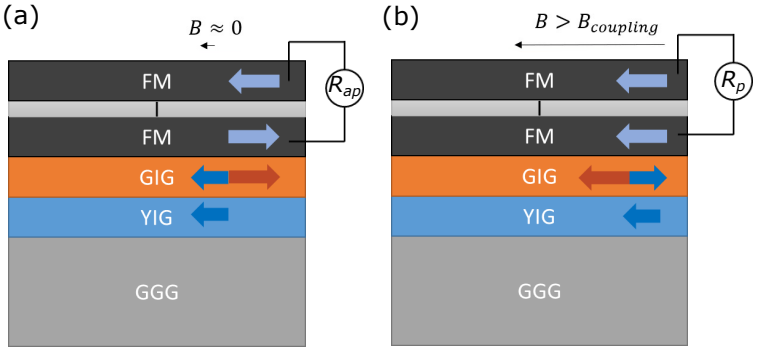


Figure 4.17.: Magnetic threshold sensor consisting of a MTJ (FM-I-FM) coupled to a YIG-GIG heterostructure. (a) In the presence of a small magnetic field, the MTJ is always in the antiparallel state, independent of the direction of the magnetic field. (b) large magnetic fields break the interlayer coupling and lead to the parallel magnetization state of the MTJ.

bottom ferromagnetic electrode of the MTJ can be magnetically coupled to the net magnetic moment of the GIG layer. Such a stack is depicted in Fig. 4.17.
In temperature region II, the net GIG moment aligns antiparallel to the field and so would the coupled FM electrode while the top FM electrode would align with the field. This would always lead to an antiparallel alignment of the FM electrodes, independent of the field direction. Only large magnetic fields, which break either the YIG-GIG or GIG-FM magnetic coupling would lead to the parallel alignment of the FM layers thus realizing a magnetic threshold sensor.
Concluding this chapter, we demonstrate the fabrication of interface exchange coupled YIG-GIG heterostructures. The extensive optimization of growth parameters led to samples of high crystalline quality. Making use of both SQUID and SMR measurements allows us to determine the phase space of YIG-GIG samples, depending on the temperature and relative thickness of the individual layers. In different regions of the parameter space, the magnetic sublattices align parallel or antiparallel to an external magnetic field. These devices are expected to be interesting candidates for a variety of application, foremost with regard to magnons. A first attempt using thermal spin currents supports the model of interface coupling, but does not show a contribution to the signal from the buried layer. This is disadvantageous for the realization of a GMR-like magnon valve. The main results of this chapter are published in a research article [S6]. In the next chapter, we will change topic and investigate the rare earth ferrite $TmFeO_3$, which could be used in different applications than the YIG-GIG heterostructures employed so far.

# 5. Electrical detection of magnetic phase transitions in bulk $TmFeO_3$

$TmFeO_3$ (TFO) is a canted antiferromagnet possessing both Néel and magnetic ordering as discussed in more detail in Sec. 2.2. In the vicinity of the spin reorientation transition (SRT), TFO has shown signs of coherent ultra-fast switching [21] between two stable magnetic configurations when subjected to THz laser pulses. However, the detection of the spin state in [21] relies on the Faraday effect which is unsuitable for device applications, not to mention that this demonstration was performed on a bulk crystal. For device integration, we want to make use of thin films and be able to access the magnetic state using spin Hall magnetoresistance (SMR), which could be implemented as a scalable on-chip read-out technique. However, thin film growth can alter the magnetic properties of the deposited material due to strain, which can complicate the interpretation of the data. We therefore first investigate bulk samples of TFO before turning to thin films in chapter 6 in order to validate our approach. For TFO single crystals, many properties are already reported in literature. This allows us to compare our results with the established parameters, which leads to confidence in the interpretation of our results.

Here, we will demonstrate possibility to read-out the magnetic state of TFO (101) single crystals using spin Hall magnetoresistance (SMR). First, the crystal structure and orientation of the surface is confirmed by XRD, where the author performed the measurements. Furthermore, Sven Becker utilized SQUID measurements to determine the temperature-dependent orientation of the magnetic moment. Magneto-optical Kerr effect (MOKE) measurements were performed by Felix Schreiber. These help to identify the presence of different magnetic domains across the sample. Andrew Ross patterned Pt Hall bars on the surface of the samples in order to enable electrical measurements. The spin Hall magnetoresistance measurements were then carried out by Sven Becker and Andrew Ross. The results of these measurements are currently being compiled into a research article [S10].

A $TmFeO_3$ crystal was grown by Ekatarina Pomjakshina at the Paul Scherrer institute (PSI). It was half a cylinder cut along the (101) crystallographic plane by our collaborators for an unrelated project. As this still provided access to both the $a$- and $c$-axis in our experimental setups, the exact orientation was not so important, but needs to be considered when interpreting the subsequent SMR data. To prepare it for measurements, the half cylinder was sliced parallel to the existing (101)-plane by the company *SurfaceNet GmbH*. As shown in Fig. 5.1 the surface of the single crystal was rather rough after the cutting process, measured by scanning electron microscopy (SEM) performed by Anja Dion. Since the surface condition is crucial for perform-

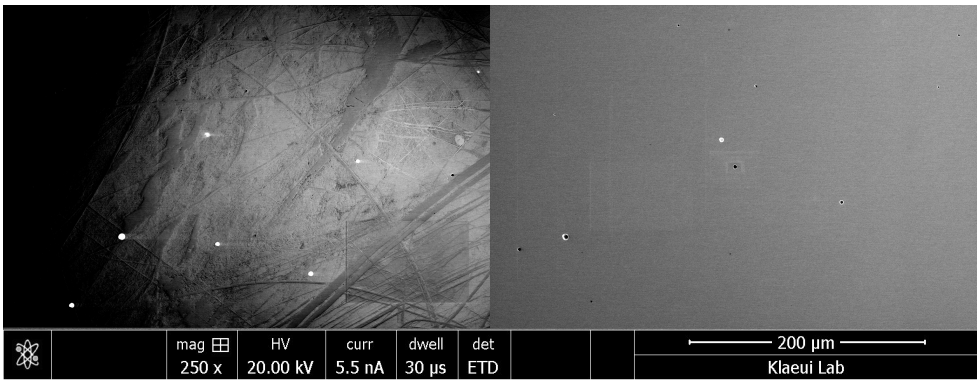


Figure 5.1.: Scanning electron microscopy image of the bulk TFO surface. Left: Measurement after cutting the single crystal into slices. Right: After polishing process performed by a company. Course surface structures are removed while single surface defects are still present. However, the density of defects is low.

ing spin Hall magnetoresistance measurements, the sample was sent to *MaTecK - Material-Technologie & Kristalle GmbH* to perform a polishing process. As shown in the right panel of Fig. 5.1, the texture on the surface could be removed by polishing. Both SEM images in Fig. 5.1 were taken under identical conditions. Single isolated defects are still present on the surface, like small particles and holes. However, the density of these defects is low, so they will not influence the electrical measurements performed on these samples.

## 5.1. Determination of structure and surface orientation

To determine the precise crystal structure, the relative orientation, as well as possible secondary phases, the crystal was measured by x-ray diffraction (XRD: Sec. 3.3). The (101) orientation was confirmed by performing $2\Theta/\omega$ measurements as shown in Fig. 5.2 (a), from which the (101) reflex can be identified by comparing with literature values. The rocking curve of the (202) reflex has a width of $\Delta\omega = 0.02°$ showing the good orientation of the unit cells to each other. Around the (202) reflex, one can detect secondary peaks of low intensity. These are also observed in unrelated samples and stem from the aluminum substrate holder used to mount samples in the XRD system. They are not related to properties of the TFO crystal. We can therefore conclude that no secondary phases can be observed by XRD in this measurement geometry.
The relative orientation of the surface normal and the $\langle 101 \rangle$-direction was determined by comparing the angle of total reflection and diffraction in two perpendicular tilt directions. This crystal has only a small miscut of around 0.3°, which can be neglected for any further measurements.
To determine the lattice parameters, $2\Theta/\omega$ measurements have been performed in the $\langle 001 \rangle$, $\langle 100 \rangle$ and $\langle 111 \rangle$ directions. The (100) reflex was found when tilting the

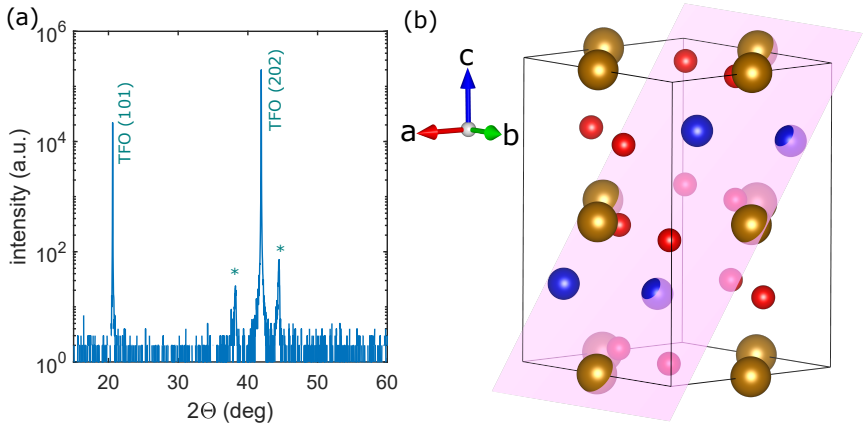


Figure 5.2.: (a) $2\Theta/\omega$-scan measured along the (101) direction perpendicular to the surface of the sample. The TFO (101) and (202) reflexes are labeled. Peaks marked with a star stem from the aluminum sample holder and are not related to the TFO crystal itself. (b) TFO unit cell with the (101) plane marked in pink. The gold, blue and red atoms are Tm, Fe and O, respectively. Drawn in Vesta [62].

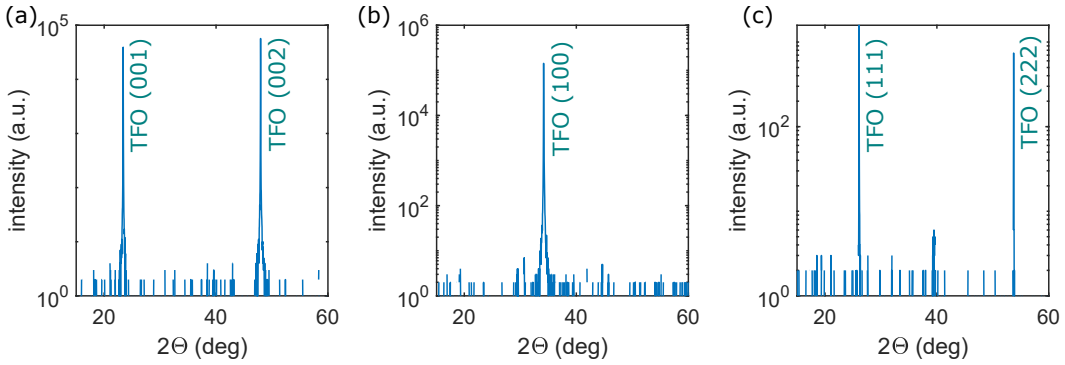


Figure 5.3.: (a) $2\Theta/\omega$-scan measured along the $\langle 001 \rangle$ direction. The respective TFO peaks are labeled. (b) $2\Theta/\omega$-scan measured along the $\langle 100 \rangle$ direction (c) $2\Theta/\omega$-scan measured along $\langle 111 \rangle$.

sample by around 55° and the (001) reflex at around 35° relative to the surface of the sample, which confirms the (101)-surface direction. These scans are given in Fig. 5.3. The width of the rocking curve for each reflex is around 0.02° (not shown), again indicating a well oriented growth of the TFO crystal. While the $a$ and $c$ lattice constants can be directly calculated from the peak positions, the $b$ lattice parameter is determined using the the standard textbook formula for orthorhombic crystal systems [109] $\frac{1}{d^2} = \frac{h^2}{a^2} + \frac{k^2}{b^2} + \frac{l^2}{c^2}$, where $(hkl)$ are the Miller indices and $d$ the lattice plane distance determined by the Bragg formula. The reflexes reproduce the literature values of the lattice parameters of $a = 5.25\,\text{Å}$, $b = 5.58\,\text{Å}$, and $c = 7.58\,\text{Å}$ [76].

Other growth directions are not detected as evident from the absence of secondary peaks in Figs. 5.2 and 5.3. This suggests that the sample is indeed a single crystal without any secondary growth direction or impurities from other material compositions.

## 5.2. Bulk magnetic properties of TFO single crystal

To gain a detailed understanding of the magnetic configuration, SQUID measurements are performed on the bare crystal (see Sec. 3.4). Measuring a bulk sample, the signal from the canted moment is expected to be large and easily to identify. SQUID magnetometry will allow us to investigate further the quality of the crystal, since small changes in stoichiometry might alter the magnetic properties without there being an indication of this in the structural analysis, since the peak positions in XRD are only sensitive to the position of the atoms. The magnetic properties on the other hand depend also on the type of atoms in the unit cell as evident from the different spin reorientation temperatures shown in table A.1. Furthermore, when performing electrical measurements, the signal will depend on the spin orientations. To ascertain effects observed in different types of measurements, it is crucial to understand the origin of the effects. We gain certainty in our interpretation by performing these measurements both on the same crystal.
First, we investigate the spin reorientation transition (SRT). The temperature depen-

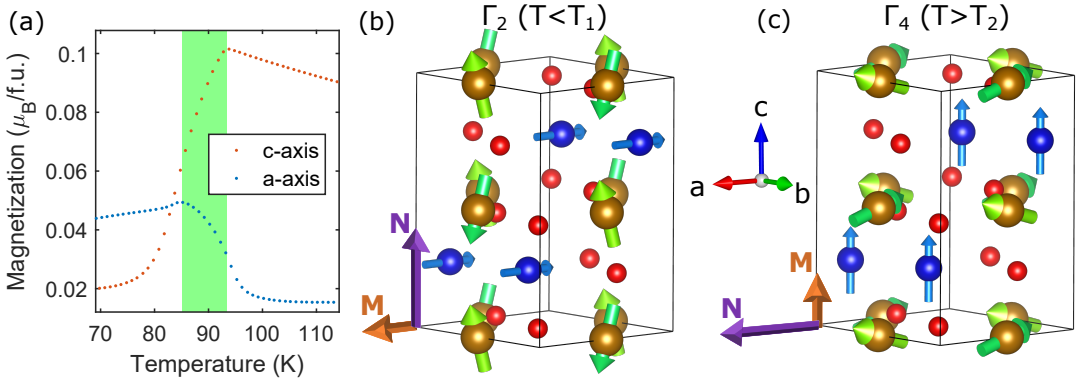


Figure 5.4.: (a) Temperature dependent magnetization measured along the $a$ and $c$ crystallographic axes, from which the SRT is extracted. The region of the SRT is indicated as green shaded area. (b)-(c) Magnetic configuration of the TFO unit cell in the respective magnetic phases. The arrows on the left side indicate the crystallographic axes. (b) In the $\Gamma_2$-phase, **M** is along $a$ and **N** is along $c$. The Tm moments are antiparallel to **M**. (c) In the $\Gamma_4$- phase, the magnetic moment **M** (orange) is along $c$ and the Néel vector **N** (purple) is along $a$. The paramagnetic Tm moment (blue) is polarized along the $c$-axis parallel to **M**. The arrows are not to scale.

dent magnetization along the $c$- and $a$-directions has been measured in SQUID with an applied field of 50 mT. Before the measurement, a field of 5 T has been applied for a short period of time to orient the magnetization. For the measurement in the $c$-direction, the field has been applied at 300 K before performing measuring during a cool-down sequence. For the measurement in the $a$-direction, the field has been applied at 20 K before measuring the magnetization while heating. In Fig. 5.4 (a) both of these curves are shown in proximity to the interesting region around the SRT. The signal consists of two contributions: the temperature-independent canting of the Fe sublattices and the paramagnetic contribution of the Tm ions. The latter is oriented by the effective exchange field from the Fe ions at the rare earth site. Towards lower temperatures, the polarized Tm moment increases according to $\propto 1/T$ (see section 2.2). Coming from high temperatures, the magnetic moment along the $c$-axis first increases due to the parallel alignment of the paramagnetic Tm moments with the canted moment of the Fe ions [71]. The relative alignment of Tm and Fe moments is shown in Fig. 5.4 (c). At around $(94 \pm 1)$ K the magnetization starts to decrease which we attribute to the spin reorientation temperature $T_2$. The uncertainty is given by the step-size of the measurement. The magnetization along $c$ decreases rapidly between $T_2$ and roughly 80 K due to the reorientation perpendicular to the measurement direction. The determination of the spin reorientation transition temperature $T_1$ is not possible from this measurement as the external magnetic field exerts a torque on the magnetization prohibiting the alignment with the $a$-axis. To determine $T_1$, the sample was remounted along the $a$-axis and measured starting at low temperature. Upon heating, first an increase of the magnetic moment along $a$ is observed due to the antiparallel alignment of paramagnetic Tm moments with the canted moment decreasing with increasing temperature. At around $(85 \pm 1)$ K the overall magnetization starts to decrease in $a$-direction, which we attribute to $T_1$. The relative alignment of Tm and Fe moments are shown in Fig. 5.4 (b). By this method we reproduce very well the literature values for the SRT. The slight deviation of 2 K for $T_1$ may stem from the magnetic field of 50 mT being applied during the measurement or an imperfect alignment of the sample in the setup.

Field-dependent measurements have been performed to support the observations in temperature-dependent measurements as shown in Fig. 5.5 (a) for the $c$-axis direction. At 200 K an easy-axis hysteresis loop is observed with a saturation magnetization of around $M_s = 0.05\ \mu_B$/f.u. and a coercive field of around $\mu_0 H_c = 80$ mT. We note that the magnetization values are only a rough estimate since the volume of the single crystal could not be precisely determined due to its irregular shape and cautions made in order to avoid damages to the polished surface. Going to 100 K, $M_s$ increases up to around 0.076 $\mu_B$/f.u. due to the paramagnetic Tm moments. The coercivity drastically decreases to around 2 mT, which is attributed to the temperature-dependent anisotropy constants. The effective anisotropy energy $H_{K2} = A_{aa} - A_{cc}$ goes zero in the SRT regime (see Sec. 2.2), which has been shown for TFO single crystals by terahertz time domain spectroscopy [20, 134] and neutron scattering experiments [135]. $H_{K2}$ is found to decrease linearly with temperature [135] from a positive energy below the SRT to a negative above. This leads not only to the reorientation of spins, but

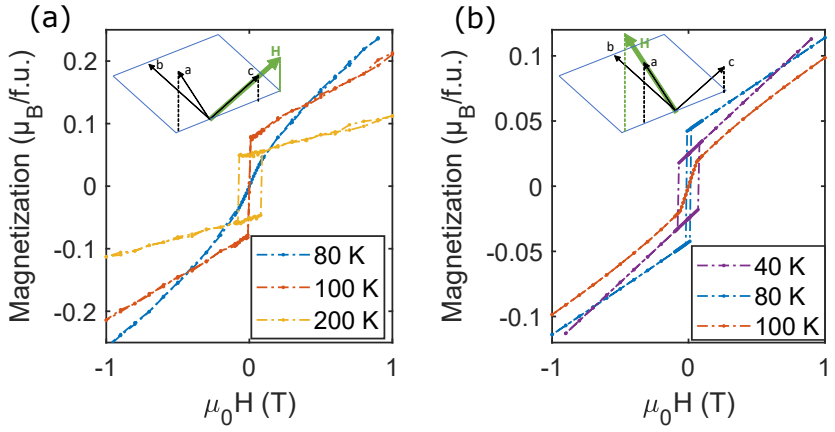


Figure 5.5.: (a) Field dependent measurements performed at different temperatures along the $c$-axis. (b) Field dependent measurements performed at different temperatures along the $a$-axis.

also to temperature-dependent coercive fields, monotonically increasing with increasing (for measurements along $c$) and decreasing temperatures (for measurements along $a$) away from the SRT. Focusing on magnetic fields larger than the coercive fields $H_c$, we observe that the susceptibility increases going from 200 K to 100 K. The increase of susceptibility is expected to originate only from the paramagnetic properties of the Tm ions since the change of canting angle of the Fe sublattices is expected to be temperature-independent because it is dominated by the temperature-independent symmetric and antisymmetric exchange energies. At 80 K, below the SRT, the shape of the curve shown in Fig. 5.5 (a) has changed fundamentally compared to the higher-temperature curves. This is expected since the magnetic moment of the Fe sublattice as well as the polarized Tm moments now lie perpendicular to the measurement direction. Therefore, one observes a hard-axis curve with a coercivity of zero. In addition to the canting angle of the Fe sublattices and the magnitude of the paramagnetic moment of the Tm ions, which are important for the curves at higher temperatures, here also the orientation angle of $\mathbf{M}$ with the $c$-axis is important. It is expected that $\mathbf{M}$ continuously rotates from the $a$- to the $c$-axis at sufficiently large fields and simultaneously $\mathbf{N}$ rotates from the $c$-axis to the $a$-axis [136]. At the spin-reorientation-field $H_{sf}$ (or spin-flop-field) this rotation is complete. One would expect a change of slope in $M(H)$ measurements at $H = H_{sf}$. This is not clear from this measurement because of the limited magnetic field range. However, measurements in the SQUID at larger magnetic field could not be performed due to the upper detection limit of the device.

In Fig. 5.5 (b), the corresponding measurements in crystallographic $a$-direction are shown. Far below the SRT at 40 K we see an easy-axis loop with a relatively large coercive field of around 144 mT. The saturation magnetization is around 0.025 $\mu_B$/f.u., which is significant lower than what has been measured along the $c$-axis due to the antiparallel alignment of the Tm moments to the canted moment of the iron sublattices.

Going closer to the SRT, at 80 K, we observe an increase of $M_s$ to around 0.043 $\mu_B$/f.u. because of the temperature-induced decrease of $m_{Tm}$. Simultaneously, the coercivity decreases due to the reduction of anisotropy energy. The susceptibility measured at $T = 40$ K is larger than at 200 K, because the paramagnetic Tm moments align antiparallel and parallel with the canted moment, respectively. The different shapes of the easy axis curves can therefore be understood. Above the SRT, at 80 K the $M(H)$ becomes a hard axis loop due to the alignment of **M** along the $c$-axis perpendicular to the measurement direction.
The field-dependent measurements support the temperature-dependent measurements and clearly show the SRT within the $ac$-plane between 85 K and 94 K. Furthermore, the temperature-dependent change of anisotropy is observed. With SQUID measurements, it was difficult to determine the spin-reorientation-field $H_{sf}$ because of the limitation of the instrument. We will see below that electrical measurement techniques are appropriate to determine $H_{sf}$. The big advantage of this method is the surface sensitivity, i.e. it does not rely on the size of the sample and is the appropriate technique when considering actual applications.

## 5.3. Magnetic domains in TFO

Knowing the magnetic domain configuration has been shown to be helpful to interpret electrical data [15, S2]. Furthermore, for other applications like magnon transport, the domain structure can have a profound impact [S2]. First evidence of the presence of magnetic domains can already be found in SQUID measurements. In Fig. 5.6 (a), a SQUID hysteresis measured at 105 K along the $a$-axis is shown. We observe a triangular feature close to zero that is not seen in the other measurements presented. The occurrence of symmetric triangular features is reported for $ErFeO_3$ [137, 138] single crystals, and can be reproduced for samples with a single magnetic domain wall [138, 139]. However, when multiple magnetic domain walls are present, these features are not reproducible and explain the asymmetric curve we observe here. To learn more about the domain configuration, the magneto-optical Kerr effect (MOKE) has been utilized by Felix Schreiber to visualize magnetic domains in the TFO single crystal. Fig. 5.6 (b) to (e) shows magnetic domains at four different temperatures, starting from higher temperature (b), where TFO is in the $\Gamma_4$ state, going to lower temperatures, through the SRT. Stripe-like domains are observed, which are directed along the $b$-axis. Upon reduction of the temperature, the width of the domains decreases, in line with earlier reports [140]. The reason for the shrinking of the domains is the reduction of the uniaxial anisotropy energy and the associated reduction of the domain wall energy [141]. In Fig. 5.6 (d), which is likely at the border of the transition temperature $T_2$[1], the stripe domains start to deform. Further decreasing the temperature

[1] An exact determination of the respective temperatures could not be performed because the MOKE setup is equipped with a He-cooled cryostat. There is no temperature sensor attached to the sample, instead it is placed at the bottom of the chamber next to the He-intake valve so that, even in thermal equilibrium, the temperature at the sensor and sample surface are different. Furthermore,

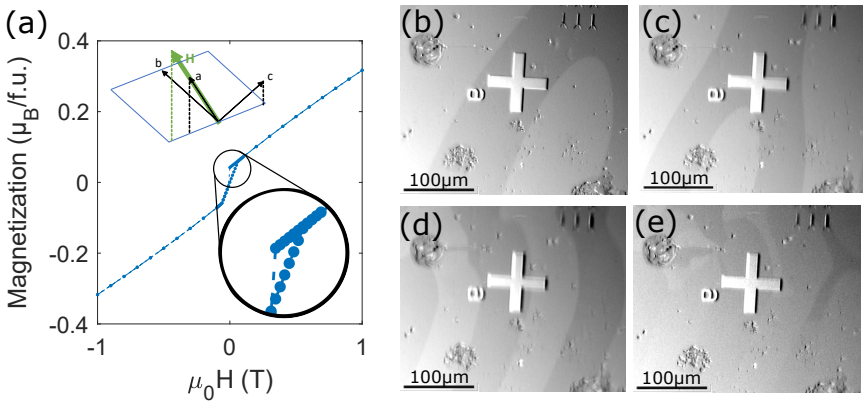


Figure 5.6.: (a) Magnetic field dependent magnetization measurement performed in SQUID along the crystallographic $a$-axis at a temperature of 105 K. The inset shows a zoomed in region. (b) to (e) Magneto-optical Kerr effect measurements performed close to the SRT going from higher temperature (a) to lower temperature (e). The Pt cross in each figure is from the lithography process and used as a reference point. Besides the Pt structures and the magnetic domains, surface defects are visible. The exact sample temperature could not be determined during the experiment

leads to complex domain dynamics, which happens within the SRT. While at higher temperatures, only two types of domains were visible, here, four types of domains are present as seen in Fig. 5.6 (e). The domains stem from the two possible directions in which **N** and **M** can reorient, when rotating in the $ac$-plane. The occurrence of four domains suggests that Fig. 5.6 (e) shows the TFO at a temperature within the SRT. We leave the complex domain dynamics within the SRT for further studies and limit our conclusion to that the TFO single crystal is magnetically homogeneous. The stripe-domains are uniformly spread over the sample. The width is of the order of the width of the Hall bars, which are also oriented along the $b$-axis.

## 5.4. Surface-sensitive electrical measurements

Electrical measurements have been performed after defining a Pt Hall bar on the (101) surface of the bulk TFO sample via lithographic techniques (see section 3.6). The Hall bar is oriented along the crystallographic $b$-direction as depicted in Fig. 5.7. We introduce a coordinate system for the Hall bar, where $x$ is the current direction, corresponding to the crystallographic $b$-axis, $y$ corresponds to the in-plane direction perpendicular to $x$ and $z$ is the out-of-plane direction.
The number of measurements performed on this sample is limited because of its large magnetic moment and uniaxial anisotropy. While single crystal hematite ($\alpha$-$Fe_2O_3$)

these MOKE images were taken during a cooling sequence making the sensor temperature even less reliable.

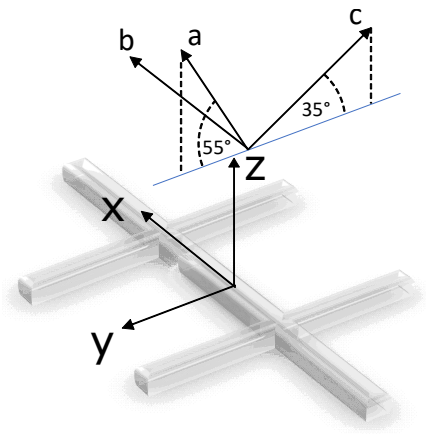


Figure 5.7.: Relative orientation of the Pt Hall bar with the crystallographic axes. The $x$-axis of the Hall bar is along the crystallographic $b$-axis (= current direction). $z$ is the out-of-plane direction and $y$ is in-plane perpendicular to the current. The crystallographic axes $a$ and $c$ both lie in the $yz$-plane. $c$ ($a$) has an angle of 35° (55°) with the surface as indicated.

samples have been measured in our setup previously, using identical techniques, we learned that it is not as straight forward with orthoferrite samples. When applying a magnetic field in an arbitrary direction with respect to the magnetic ordering, a large torque on the sample can appear since it prefers to align with the antiferromagnetic easy axis parallel to the magnetic field [142, 143]. This torque is transferred via the sample holder to the piezoelectric rotator which is not designed to endure such external torques. The forces acting on the piezoelectric elements not only prevented free rotation of the sample or the application of the field in arbitrary directions, but led to significant damage to the principle rotator after the first rotation measurement sequence (shown in appendix section A.4). At a later stage, the applied forces led to the destruction of the sample during the measurements. It is assumed that the experienced torque led to a detachment of the sample from the PCB holder, accelerating it towards the walls of the VTI where it shattered. Given that similar problems did not occur with hematite single crystals, we attribute this to the larger canted moment of TFO single crystals together with the large paramagnetic moment of the Tm sublattice.
In the following, the measurements gathered before the destruction of the sample are presented. We will see that the results are highly interesting suggesting that the set of measurements should be completed by using smaller-sized samples to reduce the total torque acting on the sample and instrumentation.

### 5.4.1. Detection of spin reorientation by longitudinal SMR

In uniaxial measurements, the field is applied in the direction of the crystallographic $a$- and $c$-axes at various temperatures around the SRT. In this geometry, a sufficiently

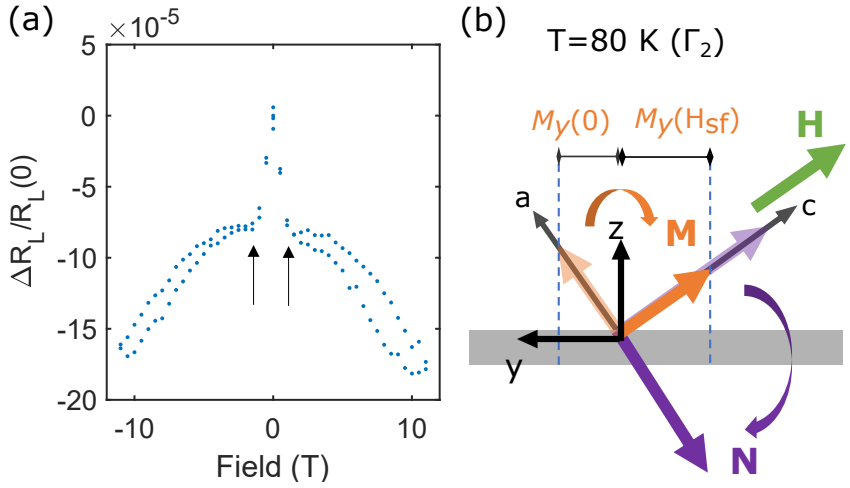


Figure 5.8.: (a) Example curve for the relative longitudinal resistivity in uniaxial field sweeps along the $c$-axis below the spin reorientation temperature $T_2$. The black arrows mark the spin reorientation field $H_{sf}$, where the maximal gradient change happens. (b) Sketch of the possible dynamics of **M** (orange) and **N** (purple) during the reorientation under a magnetic field **H** (green). Pale arrows indicate the initial configuration at $|\mathbf{H}| = 0$. Black arrows labeled with $x$ and $y$ indicated the reference frame of the Hall bar, $a$ and $c$ the crystallographic axes of TFO. For **M**, the projection along $y$ increases while for **N**, it decreases. The DMI vector is oriented in the sample plane along the $b$-axis.

large magnetic field is able to rotate the spins in the $ac$-plane so that the canted moment **M** orients with the magnetic field **H**, while the Néel vector **N** orients perpendicular to **H** as shown in Fig. 5.8 [80, 81, 144]. Around the SRT, this is possible at relatively low magnetic fields due to the reduction of uniaxial anisotropy with temperature. $H_{K2}$ is expected to have a minimum in the transition region [135].

We start by investigating the longitudinal resistivity $R_L$, which should reflect the relative contribution of **M** and **N** projected parallel to the interfacial spin accumulation, i.e. the $y$-component of each. Fig. 5.8 (a) shows an example curve for $R_L$ measured at 80 K, where TFO is in its $\Gamma_2$-phase in absence of a magnetic field. The field is applied along the $c$-direction, perpendicular to **M**, and parallel to **N** (see Fig. 5.8 (b) pale arrows).

We observe a sharp decrease of $R_L$ at low magnetic fields before $R_L(H)$ significantly changes slope. The abrupt decrease is followed by a more gradual decrease to larger magnetic fields. We expect that the $y$-components will have maximally changed once the spin reorientation is complete so we identify the point of sudden change of gradient as the spin reorientation field $H_{sf}$, where the **N** and **M** reach their final orientation. Between 0 T and $H_{sf}$, both **N** and **M** continuously and smoothly rotate. The value of $H_{sf}$ is determined as described in appendix section A.5. Our interpretation of

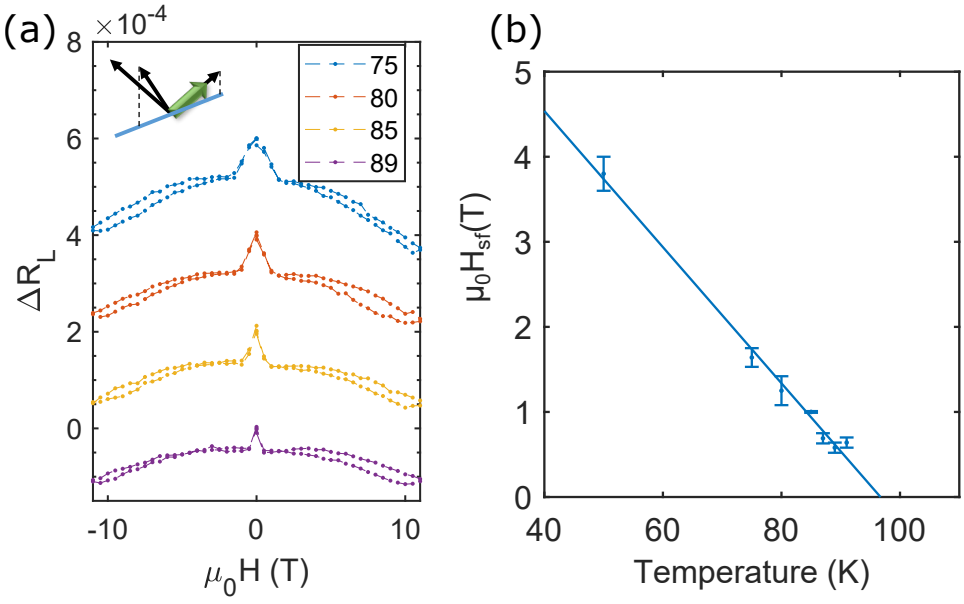


Figure 5.9.: (a) Relative longitudinal resistivity in uniaxial field sweeps along the $c$-axis at different temperatures below the spin reorientation temperature $T_2$. (b) $H_{sf}$ determined by (a) for different temperatures. The blue line indicates a linear fit.

this field being related to the rotation of the magnetic ordering in the $ac$-plane is further validated by considering the temperature evolution of $R_L$ and $H_{sf}$. Fig. 5.9 (a) shows the field-dependence of $R_L$ for several temperatures below $T_2$ for **H** applied along the $c$-axis. At all temperatures, the same general trend is observed. Moving from low temperatures to those closer to the transition temperature $T = T_2$, $H_{sf}$ decreases. We extract $H_{sf}$ for each temperature, and observe that a linear function can be fitted to the temperature-dependent spin reorientation field as shown in Fig. 5.9 (b). This temperature dependence of the spin reorientation field is in good agreement with microwave absorption experiments performed on TFO single crystals [81], and naturally follows from the temperature dependence of the magnetic anisotropy. Our linear fit to $H_{sf}$ from these measurements extrapolates to $T = 96\,\mathrm{K}$.
Taking into account the trend between $R_L(0\,\mathrm{T})$ and $R_L(H_{sf})$, we observe a net decrease of $R_L$. Comparing the $\Gamma_2$ state, which is the magnetic configuration at zero field and the $\Gamma_4$ state above $H_{sf}$, this reorientation is accompanied by an increase of the $M_y$ contribution and a simultaneous decrease of the $N_y$ contribution. Applying the model of SMR to this [16, 43], we include both possible dependencies of **N** and **M**:

$$\Delta R_L \propto \Delta R_{1,M}(1 - M_y^2) + \Delta R_{1,N}(1 - N_y^2) \tag{5.1}$$

Due to the net decrease of $R_L$, the signal appears to be dominated by $\Delta R_{1,M}$ rather than $\Delta R_{1_N}$. Further decrease of $R_L$ at large fields $H > H_{sf}$ might be due to the

increase of canting angle induced by the magnetic field as described in section 2.2. The increase of canting of the Fe sublattices leads to a further increase of $M_y$ proportional to the Zeeman energy which is quadratic given the two sublattices. We note that in this simple picture, the change of $R_L$ cannot be explained by a sole dependency of the SMR on the Néel vector. The decrease of the $y$-component of **N** would lead to an increase of $R_L$, which is not observed.
However, taking into account the trajectory of **M**, the signal can also not be completely explained by a magnetic monodomain experiencing a continuous rotation of **M**. Looking back at Fig. 5.8, the continuous rotation of **M** from the $a$-axis to the $c$-axis leads to a minimum in the net $y$ contribution within the reorientation regime, when **M** is parallel to the geometric $z$-axis. We consider this further by plotting $y$-component of **M** and **N** against the normalized magnetic field in Fig. 5.10 (a) for the case of a monodomain magnetic state. For this model, we assume a linear change of $\sin(\phi) \propto \mathbf{H}$ between $H = 0$ and $H = H_{sf}$, where $\phi$ is the angle between **M** (**N**) and the $a$- ($c$)-axis. This is a simple model for the complex interaction occurring during the SRT. The linear change of $\sin(\phi)$ with **H** is a good approximation for the field-induced $\Gamma_4 \Rightarrow \Gamma_2$ transition in $YFeO_3$ [144], however, the trajectories of **M** and **N** can be more complex and strongly temperature-dependent in other orthoferrites [145]. Nevertheless, the trajectory of both vectors is expected to be continuous and therefore a linear approximation for the SRT in TFO sufficiently describes the characteristic features in the SMR response.
From the trajectory of **M** and **N**, we can calculate the expected SMR contribution to the longitudinal resistivity, which is given in Fig. 5.10 (b). Across the field range

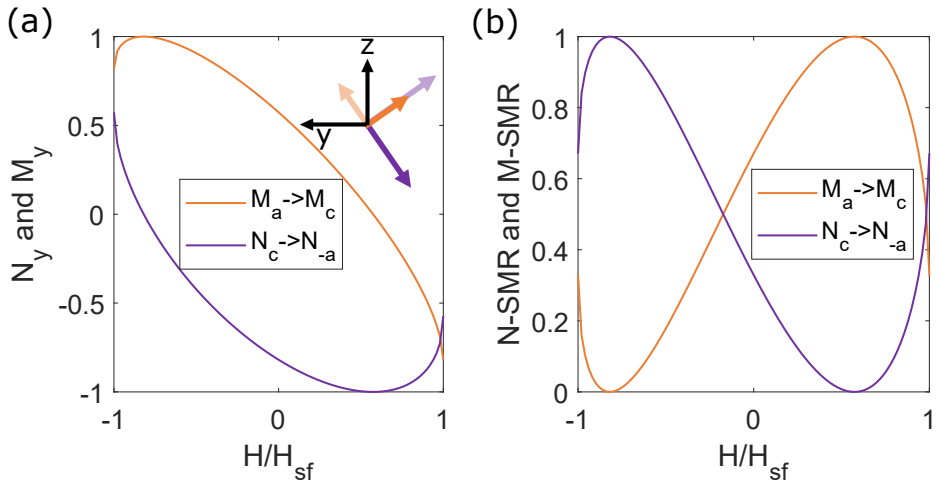


Figure 5.10.: (a) Normalized $y$-contribution of **M** and **N** during the spin reorientation transition. The inset sketches the field-dependent rotation in the $ac$-plane of **M** (orange) and **N** (purple) until the spin reorientation field $H_{sf}$ relative to the coordinate system of the Hall bar (black). (b) Relative change to the M- and N-dependent SMR, respectively.

that the SRT takes place, both the N- and M-dependent SMR describe an extremum between $H = 0$ and $H = H_{sf}$. This is not reproduced by the experimental data. However, we note that $\mathbf{M} \parallel a$ and $\mathbf{N} \parallel c$ (I) is only one out of four possible configurations in the $\Gamma_2$ state. Furthermore, the following domains are possible: $\mathbf{M} \parallel a$ and $\mathbf{N} \parallel -c$ (II), $\mathbf{M} \parallel -a$ and $\mathbf{N} \parallel c$ (III), $\mathbf{M} \parallel -a$ and $\mathbf{N} \parallel -c$ (IV). The domains are depicted in Fig. 5.11 (a). The calculation for domains II-IV is given in the appendix section A.2. When allowing for a superposition of these different trajectories, the modeled SMR describes a monotonous trend of resistivity in the transition regime. We calculate the cases $R_{1,N} = 1$, $R_{1,M} = 0$ (N-SMR) and for $R_{1,N} = 0$, $R_{1,M} = 1$ (M-SMR) according to equation 5.1. Fig. 5.11 (b) shows the case of an equal contribution of all four domains calculated as the average SMR response by

$$\Delta R_L = \frac{1}{4}\left((1 - M_y^I)^2 + (1 - M_y^{II})^2 + (1 - M_y^{III})^2 + (1 - M_y^{IV})^2\right)$$

for the M-SMR and similarly for the N-SMR. Note that for domains I and IV, the DMI vector points in the same direction, while for domains II and III it points in the opposite direction. If we allow only one global orientation of the DMI vector, this leaves us with only two different domains, either II/III or I/IV. However, the monotonous trend in the SMR can still be reproduced by this subset of two domains since SMR contributions of domains I and II and domains III and IV are the same. We can therefore conclude that the monotonous trend of the resistivity change between $H = 0$ and $H = H_{sf}$ requires the presence of multiple domains and a dependency of the SMR on $\mathbf{M}$.
Besides SMR, we also expect possible contributions from OMR and HMR. The OMR

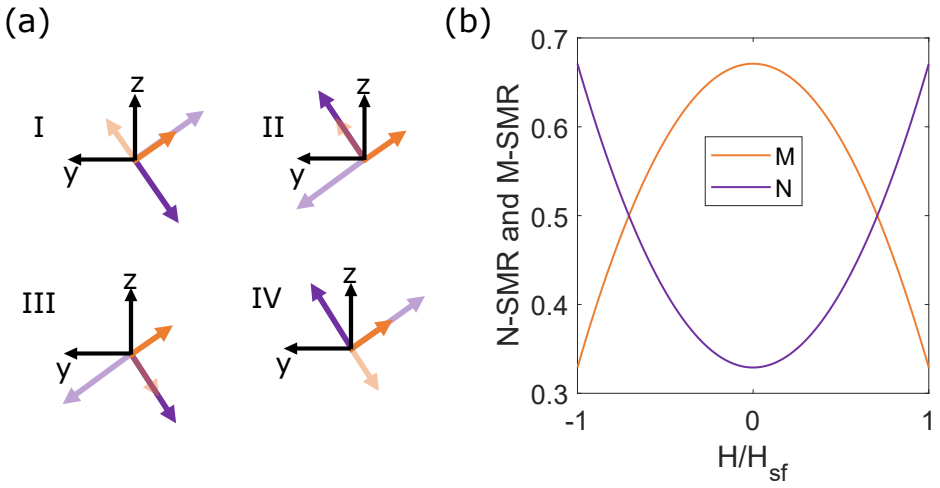


Figure 5.11.: (a) Initial (pale) and final domain configuration for a field-induced SRT from the $\Gamma_2$ state to the $\Gamma_4$ state by a field applied along the $c$-axis. (b) Average SMR response for the simultaneous presence of all possible domains.

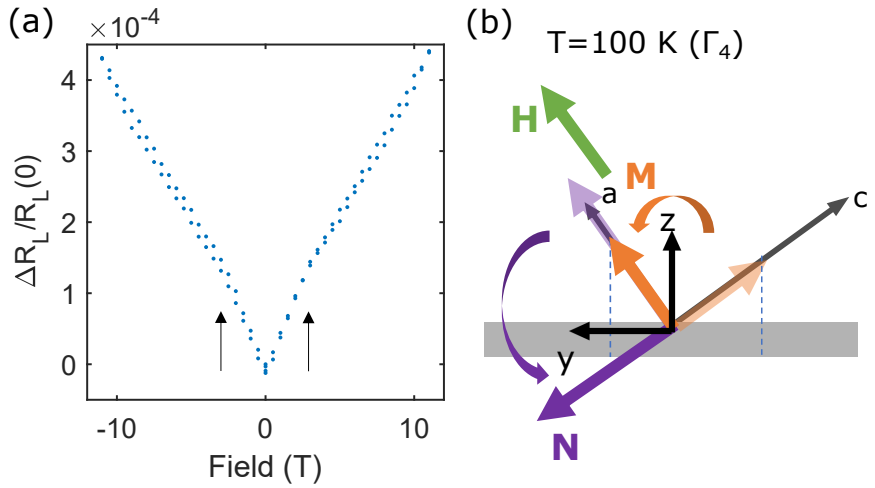


Figure 5.12.: (a) Example curve for the relative longitudinal resistivity in uniaxial field sweeps along the $a$-axis above the spin reorientation temperature $T_1$. The black arrows mark the $H_{sf}$. (b) Sketch of the possible trajectory of **M** (orange) and **N** (purple) during the reorientation under a magnetic field **H** (green). Pale arrows indicate the initial configuration at $H = 0$. Black arrows labeled with $y$ and $z$ illustrate the reference frame of the Hall bar, $a$ and $c$ are the crystallographic axes of TFO.

would lead to an increase of the resistivity [37]. The HMR, which would also lead to an increase of $R_L$ [50], contributes minimally given that the projection of **H** perpendicular to the spin accumulation $\boldsymbol{\mu}$ is small. The overall negative sign of the resistivity change leads to the conclusion that the signal is dominated by SMR, despite possible contributions from OMR and HMR, which are expected to counteract the trend of the SMR.

We repeat the experiment for the field-induced SRT from the $\Gamma_4$ to the $\Gamma_2$ phase. For this, we increase the temperature to $T > T_1$ and apply a magnetic field along the crystallographic $a$-axis.

Fig. 5.12 (a) shows the case for the longitudinal resistivity $R_L$ measured at a temperature of 100 K, where TFO is in the $\Gamma_4$-phase. Like before, the signal consists of two symmetric contributions, this time with a positive sign. A steep increase at low magnetic field is followed by a change of slope to a more gradual increase. Fig. 5.12 (b) shows one of the four possible trajectories of **M** and **N** relative to the reference frame of the Hall bar. The trajectories of all four different domains and the resulting SMR contribution is shown in the appendix section A.3. While no single domain can describe the monotonous trend in the change of resistivity, a superposition of at least two domains leads to a monotonous increase of the M-SMR.

The shape of the curve up to $H = H_{sf}$ can again be explained by M-SMR in the presence of multiple domains. Increasing the field above $H = H_{sf}$ leads to an increased canting of the spin sublattices in the direction of **H** and an increase of $M_y$, which

should contribute an increasingly negative component to the MR. However, a positive change of the resistivity is observed at $H_{sf}$ in contrast to the overall negative MR seen before. This might be explained by the different orientation of **H** relative to the Hall bar. Due to the smaller projection of **M** in $y$ compared to the previously discussed case of **H** $\parallel c$, the field-induced increase of canting angle and resulting contribution to the SMR may be shadowed by other MR effects. We note that the absolute increase of $R_L$ is about a factor of 2 larger than for the case **H** $\parallel c$. The OMR leads to an increase of the longitudinal resistivity with increasing magnetic field. Also the HMR, which is also expected to increase $R_L$, has a larger magnitude in this geometry than before due to the larger projection of **H** perpendicular to the spin accumulation $\boldsymbol{\mu}$. We further note that the shape of $R_L(H)$ at larger magnetic fields is approximately linear in this configuration, while it has a rather quadratic shape when the field is applied along the $c$-axis. This also indicates that the origin of the high field resistivity is dominated by different effects in the two configurations.

We repeat the measurement at various temperatures as shown in Fig. 5.13 (a). Focusing on the response below $H_{sf}$, we observe a temperature-dependence of $H_{sf}$ as expected from the change of uniaxial anisotropy. We note that the change of slope is less prominent in this geometry than in Fig. 5.9. However, we are able to determine the critical field at which the gradient of the slope changes as described in the appendix section A.5. The trend of $H_{sf}$ with temperature is shown in Fig. 5.13 (b).

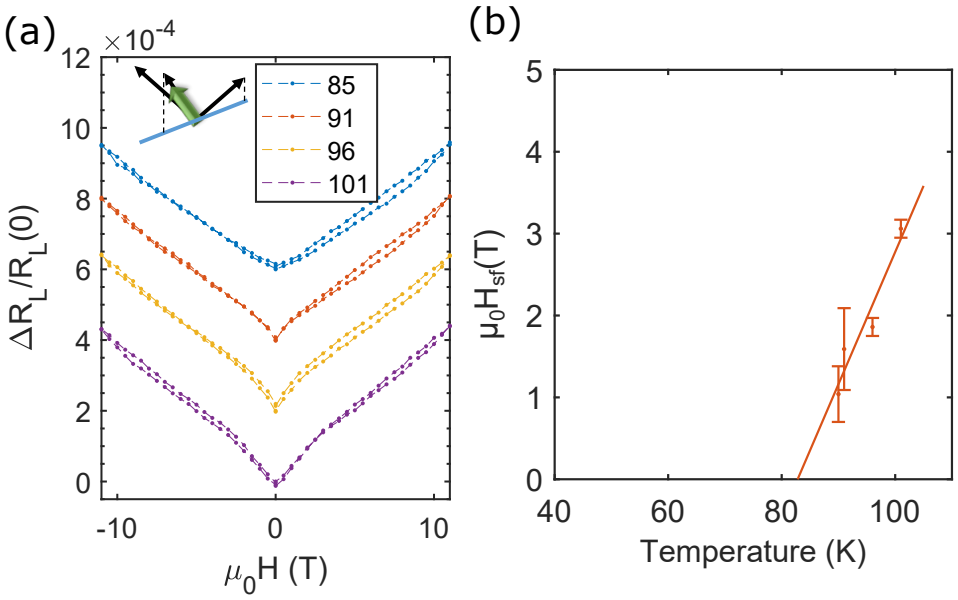


Figure 5.13.: (a) Relative longitudinal resistivity in uniaxial field sweeps along the $a$-axis at different temperatures above the spin reorientation temperature $T_1$. (b) $H_{sf}$ determined by (a) for different temperatures. The red line indicates a linear fit.

Just as for $\mathbf{H} \parallel c$, we observe a monotonic dependence of $H_{sf}(T)$, that can be fitted with a linear function as indicated by the red line. We similarly see good agreement with microwave absorption experiments in the same geometry [81].
Summarizing the measurements of the longitudinal resistivity for the two different geometries, we have seen that we can detect the spin-reorientation-field purely electrically. The linear evolution of $H_{sf}(T)$ for both $\mathbf{H}$ along $a$ and $\mathbf{H}$ along $c$ has been previously observed in microwave absorption experiments [81], validating our approach and interpretation of the SMR data given above. We can perform a linear fit of both data sets and extrapolate to $H_{sf} = 0\,\mathrm{T}$, which gives the critical temperatures of the SRT.

| Method | SQUID | SMR |
|---|---|---|
| $T_1$ (K) | $85 \pm 1$ | $83.7 \pm 3.0$ |
| $T_2$ (K) | $94 \pm 1$ | $96.6 \pm 1.7$ |

Table 5.1.: Critical temperatures of the SRT determined by different methods.

Using this method we find the critical temperatures of the SRT as presented in table 5.1, where we compare the numbers with the temperatures determined by SQUID magnetometry. The error bars for the values determined by SMR are given by the uncertainty of the fit. An additional systematical error of the temperature is expected since the different experiments have been performed in different cryostats as well as differences in environmental temperature sensor locations relative to the sample. Therefore, the similar values confirm that we are not only able to determine the spin-reorientation-fields at several temperatures using SMR, but also extract the exact spin-reorientation temperatures. Further increase of the precision could be achieved by using smaller steps in the uniaxial measurements, using thinner Pt to decrease the impact of OMR and by using a different orientation of the TFO crystal. A crystal with (001)- or (100)-orientation would allow for Hall bars to align the $y$-orientation with one crystallographic axis, which would maximize the difference of the SMR signals between $\Gamma_2$- and $\Gamma_4$-state of TFO.

### 5.4.2. Additional contribution to the transverse SMR

We now turn to focus on the transverse resistivity $R_T$ in uniaxial measurements, which is measured simultaneously with the longitudinal resistivity discussed above. Since the projection of both $\mathbf{M}$ and $\mathbf{N}$ along the $x$-direction of the Hall bar is zero, there is only a contribution from the spin Hall anomalous Hall effect (SHAHE) expected (see section 1.6.2), which is given by

$$\Delta R_T \propto \Delta R_2 M_z.$$

We therefore consider only the magnetization. Fig. 5.14 (a) shows calculations of the $M_z$ component from two different domains $\mathbf{M} \parallel a$ (I and II) and $\mathbf{M} \parallel -a$ (III and IV) during the $\Gamma_2 \rightarrow \Gamma_4$ reorientation. Here, we again assume $\sin(\phi) \propto H$ as before.

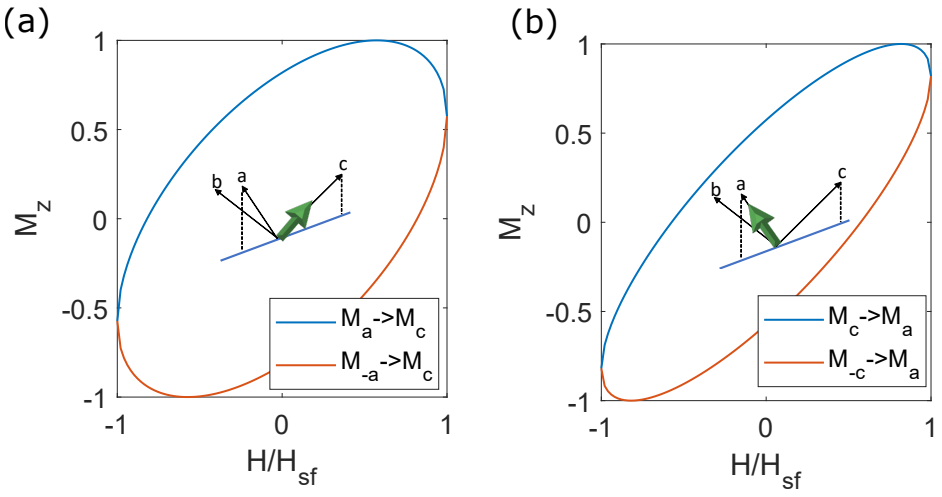


Figure 5.14.: (a) Relative transverse resistivity $R_T$ in uniaxial field sweeps along the $c$-axis at different temperatures below the spin reorientation temperature $T_2$. (b) Relative transverse resistivity $R_T$ in uniaxial field sweeps along the $a$-axis at different temperatures above the spin reorientation temperature $T_1$.

$M_z$ is plotted from -$H_{sf}$ to $H_{sf}$. We do not show the average of all possible domains (which is a linear function) since the sample area probed by the transverse resistivity is significantly smaller than for the longitudinal resistivity and more importantly smaller than the domain size, even in the reorientation regime (see Fig. 5.6). We therefore do not expect an averaged contribution from different domains and expect only one of the two possible responses due to SMR. Both possible trajectories are asymmetric with field up to the spin reorientation field $H_{sf}$. Towards higher magnetic fields, only a linear change is expected, originating from the increase of canting angle. Similarly, there are two possible trajectories for $\mathbf{M}$ in the $\Gamma_4 \rightarrow \Gamma_2$ transition as seen in Fig. 5.14 (b). For both measurement geometries, we aim to apply this model to the experimental data.

The electrical measurements of the transverse resistivity will also contain a significant contribution from the ordinary Hall effect, which appears once there is an out-of-plane component of the applied magnetic field. This effect is linear in field, and given that it has no relation to the magnetic landscape of the TFO, the raw data has been processed by removing a linear fit in order to identify the SHAHE contribution in our measurements. The resulting $R_T(H)$ curves for both $\mathbf{H} \parallel c$ and $\mathbf{H} \parallel a$ are shown in Fig. 5.15 (a) and (b) for different temperatures, respectively. We focus first on Fig. 5.15 (a). The signal consists of two contributions: an asymmetric one leading to an S-shape and a symmetric one leading to a decrease of the signal at both negative and positive high magnetic fields. The curves taken at various temperatures all have similar shapes and no clear trend with temperature is visible. We quantify the S-shape by performing three separate linear fits to the three different segments of the curve as described

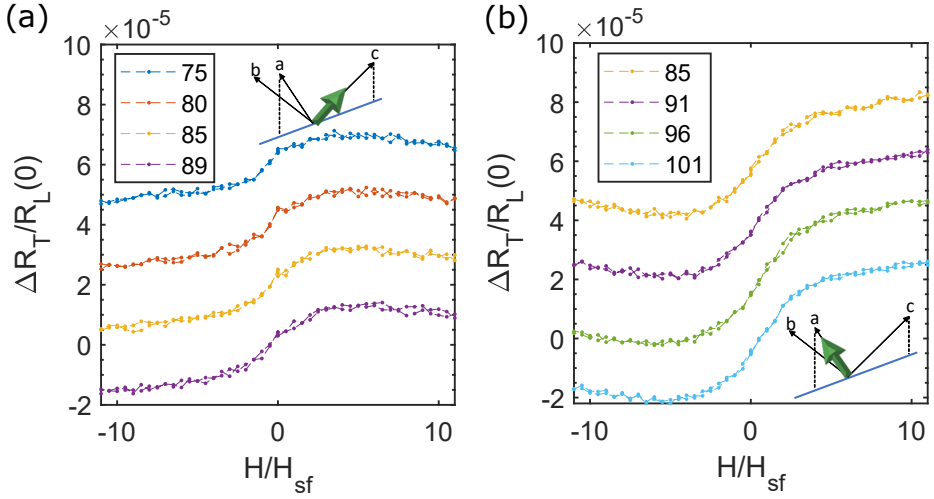


Figure 5.15.: (a) Relative transverse resistivity $R_T$ in uniaxial field sweeps along the $c$-axis at different temperatures below the spin reorientation temperature $T_2$. The inset shows the direction of the magnetic field (green arrow) with respect to the crystallographic axes. (b) Relative transverse resistivity $R_T$ in uniaxial field sweeps along the $a$-axis at different temperatures above the spin reorientation temperature $T_1$.

in the appendix section A.5. The critical fields $H_c$, at which the S-shape saturates, do not coincide with the values of $H_{sf}$ extracted from the longitudinal resistivities measured simultaneously (see Figs. 5.9 and 5.13). Changing the temperature also does not appear to change $R_T(H)$ significantly. Even at temperatures above the SRT, where TFO is in the $\Gamma_4$ phase and $\mathbf{M}$ is along $c$, a field applied along $c$ results the same response. While the $H_{sf}$ goes to zero when approaching the spin reorientation temperature $T_2$, the critical field in the transverse resistivity remains finite. In our simple picture we would expect that the shape of $R_T(H)$ would drastically change to a hysteresis-like curve, when going to the $\Gamma_4$ phase, reflecting the orientation of the net magnetic moment and emulating closely the response seen in SQUID measurements (see Fig. 5.5). However, no clear trend is visible in the transverse resistivity.

Similar behavior is observed for the case that $\mathbf{H}$ is applied along $a$. In this configuration, a dominant S-shape is also observed, as shown in Fig. 5.15 (b). In contrast to before, here, the secondary symmetric part of the curve at large fields has a positive sign, leading to an increase of $R_T$ at both large negative and positive fields. Like for the $\mathbf{H} \parallel c$-case, when $\mathbf{H} \parallel a$, $R_T(H)$ does not change shape when changing the temperature. Similarly, no correlation to $R_L(H)$ can be identified. The critical fields of $R_T$ for both measurement geometries are shown together with the spin-reorientation-fields determined through $R_L$ in Fig. 5.16 (a). We conclude that the S-shape does not originate from the orientation of $\mathbf{M}$. However, a magnetic origin of the signal is expected due to the nonlinear behavior. To further investigate the properties of $R_T(H)$,

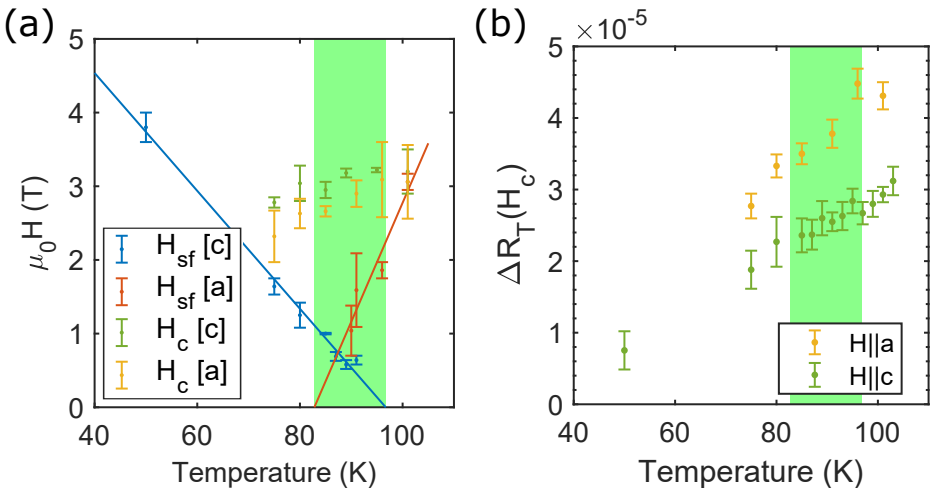


Figure 5.16.: (a) Blue (Red): temperature-dependent spin-reorientation-field determined from the longitudinal resistivity $R_L$ by applying a magnetic field in $c$- ($a$-) direction along with a linear fit. Green (Yellow): critical fields in the transverse resistivity when applying a field in $c$ ($a$) direction. (b) Amplitude of the S-shape as a function of temperature. In both graphs, the region of the SRT is indicated in green.

we define the amplitude of the S-shape as the crossing points of the linear fits to the curve (see appendix section A.5). The trend of the amplitude versus temperature is plotted in Fig. 5.16 (b) where we observe a continuous decrease of the $R_T$ amplitude towards lower temperatures. This is in contrast to the previously reported behavior of the transverse SMR of $DyFeO_3$ [146], where a continuous increase of the transverse signal has been reported, indicating a contribution from the polarized Dy moment to the SMR. The different behavior allows us to exclude the possibility of the polarized Tm moment and suggests that the S-shape in our measurements has a different origin. Corrections to the SMR signal due to an orbital contribution or chiral interfaces are two proposals for the origin for the S-shape[2]. In order to narrow the selection of possible effects, the experiment will be repeated using different Hall bars. A Cu interlayer decouples the TFO from the Pt interface and a variation of Pt thicknesses will give insight into geometric effects related to the probing material. However, these measurements and the development of a full picture to explain this spurious transverse resistivity is the subject of future and ongoing projects.

This chapter has discussed the application of spin Hall magnetoresistance to the material system of bulk TFO (101). Making use of this interface sensitive, electrical measurement technique, the spin reorientation field $H_{sf}$ was determined for a magnetic field applied along both the $c$ and $a$ axis. The application of a magnetic field in proximity to the temperature-driven spin reorientation transition allows us to achieve

[2]Discussion with Olena Gomonay, Frank Freimuth, Yuriy Mokrousov, and Dongwook Go

a complete transition to the magnetic $\Gamma_4$ and $\Gamma_2$ state, respectively. The variation of $H_{sf}$ with temperature is detected via SMR, allowing us to determine the critical temperatures of the temperature-driven spin reorientation transition to a high degree of accuracy. The longitudinal resistivity was shown to be explainable through a simple model of SMR, with a dominant sensitivity to the canted magnetic moment, by taking into account multi-domain states and the different trajectories of the magnetic order. Concurrent measurements of the transverse resistivity raised additional questions of the magnetoresistance in this system. SMR measurements in a rotating magnetic field might indicate a field-dependence of the SMR dependencies as presented in the appendix section A.4. A full understanding of the SMR contributions remains the focus of future studies. The results of this chapter are currently being compiled into a research article [S10].
In addition to the results presented in this chapter, the TFO single crystal has also been tested for potential long-distant magnon transport properties. While it has very recently been demonstrated for the related compound $YFeO_3$ [S8], we do not measure a non-local electrical signal for the TFO (101) crystal. The measurements are presented in the appendix section A.6.
The next chapter will apply the technique of SMR to high quality thin films of TFO, where bulk methods like SQUID and neutron scattering are not always possible.

# 6. $TmFeO_3$ thin films

In the previous chapter, we have seen highly interesting physics in the electrical measurements performed on bulk $TmFeO_3$ (TFO) samples. We are able to detect antiferromagnetic phase transitions from $\Gamma_2$ to $\Gamma_4$ states, and vice versa, utilizing surface-sensitive spin Hall magnetoresistance (SMR). With regard to applications, bulk antiferromagnets are undesirable. Instead, one would make use of thin film antiferromagnetic layers. However, how the scaling to thin film affects the antiferromagnetic structure and anisotropies is not clear. In this chapter, the first demonstration of thin film TFO in the orthorhombic phase will be shown. These high quality films display a spin reorientation transition with similar properties to bulk crystals, detectable from surface sensitive magnetoresistance measurements. The growth of TFO was optimized using $SrTiO_3$ (STO) (001) substrates, a standard material to grow oxide heterostructures. The crystallographic and magnetic properties properties of these samples will be discussed in the first section. Furthermore, the results from SMR measurements are presented. The key results are published in Ref. [S7]. In the second section, we will see that we can optimize the growth of orthorhombic TFO using substrates of similar orthorhombic symmetry to TFO, i.e. $TbScO_3$, $GdScO_3$ and $YAlO_3$. In the third section we will demonstrate the growth of TFO in its hexagonal phase, exhibiting different properties compared to its orthorhombic phase.

## 6.1. Orthorhombic TFO grown on STO substrates

At the time of writing, there is only one previous publication describing the growth mode of STO/TFO as "cube-on-cube growth" [147], implying the adaption of the cubic or tetragonal structure. In this publication, no further investigation is performed on these kind of samples. It is therefore up to now unclear which properties STO/TFO samples possess. Here, we will perform a detailed analysis of similar samples. TFO samples are produced in-house by the author using pulsed laser deposition. Similar to the optimization of YIG and GIG deposition parameters described in chapter 4, the growth was optimized by varying the substrate temperature and oxygen background pressure during deposition. The optimal deposition conditions were found at a substrate temperature of 630°C and an $O_2$ pressure of 0.2 mbar. Using 130 mJ output energy of the excimer laser and a repetition rate of 10 Hz, a growth rate of 1.6 nm/min was observed. The investigation of the crystallographic properties by XRD and magnetic properties have been performed by the author. XMLD and XMCD measurements have been lead by Lorenzo Baldrati during the beamtime under proposal MM23918 at Diamond Light Source. The experiments were performed with the help of Andrew Ross, Shilei Ding and Felix Schreiber with support from the beamline scientists

Francesco Maccerozzi and Dirk Backes. In order to perform electrical measurements on theses samples, Pt Hall structures where defined on the TFO thin films by Andrew Ross. Electrical measurements where then performed by the author and Andrew Ross. The structural and magnetic analysis of these samples as well as part of the electrical measurements shown below are published as a research article [S7].

### 6.1.1. Structural characterization of STO/TFO heterostructures

The growth of TFO on STO is not discussed in literature in detail. In the publication mentioned above [147], only out-of-plane x-ray diffraction (XRD) spectra are investigated. However, these measurements do not reveal the in-plane order of the grown samples. Therefore a complete profile of the structure and orientation of the unit cells of the thin films with respect to the substrate has to be determined. The crystallographic directions of the STO crystal, which has cubic symmetry, and the orthorhombic TFO differ. We therefore introduce the subset orientations $p$ and $o$ for the perovskite and orthorhombic directions, respectively. The unit cells of STO and TFO with their respective coordinate systems are shown in Fig. 6.1. The lattice parameter of cubic STO is $a_{STO} = 3.904\,\text{Å}$, while the lattice parameters of TFO are roughly $a \approx b \approx \sqrt{2}a_{STO}$ and $c \approx 2a_{STO}$.
The crystallographic structure of the fabricated thin films was investigated by XRD. In Fig. 6.2 (a) and (b) $2\Theta/\omega$ scans along the $[001]_p$ and $[112]_p$ STO directions are shown for a 200 nm thick sample, respectively. From these we identify the STO peaks from comparison with literature and attribute the others to the TFO layer. Along the $[001]_p$ direction we find peaks at $2\Theta = 23.44°$ and $2\Theta = 47.93°$. Naturally following from Bragg's law, these peaks stem from the same lattice planes, corresponding to an inter-

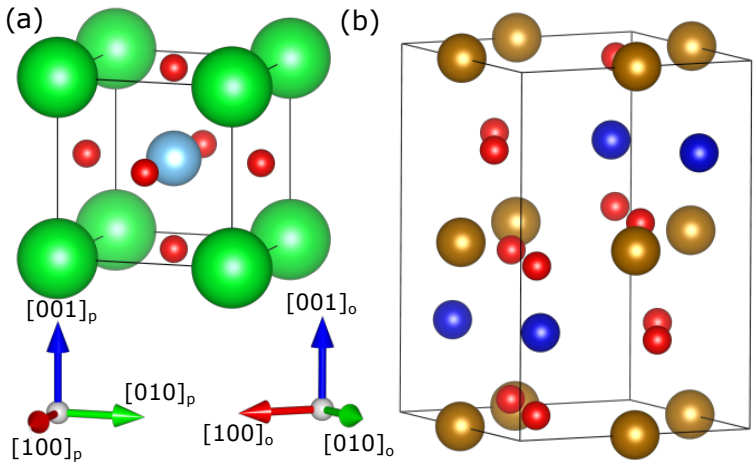


Figure 6.1.: (a) Unit cell of STO with the respective coordinate system in the bottom left (b) TFO unit cell with the respective coordinate system at the bottom right. The size of the unit cells are roughly to scale. Drawn in VESTA [62].

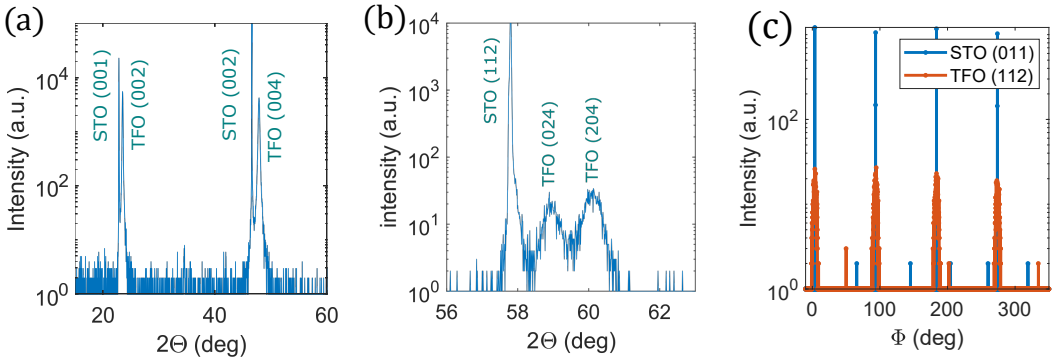


Figure 6.2.: (a) $2\Theta/\omega$ scan of a STO/TFO (200 nm) sample in the [001]-direction (b) $2\Theta/\omega$ scan in the $[112]_p$ direction. Both $(024)_o$ and $(204)_o$ TFO peaks are visible in this geometry indicating crystal twinning. (c) $\Phi$-scans around the [001]-direction with $2\Theta$ and $\omega$ fixed at STO $(011)_p$ and TFO $(112)_o$ positions. [S7]

plane distance of 7.58 Å. We note that that this coincides with the $c$-axis dimensions of the orthorhombic bulk crystal [76]. Other peaks from secondary phases are not visible in this scan. The crystallite size in common [001]-direction is calculated by the Scherrer formula and gives a value of around 70 nm, so less than the film thickness. The rocking curve (not shown) has a broadness of $\Delta\omega = 0.6°$. This is a larger value compared to the sharp rocking curve observed in YIG-GIG thin films, which means that the unit cells are less well-aligned to each other.

By introducing an in-plane component of the incident x-ray momentum, we perform a $2\Theta/\omega$ scan in the $[112]_p$ STO direction. This scan shows two peaks at $2\Theta = 58.92°$ and $2\Theta = 60.07°$, which cannot stem from the same lattice plane, as one can see from Fig. 6.2 (b). It is likely that they stem from the $(024)_o$ and $(204)_o$ TFO peaks due to the growth of twinned domains, meaning that the TFO layer consists of two crystallographic in-plane domains. From these reflexes we calculate the lattice constants $a = 5.28$ Å and $b = 5.57$ Å. The two domains share a common $c$-axis but the $b$-axis of the two domains are orthogonal to each other. This is not surprising since STO has a cubic unit cell leading to a surface with quadratic symmetry. The $ab$-plane of TFO on the other hand is rectangular. Both growth directions, with $b$ along $[110]_o$ and $[\bar{1}10]_o$, are energetically equivalent. In literature, this is labeled as oriented growth. The relative alignment of the STO and TFO unit cells is depicted in Fig. 6.3 (a).

Now, that we have determined the growth direction of the TFO crystallites on the STO substrates, one can determine the exact orientation even more precisely. In principle, it could be possible that the $[110]_o$ of TFO aligns with the $[100]_p$ axis of the STO, leading to a bad alignment of the $[100]_o$ and $[010]_o$ TFO axis with the $[110]_p$ STO axis. The other possibility is that the $[010]_o$ and $[100]_o$ axes align with the STO $[110]_p$ direction at the expense of the $[110]_o$ TFO alignment with the $[100]_p$ STO axis. This can be determined by XRD using $\Phi$ scans (see section 3.3). The $2\Theta$, $\omega$ and

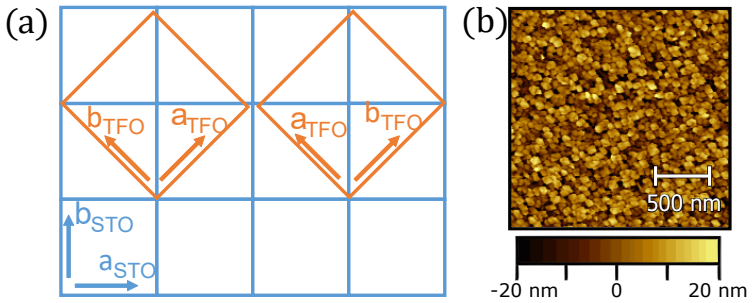


Figure 6.3.: (a) Sketch of the growth orientation of TFO (orange) on STO (blue). Both possibilities are energetically equivalent and are to be found across the sample surface. The dimensions of the drawing is to scale (b) AFM measurement of a TFO sample shows a 2x2$\mu$m area. [S7]

$\Psi$[1] angles are fixed while the sample is rotated around the $[001]_p$ axis. $\Phi$ scans are performed for the $(112)_o$ and $(204)_o$ peaks of the TFO. The position of the peaks are compared with the $(011)_p$ and $(112)_p$ peaks of the STO, respectively, as shown in Fig. 6.2 (c) for the $(112)_o$ and $(011)_p$ reflex. We find that the corresponding $\Phi$ angles are identical. However, we observe that the $(112)_o$ peak ($\Delta\Phi = 5.6°$) is broader than the $(204)_o$ peak ($\Delta\Phi = 4.3°$). This means that the unit cell axes of the TFO are aligned with the STO diagonals, at the expense of the TFO diagonal being less-well aligned with the STO axes.

Knowing the growth direction of TFO on STO, we can calculate the lattice mismatch between the materials. We compare the orthorhombic $a$- and $b$-axes of TFO with the face diagonal of the STO unit cell. We find a mismatch of -4.9% for the $a$- and +0.9% for the $b$-axis. Fig. 6.3 (a) shows a to-scale sketch of the unit cell parameters, from which the alignment of the TFO $b$-axis with the STO diagonal becomes visible.

To investigate the topographic properties, atomic force microscopy has been utilized. In Fig. 6.3 (b) an image of a 2 $\mu$m×2 $\mu$m area is depicted. One can see that we observe island-like growth. The RMS roughness of the surface is calculated to be around 8 nm. The mean lateral size of the islands is 42 nm. We assume that the grain size is the upper limit of possible magnetic domains. In contrast to that, the single crystal investigated in chapter 5 is basically a crystallographic monodomain. The magnetic domains could be observed revealing dimensions in the order of 100 $\mu$m. Electrical measurements on these samples will always represent a multidomain signal.

To sum up the structural properties of TFO thin films grown on STO, we find the orthorhombic structure like in bulk samples, which contradicts previous reports describing a box-on-box growth [147]. The crystallites are well oriented with the $c$-axis aligned along the $(001)_p$ STO axis. However, the samples show in-plane twinning, meaning that the the $b$-axis is aligned along the $[110]_p$ STO directions with a crystallite of around 42 nm. In neighboring crystallites, the $b$-axis might be oriented along

[1] $\Psi$ is the angle determining the in-plane contribution of the scattering vector

the $[\bar{1}10]_p$ STO direction. This can be prohibited by choosing a substrate with the correct symmetry as we will discuss in section 6.2. In the crystallographic measurements on STO/TFO samples, there are no indications of foreign phases of different material, so it is expected that the magnetic properties determined on the following sections solely represent the properties of thin-film TFO.

### 6.1.2. Determination of the magnetic properties

First, we perform magnetic field dependent SQUID measurements. We start with a qualitative analysis to confirm the results from XRD. This allows for the determination of the direction of the canted moment **M**, which in bulk is along the *c*-axis above the SRT ($\Gamma_4$) and along the *a*-axis below the SRT ($\Gamma_2$). The $M(H)$ measurements at 200 K along the *c*-axis reveals a soft magnetic loop as shown in Fig. 6.4, while at 40 K, the curve is more reminiscent of a hard axis loop. This confirms that the *c*-axis of TFO, and importantly the canted moment, is indeed parallel to the $[001]_p$ STO direction. Furthermore, when aligning the sample along the $(100)_p$ in the SQUID, the signal taken at small magnetic fields cannot be fitted by the routine assuming a magnetic dipole, while mounting the sample roughly 45° rotated, along the $\langle 110 \rangle_p$ axis, we can measure a large magnetic moment below the SRT while it vanishes at higher temperatures (not shown). This confirms the 45° in-plane rotated growth of TFO on STO found from previous XRD measurements.
We have seen that above the SRT, the canted moment is oriented in the *c*-direction and below the SRT along the *a*-direction. This itself is an important result since so far, neither the orthorhombic growth of TFO in thin films, nor the magnetic properties of such films have been discussed in literature. The broad hysteresis, measured at 200 K above the SRT, has a coercivity of around 1.8 T. This is much larger than what we have measured at bulk samples in the previous chapter (80 mT). The increase of coercivity

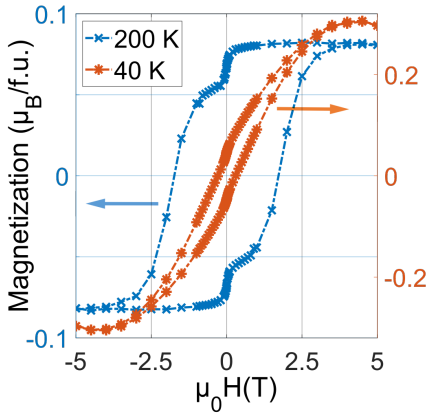


Figure 6.4.: (a) Magnetic field dependent SQUID measurement in the out-of-plane direction above (blue) and below (red) the spin reorientation transition. [S7]

might be due to strain-induced modification of the magnetocrystalline anisotropy and somewhat larger shape anisotropy due to the small magnetic domains originating in the twinned growth. We note, however, that due to the small stray fields, the shape anisotropy has only a limited impact. Additionally to the relatively broad hysteresis, we observe a secondary ferromagnetic contribution, a soft hysteresis visible at low magnetic fields. We will later analyze the soft magnetic contribution in more detail. Here, we can already state that it is not related to the TFO magnetization, but likely a parasitic contribution. Subtracting the soft magnetic contribution, we calculate a saturation magnetization of $M = 0.07\ \mu_B$/f.u. at a temperature of 200 K. For the thin films, the volume of the TFO could be determined much more precisely compared to the bulk single crystal in the previous chapter. We therefore do not compare the absolute values, but we calculate the canting angle and compare it with literature values. Two things contribute to the magnetization: the magnetic moment from the canted Fe spins and the polarized Tm moments, which are parallel to the canted moment above the SRT [71]. Both can be influenced by the strained growth of the TFO. To estimate the canting angle of the Fe moments, we assume that it is constant over a large temperature range far below the Néel temperature $T_N$ [142] and that the Tm moment increases with decreasing temperature $T$ according to $\propto 1/T$ as expected for paramagnetic materials. We measure $M_S$ for additional temperatures above the SRT and fit the data with the function $M_S = M_{Fe} + \frac{M_{Tm}}{T}$. We thereby determine a temperature-independent magnetic contribution of $M_{Fe} = 0.04\ \mu_B$/f.u. due to the Fe spin canting. Sticking to the model described above, that every iron ion has a magnetic moment of $m = 5\ \mu_B$, we can calculate the canting angle of the iron spins. We determine a canting angle by a simple two spin model and find a value of [148] $\frac{\alpha}{2} = \sin^{-1}\left(\frac{M/2}{m}\right) = 0.46°$, which agrees with the literature value of 8 mrad (0.0458°) [74]. We conclude that the symmetric and antisymmetric energies in TFO are not significantly altered compared to a bulk sample.

Below the SRT, we measure the magnetization again in the [001]-direction utilizing $M(H)$ loops. As seen in Fig. 6.4, the hysteresis has significantly changed its shape. While it consists of a similar, very soft magnetic contribution switching around 0 T seen at 200 K, the second contribution resembles more a hard magnetic hysteresis, with a linear increase over a large field range and no remnant magnetization. We note that the amplitude of the magnetization at 40 K is much larger than at 200 K. Our model does not suggest a change of canting angle because of the temperature-independent $H_d$ (DMI field) and $H_e$ (Exchange field). We suggest that the seemingly increasing of magnetization has another origin. The measurement at 40 K is done perpendicular to the canted moment and the Tm moment. An applied magnetic field in the $c$-direction leads to a continuous rotation of both. Modeling the field-induced SRT in chapter 5, we assumed a linear change of the magnetization along the $a$-direction with external magnetic field and from the measurements performed at the bulk TFO crystal, we would expect the spin reorientation field to be around $H_{sf} = 4.5$ T at 40 K. However, due to a change of anisotropies between bulk and our twinned thin films, the spin reorientation fields likely shift and it is possible that the spin flop is not yet

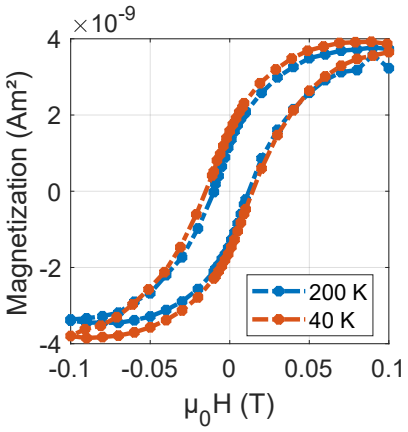


Figure 6.5.: (a) Magnetic field dependent SQUID measurement in the out-of-plane direction above (blue) and below (red) the spin reorientation transition with lower field amplitude. [S7]

completed by 4.5 T. One can see in Fig. 6.4 that the curve does not fully saturate, meaning that the rotation of the spin structure is indeed not yet complete in the investigated field range. Additionally, the procedure of subtracting the linear para- and diamagnetic contributions, which we have performed, is actually not a completely correct assumption, as evident from the missing saturation at a magnetic field of 5 T. However, we still apply this procedure, from which it becomes evident that the shape of the magnetization curve fundamentally changes. The focus of the 40 K curve is therefore not on the absolute values but the qualitative shape.

To further analyze the soft contribution that is observed in the magnetization curves, minor loops at small magnetic field amplitude have been performed in the SQUID at both temperatures. Therefore, the sample has first been magnetized applying -5 T. Then a $M(H)$ measurement has been performed with $H_{max} = \pm 0.1$ T. As seen in Fig. 6.5 we can extract the soft magnetic contributions for both temperatures. It is remarkable that neither the shape, nor the absolute values have changed when going from 200 K through the SRT to 40 K. We extract a coercive field of 11 mT (15 mT) and a overall magnetic moment of around $3.6 \cdot 10^{-9}$ Am$^2$ ($3.8 \cdot 10^{-9}$ Am$^2$) at 200 K (40 K). Note that the magnetization values are not normalized since the thickness of the soft magnetic phase is unknown.

Since for bulk TFO the magnetic properties change completely, we assume that this soft magnetic phase is not related to the orthorhombic crystallites of the TFO. It is possible that at the grain boundaries between the crystallites or close to the substrate interface, where the largest strain is to be expected, a monolayer of a strange phase with different magnetic properties may form. It is suggested for polycrystalline orthoferrite thin films [82, 83], that the soft contribution may stem from a garnet phase, a magnetite ($Fe_3O_4$) phase or the rare earth oxide. In case of TFO the garnet phase would be $Tm_3Fe_5O_{12}$ (TIG), an insulating ferrimagnet [S1, S4, S5]. However, the

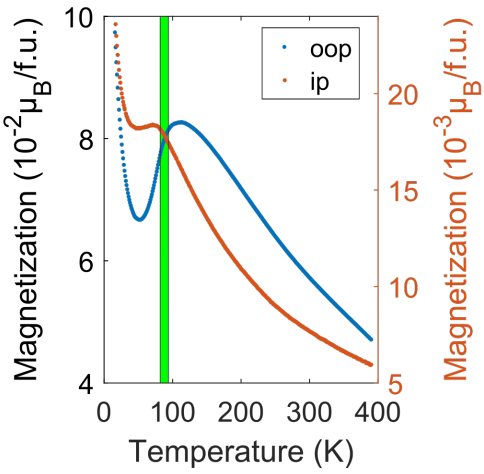


Figure 6.6.: Temperature dependent SQUID measurements for in-plane (red) and out-of-plane direction (blue). The green area depicts the spin reorientation transition in bulk TFO. [S7]

saturation magnetization of TIG is temperature-dependent so that one would expect a $\approx$ 3x larger contribution at 200 K compared to 40 K [102, S9, 149]. Magnetite on the other hand possesses a phase transition (Verwey transition) at around 125 K leading to a rapid change of properties [150]. Below this transition the coercivity of magnetite increases and the saturation magnetization decreases [151]. None of this is evident from the $M(H)$ data. Furthermore, the presence of magnetite should be visible in $M(T)$ measurements, because of the sharpness of the Verwey transition (compare Fig. 6.6). The third suggestion, $Tm_2O_3$, is a paramagnetic substance and should not manifest itself as a temperature-independent hysteresis in $M(H)$ measurements. For $\alpha$-$Fe_2O_3$ (hematite) thin films, a compound related to orthoferrites, a thin interfacial layer of ferrimagnetic $\gamma$-$Fe_2O_3$ (maghemite) is reported for several substrates [152, 153]. The saturation magnetization and coercivity of maghemite is only weakly temperature dependent in the temperature range of 40 K to 200 K. Very pure monocrystals show a saturation magnetization of around 80 emu/g and a coercivity of 2 mT, but this might vary with size and purity [154]. If one assumes that the soft hysteresis stems from maghemite, one can calculate a volume fraction of the maghemite phase of around 0.2% ($\approx$ 0.4 nm thick layer if one assumes the whole substrate area to be covered). Although we cannot be sure that the soft magnetic signal stems from a maghemite phase, we see that such an impurity might be a vanishingly small fraction of the total volume. We will later see, when performing electrical measurements on these kinds of samples, the possible strange phase will not influence the signal and is therefore of minor importance.

Fig. 6.6 shows the temperature evolution of the magnetization in a $M(T)$ measurement. For this measurement, a magnetic field of 5 T has been applied along the $c$-axis

($a/b$-axis)[2] at 390 K (20 K) for a short period of time to align the magnetization of each domain. The magnetic field has then been reduced to 30 mT (50 mT) and the sample was cooled (heated) at the rate of 2 K/min while measuring its magnetization every Kelvin. The different measurement fields have been chosen in order to avoid a compensation of dia-, para- and ferromagnetic contributions so that the finite raw signal can always be fitted by the measurement software. The change of sign of the raw data leads to jumps in the $M(T)$ curve that are unrelated to the magnetic properties of the sample. These jumps are excluded by applying a magnetic field so that the overall magnetic moment is larger than zero at every temperature. At the same time, the field was chosen to be as low as possible to minimize the influence of the magnetic field on the magnetic properties of the sample.

We observe in the out-of-plane (oop) measurement that, going from high to low temperatures, the magnetization first increases. This is due to the paramagnetic Tm moments, which are aligned parallel to the canted moment. The magnetization has a maximum at around 110 K and then decreases until around 50 K before it rises again at very low temperatures. We attribute the maximum at $T_{II} = 110$ K to the start of the SRT, where the canted moment starts to rotate away from the $c$-axis to the $a$-axis, reducing the magnetization in the oop measurement direction. The minimum at 50 K is likely due to a superposition of several effects: the rotation of $M$ away from the $c$-direction and a contribution from paramagnetic impurities in the substrate or within the sample, which contribute with decreasing temperature as $\propto 1/T$. Also, the application of a magnetic field along the $c$-axis exerts a torque on the magnetization and may prevent $\mathbf{M}$ from fully rotating to the $a$-axis. So the minimum at 50 K can not be used to determine the end of the SRT ($T_I$). To do that, we change the measurement geometry and mount the sample in-plane (ip) along the orthorhombic $a/b$-axes. Starting at 20 K, we first observe a decrease of the signal stemming from paramagnetic contributions as described above. The magnetization then plateaus, which likely is a superposition of the decrease of paramagnetic contribution from impurities plus the decrease of the paramagnetic Tm moment that is aligned antiparallel to the net magnetization in TFO. At $T_I = 72$ K, the magnetization abruptly starts to decrease and continues monotonically up to high temperatures. We attribute this temperature to the end of the spin reorientation transition. We note that the temperature $T_I = 72$ K and $T_{II} = 110$ K differ from the bulk values $T_1 = 82$ K and $T_2 = 94$ K (see Fig. 5.4). There are several explanations for the increased width of the SRT. In the work of Staub et al. [155], the SRT has been investigated in bulk samples in the near surface region. It is shown that close to the surface, the SRT is shifted to $T_{1'} = 82$ K and $T_{2'} = 120$ K. In our samples, due to the twinned domains, the thin film geometry and the granular growth, we have an enlarged surface area compared to bulk samples, which might lead to the broadening of the SRT. Additionally, we have seen that due to the substrate-induced strain, we observe a slight modification of the lattice parameters. Changing the geometrical properties of the unit cell likely also

[2] When the field is applied along 45° towards the STO crystallographic axes, this leads to a field parallel to $a$ in some TFO crystallites and along $b$ for twinned TFO domains.

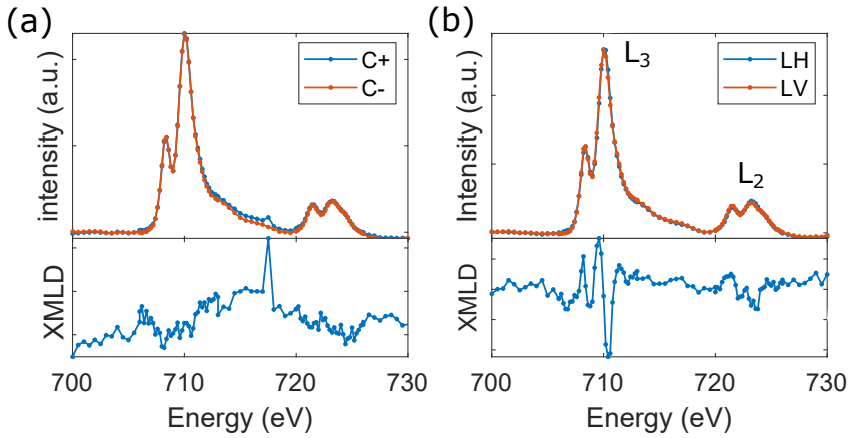


Figure 6.7.: (a) XAS for circular polarized light (top) and XMCD (bottom). (b) XAS for linear polarized light (top) and XMLD (bottom). [S7]

alters the magnetocrystalline anisotropies, which determine the SRT. The deviation of the reorientation temperatures is therefore not surprising.

To analyze the SQUID measurements we have assumed that our samples can be described by the model of a canted antiferromagnet which lead to to reasonable results. In the following we want to support our interpretation by actually showing the antiferromagnetic ordering. Thereby, we can exclude that the magnetic signals we have measured by SQUID so far stem from ferromagnetic impurities in our sample. Furthermore, SQUID is a volume based measurement, meaning that the detected signal contains contributions from everything within the probing space; the film of interest, the substrate, the non-magnetic layers, the mounting equipment etc. Although these additional contributions can (mostly) be accounted for, the resulting response still covers the volume of the film. In order to detect the antiferromagnetic phase transition in later measurements, surface sensitive spin Hall magnetoresistance measurements will be employed. As these measurements detect the *surface* nature of the magnetic ordering, from which we can access information on the bulk antiferromagnet [39, 41], characterizing the magnetic ordering at the surface is also key, especially considering the possible ferromagnetic phase detected in SQUID (Fig. 6.5).

To show antiferromagnetic ordering we use both x-ray magnetic linear dichroism (XMLD) and x-ray magnetic circular dichroism (XMCD). In preparation, a similar sample as analyzed above was capped by 2 nm Pt, deposited by sputtering, to prevent charging during the measurement. The sample was placed in a magnetic field of 5 T in $c$-direction at 300 K to align the canted moment of the individual domains prior to the dichroism measurements. At the Diamond Light Source I06 beamline, the measurements were performed by Lorenzo Baldrati, Andrew Ross, Shilei Ding and Felix Schreiber under the supervision of Francesco Maccerozzi and Dirk Backes. The sample was mounted so that the incoming and outgoing x-ray beam is in the $ac$ ($bc$ for twinned crystallites) plane of TFO, so 45° as compared to the substrate axes.

During the measurement, a temperature of 300 K is maintained, where TFO is in the $\Gamma_4$ state. The incident beam hits the sample at an angle of 16° with the surface. In this geometry, the x-ray absorption spectra (XAS) of linear horizontal (LH), linear vertical (LV), right circularly (C+) and left circularly (C-) light have been recorded. The signal is captured by measuring the electrons emitted by the sample, which have a very low mean free path inside the material. Therefore, only the topmost layer of the TFO is probed. The energy was swept around the Fe $L_2$ and $L_3$ edge from 700 eV to 730 eV. Before calculating XMCD and XMLD, the data has been corrected for fluctuations in the incoming x-ray intensity. The raw XAS spectra have been divided by the initial intensity $I_0$ to account for this. Additionally, the data has been shifted so that the background, besides the absorption peaks, equals zero. Finally, LH and C+ have been rescaled to match LV and C-, respectively. XMCD and XMLD have been calculated as follows:

$$XMCD = I_{C+} - I_{C-} \qquad \text{and} \qquad XMCD = I_{LH} - I_{LV}.$$

Here, the respective processed XAS spectra are labeled as $I_p$ with $p = LH, LV, C+, C-$. The XAS, XMCD and XMLD spectra are shown in Fig. 6.7. The XMLD signal is related to the antiferromagnetic ordering [156] of the Fe spins while the XMCD signal reflects a ferromagnetic moment [156, 157]. It can be seen that there is a clear modulation of the XMLD spectrum around the absorption edges while for XMCD there is no clear signal. This confirms the antiferromagnetic ordering of the iron spins in our TFO thin film sample and the absence of a ferromagnetic phase in the near surface region. We note that also the canted moment is not visible in this measurement.

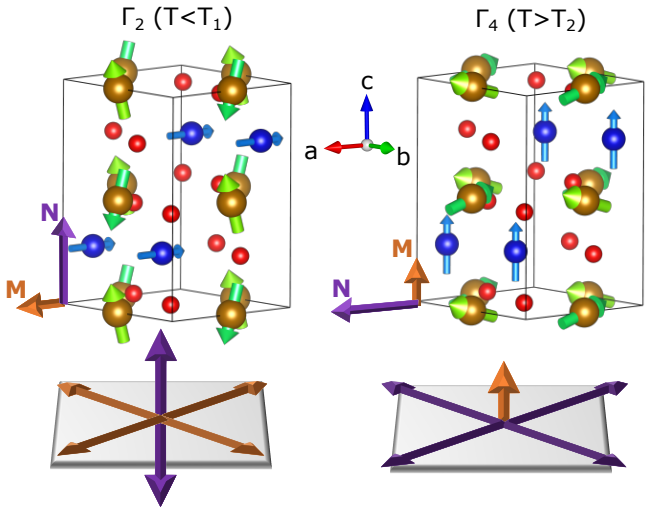


Figure 6.8.: Magnetic configuration above (left) and below (right) the spin reorientation transition for the TFO unit cell (top) and the whole sample (bottom). [S7]

Summarizing the analysis of TFO thin films up to now, we have seen that TFO can be grown in the orthorhombic structure possessing a SRT similar to bulk samples. In the twinned samples, two types of domains are present, separated by a 90° in-plane rotation. Depending on the magnetic phase of the TFO, whether $\Gamma_2$ or $\Gamma_4$, the magnetization vector **M** or the Néel vector **N** align 45° to the substrate in each domain. In the $\Gamma_4$ state, at high temperature, **M** points out of the plane and can easily be aligned by a magnetic field. The two cases are shown in Fig. 6.8 and the consequence for the large scale sample is depicted. This has first been described within research article [S7] and is an important result, showing that the material is suited for small-scale devices. However, up to now we have used bulk methods to determine the magnetic state of our samples. There is no way to integrate SQUID in on-chip devices. For actual spintronic applications, we have to access the antiferromagnetic state by electrical means. Therefore, we have chosen the all-electrical spin Hall magnetoresistance (SMR), which could be realized also for device applications.

### 6.1.3. Electrical detection of the SRT in TFO thin films

In order to perform electrical measurements, 7 nm thick Hall bars were defined on the surface of the TFO thin film as described in section 3.6. The Hall bars have a width of 10 $\mu$m and a length of 100 $\mu$m. The arms of the bar have a width of 3 $\mu$m and are separated by 55 $\mu$m. As discussed in the previous chapter, the SMR depends on the relative orientation of spin accumulation and ordering parameter of the underlying magnetically ordered material, which can either be the Néel vector **N** or net magnetic moment **M**. Since the spin accumulation is fixed by the current direction, we introduce a coordinate system for the Hall bar like in the previous chapter, where $x$ is along the Hall bar, $y$ is the ip direction perpendicular to the Hall bar and $z$ is the oop direction. This is sketched in Fig. 6.9. As described in the previous paragraphs, TFO shows crystallographic twinning leading to nm-sized domains separated by a 90° in-plane rotation. The Hall bar is defined with its $x$-axis (current direction) 45° with respect to the crystallographic in-plane axes.

#### Temperature-dependent measurements

There are two requirements for the Hall bar: it must be sufficiently thick to be electrically conducting and at the same time it must not be too thick that it suppresses any signals related to the magnetic properties of the TFO. In SMR measurements on YIG/Pt bilayers, the optimal thickness was found to be around twice the spin relaxation length in Pt, so around 4 nm [158]. Since we have observed an enhanced roughness of around 8 nm of the TFO thin films (see Fig. 6.3 (b)), we have chosen to design the Hall bars with a thickness of around 7 nm to ensure the satisfaction of the first requirement. This thickness still allows for the detection of a significant SMR signal (reduced from the maximum possible by a factor of 2) [158]. If the Pt is much thicker than the spin relaxation length, the signal is significantly attenuated. To test the properties of the Hall bar, we first perform zero-field cooling experiments

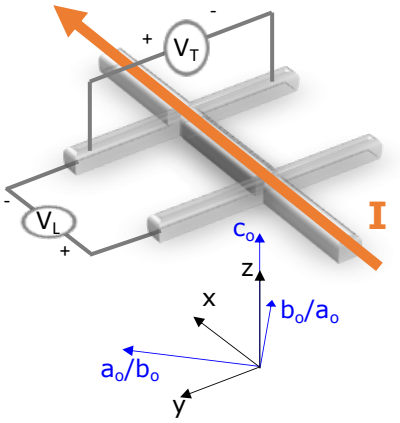


Figure 6.9.: Pt Hall bar (grey) defined on the surface of the STO/TFO sample. **I** indicates the current direction, $V_L$ and $V_T$ the points of measurement for longitudinal and transverse resistivity, respectively. The coordinate system of the Hall bar is depicted in black below with $z$ pointing out of the plane, $x$ along the current direction and $y$ along the arm of the Hall bar. Relative to this, the axes of the TFO unit cell are indicated in blue with $c_o$ in $z$-direction and $b_o$ and $a_o$ in the plane 45° relative to the Hall bar axes.

tracking the resistivity of the Hall bar. This is shown in Fig. 6.10 (a). The behavior of the $R_L(T)$ curve clearly shows metallic behavior of the Hall bar. We can therefore ascertain that the structure is continuous despite the measured roughness, and thus suitable to perform SMR measurements.
Regarding a contribution from SMR to the temperature-dependent longitudinal resistivity, this is in principle possible. A contribution from SMR would alter the purely metallic behavior in the temperature range from 110 K to 72 K, where the SRT takes place, as seen in SQUID (Fig. 6.6). From the relative orientation of crystallographic axes and Hall bar, we expect the following contributions to SMR when changing between the $\Gamma_2$ and $\Gamma_4$ state in absence of a magnetic field:

$$\Delta R_L \propto \Delta R_{1,m}(1 - M_y^2) + \Delta R_{1,n}(1 - N_y^2).$$

For the longitudinal resistivity, the magnetic properties of the underlying material are probed locally [159]. One can therefore sum over all possible domains. Since the twinning should not lead to a different sign in different domains, a finite effect can be expected. However, the change of $R_L$ due to SMR is expected to be small [3]. Indeed, the SRT cannot be observed for these samples by a simple temperature sweep.
The transverse resistivity, on the other hand, is less sensitive to temperature fluctuations. We expect no contribution from SMR to the transverse resistivity, which follows

[3] $\mathcal{O}(\mathrm{m}\Omega)$ in YIG [39] and hematite [41] compared to the change of the intrinsic change of the Pt resistivity with temperature ($\mathcal{O}(\Omega/\mathrm{K})$)

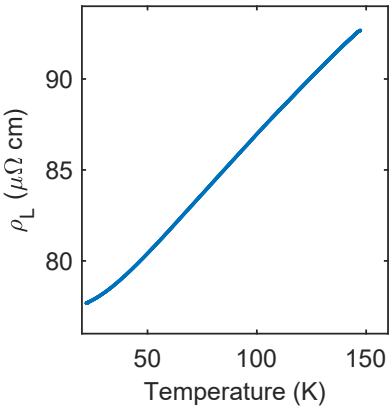


Figure 6.10.: (a) Longitudinal resistivity measured in a zero-field cooling experiment in a temperature range from 150 K to 20 K

$M_{xy}$ and $N_{xy}$ with possible contributions from $M_z$ (see chapter 5), due to the twinned domain structure. Because of the small domain size of around 42 nm, i.e. far smaller than the Hall bar dimensions, we assume an equal distribution of magnetic domains underneath the Hall bar with $\mathbf{M} \parallel \pm z$, $\mathbf{N} \parallel \pm(x \pm y)$ in the $\Gamma_4$ state and similarly an equal distribution of domains with $\mathbf{M} \parallel \pm(x \pm y)$, $\mathbf{N} \parallel \pm z$ in the $\Gamma_2$ state. The different domains lead to different signs of the SMR effect. Averaging over all domains cancels out any net effect in the transverse resistivity. Nevertheless, we record the transverse resistivity $R_T(T)$ simultaneously with $R_L$ as shown in Fig. 6.11. As one can see, the overall shape is similar to $R_L(T)$, likely due to a geometrical asymmetry of the Hall bar, leading to leaking of $R_L$ into $R_T$. In the SRT region between 110 K and 72 K no

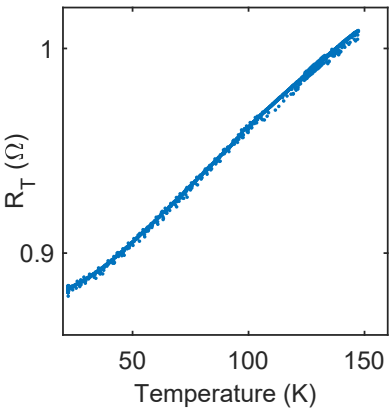


Figure 6.11.: Transverse resistivity measured in a zero-field cooling experiment in a temperature range from 150 K to 20 K simultaneously to longitudinal resistivity shown in Fig. 6.10.

deviation is visible.
The temperature-dependent longitudinal and transverse resistivity do not show any extraordinary effects around the SRT, but validate the quality of the structures. We therefore perform in the next section magnetic field sweeps at constant temperature. The field is applied in three different directions relative to the Hall bar: in $x$-direction, parallel to the current, in $y$-direction ip perpendicular to the current and in $z$-direction. Following this, we will analyze rotation measurements of this sample performed at constant temperature and constant external magnetic field. These measurements allow for better temperature stability and give a better insight into the symmetry of the signal. In these measurements the magnetic field is rotated in the $xy$-plane ($\alpha$-plane) relative to the Hall bar, the $xz$-plane ($\gamma$-plane) and the $yz$-plane ($\beta$-plane) (see section 1.6.1, Fig. 1.2).

### Spin Hall magnetoresistance measurements of thin film TFO/Pt heterostructures in an out-of-plane geometry

We start discussing the data taken in dependence of an out-of-plane (oop) magnetic field as depicted in Fig. 6.12 (a). We simultaneously measure the transverse and longitudinal resistivities. For the transverse resistivity, we assume that our signal consists of contributions from both the SHE and the OHE when there is an oop component of the external magnetic field. To account for the OHE we calculate a linear fit to high magnetic fields and subtract it from the data. The longitudinal resistivity has no such correction. Both resistivities are put relative to the value in the absence of an external field and divided by the zero-field longitudinal resistivity in order to calculate the relative change of the signal.

$$\Delta R_L/R_L = \frac{R_L(H) - R_L(H=0)}{R_L(H=0)} \qquad \Delta R_T/R_L = \frac{R_T(H) - R_T(H=0)}{R_L(H=0)}$$

Because of the proportionality between $R_L$ and $\Delta R_L/R_L$ as well as between $R_T$ and $\Delta R_T/R_L$, we will refer to the two resistivities as simply $R_L$ and $R_T$, respectively, to make this this thesis more readable.

**Transverse resistivity of thin film TFO/Pt heterostructures** Fig. 6.12 (b) shows the transverse resistivity $R_T(H)$ as a function of magnetic field for two key temperatures, above and below the spin reorientation transition. For $R_T$, the largest contribution of the signal comes from the OHE in the Pt Hall bar itself. This originates in the Lorentz force acting on the electrons as charge carriers. As seen in Pt/gadolinium gallium garnet (GGG) samples, the OHE shows a small temperature dependence [160, 161]. To account for the purely linear OHE, a linear function is fitted to the data points at large magnetic field values and subtracted from the data. Thereby we are left only with nonlinear contributions to the signal. The slope of both curves is around $7 \cdot 10^{-6}\,\frac{1}{\mathrm{T}}$ in units of relative transverse resistance change normalized to the zero-field longitudinal resistivity. We note that this includes the subtraction of all linear effects. Possible linear contributions due to SMR are thereby neglected. To reduce the noise

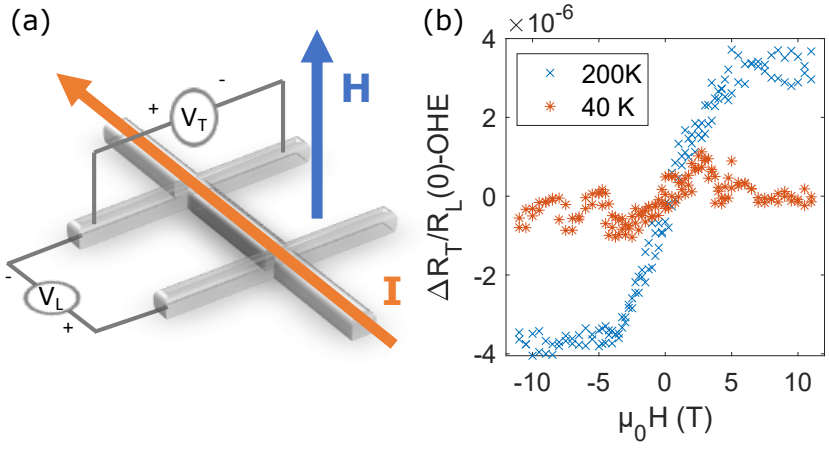


Figure 6.12.: (a) Depiction of measurement geometry for $\mathbf{H} \parallel z$ (b) Transverse resistivity vs magnetic field above (200 K) and below the SRT (40 K). [S7]

level, a moving average of 1 T has been applied. We are left with a hysteresis-like signal above the SRT at 200 K and with a vanishing signal below the SRT at 40 K. The signal at 200 K cannot occur in a free standing Pt layer and must be related to the magnetic properties of the TFO. The disappearance at 40 K shows the sensitivity of the measurement to the magnetic state. Despite the twinned growth of the sample, we can clearly identify the SRT in STO/TFO thin films. The shape of the signals can be explained by the simple model of SMR and a coupling of the spin accumulation to the $z$-component of the magnetization. In the transverse geometry, the signal depends on the magnetization as $\Delta R_T \propto \Delta R_{1,m} M_x M_y + \Delta R_{1,n} N_x N_y + \Delta R_2 M_z$. Due to the occurrence of twinned domains, any effect of $\Delta R_{1,m}$ or $\Delta R_{1,n}$ cancels out since $\mathbf{H} \parallel z$ does not favor a particular in-plane orientation of $\mathbf{M}$ or $\mathbf{N}$. At 200 K, there is only a $M_z$ component of the magnetization. Applying a magnetic field parallel and antiparallel to the surface normal leads to a switching of $M_z$ in the positive and negative $z$-direction, respectively, as seen in SQUID measurements. This leads to the modification of $R_T$ by $\Delta R_2 M_z$. We note that the $R_T$ curve as well as the SQUID curve saturate at the same magnetic field value indicating that both signals have indeed the same origin. Looking at the signal of $R_T$ at 40 K there are only minor fluctuations around the noise level. Thereby, the two magnetic phases of TFO can be distinguished by this measurement.

We note that, compared to the SQUID measurement at 200 K, we do not observe a remnant signal at $H = 0$ T. However, this agrees with the XMCD measurements shown in Fig. 6.7, where no evidence of ferromagnetic ordering in the near-surface region could be detected. The SMR measurements support the suggestion that the Pt top-layer may induce an interfacial DMI-field that counteracts the bulk DMI leading to the reduction of the canting angle of TFO at the very surface.

Since by subtracting a linear fit from the data, all linear contributions are being neglected, possible linear contributions from SMR, e.g. field-induced spin rotation [162,

163], are neglected. When applying the field along **M**, the canting of the Fe sublattices increases approximately linearly [164] (also see equation A.7). This is expected for both temperatures at sufficiently large magnetic fields, after the the magnetization in different magnetic domains switches ($\Gamma_4$) or after the spin reorientation from $\Gamma_2$ to $\Gamma_4$ is complete depending on the temperature. The field-induced SRT leads to a continuous rotation of **M** in the *ac*-plane of the respective unit cells and a monotonic increase of $M_z$ as discussed in the previous chapter. The fact that no clear hard-axis loop is visible at a temperature of 40 K could indicate that either the field applied along **N** is not sufficiently large to achieve a full spin reorientation due to additional anisotropy within the films, or both the rotation of **M** (and increase of $M_z$) and the spin-induced canting contribute to the electrical signal by the similar amounts. Due to the correction method for subtracting the dominating OHE, these contribution are inadvertently removed.

We note that in these measurements, we do not observe an asymmetric S-shape as we saw for bulk TFO samples (see Sec. 5.4.1). Though the origin of the S-shape in bulk samples is not yet known, an interfacial origin is suggested. Here, for TFO thin films, the surface orientation of the TFO unit cells is different. It seems that this, as well as possible contributions from twinning, contributes to the absence of this interface effect.

**Longitudinal resistivity of thin film TFO/Pt heterostructures** Moving to the longitudinal resistivity $R_L$ for a magnetic field applied along $z$, shown in Fig. 6.13 (a), we can also see a clear trend with temperature indicating the possibility of identifying the magnetic states of the TFO. However, we will see that the simple model of solely SMR is not able to completely explain the shape of the curves. We start by discussing the curve measured at 200 K. Here, TFO is in the $\Gamma_4$ phase and in the absence of a

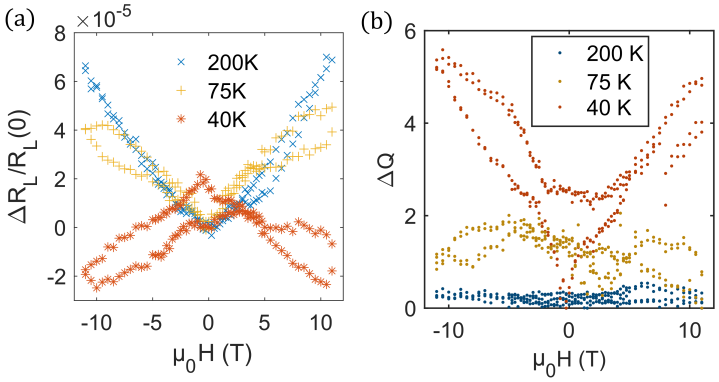


Figure 6.13.: (a) Longitudinal resistivity vs magnetic field for different temperatures measured in out-of-plane geometry. (b) Relative heating power $\Delta Q$ as a function of magnetic field. The heating power is closely linked to the sample temperature.

magnetic field, the magnetization points along the $z$-axis of the Hall bar. No $M_y$ contribution is expected, even after applying a magnetic field in the $z$-direction. Taking into account only a contribution from SMR, the increase of $R_L$ towards large magnetic fields could only be explained by the increasing canting angle leading to a decrease of $|\mathbf{N}|$ and thereby to an average decrease of $N_y$ across all magnetic domains. However, looking at the 75 K curve, we observe a steep positive MR at low fields until a critical field of around $H_c = 5\,\mathrm{T}$, followed by a less steep increase of $R_L$. This is similar to the MR curves measured in bulk samples, where we explain the steep increase by a field induced SRT and a $R_L$ dependence on $\mathbf{M}$ (see Fig. 5.8 and 5.12). At 75 K, when thin-film TFO is within the SRT range, without an external magnetic field $\mathbf{H}$, $\mathbf{M}$ and $\mathbf{N}$ are in the $ac$-plane having a finite $y$-contribution with respect to the Hall bar. An out-of-plane magnetic field leads to the reorientation of $\mathbf{M}$ and $\mathbf{N}$, reducing the $y$-component of $\mathbf{M}$ and simultaneously increasing the $y$-component of $\mathbf{N}$. The steep increase at small magnetic fields would therefore suggest a dependence on $\mathbf{M}$, rather than $\mathbf{N}$ as seen at 200 K, until the reorientation is complete.
The magnetoresistance changes sign when going to lower temperatures. At 40 K, $R_L$ decreases upon application of a magnetic field in $z$-direction. Taking into account a field-induced SRT, the application of a field is accompanied by a decrease of $|M_y|$ and an increase of $|N_y|$ locally in every magnetic domain. The negative MR therefore therefore suggests a dominance of $N_y$ for this measurement.
However, the sensitivity of the longitudinal resistivity to temperature fluctuations further complicates the interpretation of the data. As discussed in the previous section, temperature fluctuations have a large impact on the longitudinal resistivity of the Hall bar. In Fig. 6.13 (b), the heating power of the measurement setup is shown as a function of magnetic field, captured concurrently with the SMR measurements. $\Delta Q$ describes the relative change of the current through the heating wire relative to the heating current at zero external magnetic field. The heating power is closely connected to the actual sample temperature. While the temperature sensor itself can be manipulated by a magnetic field, the heating power is a reliable indicator for temperature fluctuations in the system. Here, we see a strong correlation to the temperature fluctuations and therefore cannot safely attribute the properties of the curve to SMR. A dominance of either $R_{1,m}$ or $R_{1.n}$ cannot be concluded.
Concerning other magnetoresistive effects like Hanle MR and OMR, these are expected to be only weakly temperature-dependent. A change of sign from these effects is not expected. We therefore attribute the signal shape to a combination of SMR and temperature effects.
We summarize the temperature dependence of the SMR measurements for a magnetic field applied along the $z$-direction in Fig. 6.14. There is an increase with decreasing temperature for both $R_T$ and $R_L$ and then a downturn in the region of the SRT. While we may not have a full picture of the longitudinal resistivity due to thermal fluctuations, the net trends strongly indicate that both are responding to the SRT. The transverse resistivity $R_T$ proves to be easy to interpret by the model of SMR of Chen *et al.* [43] and Manchon [16], and the canted moment can be identified as the origin of the SHAHE signal.

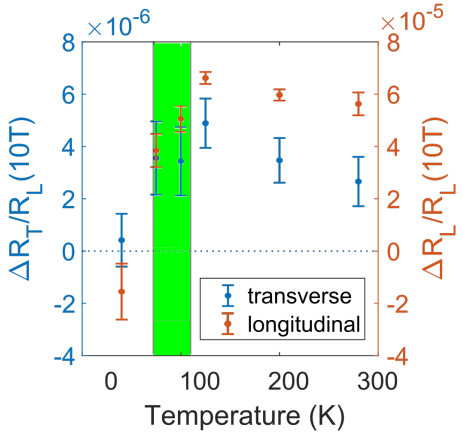


Figure 6.14.: Relative amplitudes of $R_T$ and $R_L$ measured at 10 T in out-of-plane geometry. In green the SRT determined by SQUID is indicated.

This is different from measurements performed at TFO (101) single crystal discussed in chapter 5, where a possible contribution was superimposed by a possible interface effect. The longitudinal resistivity, on the other hand, could be attributed to the behavior of the canted moment, while here, for thin films the signal cannot be explained by the simple toy model.
In the following, we perform additional uniaxial SMR measurement with the field applied along the $x$ and $y$-directions relative to the Hall bar.

**Spin Hall magnetoresistance of thin film TFO/Pt heterostructures under an in-plane magnetic field**

To gain further insight in the behavior of $R_L$ with the applied magnetic field, we perform measurements applying the field within the plane parallel and perpendicular to the Hall bar. While for bulk TFO, these directions were not accessible due to the large magneto-torque from the single crystal, the thin film has a negligible moment, which does not cause damage to the instrumentation.
We note that, when applying the magnetic field within the plane, $R_T$ is always around noise level in these measurement geometries, which is to be expected. Following from the oop measurements in Fig. 6.12 (b), there is no remanant $M_z$ at the interface. A magnetic field in $x$- or $y$-direction does not lead to an increase of $M_z$, so that the contribution from the SHAHE remains zero. This further supports the previous XMCD measurements, where evidence of the canted moment was not seen. Furthermore, the twinned domain structure guarantees that any net contribution from $N_xN_y$ or $M_xM_y$ is zero.
$R_L(H)$ curves measured at different temperatures for $\mathbf{H} \parallel \mathbf{I}$ (see sketch Fig. 6.15 (a)) are shown in Fig. 6.15 (b). We again see a strong temperature dependence of the signal as for the out-of-plane measurements shown above. Additionally, especially at lower temperatures, $R_L$ is plagued by temperature fluctuations. The change in heating

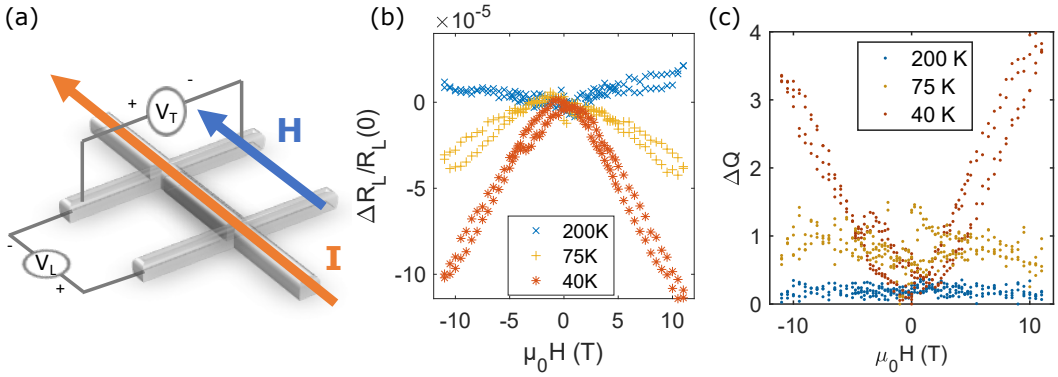


Figure 6.15.: (a) Measurement geometry for $\mathbf{H} \parallel \mathbf{I}$. (b) $R_L$ measured in this geometry for different temperatures. (c) Change of heating power as an indicator for temperature fluctuations during the measurements.

power $\Delta Q$, as a measure for the temperature stability, is shown in Fig. 6.15 (c). We observe a strong correlation with $R_L$ at 40 K, while at higher temperatures $\Delta Q$ is more stable. Ignoring the 40 K data, at 75 K we observe a negative MR of $(-3.4 \pm 0.6) \cdot 10^{-5}$ at 10 T, while at 200 K a small positive MR $((1.0 \pm 0.5) \cdot 10^{-5})$ is observed. In the picture of SMR, the decrease of resistivity is explained by an increase of the order parameter in the $y$-direction. Here, the field is applied perpendicular to both easy and intermediate magnetic axes. An increase of the magnetic moment along $y$ is therefore not expected, which rules out a simple dependence on $\mathbf{M}$. However, a dependence on $\mathbf{N}$ could not explain the change of sign going to higher temperatures. We find that again, while a simple model of SMR can explain some features of the recorded data set, it cannot explain the full range of behavior seen for $R_L(H)$, indicating a possible complex magnetic field and temperature dependence of the relative spin mixing conductances of the different order parameters as well as highlighting the need for a more detailed model for the case of antiferromagnetic orthoferrites.

Finally, $R_L(H)$ is probed for $\mathbf{H} \parallel y$, perpendicular to the charge current and shown in Fig. 6.16. Surprisingly, the shape of the individual curves closely resembles those measured of the parallel field orientation shown in Fig. 6.15. We observe again a strong temperature dependence and a change of sign when changing the temperature. The data measured at 40 K shows again a dominant negative MR of similar size compared to the previous measurement. We omit further discussion because of the strong correlation with temperature fluctuations indicated by the heating power shown in Fig. 6.16 (c). The measurements performed at 200 K show a positive MR, which appears to be larger than for $\mathbf{H} \parallel x$. We measure an amplitude of $(4.4 \pm 0.4) \cdot 10^{-5})$ at 10 T. The curve captured at 75 K changes slope when increasing the field at around 5 T. At low magnetic fields, one observes a positive MR while at larger magnetic field, the resistance decreases with increasing magnetic field amplitude. This might again indicate the reorientation of $\mathbf{M}$ and $\mathbf{N}$ as seen for TFO bulk samples (see Fig. 5.8 and 5.12) and as suggested for oop measurements of TFO thin films [see Fig. 6.13 (a)]. Like

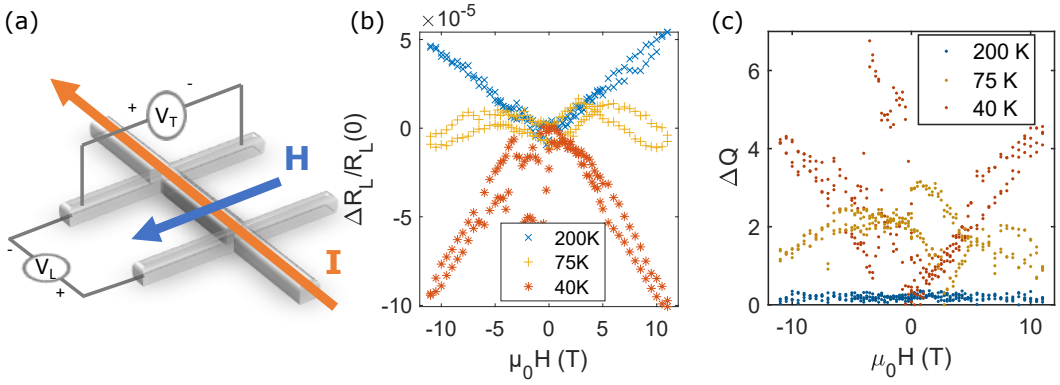


Figure 6.16.: (a) Measurement geometry for $\mathbf{H} \perp \mathbf{I}$. (b) $R_L$ measured in this geometry for different temperatures. (c) Change of heating power as in indicator for temperature fluctuations during the measurements.

for previous measurements, the simple SMR model is insufficient to explain the entire dataset simultaneously. While the data taken at 200 K would suggest a dependence on $\mathbf{N}$ in a simple SMR model, the 75 K data would suggest a mixed dependence on $\mathbf{M}$ and $\mathbf{N}$ depending on the magnitude of the external magnetic field.

In Fig. 6.17 we summarize the dependence of $R_L(H)$ in both in-plane geometries by plotting the relative amplitude at 10 T against the measurement temperature. Although the theoretical background is not sufficient to explain the data in detail, we see a clear trend correlating with the SRT of the TFO thin film. Within the temperature region of the SRT we observe that the sign of the MR changes for both field directions. The sign of the MR lets one distinguish between the $\Gamma_2$ and $\Gamma_4$ state in

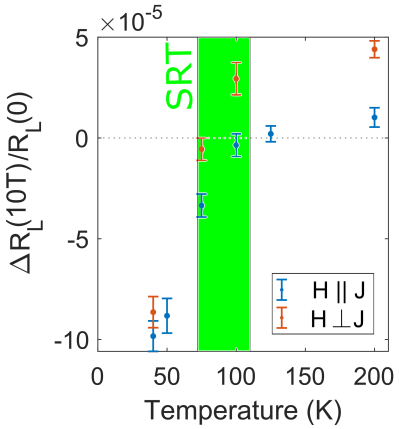


Figure 6.17.: Summary of the evolution of MR amplitude vs temperature for both in-plane measurement geometries $\mathbf{H} \parallel \mathbf{I}$ and $\mathbf{H} \perp \mathbf{I}$. In green the SRT region measured by SQUID is highlighted.

thin films of TFO. The simple model of SMR that was previously developed relies on interfacial exchange torques between the spin accumulation in the Pt and the magnetic ordering parameters **M** and **N**. Given that the two ordering parameters contribute to the SMR with opposing signs, the net response normally dictates which order parameter is dominant. Rotation measurements performed at TFO single crystals shown in the appendix chapter (see Fig. A.12) indicate that the SMR follows the net moment as well as the Néel vector. The pre-factors to the SMR, $R_{1,m}$ and $R_{1,n}$ appear magnetic field-dependent. In order to accurately describe SMR for canted antiferromagnets, especially in materials with a large intrinsic DMI, extensions to this model are necessary in order to consider, for example, all magnetic sublattices playing a role, which in the case of TFO is 4. Although $R_T$ for $H_z$ was dominated by $M_z$, the longitudinal signal in all three ordinal directions doesn't follow a single order parameter, and it would appear that the contributions of each varies with temperature. The extension of the model of Chen et al. [43] to cover some of these additional problems is a necessary advancement that, at the time of writing, has not occurred.
In order to learn more about the symmetry of the signal and to reduce the influence of the temperature to the resistivity, we performed rotation measurements at fixed temperature and field. We choose to perform the rotations in three planes ($xy$, $xz$ and $yz$) relative to the Hall bar at 40 K and 200 K and will discuss them in the following section.

**Rotational dependence of the spin Hall magnetoresistance in thin film TFO/Pt heterostructures**

Starting with a magnetic field rotated in the $xy$-plane through an angle $\alpha$ ($\alpha = 0°$ occurs for $\mathbf{H} \parallel x$), examples for $R_T(\alpha)$ and $R_L(\alpha)$ are shown in Fig. 6.18 together with the respective fit curve. The function

$$A \cdot \cos(\alpha + B)^2 + C, \tag{6.1}$$

has been fitted to the $R_L$ data and the function

$$A \cdot \cos(\alpha + B) \sin(\alpha + B) + C, \tag{6.2}$$

to the $R_T$ data. These dependencies are expected with $B = 0°$ for SMR and HMR when to the magnetic moment determines the signal as described in the theory section 1.6.2 and 1.6.3. For $R_T$, $B = 0°$ is fulfilled for all these measurements confirming that the $R_T$ is sensitive to the magnetization of the TFO (SMR) and/or the magnetic field (Hanle effect). The amplitude $A$ increases monotonically with field as shown in Fig. 6.19 (a) for both temperatures. A differentiation between SMR and HMR is not possible since **M** does not saturate but increases with increasing field due to an increasing canting angle.
$R_L$ on the other hand shows a phase shift of around $B = -10°$ to $B = -25°$ depending on the field and temperature. The positive MR can be explained by SMR being sensitive to **M**, the Hanle effect and also by AMR. From theory, a phase shift of $R_L$ of

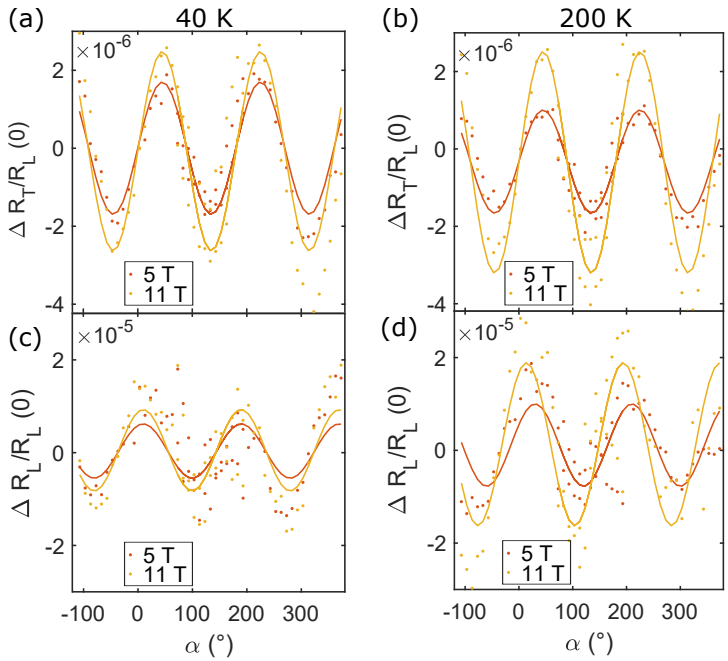


Figure 6.18.: Resistivity depending on the in-plane angle $\alpha$ of the magnetic field with the $x$-axis (current) (a) Transverse resistivity $R_L$ at 40 K (b) Transverse resistivity $R_L$ at 200 K (c) Longitudinal resistivity $R_T$ at 40 K (d) Longitudinal resistivity $R_L$ at 200 K. For easier visibility, error bars have been omitted. The solid lines represents numerical fit.

$B = 0°$ is expected for Hanle and AMR. In SMR, a phase shift is in principle possible if there is a finite angle between **M** and **H**. However, $R_L$ is plagued by a higher noise level than $R_T$ as evident from Fig. 6.18 (c) and (d). This leads to a poor quality of the fit, with an $R^2$ of only 0.6. A deeper analysis of this phenomenon from this data set is therefore not possible. Therefore, we perform additional rotations in the $xz$- and $yz$-plane.

When rotating a magnetic field in the $xz$-plane, we observe a dominant cosine dependence of $R_T$ against the rotation angle $\gamma$ as shown in Fig. 6.20 (a), where the $R_T(\gamma)$ is plotted for two different fields. This can be explained by a dominating ordinary Hall contribution, which has a $\propto \cos(\gamma)$ dependence. The function $A \cdot \cos(\gamma + B)$ has been fitted to every curve with a fit quality of $R^2 > 0.96$ for all curves. The parameter $A$ increases linearly with applied magnetic field as shown in Fig. 6.20 and $B = 0° \pm 2°$ confirming the origin from OHE.

The OHE is related to the electrons moving in the magnetic field and not related to the magnetic properties of the TFO layer. The SHAHE which we have observed in the uniaxial measurements is expected to have the same symmetry in this measurement configuration. However, it is expected to be constant for magnetic fields larger than 4 T (see SQUID measurements in Fig. 6.4). Fitting a linear function to the data points

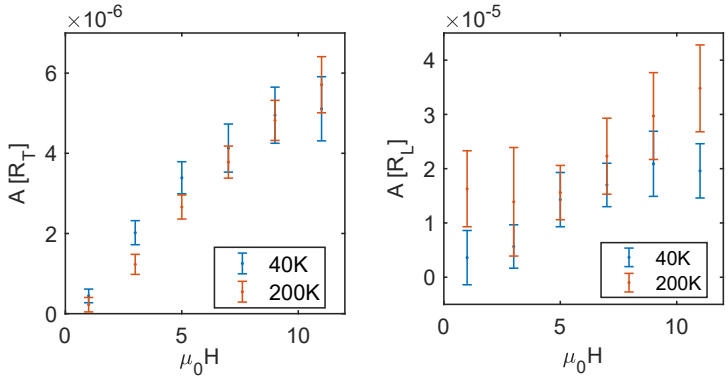


Figure 6.19.: Amplitude of the SMR determined by fitting the function 6.2 to the rotation data of $R_T(\alpha)$ (a) and the function 6.1 to the rotation data of $R_L(\alpha)$ (b). The rotations are performed in the $xy$-plane.

with $\mu_0 H \geq 5\,T$ gives for the 40 K data a negligible offset of $(0.57 \pm 2.93) \cdot 10^{-6}$ and for the 200 K data a finite offset of $(4.03 \pm 2.07) \cdot 10^{-6}$ likely stemming from the oop contribution of the canted moment at 200 K at large magnetic fields as seen in the uniaxial measurements (Fig. 6.12 (b)). The fit curves are shown in the appendix Fig. A.15. We note that a contribution from $M_x M_y$ and $N_x N_y$ is not expected since due to the twinned domain structure, the experiment is symmetric, leading to a cancellation of any net effect. A third contribution to the signal is the Hanle magnetoresistance, which also has the same symmetry as SMR. Performing rotations in the $xz$-plane, the Hanle effect contributes to $R_T \propto H_z$ [50] and therefore cannot be distinguished from the OHE in this measurement geometry.
Regarding the longitudinal resistivity $R_L(\gamma)$ measured for a rotating field in the $xz$-plane, example curves for 40 K and 200 K are shown in Fig. 6.21 (a) and (b), respec-

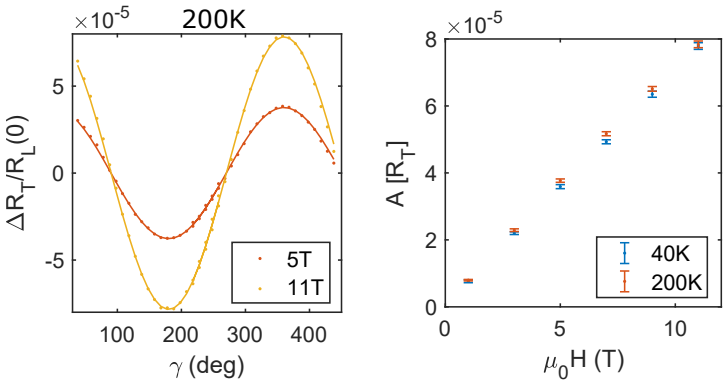


Figure 6.20.: (a) Example curves for $R_T(\gamma)$ plotted together with the fitted function $A \cdot \cos(\gamma + B)$. (b) Evolution of the fit parameter $A$ (amplitude) with magnitude of applied field.

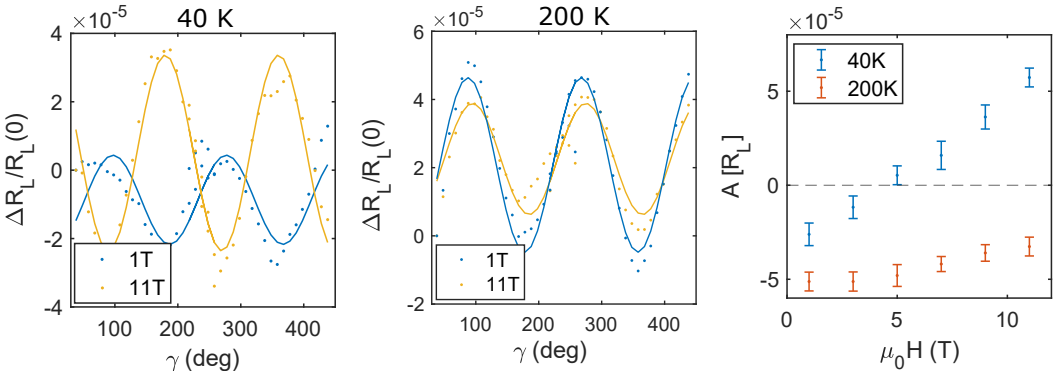


Figure 6.21.: (a) Example curves for $R_L(\gamma)$ measured at 40 K, plotted together with the fitted function 6.1. (b) Example curves for $R_L(\gamma)$ measured at 200 K, plotted together with the fitted function 6.1. (c) Evolution of the fit parameter $A$ with the of applied field.

tively. It is evident that $R_L$ behaves very differently in the respective temperature regimes. While at 40 K, where the TFO is in the $\Gamma_2$ state, we observe a $-\cos^2(\gamma)$ dependence at small magnetic field magnitudes, the sign changes when going to large magnetic fields. In the $\Gamma_4$ state at 200 K we observe only a negative MR and a weak dependence on the magnitude of the magnetic field. The amplitudes are summarized in Fig. 6.21 (c).

To understand the behavior of $R_L(\gamma)$, we need to take into account several effects. One is OMR, which will contribute by $+\cos^2(\gamma)$ as seen in Pt/MgO and Pt/NiO samples with Pt Hall bars of the same thickness [15]. The OMR increases with the magnitude of the applied magnetic field and is only small for small $\mathbf{H}$. This effect, however, is only weakly temperature dependent and cannot explain the significantly different behavior of $R_L$ in the two magnetic states of TFO and the change of sign in the MR. Regarding contributions from the HMR, this effect contributes when $\mathbf{H} \nparallel \boldsymbol{\mu}$. However, when rotating $\mathbf{H}$ in the $xz$-plane $\mathbf{H} \perp \boldsymbol{\mu}$ for all angles and so contributes a constant offset, which is also temperature-independent. In order to estimate the contribution from SMR, we have to estimate the trajectory of $\mathbf{M}$ and $\mathbf{N}$. Since the spins tend to rotate in the $ac$-plane, a rotating field in the $\gamma$-plane may lead to the alignment of $\mathbf{M}$ with the $c$-axis at $\gamma = 0°$ and to an alignment with the $a$-axis, when $\gamma = 90°$. Since the $a$-axis is aligned $\pm 45°$ with the Hall bar (depending on the magnetic domain), this leads to a finite $|M_y|$ when $\mathbf{H}$ has a component within the sample plane. The SMR should thereby lead to a resistivity variation of $+\cos(\gamma)^2$. $\mathbf{N}$, on the other hand, follows $\mathbf{M}$ in the $ac$-plane with a 90° phase shift and would lead to a variation following $-\cos(\gamma)^2$, similar to what we observe in the measurements at 200 K. However, it is surprising that the amplitude at 200 K does not change with increasing field. One would expect an increasing amplitude with increasing field since only a field $H > H_{sf}$ can completely tilt $\mathbf{N}$ away from the preferred axis as seen in measurements at bulk TFO in chapter 5. For fields $H < H_{sf}$, an incomplete reorientation of $\mathbf{N}$ and $\mathbf{M}$ is

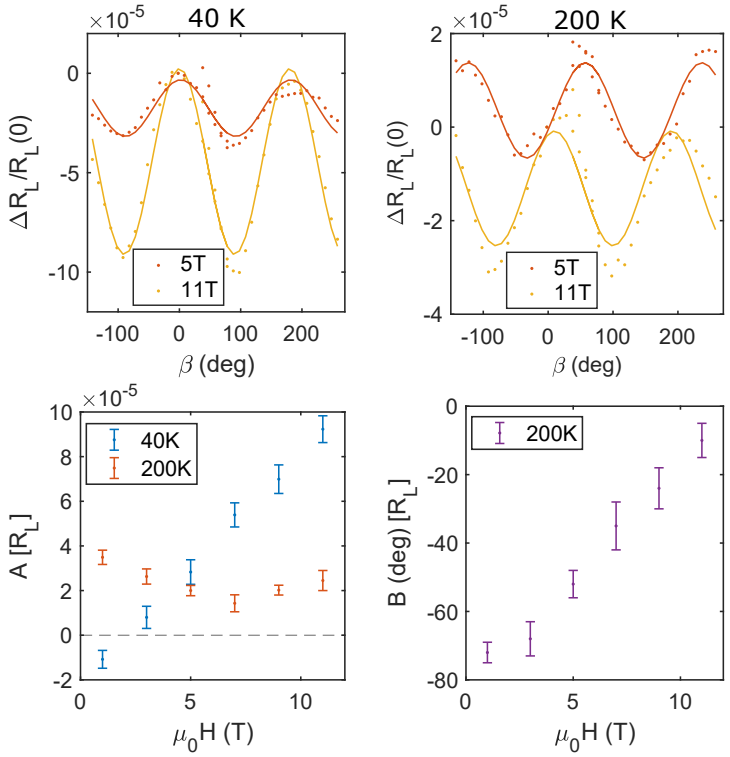


Figure 6.22.: (a) $R_L(\beta)$ for two example fields of 5 T and 11 T measured at 40 K. Solid line is a fit curve. (b) $R_L(\beta)$ for two fields at 200 K together with the respective fit curve. (c) Amplitude extracted from the fit curve plotted against the external magnetic field. (d) Phase shift observed at 200 K only, extracted from the fit curve.

expected. The sign change of $R_L$ going from small to large magnetic fields in the $\Gamma_2$ phase could suggest a temperature- and field-dependence of the pre-factors $\Delta R_{1,m}$ and $\Delta R_{1,n}$ of the SMR. Additionally, at low temperatures, the weak anti-localization effect could contribute to the signal [50]. This is an effect occurring in metallic thin films with SOC at low temperatures [165], leading to an increasing contribution by $\cos^2(\beta/\gamma)$ in $\beta$- and $\gamma$-rotations towards lower temperatures below $\approx 50$ K [50].

We repeat the measurements at different fields and temperatures for a magnetic field rotated in the $yz$-plane and determine $R_T(\beta)$ and $R_L(\beta)$. Just as for the scans in the $xz$-plane, we observe again a dominant OHE in $R_T(\beta)$. Given the strong resemblance to $R_T(\gamma)$, example plots are not shown. We perform again a fit of the amplitude vs field data in order to find the contribution from SHAHE. The fits are shown in the appendix Fig. A.16. $H \geq 5$ T gives us again a negligible offset of $(0.1 \pm 1.7) \cdot 10^{-6}$ for the 40 K data and a finite offset of $(3.5 \pm 0.7) \cdot 10^{-6}$ for the 200 K data showing the effect of the canted moment $M_z$ on the resistivity. Again, no $M_xM_y$ or $N_xN_y$ contribution is expected since the effect of twinned domains cancels the individual

domain contributions.
$R_L(\beta)$ is shown in Fig. 6.22 for both considered temperatures. We observe again a strong difference in the behavior of $R_L(\beta)$ between the two temperatures and therefore between the associated magnetic states of TFO. The evolution of amplitude with applied magnetic field is shown in Fig. 6.22 (c). At 40 K, the behavior of $R_L(\beta)$ is similar to $R_L(\gamma)$. We observe a change of sign of the MR at small **H** and a linear increase of the amplitude with increasing magnetic field. The change of sign occurs at a lower magnetic field for this rotation plane, which indicates that the canted moment dominates the signal already at small fields, likely due to the different relative projections of **M** and **N** along $y$. According to the model of SMR and the trajectory of **M** and **N** in the $ac$-plane of each TFO crystallite, we would expect the largest $M_y$ contribution when $\beta = 90°$, associated with a minimum of $R_L$ while the maximum would be observed at $\beta = 0°$. This is seen in our data at 40 K for large magnetic fields. However, at 1 T, the sign is reversed. As for the $\gamma$-rotation, this could be associated with field-dependent pre-factors $\Delta R_{1,m}$ and $\Delta R_{1,n}$ of the SMR. OMR and HMR both are expected to contribute to the signal as $+\cos(\beta)$, adding to a contribution from M-dependent SMR.
At 200 K, we observe a different behavior of $R_L(\beta)$ than observed for other rotation planes. While the amplitude of the signal changes only slightly with magnetic field as shown in Fig. 6.22 (c), we observe a continuous phase shift with increasing magnetic field, which is plotted in Fig. 6.22 (d). As discussed for 40 K, here, OMR and HMR likely contribute to the signal, but with a constant phase shift of $B = 0°$. Also, these effects should not cause a difference between the two measurements taken at different temperatures, and therefore cannot be the origin of this effect. Concerning SMR, in the $yz$ measurements, the effect is expected to contribute as $\cos(\beta)$ for M-SMR and as $-\cos(\beta)$ for N-SMR, taking into account the rotation of the spins in the $ac$-plane for the different crystallites. This simple model is insufficient to describe the course of $R_L(\beta)$ for different magnetic fields since a superposition of the two functions cannot be fitted to the data. The continuous phase shift of $R_L(\beta)$ at 200 K might suggest that the complex interaction of external magnetic field, large uniaxial anisotropy and DMI leads to a more complicated trajectory of **M** and **N** as given by the simple model used here.
Summarizing the electrical measurements on TFO/Pt samples, we have measured the longitudinal $R_L$ and transverse $R_T$ resistivities at fixed temperature below the SRT, where TFO exhibits magnetic ordering in the $\Gamma_4$, as well as above the SRT, where TFO is in the $\Gamma_4$ magnetic state. The behavior of $R_L$ and $R_T$ has been measured in uniaxial magnetic field measurements along three distinct directions relative to the Hall bar as well as in rotation measurements at fixed magnetic fields. We can clearly identify a difference between the measurements taken at the different temperatures caused by the change of magnetic state driven by the SRT. In all measurements, $R_T$ shows a dependence on magnetic field via the ordinary Hall effect and on the $z$-contribution of the magnetization via the spin Hall anomalous Hall effect. This appears to be different from the measurements which have been performed at bulk TFO samples in the previous chapter, where the the transverse signal was dominated by an effect

unrelated to the magnetic properties of the TFO. Whether the different orientations of bulk and thin film sample are the origin of these differences is still under debate.
In the following section we will see how to grow TFO thin films in different orientations. SMR measurements on those will help understanding the difference between bulk samples and thin films in future experiments. Regarding the longitudinal resistivity $R_L$ on the other hand, it has been shown to be difficult to interpret for thin film TFO because of additional MR effects, which have to be taken into account. We can, however, identify the signal being of magnetic origin. Comparing these results with measurements performed at bulk TFO we see similarities especially in the rotation measurement, where the dependency of the SMR appears to change between Néel vector dependence and magnetic moment dependence, depending on the applied magnetic field. We suggest that the simple model of SMR is not sufficient to describe the behavior of our samples. Large uniaxial anisotropy and large DMI may lead to a complex trajectory of both **M** and **N** in a magnetic field and the influence of both order parameters has to be taken into account rather than limiting the model to either **M** or **N** as done so far for other materials like YIG/Pt [39], NiO/Pt [15] or $\alpha$-$Fe_2O_3$/Pt [163].

## 6.2. Single crystalline TFO thin films

In chapter 5, we have seen that TFO single crystals are difficult to measure in our apparatus due to their large magnetic moment. Furthermore, with regard to applications, thin films are needed. In section 6.1, we have seen that TFO can be grown on cubic STO substrates to achieve the technologically relevant orthorhombic structure. However, these thin films exhibit twinned domains leading to a level of in-plane disorder, which complicates the interpretation of magnetoresistive data. We therefore aim for the growth of TFO in a high quality single crystalline fashion. For substrates with similar symmetry to TFO, monocrystalline heteroepitaxial growth might be achieved. This could further lead to a smoother surface because of the reduction of grain boundaries. For analyzing the properties of the thin film TFO, the substrate has to fulfill some additional requirements: it should not be ferromagnetically ordered in order not to influence the magnetic properties of the TFO and it should be non-conductive to make electrical measurements easier to interpret. In order to investigate the possibility for heteroepitaxially grown TFO thin films, TFO has been deposited on a series of orthorhombic substrates, which are summarized in table 6.1.
The substrates $TbScO_3$ (TSO), $GdScO_3$ (GSO), and $YAlO_3$ (YAO) are all insulating with a large band gap of 6.1 [168], 5.6 [169], and 5.3 eV [167], respectively. The substrates were only available in selected orientations, given in table 6.1.
To deposit TFO on these substrates, the same growth conditions have been chosen as for the deposition on STO substrates. No surface treatment of the substrates has been performed prior the deposition. The thickness of all samples is fixed at around 80 nm. Each sample has been analyzed in detail by XRD. The growth of the samples as well as the crystallographic and magnetic characterization was done by Sven Becker.

| Material | $a$ (Å) | $b$ (Å) | $c$ (Å) | Ref. | Orientation |
|---|---|---|---|---|---|
| $TmFeO_3$ | 5.251 | 5.576 | 7.584 | [76] | |
| $TbScO_3$ | 5.466 | 5.731 | 7.917 | [166] | (110) |
| $GdScO_3$ | 5.480 | 5.746 | 7.932 | [166] | (011) |
| $YAlO_3$ | 5.180 | 5.330 | 7.375 | [167] | (110) |

Table 6.1.: Lattice parameters of possible substrate materials compared with TFO. Last column shows the utilized substrate orientation.

**$TbScO_3$**

First, we analyze TFO samples grown on $TbScO_3$ (TSO) substrates. XRD measurements performed on TSO/TFO thin films have been performed to confirm the growth orientation and to determine the lattice constants. $2\Theta/\omega$ measurements for TSO/TFO samples are shown in Fig. 6.23. For these scans, the substrate and film peaks can be easily identified. The crystallographic axes of both TFO thin film and TSO substrate prove to be parallel to each other. The measurements performed in the $\langle 110 \rangle$-direction (out-of-plane) as well as those in the $\langle 010 \rangle$ and $\langle 111 \rangle$-directions (see Fig. 6.23 (a), (c) and (d)) do not show any secondary peaks. However, the scan in the $\langle 100 \rangle$-direction (see Fig. 6.23 (b)) reveals a secondary reflex at $2\Theta = 31.2°$. The position of the secondary reflex corresponds to a lattice constant of 5.72 Å, which is close to the TSO $b$-axis, but no corresponding length can be identified in the relaxed TFO unit cell, which indicates a secondary phase within the TSO substrate. However, a secondary strained TFO is also a possibility. Additionally, the rocking curves of substrate reflexes are in general very narrow ($\leq 0.2°$). The rocking curve of this reflex has a FWHM of $\Delta\omega = 1°$, similar to that of the TFO (200) reflex. It is therefore not clear if this peak stems from a small impurity phase in the substrate or if there is a strange phase in the TFO film. One could identify the origin of the reflex by analyzing TSO/TFO samples of varying TFO thickness, which is out of scope of this work.
Focusing on the reflexes which we identify as TFO peaks, the crystallite size is estimated by the Scherrer formula, which gives a value of 32 nm. Taking into account the whole film thickness of around 80 nm, the TFO layer did not grow as a single crystal on TSO substrates. Improvement of the TFO layer might be possibly achieved by further tuning the deposition conditions. The lattice parameters of the strained TFO film are determined from the positions of the reflexes. While the parameters of $a$- and $b$-axis can directly be extracted using the Bragg formula, the parameter of the $c$-axis is calculated via [109] $\frac{1}{d^2} = \frac{h^2}{k^2} + \frac{k^2}{b^2} + \frac{l^2}{c^2}$, where $(hkl)$ are the Miller indices and $d$ the lattice plane distance determined by the Bragg formula. To summarize, we find the following lattice parameter for TFO/TSO thin films:

$$a = 5.27\,\text{Å} \qquad b = 5.60\,\text{Å} \qquad c = 7.42\,\text{Å}.$$

We observe a modification of the unit cell due to the strained growth. Compared to the bulk lattice parameter, the $a$-axis is expanded, while both $b$- and $c$-axes are contracted. One attempt has been made to measure the magnetic properties of the TSO/TFO thin

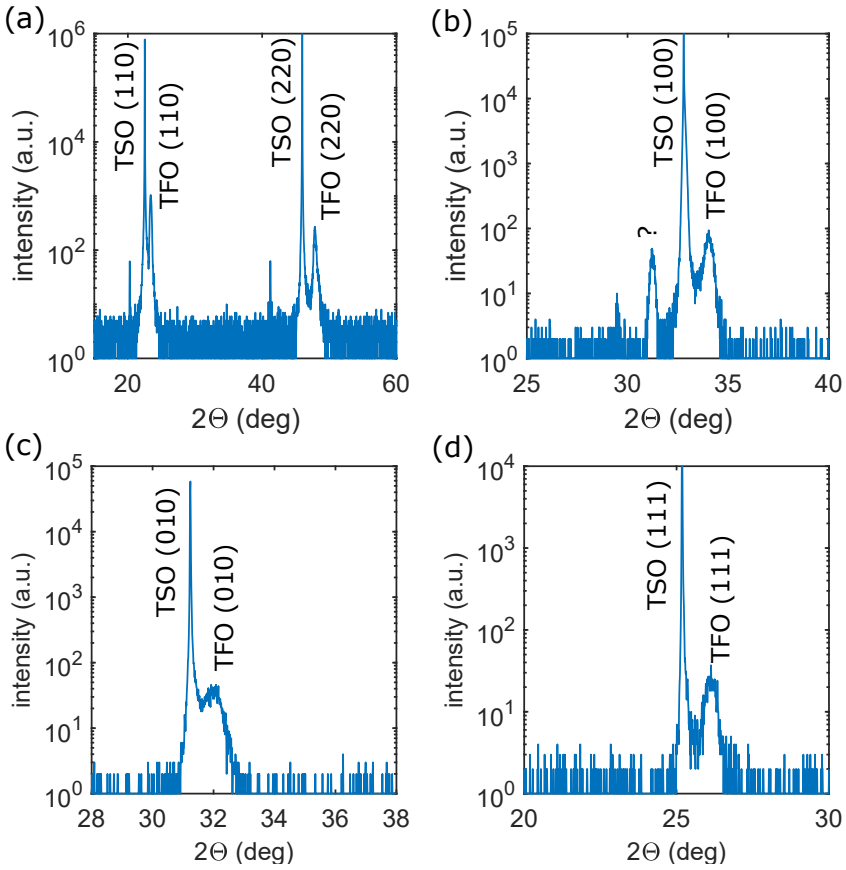


Figure 6.23.: XRD scans of a TSO/TFO sample: (a) $2\Theta/\omega$ scan in the $\langle 110 \rangle$ direction (out-of-plane) (b) in the $\langle 100 \rangle$ direction with a unknown strange phase peak (c) in the $\langle 010 \rangle$ direction (d) in (111) direction.

film in SQUID. However, the properties of the TFO could not be determined due to the large paramagnetic moment of the TSO substrate. The large increase of the moment with reducing temperature completely masks the spin reorientation transition and thus we conclude that TSO is not an ideal substrate to pursue for future studies.

### $GdScO_3$

For TFO samples grown on $GdScO_3$ (GSO) substrates, $2\Theta/\omega$ measurements have been performed in the $\langle 110 \rangle$, $\langle 100 \rangle$, $\langle 010 \rangle$ and $\langle 112 \rangle$ directions, which are shown in Fig. 6.24. No impurity phases have been observed in the XRD spectra for this sample, unlike for the films on TSO. An indication of Laue oscillations around the (110) TFO reflex (not shown) indicates a smoother growth of the TFO thin film compared to the one grown on TSO substrates. From the Scherrer formula a crystallite thickness of around 71 nm has been calculated, meaning that the majority of the 80 nm thick thin film is well oriented and epitaxial. This further underlines the high quality growth

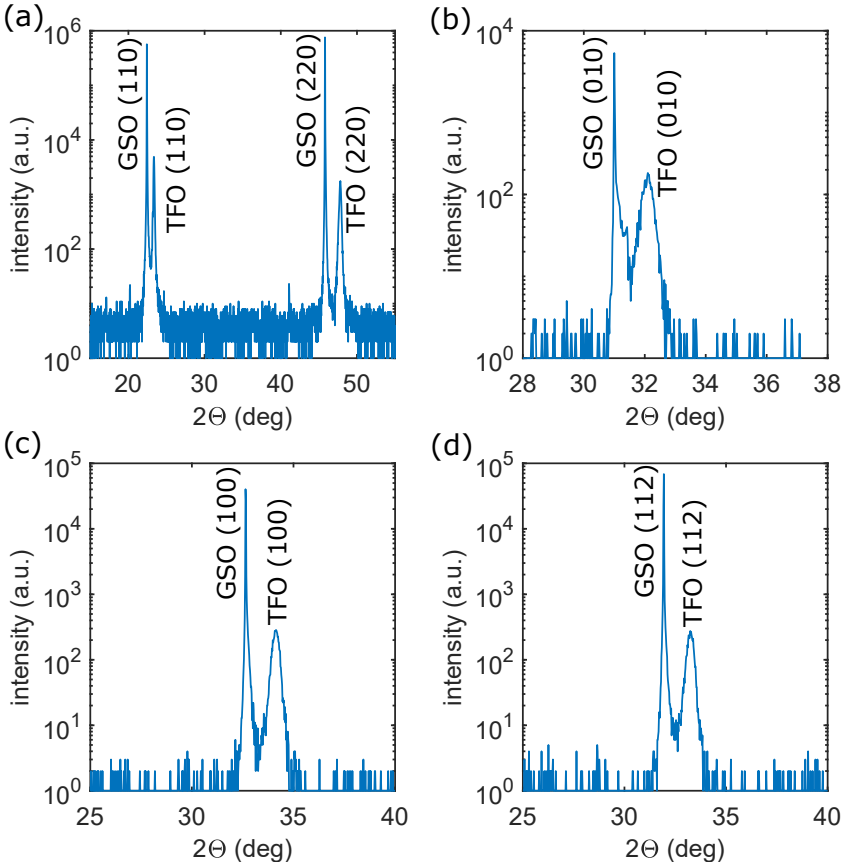


Figure 6.24.: XRD scans of a TFO/GSO sample: (a) $2\Theta/\omega$ scan in the $\langle 110 \rangle$ direction (out-of-plane) (b) in the $\langle 010 \rangle$ direction (c) in the $\langle 100 \rangle$ direction and (d) in the $\langle 112 \rangle$ direction.

of TFO on GSO. The lattice parameters of the TFO $a$- and $b$-axes can be directly extracted using Bragg formula, while the $c$-axis is calculated from the (112) reflex by the formula given in the above paragraph. The following lattice parameters have been determined for the TFO layer:

$$a = 5.25\,\text{Å} \qquad b = 5.57\,\text{Å} \qquad c = 7.59\,\text{Å}.$$

We observe unit cell parameters which are very close to the bulk values, indicating that the TFO grows in a relaxed fashion. Like for the TSO/TFO samples, the magnetization measurements of the GSO/TFO samples are inconclusive because of the large paramagnetic contribution of the Gd ions in the substrate. Field-dependent measurements go out of bounds of the SQUID at small magnetic fields and temperature dependent measurements are masked by a large paramagnetic $\propto 1/T$ contribution which is orders of magnitude larger than the canted moment. Therefore, the magnetic properties of GSO/TFO could not be determined by SQUID.

**$YAlO_3$**

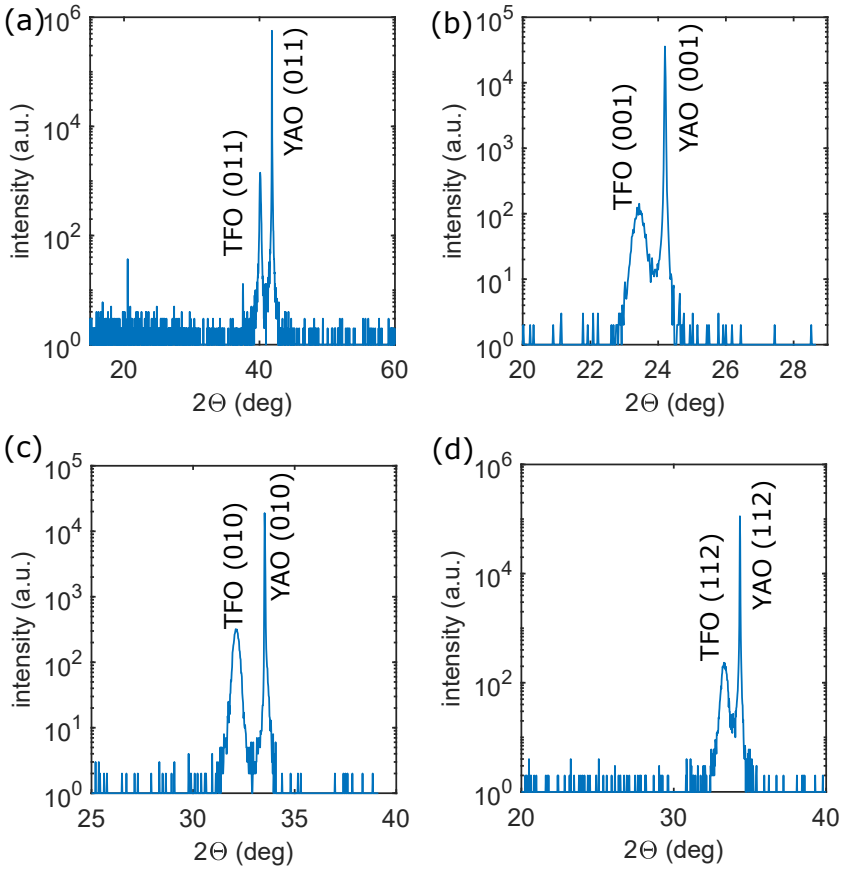


Figure 6.25.: XRD scans of a TFO/YAO sample: (a) $2\Theta/\omega$ scan in the (011) direction (out-of-plane) (b) in the (001) direction (c) in the (010) direction and (d) in the (112) direction.

Given that the Tb and Gd give big moments, we search for a nonmagnetic substrate so that SQUID can be easily performed at the samples. We therefore choose the diamagnetic $YAlO_3$ (YAO). The $2\Theta/\omega$ measurements for the TFO samples grown on YAO substrates have been performed along the $\langle 011 \rangle$, $\langle 001 \rangle$, $\langle 010 \rangle$ and $\langle 112 \rangle$ directions. The respective figures are presented in Fig. 6.25. As for the GSO/TFO samples, no impurity phase can be detected by XRD. The Scherrer formula for these samples gives a crystallite size of 55 nm perpendicular to the surface. The crystallite size is lower than for the samples with GSO substrates, but higher than for TSO substrates. The absence of Laue oscillation further indicates that the lattice planes are not as parallel as in the GSO/TFO samples. Nevertheless, the absence of secondary growth directions indicates the high quality of the thin films.
The lattice parameters of the *b*- and *c*-axes can directly be determined by the Bragg formula. The *a*-axis parameter is determined by the (112) reflex as mentioned above.

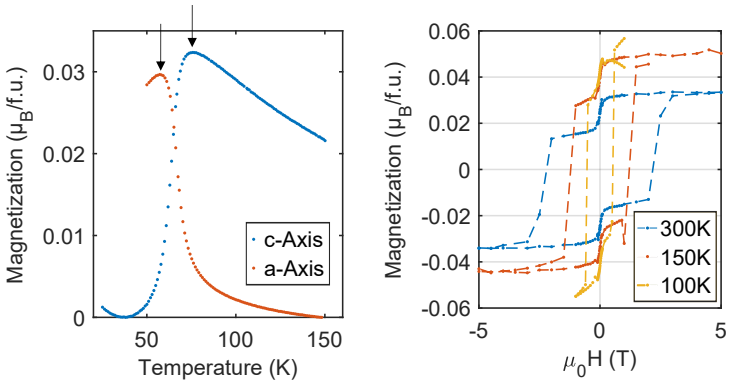


Figure 6.26.: (a) Temperature dependent magnetization of YAO/TFO measured along the $c$- and $a$-axes. The spin reorientation temperatures $T_1$ and $T_2$ are indicated by black arrows. (b) Magnetic field dependent magnetization of YAO/TFO at different temperatures. The data has been corrected for paramagnetic and diamagnetic backgrounds.

The lattice parameters of the TFO thin film are

$$a = 5.22\,\text{Å} \qquad b = 5.57\,\text{Å} \qquad c = 7.59\,\text{Å}.$$

We observe a contraction of the TFO unit cell along the $a$-axis and an expansion along the $c$-axis indicating a strained growth of TFO on YAO.
The advantage of the YAO substrate compared to the other substrates are its diamagnetic properties which allow for a straight forward determination of the magnetic properties of the TFO thin film by SQUID. Fig. 6.26 (a) shows $M(T)$ curves, which have been determined in separate measurements along the $c$-axis and $a$-axis in a cooling and heating sequence, respectively. The procedure was similar as for determining the SRT in TFO bulk samples (see Fig. 5.4) and STO/TFO thin films (see Fig. 6.6) described previously. After saturating the sample along the measurement axis, a field of 10 mT was applied during the measurement in both directions. We determine the SRT temperature as the temperatures where the magnetic moment in the respective direction starts to decrease. This is indicated in Fig. 6.26 by black arrows. Compared to the TFO bulk samples and STO/TFO thin films, we observe a significant shift of the SRT towards lower temperatures of $T_1 = 57\,\text{K}$ and $T_2 = 75\,\text{K}$. This may be attributed to the substrate-induced strain of the TFO thin film and the reduced thickness of the sample compared to STO/TFO samples discussed above. This measurement reveals that we are able to engineer the SRT regime of TFO by thin-film techniques.
We also understand the temperature-dependent magnetization away from the SRT by taking into account the paramagnetic Tm contribution to the magnetization. The magnetic moment along the $c$-axis increases with decreasing temperature due to the parallel alignment of the polarized Tm moment $M_{Tm}$ with the iron magnetic moment stemming from the sublattice canting $M_{Fe}$. Below the SRT, the magnetic moment

decreases with temperature due to the antiparallel alignment of $M_{Tm}$ and $M_{Fe}$, just as observed in bulk TFO and STO/TFO thin films.
Regarding the magnetic-field dependent magnetization, measurements have been performed along the TFO $c$-axis as shown in Fig. 6.26 (b), where TFO is in the $\Gamma_4$ phase. At all temperatures, we see a dominating easy-axis ferromagnetic hysteresis, confirming the orientation of the magnetization along the $c$-axis. The coercivity reduces with decreasing temperature due to the temperature-dependent uniaxial anisotropy approaching zero in the SRT regime. The increase of saturation magnetization stems from the polarized paramagnetic Tm moment. Like for STO/TFO thin films, we also observe a very soft magnetic contribution, which is visible in each curve as an additional step in the hysteresis around a magnetic field of 0 T. Similarly to STO/TFO samples, this contribution is temperature-independent and might stem from a maghemite phase, which is not visible in the XRD or other iron impurities from the sample handling.
Summarizing, TFO can be grown on various orthorhombic substrates leading to high quality of the TFO layer. Epitaxy proves to be a suitable tool to tune the magnetic properties of TFO. The choice of substrate material determines the strain in a thin film layer. Changes to the lattice parameters alters the magnetocrystalline anisotropy of the TFO, which is responsible for the SRT. Using epitaxial strain the SRT can be shifted several Kelvin.
The monocrystallinity of the samples is furthermore interesting for applications like magnon transport which is proven efficient in the absence of domain walls [S2].

## 6.3. Hexagonal phase of TFO

As briefly mentioned in sections 2.2 and 6.1, TFO thin films can posses a crystallographic phase different from the orthorhombic symmetry observed in bulk. The hexagonal phase is similar to that of hexagonal manganites, possessing ferroelectric and ferromagnetic order [91, 92]. While for manganites, the hexagonal phase exist in bulk, hexagonal ferrites are metastable and have to be stabilized, for example by strain from a substrate with the corresponding symmetry. It has already been shown that TFO can be grown in a metastable hexagonal phase on $Al_2O_3$ (0001) substrates with a Pt (111) buffer layer [22, 84], as well as YSZ (111) substrates [147]. Hexagonally stabilized orthoferrites posses multiferroic ordering. Hexagonal TFO (h-TFO) has a ferroelectric ordering temperature of around $T_C = 430\,\mathrm{K}$ and orders magnetically below 120 K [22]. The aim of this work was to investigate the magnetoelectric (ME) coupling of h-TFO. The magnetic response to a electric field was to be analyzed by SQUID magnetometry, for which a special rod was designed to perform ME measurements (see section 3.5). The study aimed to read the magnetic state utilizing spin Hall magnetoresistance (SMR) as done for orthorhombic bulk samples and thin films described in already in this thesis (see chapter 5 and section 6.1), and probe the bias-voltage dependent SMR signal. In this work, the growth of hexagonal TFO (h-TFO) was achieved on $Al_2O_3$ (0001) / Pt (111) and YSZ (111) / Pt (111) as well

as MgO (001) substrates, while we present only the growth on MgO and $Al_2O_3$/Pt. The samples are analyzed using atomic force microscopy. The growth and characterization of the samples was performed by Sven Becker. We present the crystallographic properties of h-TFO grown on different substrates. Despite the achievement of the desired structure in thin films, electrical measurements could not be performed. Unfortunately, this project did not yield any publishable results. The samples require an epitaxial Pt bottom electrode, which is unstable when growing h-TFO on top.

### h-TFO thin films grown on MgO substrate

We start by investigating MgO (001) / h-TFO samples. The TFO layer is deposited on the bare MgO substrate by PLD at a substrate temperature of around 700°C and an $O_2$ background pressure of 0.2 mbar. Fig. 6.27 shows the central results from the structural analysis using XRD. Fig. 6.27 (a) shows a $2\Theta/\omega$-scan performed along the (001)-direction of MgO. We identify the peak found at $2\Theta = 30°$ as the h-TFO (0004) peak. The resulting lattice constant of h-TFO is $c = 11.82$ Å. The inset of Fig. 6.27 (a) shows the rocking curve of the h-TFO (0004) peak. The rocking curve of the h-TFO (0004) reflex has a FWHM of $\Delta\omega = 3.5°$ (not shown), which is broader compared to other samples grown in this work. This means that the crystallographic domains orient only roughly with the MgO axes and growth directions differ for different crystallites across the sample surface. This is not surprising regarding the different symmetries of substrate and film material and the metastable nature of h-TFO.
The grain size is determined by the Scherrer formula and gives an average crystallite size perpendicular to the surface of around 15 nm, while XRR measurements give a thickness of around 40 nm, which further shows that the h-TFO thin film does not

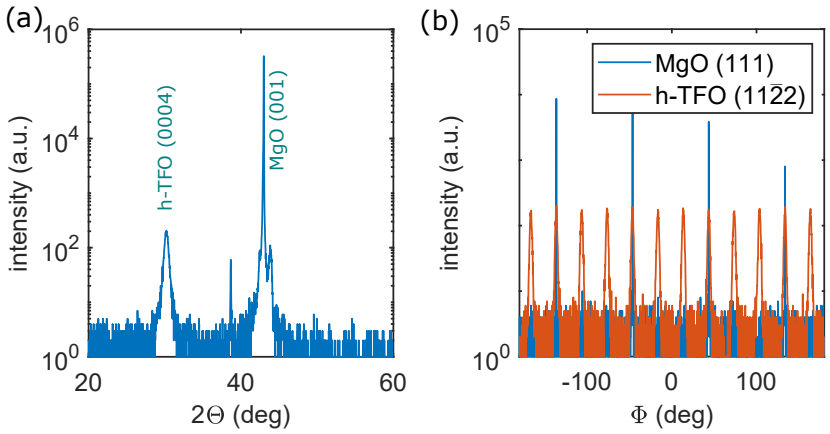


Figure 6.27.: (a) Out-of-plane XRD scan in (001) direction. Other than the substrate peak at around $2\Theta = 42°$, a second peak at around $2\Theta = 30°$ is visible, which we identify as h-TFO (0004). (b) Φ-scans at fixed $2\Theta$ on MgO (111) and h-TFO (11$\bar{2}$2) are shown to investigate the in-plane order.

grow as a single crystal. To determine the in-plane lattice constant, the $(11\bar{2}2)$ h-TFO peak is found, from which we determine an in-plane lattice constant of $a = 6.01\,\text{Å}$. However, it has to be determined if the samples possess any in-plane order. Therefore, $\Phi$-scans at $2\Theta$ fixed to the h-TFO $(11\bar{2}2)$ and MgO (111) peaks were performed. The curves are shown in Fig. 6.27 (b). One can see the four reflexes from the cubic MgO (111), as expected. They are separated by 90° typical for the cubic symmetry of the material. For the h-TFO $(11\bar{2}2)$, we observe a 12-fold symmetry, which is twice that expected for a hexagonal single crystal.

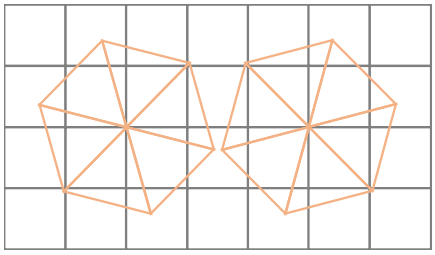

Figure 6.28.: Sketch of the in-plane order of MgO/h-TFO films. The cubic MgO unit cells are drawn in Grey, the h-TFO unit cells in Red.

This leads us to the conclusion that there are two crystallographic domains present, separated by an in-plane rotation of 30°. This can be understood by considering the geometrical symmetries of the two crystal structures, as shown in Fig. 6.28. Out of the six equivalent in-plane axes of the h-TFO unit cell, two orient along the MgO diagonal during the growth. There are two possibilities to achieve this, as evident from this sketch. Despite the twinning of the h-TFO layer, the crystallographic domains are well oriented relative to the MgO axes. To our knowledge, the hexagonal growth of TFO on MgO substrates is so far not reported. Other orthoferrites, like $SmFeO_3$ appear to grow in their bulk orthorhombic phase on MgO [170]. This indicates that the hexagonal growth of h-TFO on MgO is not universal for all $REFeO_3$, but relies on the size of the RE ion.
To measure the ferroelectric properties and magnetoelectric response, the h-TFO must be sandwiched by two conducting electrodes. To epitaxially grow the h-TFO in a similar fashion like on bare MgO, the conducting layer must possess the same symmetry, grow epitaxially on MgO and be stable at high temperatures in an oxygen atmosphere. No such material was available for deposition, which is why we choose different substrates to proceed.

### h-TFO thin films grown on $Al_2O_3$ substrate

The growth of h-TFO on $Al_2O_3$ (0001) / Pt (111) substrates has previously been reported [22]. However, the magnetoelectric properties of h-TFO were not analyzed in great detail, which motivates a deeper investigation of this material stack. The Pt layer was deposited on the $Al_2O_3$ (0001) by DC magnetron sputtering deposition at a substrate temperature of 500°C and an Ar background pressure of 0.01 mbar. The

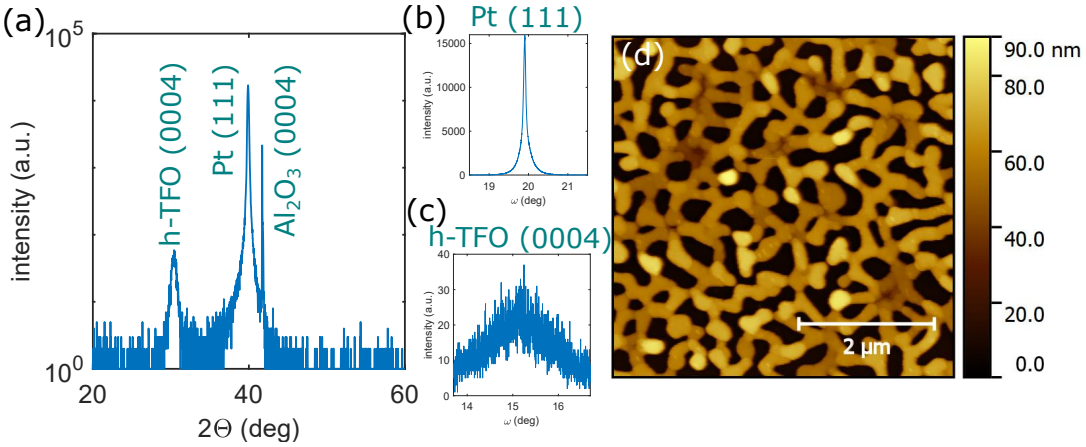


Figure 6.29.: (a) $2\Theta/\omega$ scan of a $Al_2O_3$ (0001) / Pt (111) / h-TFO (0001) sample deposited at around 700°C. The reflexes of the respective layers are indicated. (b) - (c) Rocking curve of Pt (111) and h-TFO (0004) reflex, respectively. (d) Atomic force microscopy image of the same sample.

Pt grows in the desired (111) direction as confirmed by XRD. XRR and AFM reveal a smooth surface with a RMS roughness of around 0.25 nm, which is of the order of one atomic step. The $Al_2O_3$ (0001) / Pt (111) sample is transferred ex-situ into the PLD deposition chamber, where TFO is deposited at an $O_2$ background pressure of 0.2 mbar. The choice of temperature during the h-TFO deposition strongly affects the underlying Pt layer.

In Fig. 6.29 a sample grown at a temperature of around 700°C, the same conditions as for the MgO/h-TFO sample, is shown. In the $2\Theta/\omega$ scan, Fig. 6.29 (a), only h-TFO, Pt and substrate peaks are found, with no indications of an impurity phase. Fig. 6.29 (b) shows the rocking curve of the Pt (111) reflex possessing a width of $\Delta\omega = 0.37°$. The rocking curve of the h-TFO (0004) reflex shown in Fig. 6.29 has a broadness of $\Delta\omega = 2.16°$, which is slightly less than found in the MgO/h-TFO sample. However, analyzing the surface structure by atomic force microscopy, one detects an unusual surface structure as shown in Fig. 6.29 (d). The origin of this surface structure is likely dewetting of the Pt layer [171], which is a well-known phenomenon for metal/dielectric layer systems. Weak interaction between the different materials and the mobility of the metal atoms due to high temperature lead to an agglomeration of the Pt thin film. In order to avoid the dewetting of the Pt layer, the h-TFO layer was deposited at a lower temperature. The h-TFO layer of the sample shown in Fig. 6.30 is deposited at around 640°C, keeping other deposition parameters fixed. In the $2\Theta/\omega$ scan shown in Fig. 6.30 (a), one can still identify the reflexes of the individual layers as indicated. Compared to the sample deposited at higher temperature, the crystallite size of the h-TFO layer is increased. According to the Scherrer formula the average grain size in out-of-plane direction is around 16 nm. Additionally, Laue oscillations around the Pt (111) peak indicate, that the Pt layer is much smoother than the previously shown

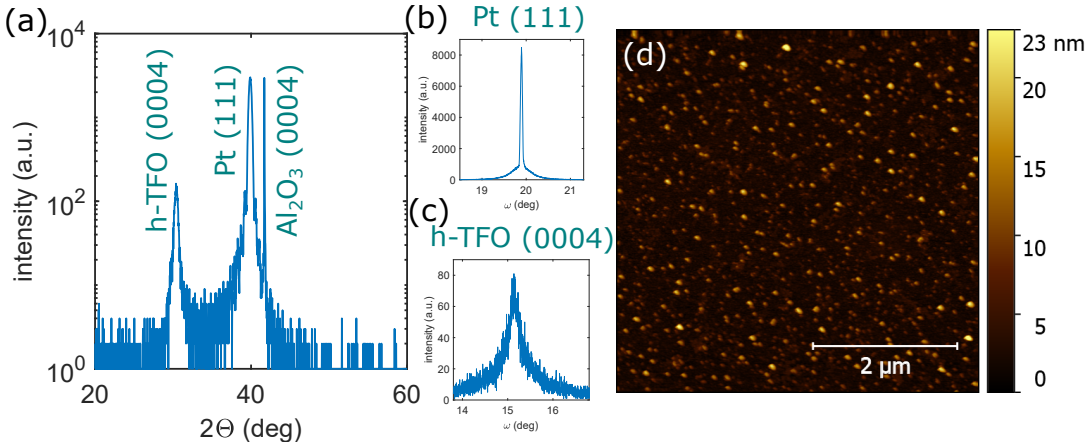


Figure 6.30.: (a) $2\Theta/\omega$ scan of $Al_2O_3$ (0001) / Pt (111) / h-TFO (0001) deposited at around 640°C. The reflexes of the respective layers are indicated. (b) - (c) Rocking curve of Pt (111) and h-TFO (0004) reflex, respectively. (d) Atomic force microscopy image of the same sample.

sample. Both rocking curves have decreased in FWHM as shown in Fig. 6.30 (b) and (c) to $\Delta\omega = 0.05°$ and $\Delta\omega = 0.8°$ for the Pt (111) and the h-TFO (0004) peak, respectively, which indicates a more uniform growth direction of the crystallites. Finally, the conservation of the flat Pt is confirmed locally by AFM measurements as shown in Fig. 6.30 (d). The unit cell parameters of the h-TFO layer are determined to be $c = 11.75\,\text{Å}$ and $a = 6.05\,\text{Å}$. Φ-scans reveal a 6-fold in-plane symmetry of both h-TFO and Pt, reducing the number of in-plane orientations compared to the h-TFO grown on MgO substrates. The axes of h-TFO $(11\bar{2}0)$, Pt $(\bar{1}\bar{1}2)$ and $Al_2O_3$ $(11\bar{2}0)$ are aligned with each other, as seen from h-TFO $(11\bar{2}2)$, Pt (001) and $Al_2O_3$ $(11\bar{2}2)$ peaks occurring at the same angle in Φ scans (not shown).

To measure the ferroelectric domains of such a sample, piezoresponse force microscopy (PFM) has been utilized. This is a scanning probe microscopy technique that utilizes an AC voltage between the scanning probe and the bottom electrode of the sample to image the polarization direction across the surface. An initial measurement shows a uniform polarization (not shown). In a second step the domain structure is manipulated by applying a DC voltage between the scanning probe and the bottom electrode. A sufficiently large electric field leads to the switching of domains. In a $5 \times 5\,\mu\text{m}$ square, +12 V is applied. Afterwards, -12 V is applied in a $3 \times 3\,\mu\text{m}$ square inside the first one, in order to demonstrate reversible switching. The PFM images after the so called PFM lithography step are shown in Fig. 6.31.

We see a prominent change in the signal in the region where PFM lithography has been performed. Especially in the phase image, Fig. 6.31 (c), the reversible switching of domains is indicated by the contrast between the inner and the outer square. Note that the vertical change of background noise is due to the measurement close to contact resonance. This means that the cantilever oscillates in a resonant manner while the

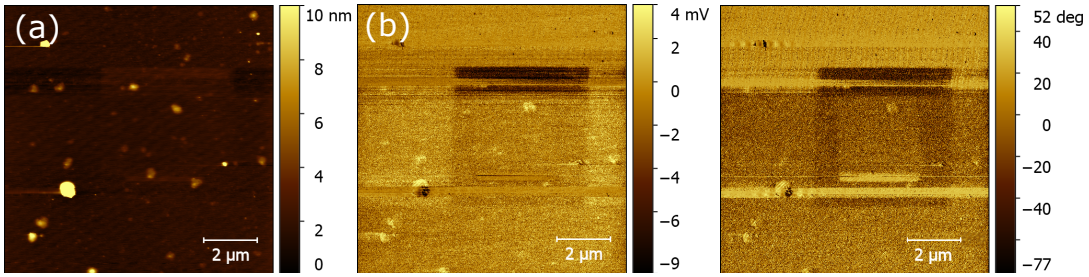


Figure 6.31.: PFM image of a $Al_2O_3$ (0001) / Pt (111) / h-TFO (0001), (a) topography image (b) PFM amplitude and (c) PFM phase measured simultaneously.

resonant frequency relies on the surface-tip interaction Slight changes to the probe (e.g. the tip picks up contaminating material) are visible in the signal due to the change of resonance frequency. We note that also slight changes in the topography are visible in Fig. 6.31 (a), which indicate that here, the application of the DC voltage lead to local, structural changes of the sample. In order to support the PFM data indicating ferroelectric properties of the samples, polarization measurements utilizing a Sawyer-Tower circuit were planned.

To generate a capacitor structure, a shadow mask was placed on the sample to deposit Pt top electrodes of a defined size by DC magnetron sputtering at room temperature. However, all of the fabricated top electrodes were short circuited to the bottom electrode, so that a quantitative analysis of the electrical properties of h-TFO was not possible. A deeper investigation by AFM revealed scratches on the samples surface, probably caused by the metal shadow mask. Additionally, pinholes were detected as shown in Fig. 6.32 which have initially not been detected in these samples.

The occurrence of these pinholes is likely due to localized dewetting of the underlying Pt layer at defect locations [171]. The number of defects could be reduced by careful substrate preparation and proper cleaning of the Pt target prior to the deposition step. Another possibility is to increase the thickness of the Pt bottom electrode

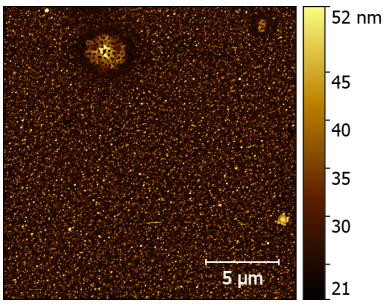


Figure 6.32.: $20 \times 20\,\mu$m AFM image of a $Al_2O_3$ (0001) / Pt (111) / h-TFO (0001) sample showing two defects in the bilayer due to localized dewetting of the Pt layer.

since it is expected that the critical temperature at which the dewetting starts to occur shifts to higher temperature with increasing Pt thickness [171]. However, this is disadvantageous for the aim of measuring SMR at this kind of samples. The amplitude of the SMR decreases with increasing thickness of the heavy metal above a thickness of around twice the spin relaxation length, which is around 4 nm in Pt/YIG samples [158]. At a thickness of 50 nm, where the critical temperature for the dewetting increases to around 850 K [171], the SMR signal is effectively zero [158]. One could ignore the fact that the Pt bottom electrode might be too thick to measure the SMR thickness, if one would be using a top electrode instead, which could be deposited at room temperature and which was planned in the device design to be able to switch the h-TFO layer.

However, this is hindered by the fact that the h-TFO phase is only meta-stable. Point defects that occur during the growth of the h-TFO layer lead to local relaxation points, where the orthorhombic phase of TFO forms. A large fraction of the h-TFO phase is therefore expected only close to the bottom interface. This is confirmed by the deposition of thick h-TFO samples. Although strange phases are not detected in $2\Theta/\omega$ scans along the (0001) $Al_2O_3$ direction, the intensity of the h-TFO reflexes does not increase when increasing the duration of the TFO deposition. Consequently, the deposited TFO at large thicknesses presumably does not form the h-TFO phase oriented parallel to the substrate.

This chapter has considered different applications of thin film TFO deposited by pulsed laser deposition for devices and THz emitters etc. The high quality epitaxial growth of orthorhombic growth is achieved on STO and the magnetic properties are similar to bulk. Making use of surface sensitive measurements, the SRT is resolved and it is shown that the naive SMR model based on exchange torques is not able to accurately describe the entire dataset, and thus needs to be modified to consider the multiple sublattices, DMI vectors and canted moments of orthoferrites as well as possibilities for strong temperature- and field-dependence of the spin mixing conductance.

The twinning observed in STO/TFO thin films can be overcome by the choice of a fitting substrate. While best growth was achieved on TSO substrates, evident from the TFO grain size perpendicular to the surface, YAO substrates have the advantage of being diamagnetic, facilitating investigations of the TFO thin film. The choice of substrate changes the strain in the TFO layer and proves to modify the magnetocrystalline anisotropies. With regard to device applications,

Finally, the meta-stable phase of h-TFO was grown on substrates with the aim to grow magnetoelectric capacitor structures. Although high quality films were developed, necessary steps for accessing the ferroelectric properties led to short circuits across the sample. Future work should consider tackling the stability of the bottom electrode. Potentially, different metallic compounds can be grown epitaxially and provide the appropriate symmetry for the h-TFO phase. Furthermore, for different $REFeO_3$ compounds, the deposition conditions might vary so that the growth of the hexagonal multiferroic phase can be performed at lower temperatures, avoiding the dewetting of the Pt bottom electrode.

# 7. Summary and outlook

In this thesis, the properties of magnetically ordered oxides have been investigated since they are promising candidates for different future spintronic applications such as magnon valves and antiferromagnetic memory devices.
We have shown that magnetically interface-coupled YIG-GIG ($Y_3Fe_5O_{12}$-$Gd_3Fe_5O_{12}$) heterostructures can be grown via pulsed laser deposition (PLD). The high quality crystallographic properties have been demonstrated using x-ray diffraction (XRD). The coupling has been proven using different superconducting quantum interference device (SQUID) magnetometry measurements. Using spin Hall magnetoresistance (SMR) measurements, we can determine the magnetic behavior of the top layer in these structures.
The interface coupling proves to be strong making the YIG-GIG heterostructures interesting candidates for robust spintronic devices. Only large field can break the magnetic coupling leading to a continuous rotation of the antiparallel coupled magnetization of YIG (GIG) layer at low (intermediate) temperatures. YIG-GIG heterostructures are tunable devices with defined magnetic properties. The phase space of the relative alignment of the magnetic sublattices has been identified, dependent on the relative layer thickness, external magnetic field and temperature.
A possible application for YIG-GIG heterostructures is magnon valves, where there are defined magnetic states with different magnon conductivities. We investigate the transmission of thermal spin currents in YIG-GIG samples using spin Seebeck effect (SSE) measurements. The SSE measurements confirm the interfacial exchange coupling. The magnon valve effect, however, is not visible in the temperature range investigated for the selected samples. In the future, different sample stacks like YIG-GIG-YIG and GIG-YIG-GIG, as well as superlattice structures could be investigated. SSE measurements done at higher temperature are expected to excite different magnon branches that might be eligible to show the magnon valve effect.
Secondly, we demonstrated that the surface sensitive spin Hall magnetoresistance is a useful tool to probe the bulk magnetic properties of both $TmFeO_3$ (TFO) bulk samples as well as thin films. This is motivated by the fact that the magnetic state of antiferromagnets is usually accessed by large-scale experiments like neutron scattering or antiferromagnetic resonance, which are not useful with regard to device applications. Focusing on measurements on bulk TFO crystals we first investigated its bulk properties by means of XRD and SQUID measurements. XRD reveals the crystallographic properties of the sample, confirming the orthorhombic structure, the (101)-orientation of the surface and the absence of impurity phases. SQUID measurements further show the occurrence of the spin reorientation transition (SRT) in a temperature range between 94 K and 85 K, where the spins of the TFO continuously rotate from the $a$-axis

to the *c*-axis due to the temperature-dependent anisotropy fields. In the region around the transition, where the uniaxial anisotropy is small, we are able to rotate the spins in the *ac*-plane when applying an external magnetic field, prematurely inducing the temperature-driven transition.
Using surface-sensitive spin Hall magnetoresistance (SMR) measurements, we can access the magnetic properties of the TFO by measuring the transverse as well as the longitudinal resistivity at a Pt Hall bar defined on the surface of the TFO. The magnetic properties extracted from these surface-sensitive measurements were shown to be accurate representations of the bulk magnetic behavior, validating the approach and highlighting its potential application for thin film devices. While for many materials, the SMR signal was found to be dependent either on the magnetic moment or the Néel vector, depending on the material under investigation, our measurements appear to depend on both order parameters simultaneously as revealed by measuring by measurements performed with a rotating magnetic field.
Applying the field along the crystallographic axes of the TFO we can detect not only the spin flop, at which the spins perform a full 90° rotation, but also the spin reorientation temperatures $T_1$ and $T_2$. The ability to detect the spin reorientation in canted antiferromagnets using only the surface sensitive SMR opens a large field for spintronic applications of antiferromagnetic memory devices. However, not all results can be explained using a simple model of SMR. The transverse resistivity of bulk (101)-oriented TFO shows a behavior that is of magnetic origin, but does not correlate with the spin-reorientation transition, which is itself clearly visible in the longitudinal resistivity.
Our SMR measurements reveal that the current level of understanding the interfacial effects between the spin accumulation and the magnetic order parameters of canted antiferromagnets is insufficient to explain all observed effects. This also highlights that the interface of canted orthoferrites can represent a different magnetic landscape to the bulk magnetic ordering. Currently, improved models are being developed, which may include the effect of large uniaxial anisotropies, Dzyaloshinsky-Moriya interaction (DMI) and possible orbital contributions. Further measurements on orthoferrites will be necessary to support these upcoming models.
The family of orthoferrites is large and future experiments will reveal if other components show similar behavior. Some may even enable large magnon decay lengths enabling long-distant magnon transport like hematite as very recently shown for $YFeO_3$ [S8].
In the final part of this thesis, we have shown that TFO thin films can be grown in the desired orthorhombic phase using PLD. The growth of TFO has been optimized using standard thin-film substrates $SrTiO_3$ (STO). Our samples grown on STO substrates show oriented growth, where the individual crystallites share a common *c*-axis, but posses a twinned in-plane order with two possible orientations, aligned at 45° with respect to the STO axes. The topography of the thin films is much rougher than for the polished single crystal. It is likely that the grain boundaries between the differently oriented crystallites favor the island-like growth.
The magnetic properties are found to be similar to bulk samples. We confirm anti-

ferromagnetic ordering of the Fe sublattices using XMLD measurements, meanwhile SQUID measurements confirm the SRT of STO/TFO thin films takes place within a larger temperature region compared to bulk, between 110 K and 72 K. While coercivity and the SRT region appear to be altered by the strained growth of TFO, the canting angle of the Fe sublattices appears to be unchanged, indicating that the strain alters the anisotropy fields, but not the relative strengths of the symmetric and anitsymmetric exchange fields.
Despite the twinning and roughness, we are able to perform electrical measurements at the TFO thin films, from which we can identify the different magnetic phases of the TFO using all-electrical surface sensitive SMR. Like in the measurements performed at TFO single crystals, we observe that the signal does not seem to depend on either the Néel vector or the canted moment, but rather on both simultaneously.
Since the twinning of the TFO complicates the interpretation of the electrical data, we suggest to use substrates of similar symmetry for the growth of TFO. We show that TFO grows epitaxially on $TbScO_3$, $GdScO_3$, and $YAlO_3$ substrates. While $TbScO_3$ and $GdScO_3$ substrates possess paramagnetic properties which may complicate the analysis of (volume) magnetic measurements, diamagnetic $YAlO_3$ appears to be the best candidate for growing TFO thin films with the surface orientation defined by the substrate orientation. The SRT in these samples can easily be identified by SQUID. Due to the reduced net magnetic moment of the TFO thin films, electrical measurements are expected to be easier to perform as the large moment of the TFO bulk crystals has caused difficulties when measuring it on a piezoelectric rotator in a cryostat.
The dependence of the TFO properties on the underlying substrate has further been demonstrated by growing it in its hexagonal phase (h-TFO), a metastable phase different from the orthorhombic phase shown above. The h-TFO can be stabilized on e.g. MgO (001) and $Al_2O_3$ (0001) substrates. We are able to demonstrate the ferroelectric properties of h-TFO using piezoresponse force microscopy. However, we are unable to analyze its magnetoelectric coupling due to the instability of the bottom electrode. We suggest using a magnetic bottom electrode that also allows for heteroepitaxial growth of the h-TFO top layer, but is more stable against high temperature and oxide background pressure than the pure Pt used here. Furthermore, in-situ transfer between the deposition chambers may reduce the amount of defects incorporated into the bottom electrode.
All the results show that the magnetic oxides presented here are interesting candidates for future spintronic applications.

# A. Appendix

## A.1. Mathematical calculation of the free energy in $REFeO_3$

When investigating the behavior of orthoferrites in an external magnetic field, it is helpful to describe the properties of the system via the free energy. While the mathematical description of the system is not a focus of this thesis, it is still helpful for understanding the behavior of the magnetic sublattices. We therefore present this summary, which exceeds the description given in section 2.2, here in the appendix.

We can describe the $\Gamma_4$ state using the energy terms introduced in the theory section 1.1 and by reducing the magnetic structure to two sublattices. Calculations have been performed in very detail by Yamaguchi [172]. Here, a simplified 2-Fe-sublattice-model is presented as introduced by Herrmann [164]. We will first describe the equilibrium position by a Hamiltonian and later analyze the effect of an external magnetic field and temperature.

The most important terms are the exchange energy $E_{ex} = \mathcal{J}\mathbf{m_1} \cdot \mathbf{m_2}$, the DMI energy $E_D = \mathbf{D} \cdot (\mathbf{m_1} \times \mathbf{m_2})$ and the magnetocrystalline anisotropy energies up to the second order: $E_{Ka} = -A_{aa}(m_{1a}^2 + m_{2a}^2)$ and $E_{Kc} = -A_{cc}(m_{1c}^2 + m_{2c}^2)$ for $a$ and $c$-direction, respectively, as well as the cross term $E_{kac} = -A_{ac}(m_{1a}m_{1c} - m_{2a}m_{2c})$. We introduce a coordinate system for our two magnetic sublattices $\mathbf{m_1}$ and $\mathbf{m_2}$, by labeling the angle between the canted moment $\mathbf{M} = \mathbf{m_1} + \mathbf{m_2}$ with the $c$-axis as $\beta$ and the angle between the antiferromagnetic vector $\mathbf{N} = \mathbf{m_1} - \mathbf{m_2}$ with $\mathbf{m_1}$ as $\gamma$ (canting angle) as shown in the sketch below. So we have

$$\mathbf{m_{1/2}} = m_0 \begin{pmatrix} \pm\cos(\gamma \pm \beta) \\ 0 \\ \sin(\gamma \pm \beta) \end{pmatrix}$$

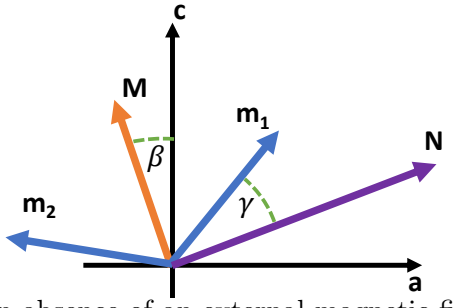


and a resulting equation for the energy $\mathcal{E}$ in absence of an external magnetic field up

to the first order of anisotropy:

$$\begin{aligned}
\mathcal{E} =& E_{ex} + E_D + E_{Ka} + E_{Kc} + E_{Kac} \\
=& \mathcal{J}\mathbf{m_1} \cdot \mathbf{m_2} \\
&+ \mathbf{D} \cdot (\mathbf{m_1} \times \mathbf{m_2}) \\
&- A_{aa}(m_{1a}^2 + m_{2a}^2) \\
&- A_{cc}(m_{1c}^2 + m_c^2) \\
&- A_{ac}(m_{1a}m_{1c} - m_{2a}m_{2c}) \\
=& - \mathcal{J}m_0^2 \left(\cos(\gamma-\beta)\cos(\gamma+\beta) - \sin(\gamma-\beta)\sin(\gamma+\beta)\right) \\
&- \mathcal{D}m_0^2 \left(\cos(\gamma+\beta)\sin(\gamma-\beta) + \cos(\gamma-\beta)\sin(\gamma+\beta)\right) \\
&- A_{aa}m_0^2 \left(\cos^2(\gamma+\beta) + \cos^2(\gamma-\beta)\right) \\
&- A_{cc}m_0^2 \left(\sin^2(\gamma+\beta) + \sin^2(\gamma-\beta)\right) \\
&- A_{ac}m_0^2 \left(\cos(\gamma+\beta)\sin(\gamma+\beta) + \cos(\gamma-\beta)\sin(\gamma-\beta)\right) \\
=& - \mathcal{J}m_0^2 \cos(2\gamma) \\
&- \mathcal{D}m_0^2 \sin(2\gamma) \\
&- A_{aa}m_0^2 \left(\cos(2\gamma)\cos(2\beta) + 1\right) \\
&- A_{cc}m_0^2 \left(1 - \cos(2\gamma)\cos(2\beta)\right) \\
&- A_{ac}m_0^2 \left(\sin(2\gamma)\cos(2\beta)\right)
\end{aligned} \tag{A.1}$$

In the above calculation, it was taken into account that $\mathbf{D} = \mathcal{D}\hat{\mathbf{b}}$ is aligned with the crystallographic $b$-axis, which is antiparallel to the cross product $\mathbf{m_1} \cdot \mathbf{m_2}$[25]. To find the equilibrium position of the order parameter, we minimize $\mathcal{E}$ with respect to the orientation angle $\beta$:

$$\begin{aligned}
\frac{\partial \mathcal{E}}{\partial \beta} = 0 =& - 0 \\
&- 0 \\
&- A_{aa}m_0^2 \left(-2\cos(2\gamma)\sin(2\beta)\right) \\
&- A_{cc}m_0^2 \left(2\cos(2\gamma)\sin(2\beta)\right) \\
&+ A_{ac}m_0^2 \left(2\sin(2\gamma)\sin(2\beta)\right) \\
=& + 2(A_{aa} - A_{cc})m_0^2 \cos(2\gamma)\sin(2\beta) + 2A_{ac}m_0^2 \sin(2\gamma)\sin(2\beta) \\
=& \sin(2\beta)\left((A_{aa} - A_{cc})\cos(2\gamma) + A_{ac}\sin(2\gamma)\right) \\
& \beta = 0^\circ \qquad \vee \qquad \beta = 90^\circ \qquad \vee \qquad \frac{A_{cc} - A_{aa}}{A_{ac}} = \tan(2\gamma)
\end{aligned} \tag{A.2}$$

We calculate the second derivative to determine if these extrema are minima:

$$\frac{\partial^2 \mathcal{E}}{\partial \beta^2} = \cos(2\beta) 4m_0^2 \left((A_{aa} - A_{cc})\cos(2\gamma) - A_{ac}\sin(2\gamma)\right) \tag{A.3}$$

We evaluate $\frac{\partial^2 \mathcal{E}}{\partial \beta^2}$ to see that for either $A_{aa} > A_{cc} + A_{ac}\tan(2\gamma)$ and $\beta = 0°$ or $A_{aa} < A_{cc} + A_{ac}\tan(2\gamma)$ and $\beta = 90°$ we have in fact an energy minimum. The other extremum turns out to be a saddle point. (Because of the equivalence of $\beta = 0°$ and $\beta = 180°$, we restrict the problem to the first quadrant).
Minimizing $\mathcal{E}$ with respect to the canting angle $\gamma$:

$$\begin{aligned}
\frac{\partial \mathcal{E}}{\partial \gamma} = 0 = &+ 2\mathcal{J}m_0^2 \sin(2\gamma) \\
&- 2\mathcal{D}m_0^2 \cos(2\gamma) \\
&+ 2A_{aa}m_0^2 \sin(2\gamma)\cos(2\beta) \\
&- 2A_{cc}m_0^2 \sin(2\gamma)\cos(2\beta) \\
&- 2A_{ac}m_0^2 \cos(2\gamma)\cos(2\beta) \qquad (A.4)\\
(\mathcal{D} + A_{ac}\cos(2\beta))\cos(2\gamma) = &(\mathcal{J} + (A_{aa} - A_{cc})\cos(2\beta))\sin(2\gamma) \\
\frac{\mathcal{D} + A_{ac}\cos(2\beta)}{\mathcal{J} + (A_{aa} - A_{cc})\cos(2\beta)} &= \tan(2\gamma) \\
{}_{\beta=0 \text{ or } 90°} \Leftrightarrow \frac{\mathcal{D} + A_{ac}}{\mathcal{J} + A_{aa} - A_{cc}} &= \tan(2\gamma)
\end{aligned}$$

From equation A.4, we see that in order to minimize $\mathcal{E}$, the canting angle has to be nonzero. Second derivative to determine if extremum is minimum:

$$\begin{aligned}
\frac{\partial^2 \mathcal{E}}{\partial \gamma^2} = &+ 4\mathcal{J}m_0^2 \cos(2\gamma) \\
&+ 4\mathcal{D}m_0^2 \sin(2\gamma) \\
&+ 4A_{aa}m_0^2 \cos(2\gamma)\cos(2\beta) \\
&- 4A_{cc}m_0^2 \cos(2\gamma)\cos(2\beta) \\
&+ 4A_{ac}m_0^2 \sin(2\gamma)\cos(2\beta) \qquad (A.5)\\
= &+ 4m_0^2 \cos(2\gamma)(\mathcal{J} + (A_{aa} - A_{cc})\cos(2\beta)) \\
&+ 4m_0^2 \sin(2\gamma)(\mathcal{D} + A_{ac}\cos(2\beta))
\end{aligned}$$

We note that $\mathcal{J}$ is orders of magnitude larger than the other values, therefore one can safely assume that the extremum found above is always a minimum.
As mentioned in section 2.2, orthoferrites are in general in the $\Gamma_4$ state just below $T_N$ and therefore they can be described by $\beta = 0°$ and $A_{aa} > A_{cc} + A_{ac}\tan(2\gamma)$. Assuming for now that the rare earth orthoferrite is in the $\Gamma_4$ state, we now focus on the canting angle $\gamma$. Knowing that $\beta = 0°$, we can further simplify equation A.4 to

$$\tan(2\gamma) = \frac{\mathcal{D} + A_{ac}}{\mathcal{J} + A_{aa} - A_{cc}}, \qquad (A.6)$$

The term $A_{ac}$ is often set to zero since it is much smaller than $\mathcal{D}$ [136, 173–175]. The exchange field was found to be of the order of $\mu_0 H_e \approx 600\,\mathrm{T}$, the DMI field is of the

order of $\mu_0 H_d \approx 10\,\mathrm{T}$ and the anisotropy field of the order of $\mu_0 H_k \approx 10^{-2}\,\mathrm{T}$ [73]. We can therefore safely approximate

$$\tan(2\gamma) = \frac{H_D}{H_E} = \frac{M}{m_0} \tag{A.7}$$

with the exchange field $\mu_0 H_E = \mathcal{J}/m_0$ , the DMI field $\mu_0 H_D = \mathcal{D}/m_0$. This has been shown in general by Moriya [27] and in detail for orthoferrites e.g. by Treves [73]. With the second equation in A.7 we link the canting angle to measurable parameters. In an experiment, the canting angle can be determined by the ratio of canted moment to sublattice magnetization. Under an external magnetic field $H_{ext}$, we also add a Zeeman energy term to the energy $\mathcal{E}$. We skip the calculation and show the result for two interesting special cases for the $\Gamma_4$ state: A field $H_c$ applied along the $c$-axis and a field $H_a$ applied along the $a$-axis. For $H_{ext} = H_c$ as shown by Herrmann [164], we obtain

$$\tan(2\gamma) = \frac{\mathcal{D} + A_{ac} + H_c}{\mathcal{J} + A_{aa} - A_{cc}}. \tag{A.8}$$

Our simple model suggest that an external magnetic field along $c$ increases the canting angle monotonically when it is applied in the direction of the magnetization. Minimizing $\mathcal{E}$ with respect to $\beta$ shows that the direction of $M$ does not change its direction in the $\Gamma_4$ state.

Applying an external field $H_a$ leads to a 90° rotation of **M** and **N**, when the field exceeds [136, 144, 176]

$$H_x > \frac{1}{2}\left(-H_D + \sqrt{H_D^2 + 8 H_e H_{K2}}\right) = H_{sf}. \tag{A.9}$$

In the cited calculations, the term $A_{ac}$ has been assumed to be much smaller than $\mathcal{D}$ and therefore been set to zero as suggested by [73]. $H_{K2}$ is the anisotropy field equal to $(A_{aa} - A_{cc})$. The critical field $H_{sf}$ is called spin-flop field or spin-reorientation field. The spin reorientation does not appear as a abrupt transition as for example seen e.g. in hematite [78] or $MnF_2$ [79], but happens gradually. This means that already small magnetic fields of a few T can lead to a reorientation within the $ac$-plane of **N** and **M** by a few degrees. Measurements at $YFeO_3$ (YFO) [144] and $ErFeO_3$ (EFO) [177] have shown this experimentally. In these samples, the reorientation takes place over a magnetic field range from 0 to around 8 T for YFO and, depending on the temperature of the EFO, between 0 and 6.5 T at 130 K and between 0 and 10 T at 270 K.

We have seen that the magnetization of orthoferrites can be rotated by 90° with a sufficiently large field applied along the $a$-axis. The sample is then in the $\Gamma_2$ state ($G_z C_y F_x$ [75]).

In some orthoferrites this magnetic transition appears even without an external field, but when lowering the temperature. This happens for some orthoferrites with a paramagnetic RE ion (e.g. RE = Sm, Er, Tm) [71, 189]. In this temperature-induced spin reorientation transition (SRT) **M** (**N**) rotates continuously over a finite temperature range from $c$-axis ($a$-axis) [$\Gamma_4$ state] to the $a$-axis ($c$-axis) [$\Gamma_2$ state]. This can be formulated by a temperature dependence of the magnetocrystalline anisotropy. To describe

| RE ion | $T_N$ (K) | $\gamma$ (mrad) | $H_{sf}$ | SRT |
|---|---|---|---|---|
| Dy | 645 [74] | 8.0 [74] | 270 K: 9.3 T [178]<br>130 K: 6.5 T [178]<br>77 K: 4.5 T [178] | 40 K: $\Gamma_4$ to $\Gamma_1$ [179] |
| Er | 639 [74] | 8.1 [74] | 273 K: 10.0 T [180]<br>140 K: 6.3 T [180] | 95 K...85 K: $\Gamma_4$ to $\Gamma_2$ [137] |
| Eu | 662 [74] | 8.0 [74] | 4.2 K: 6.7 T [181] | - |
| Gd | 657 [74] | 9.8 [74] | 293 K: 7.6 T [182]<br>77 K: 8.1 T [182]<br>4.2 K: 1.2 T [182] | - |
| Ho | 639 [74] | 8.2 [74] | 293 K: 8.1 T [180]<br>140 K: 4.4 T [180]<br>77 K: 1.7 T [180] | 58 K...49 K: $\Gamma_4$ to $\Gamma_2$ [183] |
| La | 740 [74] | 9.1 [74] | ? | - |
| Lu | 600 [184] | 10.7 [142] | 300 K: >20 T [80] | - |
| Nd | 687 [74] | 8.5 [74] | ? | 170 K...100 K: $\Gamma_4$ to $\Gamma_2$ [183] |
| Pr | 707 [74] | 8.5 [74] | 300 K: 12 T [80] | 200 K...172 K: $\Gamma_4$ to $\Gamma_2$ [185] |
| Sm | 674 [74] | 8.2 [74] | 300 K: 6.8 T [80] | 478 K...450 K: $\Gamma_4$ to $\Gamma_2$ [186] |
| Tb | 647 [74] | 7.8 [74] | 300 K: 7.0 T [80] | 8 K...6.8 K: $\Gamma_4$ to $\Gamma_2$ [187] |
| Tm | 632 [74] | 8.0 [74] | 300 K: 11.0 T [80] | 94 K...82 K: $\Gamma_4$ to $\Gamma_2$ [72] |
| Y | 640 [74] | 8.9 [74] | 293 K: 6.5 T [144]<br>4.2 K: 7.7 T [144] | - |
| Yb | 627 [80] | 8.9 [74] | 300 K: >20 T [80] | 7.8 K...6.5 K: $\Gamma_4$ to $\Gamma_2$ [188] |

Table A.1.: List of orthoferrites ordered by rare earth ion. $T_N$ is the Néel temperature, $\gamma$ the canting angle, $H_{sf}$ the spin-flop field and SRT the spin reorientation transition.

this phenomenon properly, a fourth order anisotropy is introduced [190], which can be written as $E_{K4} = K_4(m_{1c}^4 + m_{2c}^4)$. To make calculations easier, the Hamiltonian can be transferred to Landau theory [191]. The free energy is then expressed as

$$F(T) = F_0 + \frac{1}{2}K_2(T)\cos(2\beta) + K_4\cos(4\beta),$$

where $F_0$ summarizes all terms independent from $\beta$. Minimizing the expression with respect to $\beta$ lets one identify the energy minima which are

$$\begin{aligned} I &: \beta = 0^\circ \text{ for } K_2(T) < -8K_4,\ \mathrm{T} \geq \mathrm{T}_2 \\ II &: \beta = 90^\circ \text{ for } K_2(T) > 8K_4,\ \mathrm{T} \leq \mathrm{T}_1 \\ III &: \cos(2\beta) = -\frac{K_2}{8K_4} \text{ else, } \mathrm{T}_1 \leq \mathrm{T} \leq \mathrm{T}_1. \end{aligned} \tag{A.10}$$

As already indicated in the equations A.10, one can model the SRT with a temperature-independent anisotropy constant $K_4$ and a temperature-dependent anisotropy constant $K_2$, which changes sign within the transition.

For the sake of completeness it is to be mentioned that a third magnetic state besides $\Gamma_2$ and $\Gamma_4$ is possible for orthoferrites. In the $\Gamma_1$ ($A_xG_yC_z$) the spins order along the $b$-axis forming a collinear antiferromagnet. The $\Gamma_4 \rightarrow \Gamma_1$ transition can be observed for example in $DyFeO_3$ [71]. The $\Gamma_1$ state is beyond the scope of this work as it is not observed in the orthoferrite investigated here.
For all rare earth orthoferrites, the RE-RE interaction is relatively weak so that they do not couple magnetically at temperatures above 10 K. However, besides the increase of susceptibility as mentioned before, the overall magnetization is altered. The effective field from the iron magnetization at the RE site induces a polarization of the RE ions. Since the behavior is like a paramagnet in an external field, the additional magnetization has a $\frac{1}{T}$ dependence. The overall magnetization can be written as $m_{tot} = m_{Fe}(1 + d/T)$ [74], where $m_{Fe}$ is the canted moment by the iron ions, $T$ the temperature of the sample and $d$ is a pre-factor that can be positive or negative, depending on the RE and the magnetic phase. Table A.1 summarizes some of the parameters described in this section for several orthoferrites.

## A.2. Trajectory of $\mathrm{M}$ and $\mathrm{N}$ for a field-induced SRT from $\Gamma_2$ to $\Gamma_4$ in TFO

The following figures show three out of four possible field-induced $\Gamma_2 \Rightarrow \Gamma_4$ transitions. The remaining is given in the main text in section 5.4.1. The initial and final orientation of **M** and **N** is given in (a) of each figure. (b) shows the SMR response for a $R_{1,n} = 1$, $R_{1,m} = 0$ (N-SMR) and for $R_{1,n} = 0$, $R_{1,m} = 1$ (M-SMR).

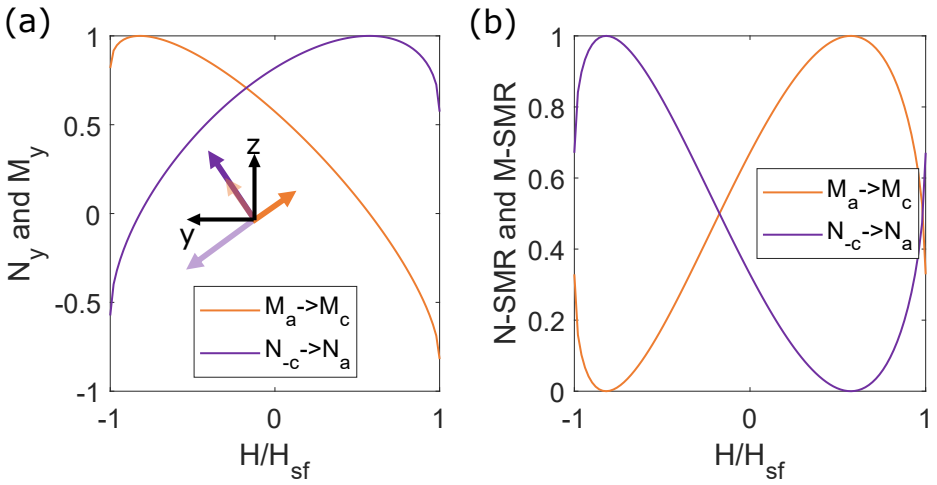


Figure A.1.: (a) Normalized $y$-contribution of **M** and **N** during the spin reorientation transition. The inset sketches the field-dependent rotation of **M** (orange) and **N** (purple) until the spin reorientation field $H_{sf}$ relative to the coordinate system of the Hall bar (black). (b) Relative change to the M- and N-dependent SMR, respectively.

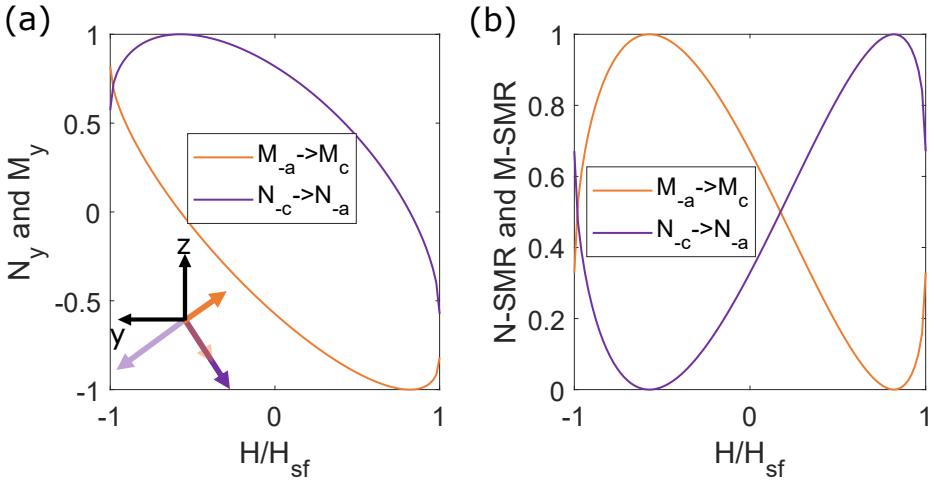


Figure A.2.: (a) Normalized $y$-contribution of **M** and **N** during the spin reorientation transition. The inset sketches the field-dependent rotation of **M** (orange) and **N** (purple) until the spin reorientation field $H_{sf}$ relative to the coordinate system of the Hall bar (black). (b) Relative change to the M- and N-dependent SMR, respectively.

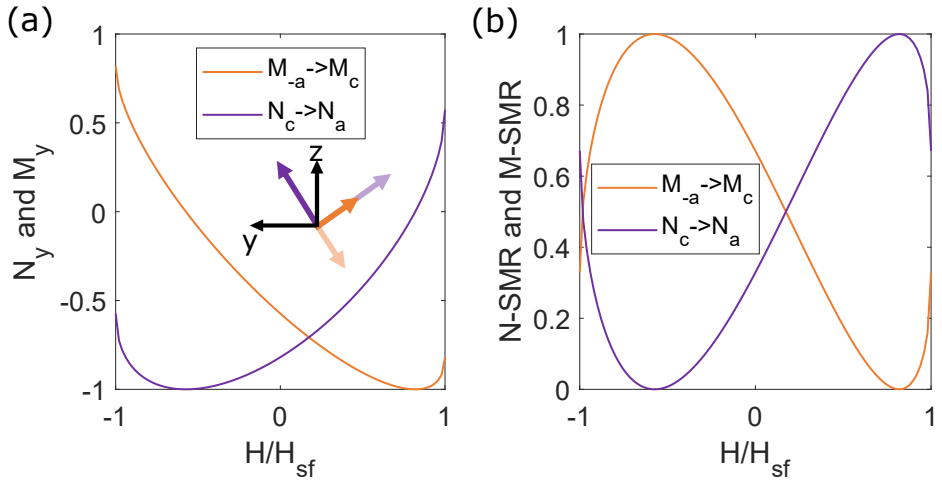


Figure A.3.: (a) Normalized $y$-contribution of **M** and **N** during the spin reorientation transition. The inset sketches the field-dependent rotation of **M** (orange) and **N** (purple) until the spin reorientation field $H_{sf}$ relative to the coordinate system of the Hall bar (black). (b) Relative change to the M- and N-dependent SMR, respectively.

## A.3. Trajectory of M and N for a field-induced SRT from $\Gamma_4$ to $\Gamma_2$ in TFO

The following figures show all four possible field-induced $\Gamma_4 \Rightarrow \Gamma_2$ transitions. The initial and final orientation of **M** and **N** is given in (a) of each figure. (b) shows the SMR response for a $R_{1,n} = 1$, $R_{1,m} = 0$ (N-SMR) and for $R_{1,n} = 0$, $R_{1,m} = 1$ (M-SMR).
Fig. A.8 shows all four possible SRTs in (a) as a sketch. In (b), a linear combination of the SMR effect of all four possible domain is given.

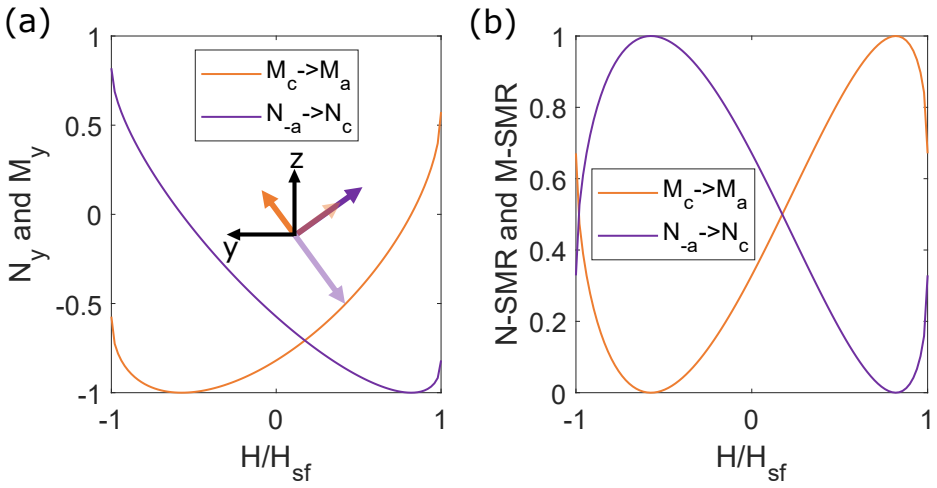


Figure A.4.: (a) Normalized $y$-contribution of **M** and **N** during the spin reorientation transition. The inset sketches the field-dependent rotation of **M** (orange) and **N** (purple) until the spin reorientation field $H_{sf}$ relative to the coordinate system of the Hall bar (black). (b) Relative change to the M- and N-dependent SMR, respectively.

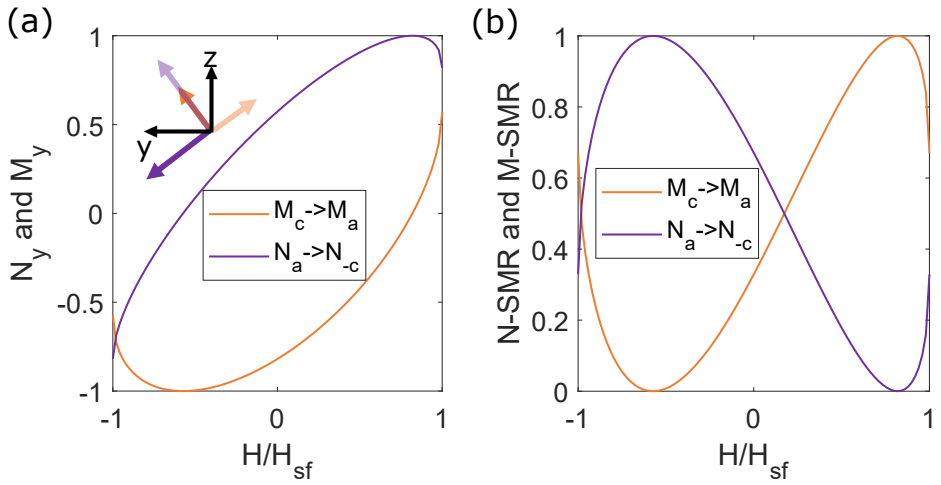


Figure A.5.: (a) Normalized $y$-contribution of $\mathbf{M}$ and $\mathbf{N}$ during the spin reorientation transition. The inset sketches the field-dependent rotation of $\mathbf{M}$ (orange) and $\mathbf{N}$ (purple) until the spin reorientation field $H_{sf}$ relative to the coordinate system of the Hall bar (black). (b) Relative change to the M- and N-dependent SMR, respectively.

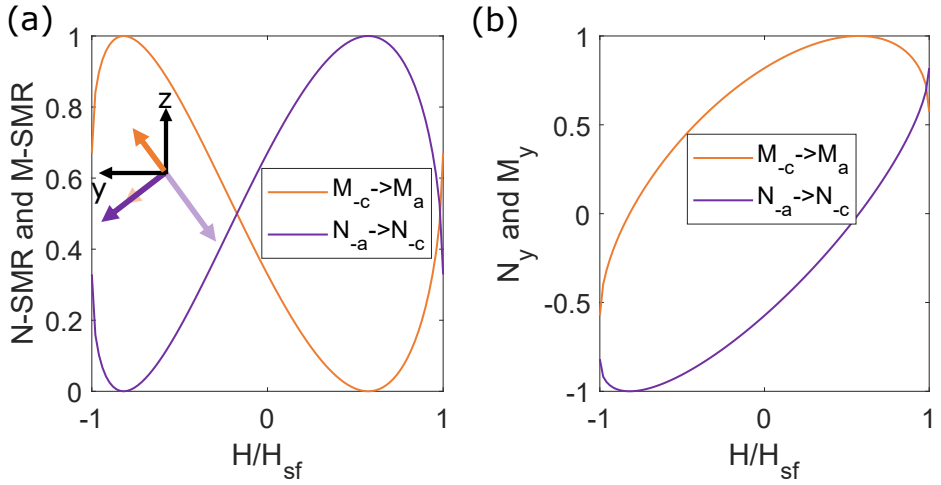


Figure A.6.: (a) Normalized $y$-contribution of $\mathbf{M}$ and $\mathbf{N}$ during the spin reorientation transition. The inset sketches the field-dependent rotation of $\mathbf{M}$ (orange) and $\mathbf{N}$ (purple) until the spin reorientation field $H_{sf}$ relative to the coordinate system of the Hall bar (black). (b) Relative change to the M- and N-dependent SMR, respectively.

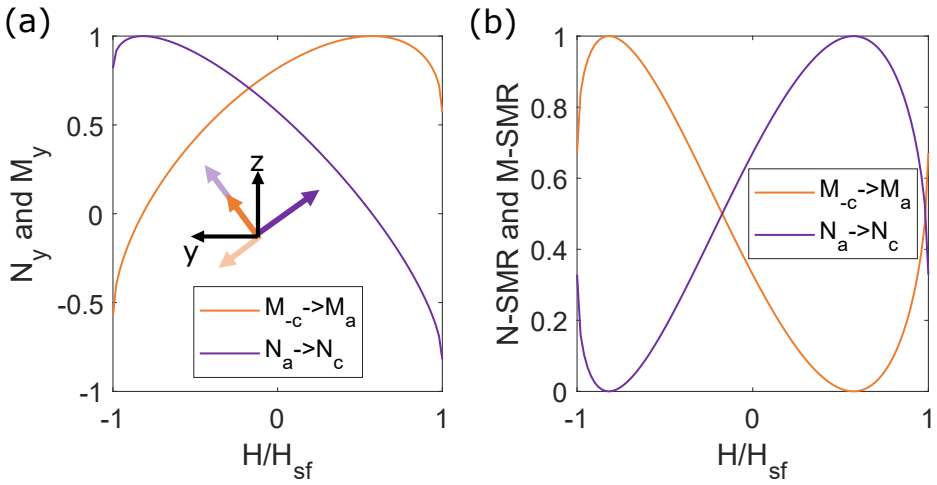


Figure A.7.: (a) Normalized $y$-contribution of **M** and **N** during the spin reorientation transition. The inset sketches the field-dependent rotation of **M** (orange) and **N** (purple) until the spin reorientation field $H_{sf}$ relative to the coordinate system of the Hall bar (black). (b) Relative change to the M- and N-dependent SMR, respectively.

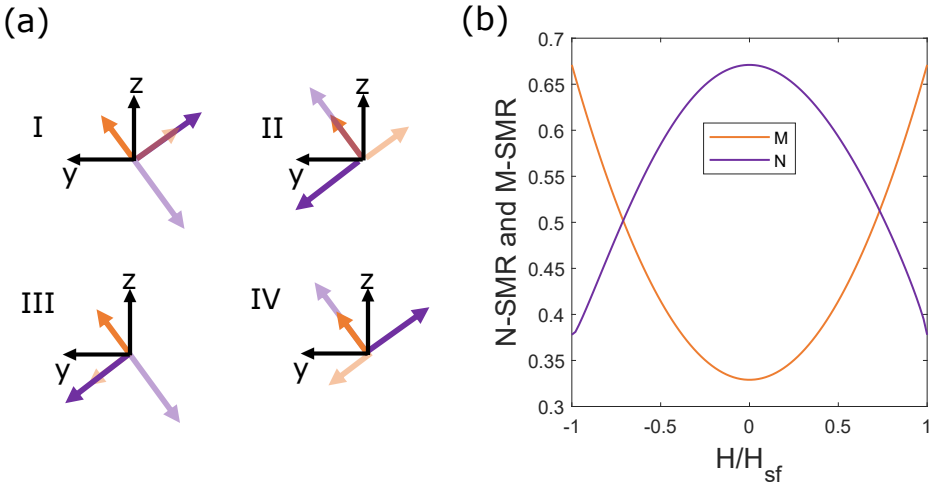


Figure A.8.: (a) Sketch of all four possible cases for the orientation of **M** and **N** during the spin reorientation transition. **M** (orange) depicts the magnetization and **N** (purple) the Néel vector in the $\Gamma_4$ state (pale) at $\mathbf{H} = 0$ and in the $\Gamma_2$ state at $\mathbf{H} = H_{sf}$ relative to the coordinate system of the Hall bar (black). (b) Averaged over all four possible domains: Relative change to the M- and N-dependent SMR, respectively.

## A.4. SMR measurements at bulk TFO in a rotating magnetic field

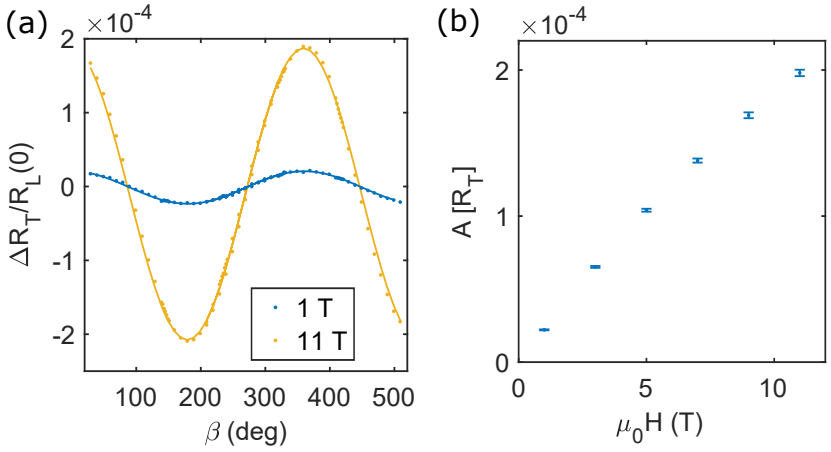


Figure A.9.: (a) Example curves for the behavior of relative transverse resistivity depending on the angle $\beta$ of magnetic field measured at 300 K. (b) Amplitude $A$ of the relative transverse resistivity extracted from the fit curve increasing monotonically with applied magnetic field. Error bars are given only by the uncertainty of the fit and do not contain other sources of error.

We perform rotation measurements at 300 K. At this temperature, the TFO is in the $\Gamma_4$ state. The Néel vector $\mathbf{N}$ is oriented along the crystallographic $a$-axis while the canted moment $\mathbf{M}$ points along the $c$-axis. A fixed magnetic field is rotated in the crystallographic $ac$-plane around the angle $\beta$, corresponding to an out-of-plane rotation perpendicular to the current in the $xy$-plane. At $\beta = 0°$, the field is applied perpendicular to the sample surface. The measurement is repeated for several fields between 1 and 11 T and transverse as well as longitudinal resistivity are measured simultaneously as described in section 3.6. To compensate for temperature fluctuations in the longitudinal resistivity $R_L$, we perform a linear drift correction. The transverse resistivity $R_T$ on the other hand is not being corrected since it is less sensitive to temperature fluctuations.
The transverse resistivity $R_T$ shown in Fig. A.9 (a) for two example fields is given as relative to the 90°-value and normalized to the longitudinal resistivity $R_L$ at 0°. $\beta = 0°$ corresponds to the out-of-plane direction. We choose the normalization like this because the dominant signal stems from the ordinary Hall effect (OHE). The OHE is minimum when $H_z$ is minimum, i.e. at $\beta = 90°$. We write $\frac{R_T(H)-R_T(90°)}{R_L(0°)}$ more compactly as $\frac{\Delta R_T}{R_L(0)}$ and refer to it as $R_T$ as it obeys the same shape as the raw signal and improves the readability of this thesis.
The data points can be fitted by $A \cdot \cos(x + B) + C$ as expected for the OHE dominat-

ing the signal, described in section 1.6.1. The amplitude increases monotonically with magnetic field as shown in Fig. A.9 (b). We observe a small deviation from the purely linear OHE. At high magnetic fields the amplitude tends to be decreased from the linear evolution with field. This indicates that there might be a second contribution to $R_T$.
Other effects that contribute to the transverse resistivity in this measurement geometry are Hanle magnetoresistance, HMR (see section 1.6.3), and spin Hall magnetoresistance, SMR (see section 1.6.2). While HMR also contributes linearly with magnetic field and could not be distinguished from OHE, the transverse SMR depends on the $z$ component of the magnetic moment, which has in general a more complex dependence on **H** (SHAHE). We note that the transverse SMR also depends on $M_xM_y$ and $N_xN_y$. However these dependencies can be discarded here since **N** and **M** are expected only to rotate in the crystallographic $ac$ plane, which coincides with the $yz$-plane of the Hall bar. Therefore, at no time and independent from the magnetic state of TFO, an $M_x$ or an $N_x$ component is to be expected. We can therefore focus on the $M_z$ component, only.
From SQUID measurements, we know that a relatively small field of a few mT is sufficient to reorient **M** parallel or antiparallel to $c$ at 300 K. However, to align it with the $a$-axis, larger fields are needed. A small field applied along the crystallographic $a$-direction leads to a small tilting only, as described in section 2.2. Increasing the magnetic field in rotation measurements causes an increase of the angle of **M** with the crystallographic $c$ axis. Once the spin-flop-field $H_{sf}$ is reached, **M** follows **H** in the entire $ac$-plane. The amplitude of the orientation angle does not necessarily change in a linear fashion with the applied magnetic field as demonstrated for $ErFeO_3$ [177] and $YFeO_3$ [144] in Mößbauer experiments. This may lead to a non-linear evolution of the $M_z$ component and may explain the small deviation from the linear behavior. Further increase of the signal due to SMR would be achieved by an increase of $M_z$ due to an increasing canting angle $\gamma$ of the Fe sublattices. Therefore, it is expected that the amplitude $A(H)$ in rotation measurements changes slope when reaching $H_{sf}$. Below $H_{sf}$, the signal increases due to OHE + increasing reorientation angle of **M**. Above $H_{sf}$, the signal increases due to OHE + increase of canting angle. To observe this, larger magnetic fields would be necessary in this measurement geometry since it is expected that $H_{sf}$ is at the very border of our field range at 11 T for TFO at 300 K [80]. Further insight would also give a TFO crystal with a different orientation, which will be the subject of future studies.
We subtract the cosine fit from the data to inspect further contributions to the transverse resistivity. This allows us to identify a signal with another symmetry than pure cosine. As shown in Fig. A.10 (a) for an example curve measured at 11 T, we indeed identify a contribution to the transverse resistivity, which is asymmetric with the applied field. To understand this better, we plot the signal for positive and negative magnetic field against the real angle $\beta$, which means that here, we do not perform the correction described in section 3.6 for positive and negative fields. Thereby, we can directly compare the signal for both field directions. For both field directions, we see a $\pi$-periodic residual signal and different signs for the two field directions. We are

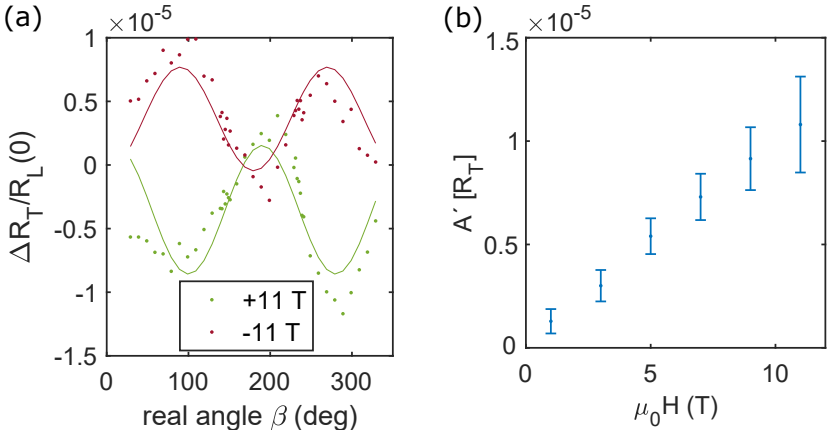


Figure A.10.: (a) Example curves for the relative transverse resistivity in $\beta$-scans after subtraction of a cosine fit. The term real angle refers to the actual position of the rotator without corrections performed. (b) Mean absolute amplitude of the residual signal for different external field amplitudes.

able to fit a function of the form $A' \cos^2(\beta + B) + C$ to every data set. Despite the low amplitude of the signal the goodness of fit still shows values between $R^2 = 0.6$ and $R^2 = 0.8$. Only for the 1 T curve the $R^2$ drops below 0.4 due to the small signal-to-noise ratio. The amplitude of the signal increases monotonically with magnetic field as shown in Fig. A.10 (b).

The $\propto \cos^2(\beta)$-dependence rules out a contribution to the signal stemming from the $z$-component of the magnetization due to spin Hall anomalous Hall effect (SHAHE) [43]. For this effect a $2\pi$-periodic signal is expected. One may argue that the residual signal might stem from a misalignment between the $x$-axis and the magnetic field $\mathbf{H}$ (not perpendicular). Indeed, if the magnetic field has a component $H_x \neq 0$, HMR would contribute by $\propto H_x H_y$ according to equation 1.14. Also, if the magnetic moment is dragged out of the $ac$-plane, SMR would additionally contribute by $\propto M_x M_y$ according to equation 1.9. In Fig. A.11 we illustrate the misalignment of $\mathbf{H}$ with the $ac$ plane. The case is shown, that the sample is rotated on the sample holder around the $z$-axis such that a magnetic field possesses a $H_y$ and an additional $H_x$ contribution in the reference frame of the Hall bar. If the surface is parallel to the magnetic field, this gives the maximum $H_x H_y$ contribution, which leads to a contribution to $R_T$ by HMR. When the sample is rotated by 180°, the field has now a contribution of $-H_y$ and $-H_x$ so that according to $(-H_x)(-H_y) = H_x H_y$, this would lead to the same sign of the residual signal. Indeed, a rotation of the sample by 180° leads to the same signal as seen in Fig. A.10 (a). However, the rotation of the sample leads to the same geometry as reversing the magnetic field. From this consideration, a field in positive direction should give the same signal as a field applied in the opposite direction. This is not seen in our data as the signal changes sign when reversing the field. We note that misalignment due to rotation around the other axes than the $z$-axis as discussed

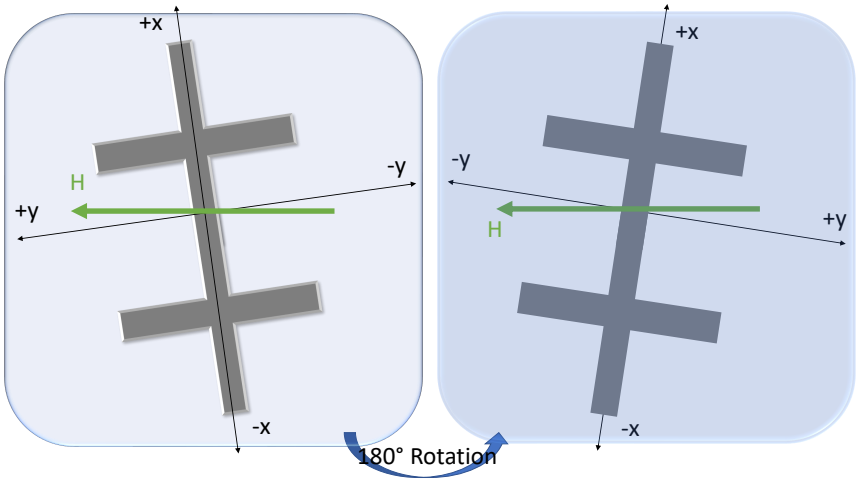


Figure A.11.: Illustration of magnetic field being misaligned with the crystallographic *ac* plane of the TFO sample. Note that the *ac*-plane coincides with the *xy*-plane of the Hall bar. The situation is shown for two cases, separated by a 180° rotation of the sample.

here lead to a similar behavior (rotation around $y$) or just an arbitrary phase to the signal (rotation around $x$). A simple misalignment can therefore not explain the signal in our experiments due to the equivalence of a sample rotation and a field rotation. Even when considering magnetothermal effects like spin Seebeck effect or anomalous Nernst effect due to resistive heating of the Pt Hall bar, the asymmetric signal cannot be explained. It must stem from the spin structure which is in fact more complicated than introduced in section 2.2 [1]. To understand this, four magnetic Fe sublattices have to be introduced with three DMI vectors describing the canting in all directions [172]. These considerations allow for a non-symmetric behavior under reversion of magnetic field. However, these considerations are out of scope of this work and require deep theoretical description of the spin system. We focus now on the longitudinal resistivity $R_L$, which is shown for two magnetic fields in Fig. A.12 (a). Assuming solely the model of SMR one would expect a $\propto \cos^2(\beta)$-dependence in case of sensitivity to the canted moment $\mathbf{M}$, if $\mathbf{M}$ follows strictly the direction of the external magnetic field $\mathbf{H}$. On the other hand, a $\propto \sin^2(\beta)$-dependence is expected in case of sensitivity to the Néel vector $\mathbf{N}$, if $\mathbf{N}$ rotates with a phase shift of 90° to $\mathbf{H}$ in the *ac*-($yz$)-plane (see 1.6.2). This is expected since, although the Zeeman energy allows for $\mathbf{N}$ to orient in any direction perpendicular to $\mathbf{H}$, the large anisotropy in TFO suggests only a rotation in the *ac*-plane. However, for TFO, this is only expected for magnetic fields $\mathbf{H} > H_{sf}$. For smaller fields, a complete spin rotation is not expected.
$R_L$ has been normalized to the resistance at $\beta = 0°$ as $\Delta R_L/R_L(0) = \frac{R_L(\beta)-R_L(\beta=0°)}{R_L(\beta=0°)}$. The function $A \cdot \cos^2(\beta + B)$ has been fitted to the normalized data. The amplitude

[1] private communications with O. Gomanay

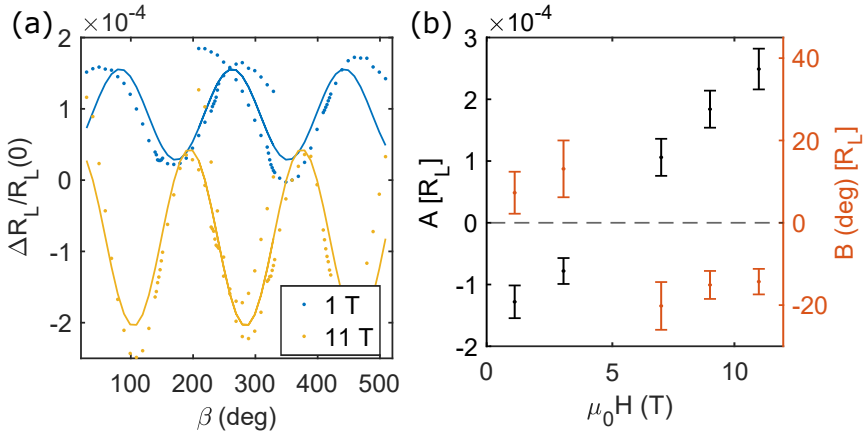


Figure A.12.: (a) Example curves for the relative longitudinal resistivity in $\beta$-scans. (b) Amplitude $A$ (black) and phase $B$ (red) of the relative longitudinal resistivity against magnetic field.

$A$ and the phase $B$ is shown in Fig. A.12 (b). We observe a $\propto -\cos^2(\beta)$-dependence for low magnetic fields, which is equal to a $\propto \sin^2(\beta)$-dependence taking into account the arbitrary normalization relative to $R_L(0°)$. At large magnetic fields, a $\propto \cos^2(\beta)$-dependence is observed. Similar behavior has been observed for SMR measurements performed at the ferrimagnet $Gd_3Fe_5O_{12}$ (GIG) in its canted phase [192] and the chiral magnet $Cu_2OSeO_3$ (CSO) [159], but so far not for a canted antiferromagnet. While for GIG, the origin of the sign change in SMR roots in different ordering of Iron and Gadolinium sublattices, in CSO the sign change occurs in its conical state and appears at a distinct cone angle, where the projection of the moments along the field exceeds a critical value. However, in the whole range of CSO, the dependence of the SMR is given by the local magnetization averaged over the area under the Hall bar. In our case, the mechanism is different. We observe a competition between Néel order dependence and magnetization dependence. Up to now, there is no report on a material that exhibits a dependency on **N** and **M** in the same magnetic phase. We combine formulas 1.10 and 1.11 in formula 5.1. Here, $\Delta R_{1,m}(H)$ and $\Delta R_{1,n}$ are the field-dependent pre-factors determining the sensitivity of the longitudinal SMR to the **M** and **N**. Our measurements suggest a linear behavior of the two pre-factors with external magnetic field.

We note that there are more MR effects which have not been taken into account so far. Regarding OMR as an additional effect, this would contribute by $\propto \cos(\beta)^2$ like "positive" SMR because of the asymmetric cross section of the Hall bar [15]. With increasing field, the OMR has shown to increase superlinearly [37], while the combination of SMR and OMR increases almost linearly in Pt/CFO layers in a certain thickness range of the Pt layer [37]. And yet, both signals contribute on the same scale so that none of them dominates the signal. To distinguish SMR from OMR in this experiment, more samples with varying Pt thicknesses would be needed and are

the object of future investigations.
HMR is expected to have the same shape as SMR and since the magnetization of TFO is not saturated due to the slowly increasing canting angles, it is expected that HMR cannot be distinguished from SMR in this measurement.
AMR as a further MR effect is not expected to be visible in the measurement geometry. While it is in principle possible to observe proximity-induced magnetization in Pt [193], here, the magnetic field is always perpendicular to the charge current.
In addition to the sign change of $A$, there is a phase to the signal of around $B = 10°$ to $20°$ for $H < 5\,\mathrm{T}$ and $B = -15°$ to $-20°$ for $H > 5\,\mathrm{T}$. The phase changes sign together with the amplitude $A$. The occurrence of a phase can only be explained by a magnetic contribution from the TFO layer being out of phase with the external magnetic field, since every effect that could be observed in a free standing Pt wire would depend directly on **H** and could therefore not possess a phase shift. The origin of this phase shift might be the large uniaxial anisotropy in TFO, the large DMI fields or a contribution from the Tm moment, which could be investigated by performing the measurement at different temperatures and by rotation measurements within the two remaining planes.
However, due to the difficulties in performing rotational measurements, we focused on performing uniaxial measurements with the field applied along the magnetic easy and intermediate axes to reduce the torque on the sample. We figured out that in the vicinity of the SRT, a relatively small magnetic field is sufficient to induce a field-induced spin reorientation.

## A.5. Determination of critical fields from electrical measurements performed at TFO bulk samples

Different approaches have been utilized to determine the critical fields in the transverse and longitudinal resistivity for the SMR measurements performed on bulk TFO samples.
For the transverse resistivity, the S-shape curve has been parted in three segments. The low-field region and two high-field regions at large positive and negative fields, where the resistivity change is close to linear, respectively. A linear function has been fitted to every segment. The two crossing points of the low-field fit with the other two determines the critical field $H_c$. An example curve is shown in Fig. A.13 (a).
For the longitudinal resistivity, another technique has been utilized since the resistivity does not change linearly. Because of the relatively low density of data points compared to the magnitude of $H_{sf}$ close to the spin reorientation temperatures, the data points have been interpolated by cubic splines. Between the zero-field value and the most outer points at $\pm 11\,\mathrm{T}$ a line has been drawn. The largest distance between the line and the smoothed data has been determined, which gives a value for $H_{sf}$. An example curve is shown in Fig. A.13 (b).

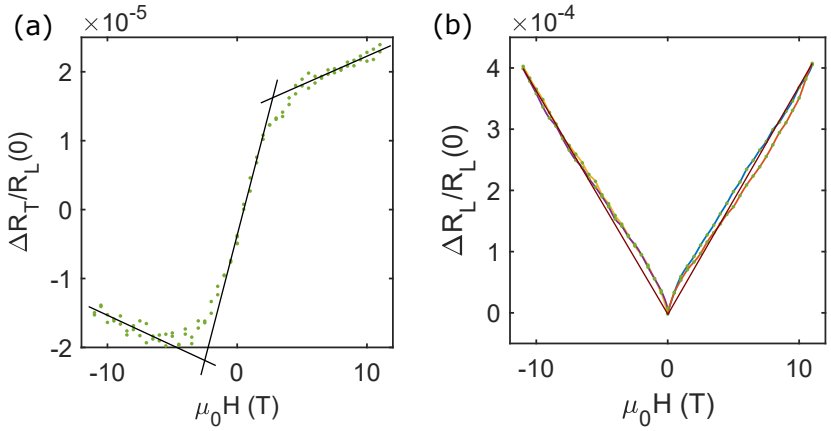


Figure A.13.: (a) Example curve for transverse resistivity in dependence of magnetic field applied along the $a$-axis. The curve is parted in three segments. For each segment a linear function (black) is fitted to the data points (green). (b) Example curve for longitudinal resistivity in dependence of magnetic field applied along the $a$-axis. The data points (green) are interpolated by cubic splines (Blue, orange, purple and yellow). The distance of the interpolated data and a straight line (red) is taken as $H_{sf}$.

## A.6. Non-local spin transport in bulk TFO

The TFO single crystal has been further investigated with regard to its spin transport properties. It has been shown before that magnons can travel large distances in the canted antiferromagnet hematite [34, S2] and the insulating ferrimagnet YIG [4, 194]. Very recently, we could also demonstrate that the canted antiferromagnet $YFeO_3$ is an efficient magnon conduit although the mechanisms are drastically different from those seen in hematite despite the similar crystal and magnetic structures [S8]. It is up to now unclear whether other insulating antiferromagnets exhibits similar properties.
Since TFO is a related compound to hematite and $YFeO_3$, the crystal has been prepared to perform non-local transport measurements at various temperatures. Therefore, Pt stripes have been defined along the crystallographic *b*-axis on the surface using lithography methods (see Sec. 3.6). The width of each stripe is 250 nm. For the experiment, two parallel platinum stripes are used. The patterning of the non-local structures was performed by Andrew Ross while the electrical measurements where done by Sven Becker and Andrew Ross.
When sending a current through one (injector), SHE leads to a spin accumulation at the Pt/TFO interface. The interaction between the spin accumulation and the magnetic order of the TFO does not only lead to the change of resistivity due to SMR, but also to an injection of spin current into the TFO. The spin current leads to excitation of the TFO spin system. These collective spin excitations are called magnons (see Sec. 1.5). The additional magnons cause an imbalance of local occupation and therefore travel diffusely through the crystal. If these magnons reach the neighboring Pt stripe (detector), they act as a perpendicular spin current in the Pt, which is converted into a charge current by ISHE. Varying the distance between the Pt allows one to conclude on the propagation length of the magnons in TFO. In canted antiferromagnets, two types of magnons are present, quasi ferromagnetic (qFM) and quasi antiferromagnetic (qAFM) ones. Both of these can principally contribute to the transport of angular momentum across the crystal.
Another family of effects, that are observed in this measurement geometry are thermal effects like the spin Seebeck effect (SSE) (see Sec. 1.7.1), which describes thermal excitation of magnons [52]. Here, the excitation happens by resistive heating of the injector due to the charge current passing through the Pt. The heat is transported to the TFO, where a heat gradient across the crystal causes the diffusion of magnons. This process is driven by the thermal occupation of magnons and a resulting imbalance across the crystal. These magnons also cause a current in the detector via ISHE. The difference between these two sources of magnons is that for the SSE, it is not important in which way the current flows through the injector since the creation relies only on the heating process. For hematite, preferably the qFM modes where excited due to the SSE. On the other hand, by the SHE, polarized magnons dependent on the spin accumulation are created. Thereby, a change of sign is observed in the detector when reversing the current direction, which is not the case for magnons generated by SSE. We can thereby distinguish electrical and thermal spin injection by reversing the current direction in the injector. We introduce the non-local voltage due to the

electrically generated magnons as

$$V_{el} = (V_{I+} - V_{I-})/2$$

and the non-local voltage due to the thermal generation of magnons as

$$V_{th} = (V_{I+} + V_{I-})/2$$

where $V_{I+}$ ($V_{I-}$) is the voltage measured at the detector for the different current directions in the injector. We normalize the voltage to the current passing through the injector with respect to the the origin as [34]

$$R_{el} = V_{el}/I \qquad\qquad R_{th} = V_{th}/I^2.$$

Fig. A.14 shows two example curves measured at two different devices with a Pt wire separation of 350 and 400 nm distance at a temperature of 76 K. Panel (a) shows the field-dependent electrical and thermal signal for a magnetic field applied in the crystallographic $c$-direction for the 350 nm-device. Panel (b) shows the same for a magnetic field applied in $a$-direction. In both measurement geometries, the $R_{el}$ does not show any dependence on applied magnetic field. This indicates that the magnons are unable to travel large distances in this TFO crystal.
Magnetic damping might lead to the suppression of long-distant spin transport in TFO. Compared to $YFeO_3$ ($\alpha = 0.0003$) [195], where long-distant spin transport has now been observed [S8], TFO possesses an additional magnetic sublattice occupied by Tm moments. These may lead to additional damping and can disrupt the mode mixing and it is not clear how the polarised moment affects the mode polarisation. However, we note that long-distant spin transport in ferromagnets was mostly observed when the spin accumulation, magnetization vector, and propagation direction are collinear [4]. It might therefore be beneficial to investigate different growth orientations of TFO. Future experiments might also focus on other orthoferrites with non-magnetic RE-ion, like Lu and La.
With regard to the thermal signal, $R_{th}$ decreases linearly as shown by the orange curves in Fig. A.14 (a) and (b) for the wire-separation of 350 nm. According to the SMR measurements, a magnetic field of $H = 1.5$ T applied in $c$-direction would lead to the spin-reorientation, while a field of only a few mT applied in $a$-direction would lead to the 180° switch of **M** as seen in SQUID. There is no correlation between the magnetic properties of the TFO and $R_{th}$. In a second experiment on a different device, the position of injector and detector are swapped. The field-dependence of $R_{el}$ and $R_{th}$ are shown in Fig. A.14 (c) and (d). Here, the wire separation is 400 nm. Again, we do not observe any sensitivity of $R_{el}$ to the magnetic field for both measurement geometries. On the other hand, $R_{th}$ increases linearly with magnetic field. We note that the change of slope does not correlate with the wire separation, but with the relative orientation of injector and detector. This indicates that the dominating signal origins in an in-plane temperature gradient in $y$-direction (perpendicular to the wires), which switches sign when changing the position of detector and injector.

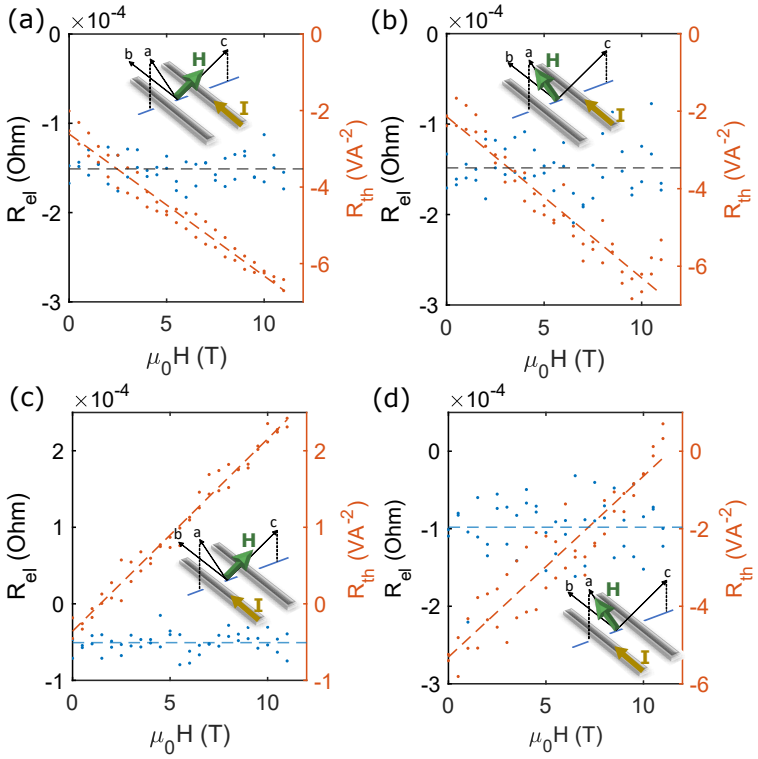


Figure A.14.: Non-local signals from thermal and electrical origin measured at 76 K in the $\Gamma_2$ phase. (a) Magnetic field applied along the crystallographic $c$-direction. (b) Magnetic field applied along the crystallographic $a$-direction. The inset depicts the respective measurement geometry. The broken lines are mean values (blue) and linear fits to $R_{th}$ (red). The distance between injector (right) and detector (left) is 350 nm. (c) - (d) Same temperature and measurement geometry as (a) and (b), respectively. Here, the wire separation is 400 nm and injector and detector position are swapped.

Summarizing, the TFO (101) single crystal investigated here, does not show hints for long-distant magnon conduction. While these properties have been found in hematite [34, S2] and $YFeO_3$ [S8], the additional magnetic contribution by the Tm sublattice might increase the Gilbert damping in TFO. While this is still to be confirmed by the investigation of different crystallographic orientations of the single crystal, there are more promising candidates among the family of orthoferrites, like $LaFeO_3$ and $LuFeO_3$.

## A.7. SHAHE contribution in rotation measurements of STO/TFO thin films

Rotation measurements have been performed on STO/TFO samples around the $\gamma$- and $\beta$ plane. In these measurements the out-of-plane component of the magnetic field leads to a dominating signal stemming from the OHE, which increases linearly with applied magnetic field. The rotation measurements have been performed at 20 K and 200 K in the $\Gamma_2$ and $\Gamma_4$ phase of TFO, respectively. At each temperature, magnetic fields between 1 and 11 T have been applied during the rotation. Fig. A.15 shows the amplitudes of the transverse resistivity $R_T(\gamma)$ extracted from fitting a $\propto \cos(\gamma)$-function to each measurement curve. The error bars indicate the uncertainty of each fit. In red, a linear fit is indicated to which only the data point in blue contribute. The data point in yellow have been excluded from the linear fit to indicate the contribution from SMR saturating at around 4 T at 200 K. The contribution from SMR manifests in a zero-field offset of the linear fit.
Fig. A.16 shows the same measurements and calculations discussed in the previous paragraph for rotation measurements in the $\beta$-plane.

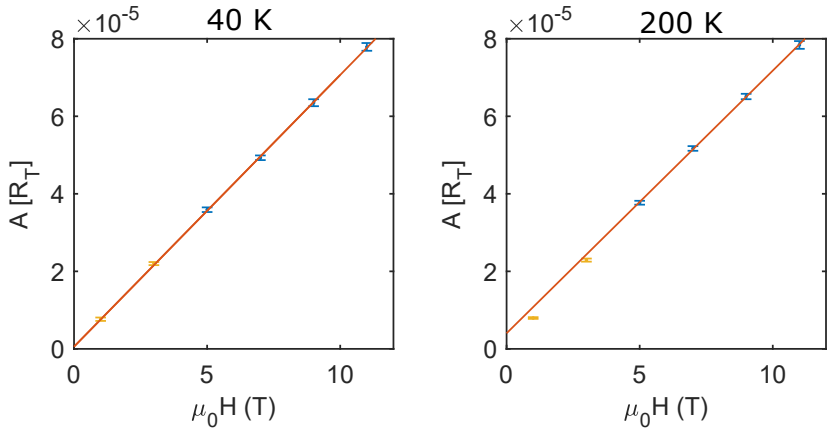


Figure A.15.: Amplitudes of $R_T(\gamma)$ vs external field. In red, a linear function fitted to the data points in blue. In yellow data points that are not considered in the fit. (a) for 40 K (b) for 200 K

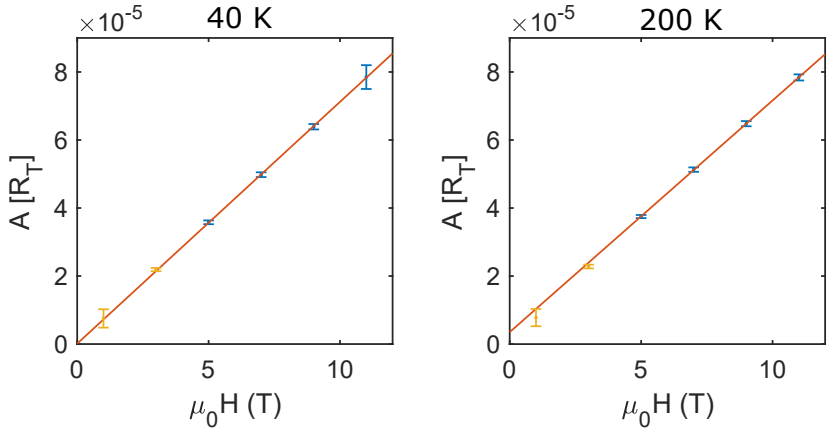


Figure A.16.: Amplitudes of $R_T(\beta)$ vs external field. In red, a linear function fitted to the data points in blue. In yellow data points that are not considered in the fit. (a) for 40 K (b) for 200 K

## A.8. $RuO_2$ thin films and novel spin transport effects

Regarding electronic transport measurements, a new effect has recently been predicted. However, it is not expected to occur in our TFO or YIG-GIG samples, but in some conducting collinear antiferromagnets. We therefore apply our knowledge about thin film growth on a different material, namely $RuO_2$. The $RuO_2$ thin films are investigated using established techniques to identify general properties of the samples. Then transport measurements are performed aiming the identification of the novel crystal Hall effect (CHE). This chapter is not part of the main results of the thesis since key measurements are yet to be performed. Here, we briefly present the idea of the CHE. The growth of $RuO_2$ thin films and the crystallographic and magnetic properties are presented. A first attempt to measure the CHE is discussed, leading to no conclusive result. Currently, a new setup is being build in the laboratories, providing magnetic fields up to 35 T in order to manipulate the Néel order in $RuO_2$. Simultaneously, $RuO_2$ samples are measured in spin- and angular resolved photo emission spectroscopy (AG Elmers) in order to determine the spin-polarized band structure of $RuO_2$ thin films.

From a symmetry point of view, the anomalous Hall effect (AHE) relies on broken time-reversal symmetry. In ferromagnets, the symmetry is broken by the magnetic atoms. In collinear AFMs the magnetic atoms do not break the time-reversal symmetry and therefore no AHE is expected. However, it was recently predicted [196] that in special crystal structures, the time-reversal symmetry is broken by non-magnetic ions leading to a sizeable Hall effect, named the crystal Hall effect (CHE). While for FMs and non-collinear AFMs the sign of the AHE flips when the (net) magnetic moment changes sign, for collinear AFMs the sign of the CHE flips, when the term $\mathbf{N} \cdot \boldsymbol{\chi}$ changes sign. Here, $\mathbf{N}$ is the Néel vector and $\boldsymbol{\chi}$ the crystal chirality, which is

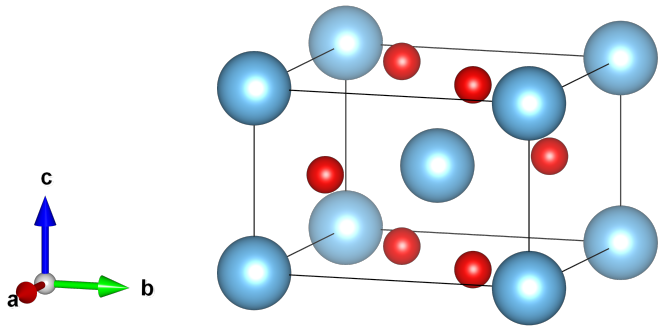


Figure A.17.: Rutile structure of $TiO_2$ with Ti atoms in blue and O atoms in red. Drawn in Vesta [62].

determined by the arrangement of the non-magnetic atoms.
The CHE would be easiest to be observed in transport experiments, if the sign of the CHE switches during the measurement. Since the relative orientation of $\mathbf{N}$ and $\boldsymbol{\chi}$ is important, we want to discuss the two extreme cases: $\mathbf{N} \parallel \boldsymbol{\chi}$ and $\mathbf{N} \perp \boldsymbol{\chi}$. For the first case, the CHE would contribute to the transverse signal even at zero external force leading to a finite Hall voltage. If $\mathbf{N}$ rotates by 180°, the sign of the CHE would change also reversing the sign in the transverse signal. However, switching $\mathbf{N}$ by 180° through external forces is difficult. A magnetic field for example, leads due to the minimization of Zeemann energy to the alignment if $\mathbf{N}$ perpendicular to $\mathbf{H}$, making it impossible to switch $\mathbf{N}$. On the other hand, for the case $\mathbf{N} \perp \boldsymbol{\chi}$, there is no contribution at zero external field in this system. Only an induced reorientation of $\mathbf{N}$ would lead to a CHE contribution and the sign would depend on the direction of the reorientation. We note that $\boldsymbol{\chi}$ cannot be changed by an external force acting on the grown material since it would require to change the arrangement of atoms in every unit cell. The arrangement of the non-magnetic atoms is only determined by the growth.
Regarding established properties of $RuO_2$, it has a structure of rutiles, which are also oxygen compounds and can therefore in principle be grown in our pulsed laser deposition setup (see section 3.1).To grow single crystalline thin films, the substrate needs to be of similar symmetry, so $TiO_2$ and $MgF_2$ have been chosen, which also possess rutile structure. A rutile unit cell is depicted in figure A.17. It is tetragonal with equally long $a$- and $b$-axes and a shorter $c$-axis. The oxygen (fluorine) ions form an octahedron around the metal ion.

### $MgF_2$

Magnesium fluoride is an insulating material that is used in optical devices for anti-reflective coatings or light polarization [197]. In this work it has been chosen as a substrate material to grow $RuO_2$ thin films because of its similar crystal structure. The lattice constants are given as $a = b = 4.621\,\text{Å}$ and $c = 3.052\,\text{Å}$ [198]. The bonds are highly ionic [199]. The $Mg^{2+}$ and the $F^-$ ions both have electron configuration of a noble gas and therefore the material is purely diamagnetic.

### $TiO_2$

Titanium dioxide has many applications. It is used as a white pigment in paint, sunscreen and even food. It can also act as a photocatalyst or gas sensor [200]. It occurs in three different crystallographic phases: anatase, ilmentile and rutile. In this work the rutile phase of $TiO_2$ has been used as a substrate material for $RuO_2$ thin films. The lattice parameters are $a = b = 4.593\,\text{Å}$ and $c = 2.959\,\text{Å}$ [201]. The bonds are described as ionic with a small covalent contribution [202]. The material is diamagnetic and insulating.

### $RuO_2$

Ruthenium dioxide is conducting [203] and chemically very stable. This is why it is already used as electrode material for example in catalysis devices [204]. The unit cell parameters are $a = b = 4.492\,\text{Å}$ and $c = 3.106\,\text{Å}$ [205]. The lattice mismatch with the $TiO_2$ substrate is -3% (+5%) for the $a$- ($c$-) axis and -3% (+2%) with $MgF_2$ substrates. The magnetic properties of $RuO_2$ have long not been a focus of research for it was believed to be paramagnetic until recently its antiferromagnetic properties were discovered by polarized neutron diffraction [206] and resonant x-ray scattering [207]. Both experiments indicate that the Néel vector is along the $c$-axis and that the antiferromagnetic order is preserved even at room temperature. In thin films, the orientation of $\mathbf{N}$ may differ [207]. The crystal chirality $\boldsymbol{\chi}$ is defined as the cross product of the vectors $\mathbf{d}$ connecting two Ru atoms $A$ and $B$ via an oxygen atom $O$ [196]:

$$\boldsymbol{\chi} = \mathbf{d}_{AO} \times \mathbf{d}_{OB}.$$

The geometric interpretation in shown in Fig. A.18. The change of chirality is accompanied by the rotation of the oxygen octahedron in the $RuO_2$ unit cell. The two possible orientations of $\boldsymbol{\chi}$ are along the $\pm[110]$ direction.
In the band structure of $RuO_2$, the CHE manifests itself in the spin-dependent splitting of the bands. This is shown in Fig. A.19, where along the $\Gamma - S$-direction a band splitting of up to 1 eV is expected between two different $\boldsymbol{\chi}$ and same $\mathbf{N}$. To be able to observe the CHE in transport experiments, the relative orientation between $\mathbf{N}$ and $\boldsymbol{\chi}$ is important. While $\boldsymbol{\chi}$ is fixed by the growth of the crystal, an external magnetic field $\mathbf{H}$ might alter $\mathbf{N}$. In $RuO_2$ bulk crystals, $\mathbf{N}$ is oriented along crystallographic $c$-axis

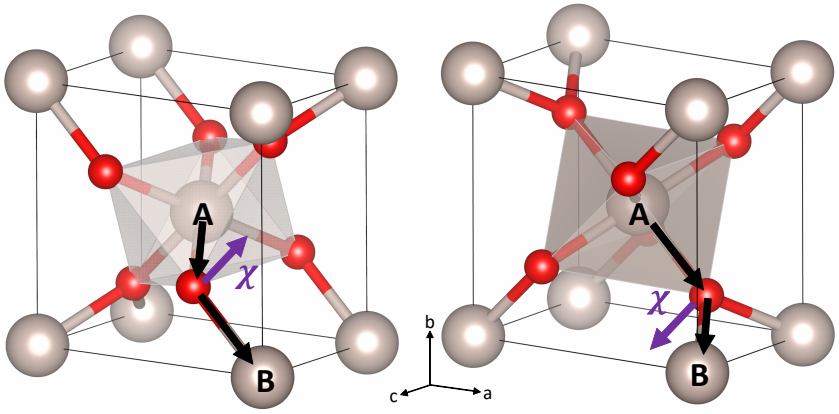


Figure A.18.: $RuO_2$ unit cell with Ru in gray and oxygen atoms in red. Two Ru atoms are marked with A and B and the connecting vectors $\mathbf{d}_{AO}$ and $\mathbf{d}_{OB}$ are drawn in black. The resulting chirality vector $\boldsymbol{\chi}$ is indicated in purple for the two different cases.

[206, 207] and therefore perpendicular to $\boldsymbol{\chi}$. So in this configuration no zero-field contribution of the CHE is expected. A sufficiently strong magnetic field might lead to a reorientation of **N** to one or the other direction, leading to a positive or negative sign of the CHE. To achieve a reorientation of **N**, **H** needs to have a component parallel to **N**. To minimize the the energy at sufficiently large magnetic fields, **N** will tend to align perpendicular to **H** in order to minimize the Zeeman energy.

### Growth of heteroepitaxial $RuO_2$ thin films

$RuO_2$ thin films have so far been grown on a variety of different substrates like STO [207, 208], $LaAlO_3$ [209, 210], MgO [208, 210], YSZ [211], Si/YSZ [212], glass or stain-

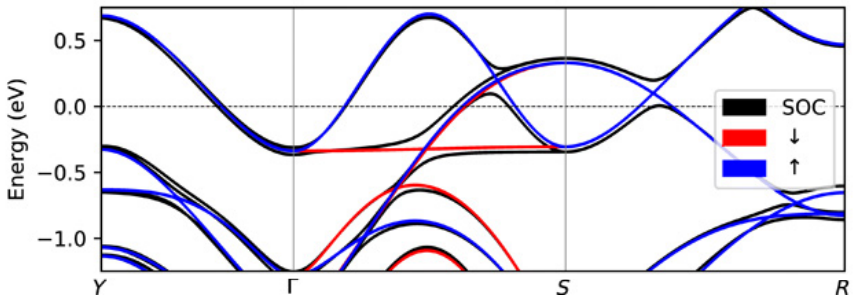


Figure A.19.: Band structure calculation for $RuO_2$ for the two cases (**N**,$\boldsymbol{\chi}$) and (**N**,-$\boldsymbol{\chi}$). Along the $\Gamma - S$-direction a prominent spin-dependent band splitting is expected. [196]

less steel [213]. The thin films in these reports show polycrystalline or even amorphous growth or a bad in-plane order because of twinning. For observing the CHE, large magnetic domains are needed, which can only exist in crystallographic monodomain epitaxial samples. Only few publications report the monocrystalline epitaxial growth of $RuO_2$. Utilizing reactive magnetron sputtering, it has been achieved on $Al_2O_3$ (1102) substrates, on which $RuO_2$ grows in (011) orientation [214, 215], and on $TiO_2$ (110) substrates by molecular beam epitaxy [216] and $Ru_3(CO)_{12}$ decomposition [217]. However, these reports focus mostly on the crystallographic and electric properties not taking into account a CHE contribution.

Here, we choose substrates that possess the same crystallographic symmetry as bulk $RuO_2$, namely $TiO_2$ and $MgF_2$. By choosing the substrate orientation we determine the growth direction of the $RuO_2$ thin film, since for a close matching of the unit cell parameters, a box-on-box growth is expected like we have seen in chapter 6.2, where we grew single crystalline $TmFeO_3$ on substrates with similar symmetry. For our $RuO_2$ samples, we choose (100)-cut ($a$-axis) substrates to grow $RuO_2$ in the same orientation. It is suggested that the CHE can be observed in $b$-oriented $RuO_2$ samples by transport measurements [196]. However, we note that the unit cell parameters $a$ and $b$ in bulk $RuO_2$ are equivalent, meaning that the orientation of the oxygen octahedron within the unit cell has no preferred orientation. Therefore, $a$- and $b$-axis orientation are equivalent from a crystallographic point of view.

$RuO_2$ thin films have been prepared by pulsed laser deposition on $MgF_2$ and $TiO_2$ substrates. Since this is the first time $RuO_2$ is grown in this chamber, a small test series was performed to determine the growth parameters. Only a few substrates where available for the optimization. Because it is reported that the properties of the twinned $RuO_2$ thin film deposited on $LaAlO_3$ by PLD is only weakly dependent on the deposition for PLD deposition from a stoichiometric target [209], the oxygen pressure was fixed at 0.02 mbar. The temperature on the other hand, has a larger influence. High temperatures larger than around 660°C lead to a decrease of growth rate as observed when optimizing the deposition parameters. This likely origins in the formation of $RuO_4$, which is extremely volatile (boiling point: 40°C [218]). Reducing the temperature leads to an increase of the electrical resistivity as reported for twinned $RuO_2$ samples indicating an increase of defect locations [209, 210]. However at a deposition temperature of 400°C, we observe the most narrow $RuO_2$ (200) rocking curves indicating well aligned $RuO_2$ unit cells. The deposition conditions are summarized in table A.2.

The samples have been analyzed for their structural properties using XRD. Fig. A.20 show $2\Theta/\omega$ scans along the [100] direction for 85 nm $RuO_2$ samples grown in $TiO_2$ (a) and $MgF_2$ (b), grown simultaneously to ensure equal growth conditions. The peaks are labeled with the respective Miller indices. No secondary peaks are being detected indicating impurity-free thin films. The inset shows the rocking curve measured at the $RuO_2$ (200) reflection with a FWHM of $\Delta\omega = 0.04°$ and $\Delta\omega = 0.43$ for the film grown on $TiO_2$ and $MgF_2$, respectively. We observe a narrow rocking curve for $TiO_2$ substrates indicating smooth growth of $RuO_2$ with parallel lattice planes. Compared to that, the $RuO_2$ grown on $MgF_2$ shows a broader rocking curve indicating some

| Parameter | value |
|---|---|
| Deposition temperature (°C) | 400 |
| $O_2$ pressure (mbar) | 0.02 |
| Substrate-target distance (cm) | 5.5 |
| Laser energy per pulse (mJ) | 120 |
| Laser spot size ($mm^2$) | 9 |
| Laser pulse frequency (Hz) | 10 |
| Cooling rate after dep. (K/min) | 25 |
| Growth rate (nm/min) | 2.5 |

Table A.2.: Deposition conditions for $RuO_2$.

more buckling of the individual $RuO_2$ unit cells relative to each other.

From these $2\Theta/\omega$ scans and the ones along the $\langle 101 \rangle$ and $\langle 110 \rangle$ direction displayed A.21 and A.22, the lattice parameters of the respective $RuO_2$ thin films are calculated and summarized in table A.3.

To determine the in-plane order, additional $\Phi$ scans have been performed along the $RuO_2$ (101) reflex. In a 360° $\Phi$ scan, the peak occurs only twice for both substrates (not shown), suggesting that no twinned domains are present. The $RuO_2$ thin films are therefore highly ordered crystallographic monodomain, which is important for detecting the CHE [196]. Moreover, we can observe that the degeneracy between *a*- and *b*-axis for both kinds of thin films is lifted, reducing the symmetry of the $RuO_2$ unit cells. We can see that by the choice of substrate we access differently strained

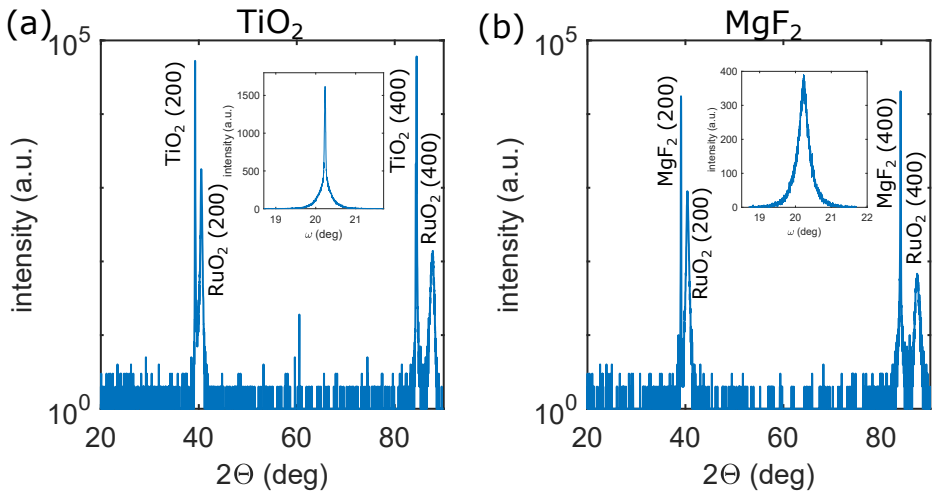


Figure A.20.: (a) $2\Theta/\omega$ scan for a 85 nm $TiO_2/RuO_2$ sample. The inset shows the rocking curve of the $RuO_2$ (200) peak. (b) $2\Theta/\omega$ scan for a 85 nm $MgF_2/RuO_2$ sample. The inset shows the rocking curve of the $RuO_2$ (200) peak.

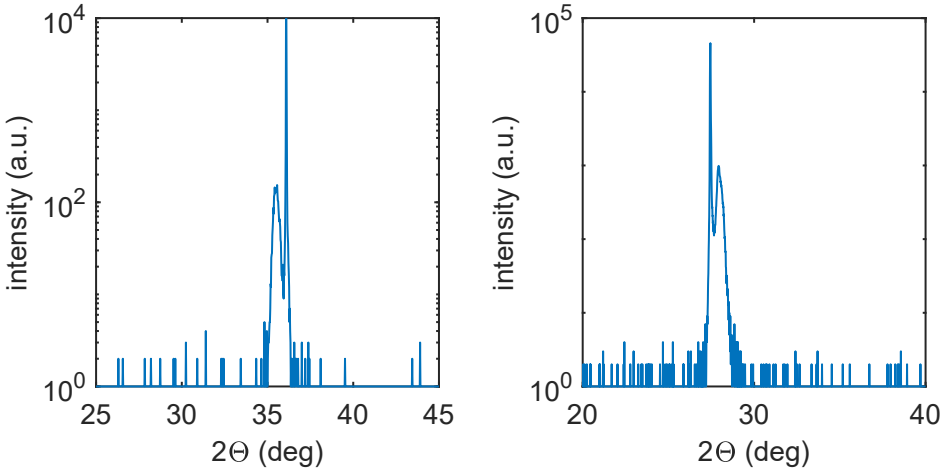


Figure A.21.: XRD scans of a $TiO_2/RuO_2$ sample: (a) $2\Theta/\omega$ scan in $\langle 101 \rangle$ direction (b) in $\langle 110 \rangle$ direction.

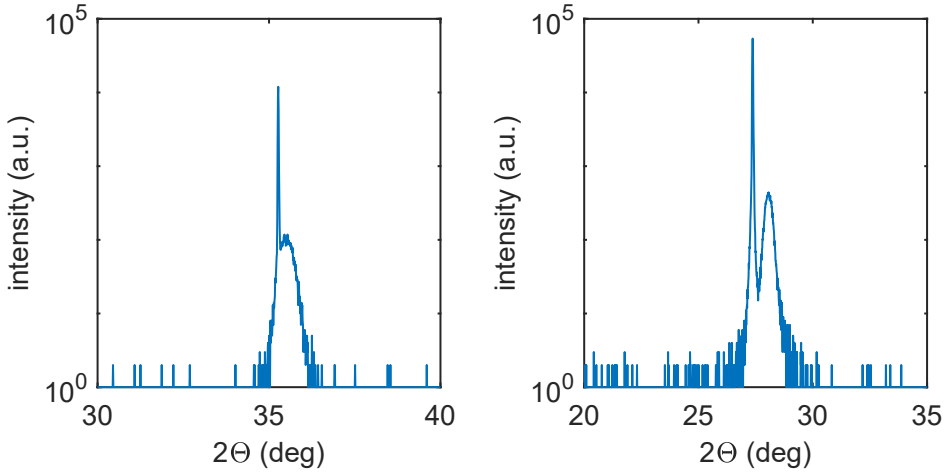


Figure A.22.: XRD scans of a $MgF_2/RuO_2$ sample: (a) $2\Theta/\omega$ scan in $\langle 101 \rangle$ direction (b) in $\langle 110 \rangle$ direction.

$RuO_2$ layers that may influence the magnetic properties. In bulk samples, it has been shown that the Néel vector is aligned with the $c$-axis. In twinned thin films a small tilt away from the high symmetry axis might be possible [207]. In the future resonant x-ray scattering or neutron diffraction experiments will show the Néel order in our thin films. In this study, we are limited to SQUID magnetometry to determine the magnetic properties.

To perform electric measurements the $RuO_2$ thin films have been patterned into Hall bars as described in section 3.6. The relative alignment of the Hall bar with the

| Bulk lattice | a (Å) | b (Å) | c (Å) |
|---|---|---|---|
| $RuO_2$ [205, 219] | 4.492 | 4.492 | 3.106 |
| $TiO_2$ [201] | 4.593 | 4.593 | 2.959 |
| $MgF_2$ [198] | 4.621 | 4.621 | 3.052 |

$RuO_2$thin films

| Substrate | a (Å) | b (Å) | c (Å) |
|---|---|---|---|
| $TiO_2$ | 4.45 | 4.57 | 3.07 |
| $MgF_2$ | 4.46 | 4.53 | 3.07 |

Table A.3.: Unit cell parameters of Bulk crystals according to literature (top) and $RuO_2$ thin films (85 nm) grown on different substrates (bottom).

crystallographic axes is shown in Fig. A.23. Panel (a) shows the $RuO_2$ unit cell relative to the Hall bar shown in panel (b). We note that here, we do not use a Pt top layer like in the electrical measurements performed at the YIG-GIG and TFO samples discussed in the main results chapters, but the $RuO_2$ layer itself is structured. In the following we will analyze the films grown on $TiO_2$ separately from those grown on $MgF_2$.

**$TiO_2$/$RuO_2$ samples**

The room temperature resistivity of an epitaxial 85 nm $TiO_2$/$RuO_2$ sample is around 125 $\mu\Omega$cm. For comparison: Single crystals possess a resistivity of around 35 $\mu\Omega$cm at 300 K [220], similar to heteroepitaxial thin films [209, 210]. The fact that we measure a relatively high resistivity might be due to the large strain modifying the electronic properties due to the deformation of the unit cell or a high defect concentration. To

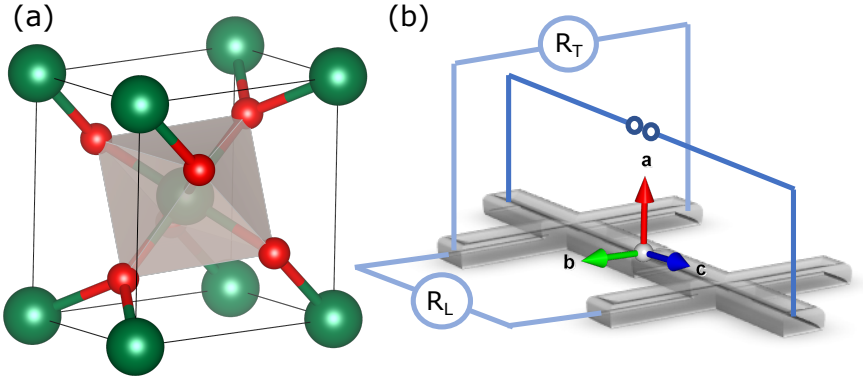


Figure A.23.: (a) $RuO_2$ unit cell drawn in VEST [62] with its relative orientation to the Hall bar shown in (b). (b) Hall bar defined along the crystallographic $c$ direction. The arms are along $b$ direction. The transverse and longitudinal resistivities are measured as indicated by $R_T$, and $R_L$, respectively.

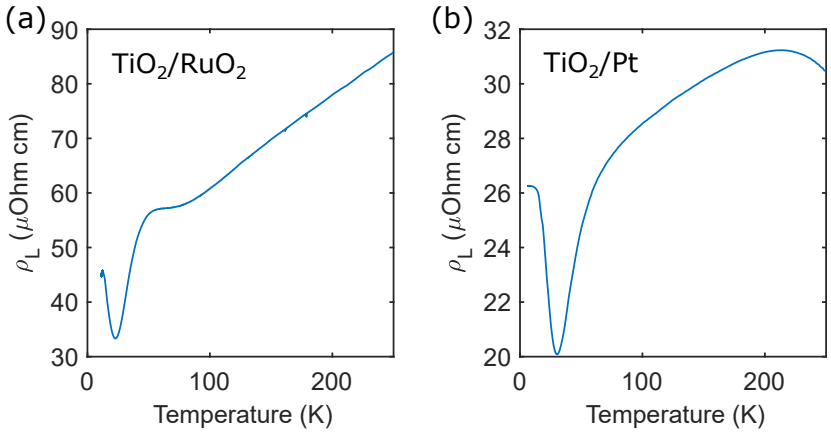


Figure A.24.: (a) Temperature dependence $\rho_L(T)$ of a $RuO_2$ Hall bar (85 nm thickness) patterned on $TiO_2$. (b) Test sample of a Pt Hall bar patterned on $TiO_2$.

understand the origin of the relatively high resistivity, a more intensive optimization of deposition conditions is suggested.

The temperature-dependent resistivity for a Hall bar defined along the (001) crystallographic direction is shown in Fig. A.24 (a). Starting from high temperature, we observe a monotonic decrease of $\rho_L$ with temperature, which is characteristic for a normal conductor. This confirms the metallic behavior reported for most $RuO_2$ thin films [210, 211, 215], while in some cases semiconducting behavior is reported [213]. However, below around 80 K, $\rho_L(T)$ shows an unusual behavior. Between 80 K and 50 K the slope changes and $\rho_L(T)$ almost plateaus. Below 50 K the resistivity rapidly decreases, describes a minimum at around 23 K before rising again at lower temperatures. This unusual behavior is not reported for metallic $RuO_2$ thin films so far [210, 211, 215].

To identify the origin of this behavior, a test sample of Pt $TiO_2$/Pt (3 nm) has been prepared and patterned into Hall structures in a similar fashion. As one can see in Fig. A.24 (b), this sample also shows this unusual behavior. It turns out that the originally diamagnetic and insulating $TiO_2$ substrate changes properties at its surface. The Ar ion beam used for patterning the Hall structures leads to a reduction of the $Ti^{4+}$ by oxygen removal [221]. $Ti_nO_{2n-1}$ with $n$= 2, 3, 4, 6 is conducting [222] and the ions $Ti^{x+}$ with $x$=1, 3 and $J = \frac{3}{2}, \frac{1}{2}$, respectively, are magnetic. It cannot be ruled out that a variety of $Ti_nO_{2n-1}$ are present at the $TiO_2$ surface, complicating the analysis of $RuO_2$ thin film properties.

To avoid the reduction of the $TiO_2$ surface during the etching process, Oxygen plasma should be used. However, it is reported that even in unetched $TiO_2$/$RuO_2$ films, there might be a charge transfer at the interface from the electron-rich $RuO_2$ to the $TiO_2$ leading to the presence of $Ti^{3+}$ ions at the interface [217], even in unetched samples. The CHE could still be measured in $TiO_2$/$RuO_2$ samples making use of spin-resolved

band structure measurements instead of transport measurements. The CHE manifests in a spin-dependent band-splitting that could be measured using spin- and angle-resolved photoemission spectroscopy (spin-ARPES) where one can probe the band structure of the samples at the surface. Since at the surface, no Ti contamination is expected in unpatterned samples, spin-ARPES is the suited tool to find hints for the novel transport effect. These measurements will be conducted in the group of Prof. Elmers in near future with our high quality thin film samples.
However, the impact of secondary contributions in our transport measurements lets us focus more on $MgF_2$ as a substrate for now, despite the slightly worse crystallographic properties of the $RuO_2$ grown on these.

### $MgF_2/RuO_2$ samples

Here, we investigate the properties of $MgF_2/RuO_2$ samples. From the lower lattice mismatch between $RuO_2$ and $MgF_2$ compared to $TiO_2$ substrates, one would intuitively expect better crystalline properties of $RuO_2$ grown on $MgF_2$ substrates. However, as we have seen in Fig. A.20, the rocking curve of $RuO_2$ reflexes of $MgF_2/RuO_2$ samples is broadened compared to $TiO_2/RuO_2$ samples, despite equal deposition conditions. Several reasons might lead to this effect. $MgF_2$ substrates react with oxygen at high temperatures and form MgO on the surface [223, 224]. While for pure $MgF_2$ the reaction temperature is around 800°C, the temperature is reduced in the presence of defects. Additionally, we observe that the surface of the $MgF_2$ substrates is rougher compared to other substrates used in this work. As shown in Fig. A.25 the AFM image shows deep scratches probably stemming from an improper surface treatment by the manufacturer. The inhomogeneous surface may contribute to the tilting of crystallites and thereby to the broadening of the rocking curve. The re-polishing process by the company lead to an improvement of surface roughness, but the overall RMS of 2 nm of the re-polished substrates still exceeds the roughness of other substrates used in this work, including the $TiO_2$ substrates ($< 0.5$ nm).
The room temperature resistivity of a 85 nm $MgF_2/RuO_2$ sample is around 131 $\mu\Omega$ cm, similar to the $TiO_2/RuO_2$ sample. The temperature dependent resistivity $R_L(T)$

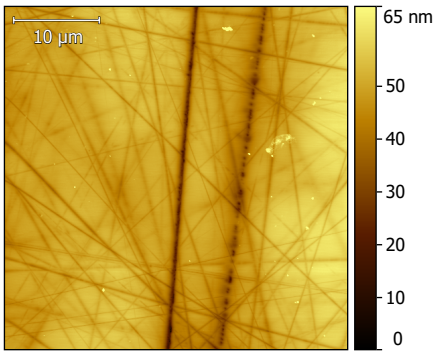


Figure A.25.: Atomic force microscopy image of a $MgF_2$ substrate surface.

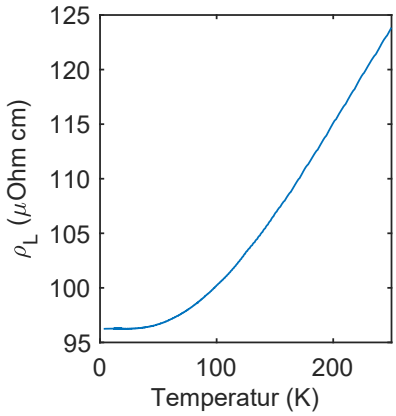


Figure A.26.: (a) Temperature dependence $\rho_L(T)$ of a $RuO_2$ Hall bar (85 nm thickness) patterned on $MgF_2$.

is shown in Fig. A.26. At low temperatures, the resistivity flattens off due to electrons scattering at defects and surfaces more than at phonons. The residual resistance ratio between 300 K and 10 K is around $RRR = 1.36$, smaller than for $RuO_2$ single crystals, where values of $RRR \geq 20$ have been achieved [220, 225] and also smaller than for other heteroepitaxial thin films with up to $RRR \approx 5$ [210]. These values indicate that in our samples, the defect rate is relatively high and suggest to improve the deposition parameters. Temperature treatment after the deposition might also lead to a reduction of defect density, improving the electronic properties of the sample.

Having determined the crystal structure of the $MgF_2/RuO_2$ samples, we now turn towards the investigation of the magnetic properties. $RuO_2$ is expected to order antiferromagnetically, however, the anisotropy in heteroepitaxial thin films is so far unknown. Whether the Néel vector can be manipulated by an external magnetic field is therefore an unsolved questions. Here, we employ SQUID measurements in different crystallographic directions in order to identify a possible contribution from the field-induced spin canting of $RuO_2$. Fig. A.27 (a) and (b) show measurements of the temperature- and field-dependent magnetization of a 70 nm $MgF_2/RuO_2$ sample measured in SQUID. For the field-cooled (FC) curve, the measurement has been performed along the *b*-axis, where one would expect the canted moment, when the Néel vector is oriented along *c*. The sample has been cooled under an applied field of 1 T. The magnetization of the heating sample has been measured under an applied field of 0.2 T. Similarly, the zero-field-cooled (ZFC) curve has been acquired after the sample has been cooled without the application of an external magnetic field. The signals have been corrected for diamagnetic contributions stemming from the substrate and mounting equipment by subtracting a constant. There is no prominent change of magnetization observed in either curve. A larger increase of the FC at low temperatures might be indicated. However, this likely stems from paramagnetic impurities from sample handling and hydration of the sample [226]. The absence of a magnetic

order transition is not surprising as it has not been observed in this temperature range for $RuO_2$ single crystals [220]. Indications of AFM ordering have been first observed when measuring the temperature-dependent susceptibility up to 1000 K [206]. However, here, we rule out that the AFM ordering temperature is reduced to below room temperature due to the strained thin-film growth of $RuO_2$.

In order to find evidence of the canted moment, field dependent measurements have been performed as shown in Fig. A.27 (b). Two curves, measured at 50 K, along the *b*- and *c*-axis, respectively, are shown. The magnetic moment is normalized to the volume of the $RuO_2$ film. In each curve we observe a prominent S shape at low magnetic fields which saturates at around $4 \times 10^{-3}$ $\mu_B$/f.u. for the measurement along *b* and at around $5 \times 10^{-3}$ $\mu_B$/f.u. along *c*. For both curves the coercive field is around 50 mT. The similarity between the curves indicates that the S shape does not stem from the magnetic properties of the $RuO_2$ thin film, since we measure once along **N** (*c*) and once perpendicular to it, where the canted moment is to be expected. The magnetic response seen in Fig. A.27 likely stems from iron contamination due to sample handling. Note that for the growth of the samples, the substrate is glued to an holder made out of a Nickel Iron alloy (Inconel). Despite a cleaning process after the deposition, the contamination with small magnetic particles cannot be completely ruled out.

We conclude that we find no evidence of the canted antiferromagnetism in our measurements with external magnetic fields up to 5 T. This might either be due to the absence of any magnetic ordering or due to large magnetic anisotropies shifting the critical fields at which **N** can be manipulated, to higher magnetic fields out of range of our setup. In neutron reflectivity experiments, a canted moment of 0.05 $\mu_B$/f.u.

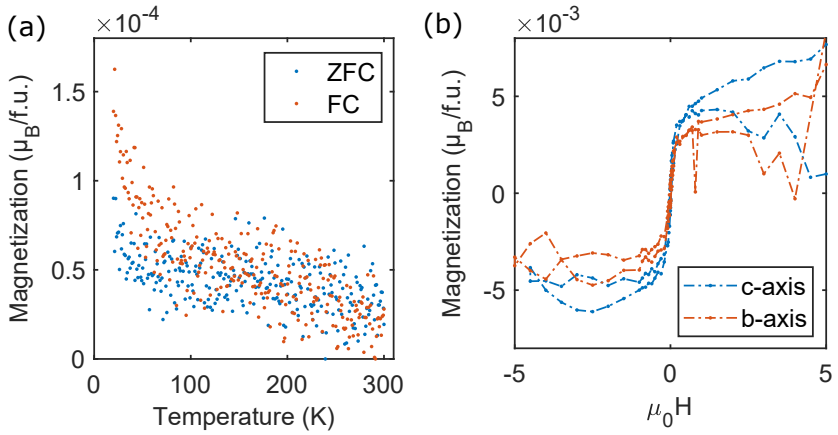


Figure A.27.: (a) Field-cooled (FC) and zero-field-cooled (ZFC) curves for a 70 nm $MgF_2/RuO_2$ sample measured between 20 K and 300 K. Both curves have been measured along the crystallographic *b*-axis. (b) field-dependent magnetization measured at 20 K and 50 K along the *b*- and *c*-axis.

was measured [206]. We do not find evidence of this moment in SQUID likely because the magnetic field used in these measurements is not sufficient to switch the canted moment. To extend our magnetic field range, we perform Hall effect measurements in a cryostat, where magnetic fields up to 11 T can be applied.
To measure the magnetic field dependent electric transport properties, $R_T(H)$ was measured at different temperatures. The current $I$ was applied along crystallographic $c$-direction, the magnetic field along crystallographic $a$ direction as proposed to measure the CHE [196] and as shown in Fig. A.23. The $a$-direction corresponds to the out-of-plane (oop) direction, so the occurrence of ordinary Hall effect (OHE) is to be expected, which contributes in a linear fashion, while the CHE should adapt a AHE-like signal [2]. Hall-geometry measurements have been performed over a temperature

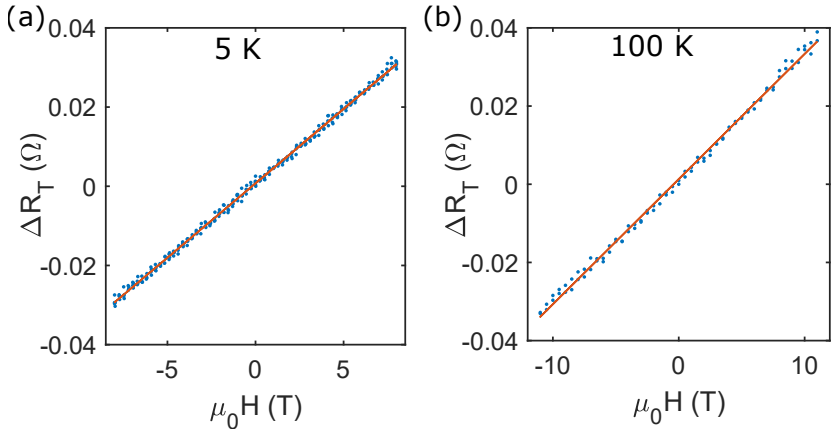


Figure A.28.: (a) Relative transverse resistivity measured as a function of applied magnetic field at 5 K (b) Similar measurement at 100 K. The red line indicates a linear function fitted to each curve.

range from 5 K to 100 K. Examples for $R_T(H)$ are shown in Fig. A.28 $R_L(H)$. One does not observe any contribution besides a linear one, which likely stems from the OHE.
To understand why we do not observe the CHE in our samples, we have again a look at the requirements that needs to be fulfilled to observe the effect. Essential is the relative orientation of the crystal chirality $\boldsymbol{\chi}$ and the Néel vector $\mathbf{N}$. The sign of the CHE is given by the product $\boldsymbol{\chi} \cdot \mathbf{N}$ [196]. In our samples, we have not found evidence of the antiferromagnetic ordering. However, for this consideration we want to assume bulk-like properties, so that $\mathbf{N}$ is oriented along the $c$-axis [206] and $\boldsymbol{\chi}$ points along the $\pm\langle 110\rangle$ direction, depending on the orientation of the oxygen octahedron within the unit cell. In the absence of any external perturbation we therefore should observe $\boldsymbol{\chi} \cdot \mathbf{N} = 0$, i.e. no zero-field CHE. Note that in twinned STO/$RuO_2$thin films a projection of $\mathbf{N}$ in the $ac$ plane is indicated [207]. This would indeed allow for a nonzero effect at zero field. Whether the canting of $\mathbf{N}$ away from the $c$ axis is also

[2]Private communications with L. Šmejkal

present in epitaxial $RuO_2$ thin films is still to be investigated.
For further consideration, we assume that $\mathbf{N} \parallel c$. In our experiment, we have applied the magnetic field out of the sample plane, which coincides with the crystallographic $a$- or $b$-axis. We cannot distinguish between the two crystallographic axis by XRD measurements available in our lab, since we are not sensitive to the oxygen positions in the unit cell. However, either direction for the applied magnetic field does not lead to the manipulation of the Néel vector in our simple picture, since the Zeeman energy is minimum for $\mathbf{H} \perp \mathbf{N}$, which is fulfilled for both possibilities. Therefore, considering a simple collinear antiferromagnet, we in fact should not be able to observe the CHE in the suggested measurement configuration.
Manipulating $\mathbf{N}$ by a perpendicular magnetic field is only possible in the presence of a large DMI like for the canted antiferromagnet hematite ($\alpha$-$Fe_2O_3$) in its easy-axis phase and $DyFeO_3$ in its $\Gamma_1$ phase. For hematite, a field perpendicular to $\mathbf{N}$ leads to the rotation of $\mathbf{N}$ by 90° within the plane perpendicular to $\mathbf{H}$ [41]. For $DyFeO_3$, a field along the crystallographic $b$-axis at low temperature leads to a transition $\Gamma_1 \rightarrow \Gamma_4$ or $\Gamma_1 \rightarrow \Gamma_2$ depending on the magnetic field direction, while both also correspond to a 90° rotation of $\mathbf{N}$ in the plane perpendicular to $\mathbf{H}$ [178]. If $RuO_2$ possesses similar properties, indeed, the observation of the CHE would be possible in transport measurements, since a rotation away from the $c$-axis would led to a non-zero projection of $\mathbf{N}$ along $\boldsymbol{\chi}$. However, the sole presence of DMI does not guarantee for the rotation of $\mathbf{N}$ upon the application of a magnetic field. The DM field must be collinear with $\mathbf{N}$.
The properties of these materials are characterized by collinear antiferromagnetism and absence of a canting. Since a canting is observed for $RuO_2$ bulk samples [206], such behavior is not expected to occur in our thin films, if they possess bulk-like magnetic properties. We therefore assume that the linear change of transverse resistance shown in Fig. A.28 is indeed only due to OHE. The response changes only weakly with temperature.
In preparation of this thesis, the observation of CHE in $MgO/RuO_2$ samples was reported [227] doing transport measurements and magnetic fields up to 50 T. At first sight, this is surprising, since $RuO_2$ thin films grown on MgO are reported to exhibit twinned growth [208] while large magnetic domains are required to observe the CHE [196]. On MgO, $RuO_2$ grows in two different in-plane directions with $[\bar{1}10]_{RuO_2} \parallel [110]_{MgO}$ and $[\bar{1}10]_{RuO_2} \parallel [\bar{1}10]_{MgO}$, while both crystallites share a common [110] axis pointing out of the sample plane parallel to the MgO $c$-axis. This is depicted in Fig. A.29 (a). In their experiment, the magnetic field is applied out of the plane, along the [110] $RuO_2$ axis, which is perpendicular to the $c$-axis and coincides with the axis of crystal chirality as introduced in Fig. A.18. To minimize the Zeeman energy, there is no need for $\mathbf{N}$ to rotate away from its initial orientation. It is therefore argued, that $\mathbf{N}$ is initially not perfectly aligned with the $c$-axis. Note that resonant x-ray measurements [207] *may* indicate a canting of $\mathbf{N}$ away from $c$ by an angle of around 20° in single crystals as depicted in Fig. A.29 (b). This would imply a non-zero CHE contribution at zero field for a single crystallite.
The absence of zero field signal suggests a distribution of Néel vector orientations with crystallites having a contribution in $\langle 110 \rangle$ and as many crystallites with a contribution

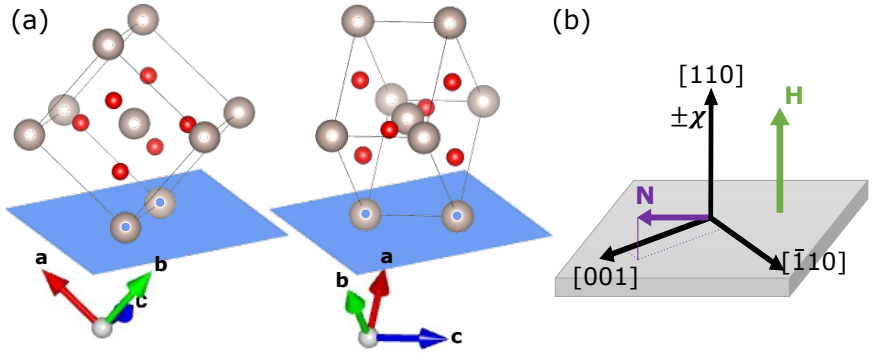


Figure A.29.: (a) Relative orientation of the $RuO_2$ unit cells with the MgO substrate. The blue square indicates the surface symmetry of MgO with the [100] and [010] axes along its edges. The arrows at the bottom indicate the $RuO_2$ crystallographic axes. Due to twinning, nm-sized domains with a random distribution of the two possible orientations, as well as the 180° rotated orientations, are present across the sample. (b) Possible orientation of the Néel vector **N** in one of the nm-sized domains. Note that **N** is rotated in other domains according to the orientation of the crystallographic axes. $\boldsymbol{\chi}$ describes the crystal chirality, which point along a common axis.

in $\langle \bar{1}\bar{1}0 \rangle$-direction. The application of a magnetic field out of the plane now favors the alignment of **N** with the sample plane to minimize Zeeman energy. This further leads to the vanishing of the product $\boldsymbol{\chi} \cdot \mathbf{N}$ and a resulting zero contribution from CHE. The vanishing of CHE is symmetric concerning the orientation of the magnetic field. It is therefore surprising that an asymmetric signal is observed in these experiments.

# Own and Contributed Works


S1. Ding, S., Ross, A., Lebrun, R., **Becker, S.**, Lee, K., Boventer, I., Das, S., Kurokawa, Y., Gupta, S., Yang, J., Jakob, G. & Kläui, M. Interfacial Dzyaloshinskii-Moriya interaction and chiral magnetic textures in a ferrimagnetic insulator. *Phys. Rev. B* **100,** 100406. doi:10.1103/PhysRevB.100.100406 (10 Sept. 2019).

S2. Ross, A., Lebrun, R., Gomonay, O., Grave, D. A., Kay, A., Baldrati, L., **Becker, S.**, Qaiumzadeh, A., Ulloa, C., Jakob, G., Kronast, F., Sinova, J., Duine, R., Brataas, A., Rothschild, A. & Kläui, M. Propagation Length of Antiferromagnetic Magnons Governed by Domain Configurations. *Nano Letters* **20,** 306–313. doi:10.1021/acs.nanolett.9b03837 (Dec. 2019).

S3. **Becker, S.**, Heinz, S., Vafaee, M., Kläui, M. & Jakob, G. The challenge in realizing an exchange coupled $BiFeO_3$-double perovskite bilayer. *Journal of Magnetism and Magnetic Materials* **506,** 166766. doi:10.1016/j.jmmm.2020.166766 (July 2020).

S4. Ding, S., Baldrati, L., Ross, A., Ren, Z., Wu, R., **Becker, S.**, Yang, J., Jakob, G., Brataas, A. & Kläui, M. Identifying the origin of the nonmonotonic thickness dependence of spin-orbit torque and interfacial Dzyaloshinskii-Moriya interaction in a ferrimagnetic insulator heterostructure. *Phys. Rev. B* **102,** 054425. doi:10.1103/PhysRevB.102.054425 (5 Aug. 2020).

S5. Ding, S., Ross, A., Go, D., Baldrati, L., Ren, Z., Freimuth, F., **Becker, S.**, Kammerbauer, F., Yang, J., Jakob, G., Mokrousov, Y. & Kläui, M. Harnessing Orbital-to-Spin Conversion of Interfacial Orbital Currents for Efficient Spin-Orbit Torques. *Phys. Rev. Lett.* **125,** 177201. doi:10.1103/PhysRevLett.125.177201 (17 Oct. 2020).

S6. **Becker, S.**, Ren, Z., Fuhrmann, F., Ross, A., Lord, S., Ding, S., Wu, R., Yang, J., Miao, J., Kläui, M. & Jakob, G. Magnetic Coupling in $Y_3Fe_5O_{12}/Gd_3Fe_5O_{12}$ Heterostructures. *Phys. Rev. Applied* **16,** 014047. doi:10.1103/PhysRevApplied.16.014047 (1 July 2021).

S7. **Becker, S.**, Ross, A., Lebrun, R., Baldrati, L., Ding, S., Schreiber, F., Maccherozzi, F., Backes, D., Kläui, M. & Jakob, G. Electrical detection of the spin reorientation transition in antiferromagnetic $TmFeO_3$ thin films by spin Hall magnetoresistance. *Phys. Rev. B* **103,** 024423. doi:10.1103/PhysRevB.103.024423 (2 Jan. 2021).

S8. Das, S., Ross, A., Ma, X. X., **Becker, S.**, Schmitt, C., van Duijn, F., Fuhrmann, F., Syskaki, M. .-., Ebels, U., Baltz, V., Barra, A. .-., Chen, H. Y., Jakob, G., Cao, S. X., Sinova, J., Gomonay, O., Lebrun, R. & Kläui, M. *Anisotropic long-range spin transport in canted antiferromagnetic orthoferrite $YFeO_3$* 2021. arXiv: 2112.05947 [cond-mat.str-el].

S9. Ding, S., Liang, Z., Yun, C., Wu, R., Xue, M., Lin, Z., Ross, A., **Becker, S.**, Yang, W., Ma, X., Chen, D., Sun, K., Jakob, G., Kläui, M. & Yang, J. Anomalous Hall effect in magnetic insulator heterostructures: Contributions from spin-Hall and magnetic-proximity effects. *Phys. Rev. B* **104,** 224410. doi:10.1103/PhysRevB.104.224410 (22 Dec. 2021).

S10. **Becker, S.**, Ross, A., Galindez Ruales, E., Fuhrmann, F., Freimuth, F., Gomonay, O., Lebrun, R., Pomjakushina, E., Schreiber, F., Go, D., Kläui, M., Mokrousov, Y. & Jakob1, G. Interface effects antiferromagnet-Pt heterostructures measured by spin Hall magnetoresistance. *In preparation.*

# Bibliography


1. Kent, A. D. & Worledge, D. C. A new spin on magnetic memories. *Nature Nanotechnology* **10,** 187–191. doi:10.1038/nnano.2015.24 (Mar. 2015).
2. Waldrop, M. M. The chips are down for Moore's law. *Nature* **530,** 144–147. doi:10.1038/530144a (Feb. 2016).
3. Chumak, A. V., Vasyuchka, V. I., Serga, A. A. & Hillebrands, B. Magnon spintronics. *Nature Physics* **11,** 453–461. doi:10.1038/nphys3347 (June 2015).
4. Cornelissen, L. J., Liu, J., Duine, R. A., Youssef, J. B. & van Wees, B. J. Long-distance transport of magnon spin information in a magnetic insulator at room temperature. *Nature Physics* **11,** 1022–1026. doi:10.1038/nphys3465 (Sept. 2015).
5. Baibich, M. N., Broto, J. M., Fert, A., Van Dau, F. N., Petroff, F., Etienne, P., Creuzet, G., Friederich, A. & Chazelas, J. Giant Magnetoresistance of (001)Fe/(001)Cr Magnetic Superlattices. *Phys. Rev. Lett.* **61,** 2472–2475. doi:10.1103/PhysRevLett.61.2472 (21 Nov. 1988).
6. Binasch, G., Grünberg, P., Saurenbach, F. & Zinn, W. Enhanced magnetoresistance in layered magnetic structures with antiferromagnetic interlayer exchange. *Phys. Rev. B* **39,** 4828–4830. doi:10.1103/PhysRevB.39.4828 (7 Mar. 1989).
7. Fert, A. Nobel Lecture: Origin, development, and future of spintronics. *Rev. Mod. Phys.* **80,** 1517–1530. doi:10.1103/RevModPhys.80.1517 (4 Dec. 2008).
8. Cramer, J., Seifert, T., Kronenberg, A., Fuhrmann, F., Jakob, G., Jourdan, M., Kampfrath, T. & Kläui, M. Complex Terahertz and Direct Current Inverse Spin Hall Effect in YIG/$Cu_{1-x}Ir_x$ Bilayers Across a Wide Concentration Range. *Nano Lett.* **18,** 1064–1069. doi:10.1021/acs.nanolett.7b04538 (Jan. 2018).
9. Wu, H., Huang, L., Fang, C., Yang, B. S., Wan, C. H., Yu, G. Q., Feng, J. F., Wei, H. X. & Han, X. F. Magnon Valve Effect between Two Magnetic Insulators. *Phys. Rev. Lett.* **120,** 097205. doi:10.1103/PhysRevLett.120.097205 (9 Mar. 2018).
10. Guo, C. Y., Wan, C. H., Wang, X., Fang, C., Tang, P., Kong, W. J., Zhao, M. K., Jiang, L. N., Tao, B. S., Yu, G. Q. & Han, X. F. Magnon valves based on YIG/NiO/YIG all-insulating magnon junctions. *Phys. Rev. B* **98,** 134426. doi:10.1103/PhysRevB.98.134426 (13 Oct. 2018).

11. Olejník, K., Seifert, T., Kašpar, Z., Novák, V., Wadley, P., Campion, R. P., Baumgartner, M., Gambardella, P., Němec, P., Wunderlich, J., Sinova, J., Kužel, P., Müller, M., Kampfrath, T. & Jungwirth, T. Terahertz electrical writing speed in an antiferromagnetic memory. *Science Advances* **4,** eaar3566. doi:10.1126/sciadv.aar3566 (Mar. 2018).

12. Jungwirth, T., Marti, X., Wadley, P. & Wunderlich, J. Antiferromagnetic spintronics. *Nature Nanotechnology* **11,** 231–241. doi:10.1038/nnano.2016.18 (Mar. 2016).

13. Baltz, V., Manchon, A., Tsoi, M., Moriyama, T., Ono, T. & Tserkovnyak, Y. Antiferromagnetic spintronics. *Rev. Mod. Phys.* **90,** 015005. doi:10.1103/RevModPhys.90.015005 (1 Feb. 2018).

14. Jungwirth, T., Sinova, J., Manchon, A., Marti, X., Wunderlich, J. & Felser, C. The multiple directions of antiferromagnetic spintronics. *Nature Physics* **14,** 200–203. doi:10.1038/s41567-018-0063-6 (Mar. 2018).

15. Baldrati, L., Ross, A., Niizeki, T., Schneider, C., Ramos, R., Cramer, J., Gomonay, O., Filianina, M., Savchenko, T., Heinze, D., Kleibert, A., Saitoh, E., Sinova, J. & Kläui, M. Full angular dependence of the spin Hall and ordinary magnetoresistance in epitaxial antiferromagnetic NiO(001)/Pt thin films. *Phys. Rev. B* **98,** 024422. doi:10.1103/PhysRevB.98.024422 (2 July 2018).

16. Manchon, A. Spin Hall magnetoresistance in antiferromagnet/normal metal bilayers. *physica status solidi (RRL) - Rapid Research Letters* **11,** 1600409. doi:10.1002/pssr.201600409 (Jan. 2017).

17. Kimel, A. V., Kirilyuk, A., Tsvetkov, A., Pisarev, R. V. & Rasing, T. Laser-induced ultrafast spin reorientation in the antiferromagnet $TmFeO_3$. *Nature* **429,** 850–853. doi:10.1038/nature02659 (June 2004).

18. Kimel, A. V., Ivanov, B. A., Pisarev, R. V., Usachev, P. A., Kirilyuk, A. & Rasing, T. Inertia-driven spin switching in antiferromagnets. *Nature Physics* **5,** 727–731. doi:10.1038/nphys1369 (Aug. 2009).

19. Baierl, S., Hohenleutner, M., Kampfrath, T., Zvezdin, A. K., Kimel, A. V., Huber, R. & Mikhaylovskiy, R. V. Nonlinear spin control by terahertz-driven anisotropy fields. *Nature Photonics* **10,** 715–718. doi:10.1038/nphoton.2016.181 (Oct. 2016).

20. Zhang, K., Xu, K., Liu, X., Zhang, Z., Jin, Z., Lin, X., Li, B., Cao, S. & Ma, G. Resolving the spin reorientation and crystal-field transitions in $TmFeO_3$ with terahertz transient. *Scientific Reports* **6.** doi:10.1038/srep23648 (Mar. 2016).

21. Schlauderer, S., Lange, C., Baierl, S., Ebnet, T., Schmid, C. P., Valovcin, D. C., Zvezdin, A. K., Kimel, A. V., Mikhaylovskiy, R. V. & Huber, R. Temporal and spectral fingerprints of ultrafast all-coherent spin switching. *Nature* **569,** 383–387. doi:10.1038/s41586-019-1174-7 (May 2019).

22. Ahn, S.-J., Lee, J.-H., Jang, H. M. & Jeong, Y. K. Multiferroism in hexagonally stabilized $TmFeO_3$ thin films below 120 K. *J. Mater. Chem. C* **2,** 4521–4525. doi:10.1039/C4TC00461B (23 2014).

23. Bibes, M. & Barthélémy, A. Towards a magnetoelectric memory. *Nature Materials* **7,** 425–426. doi:10.1038/nmat2189 (June 2008).

24. Anderson, P. W. Antiferromagnetism. Theory of Superexchange Interaction. *Phys. Rev.* **79,** 350–356. doi:10.1103/PhysRev.79.350 (2 July 1950).

25. Blundell, S. *Magnetism in condensed matter* eng. ISBN: 0198505922 (Oxford University Press, Oxford, 2001).

26. Dzyaloshinsky, I. A thermodynamic theory of weak ferromagnetism of antiferromagnetics. *Journal of Physics and Chemistry of Solids* **4,** 241–255. doi:10.1016/0022-3697(58)90076-3 (Jan. 1958).

27. Moriya, T. Anisotropic Superexchange Interaction and Weak Ferromagnetism. *Physical Review* **120,** 91–98. doi:10.1103/physrev.120.91 (Oct. 1960).

28. Gross, R. & Marx, A. *Festkörperphysik* doi:10.1524/9783486714869 (Oldenbourg Wissenschaftsverlag Verlag, 2012).

29. Kimura, T., Goto, T., Shintani, H., Ishizaka, K., Arima, T. & Tokura, Y. Magnetic control of ferroelectric polarization. *Nature* **426,** 55–58. doi:10.1038/nature02018 (Nov. 2003).

30. Eerenstein, W., Mathur, N. D. & Scott, J. F. Multiferroic and magnetoelectric materials. *Nature* **442,** 759–765. doi:10.1038/nature05023 (Aug. 2006).

31. Scott, J. F. Multiferroic memories. *Nature Materials* **6,** 256–257. doi:10.1038/nmat1868 (Mar. 2007).

32. Gajek, M., Bibes, M., Fusil, S., Bouzehouane, K., Fontcuberta, J., Barthélémy, A. & Fert, A. Tunnel junctions with multiferroic barriers. *Nature Materials* **6,** 296–302. doi:10.1038/nmat1860 (Mar. 2007).

33. Geprägs, S., Kehlberger, A., Coletta, F. D., Qiu, Z., Guo, E.-J., Schulz, T., Mix, C., Meyer, S., Kamra, A., Althammer, M., Huebl, H., Jakob, G., Ohnuma, Y., Adachi, H., Barker, J., Maekawa, S., Bauer, G. E. W., Saitoh, E., Gross, R., Goennenwein, S. T. B. & Kläui, M. Origin of the spin Seebeck effect in compensated ferrimagnets. *Nature Communications* **7.** doi:10.1038/ncomms10452 (Feb. 2016).

34. Lebrun, R., Ross, A., Bender, S. A., Qaiumzadeh, A., Baldrati, L., Cramer, J., Brataas, A., Duine, R. A. & Kläui, M. Tunable long-distance spin transport in a crystalline antiferromagnetic iron oxide. *Nature* **561,** 222–225. doi:10.1038/s41586-018-0490-7 (Sept. 2018).

35. Hall, E. H. On a New Action of the Magnet on Electric Currents. *American Journal of Mathematics* **2,** 287. doi:10.2307/2369245 (Sept. 1879).

36. Kohler, M. Zur magnetischen Widerstandsänderung reiner Metalle. *Annalen der Physik* **424,** 211–218. doi:10.1002/andp.19384240124 (1938).

37. Isasa, M., Vélez, S., Sagasta, E., Bedoya-Pinto, A., Dix, N., Sánchez, F., Hueso, L. E., Fontcuberta, J. & Casanova, F. Spin Hall Magnetoresistance as a Probe for Surface Magnetization in $Pt/CoFe_2O_4$ Bilayers. *Phys. Rev. Applied* **6,** 034007. doi:10.1103/PhysRevApplied.6.034007 (3 Sept. 2016).

38. Sinova, J., Valenzuela, S. O., Wunderlich, J., Back, C. H. & Jungwirth, T. Spin Hall effects. *Rev. Mod. Phys.* **87,** 1213–1260. doi:10.1103/RevModPhys.87.1213 (4 Oct. 2015).

39. Nakayama, H., Althammer, M., Chen, Y.-T., Uchida, K., Kajiwara, Y., Kikuchi, D., Ohtani, T., Geprägs, S., Opel, M., Takahashi, S., Gross, R., Bauer, G. E. W., Goennenwein, S. T. B. & Saitoh, E. Spin Hall Magnetoresistance Induced by a Nonequilibrium Proximity Effect. *Phys. Rev. Lett.* **110,** 206601. doi:10.1103/PhysRevLett.110.206601 (20 May 2013).

40. Hajiri, T., Baldrati, L., Lebrun, R., Filianina, M., Ross, A., Tanahashi, N., Kuroda, M., Gan, W. L., Menteş, T. O., Genuzio, F., Locatelli, A., Asano, H. & Kläui, M. Spin structure and spin Hall magnetoresistance of epitaxial thin films of the insulating non-collinear antiferromagnet $SmFeO_3$. *Journal of Physics: Condensed Matter* **31,** 445804. doi:10.1088/1361-648x/ab303c (Aug. 2019).

41. Lebrun, R., Ross, A., Gomonay, O., Bender, S. A., Baldrati, L., Kronast, F., Qaiumzadeh, A., Sinova, J., Brataas, A., Duine, R. A. & Kläui, M. Anisotropies and magnetic phase transitions in insulating antiferromagnets determined by a Spin-Hall magnetoresistance probe. *Communications Physics* **2.** doi:10.1038/s42005-019-0150-8 (May 2019).

42. Baldrati, L., Gomonay, O., Ross, A., Filianina, M., Lebrun, R., Ramos, R., Leveille, C., Fuhrmann, F., Forrest, T. R., Maccherozzi, F., Valencia, S., Kronast, F., Saitoh, E., Sinova, J. & Kläui, M. Mechanism of Néel Order Switching in Antiferromagnetic Thin Films Revealed by Magnetotransport and Direct Imaging. *Phys. Rev. Lett.* **123,** 177201. doi:10.1103/PhysRevLett.123.177201 (17 Oct. 2019).

43. Chen, Y.-T., Takahashi, S., Nakayama, H., Althammer, M., Goennenwein, S. T. B., Saitoh, E. & Bauer, G. E. W. Theory of spin Hall magnetoresistance (SMR) and related phenomena. *Journal of Physics: Condensed Matter* **28,** 103004. doi:10.1088/0953-8984/28/10/103004 (Feb. 2016).

44. Brataas, A., Nazarov, Y. V. & Bauer, G. E. W. Finite-Element Theory of Transport in Ferromagnet-Normal Metal Systems. *Phys. Rev. Lett.* **84,** 2481–2484. doi:10.1103/PhysRevLett.84.2481 (11 Mar. 2000).

45. Fischer, J., Gomonay, O., Schlitz, R., Ganzhorn, K., Vlietstra, N., Althammer, M., Huebl, H., Opel, M., Gross, R., Goennenwein, S. T. B. & Geprägs, S. Spin Hall magnetoresistance in antiferromagnet/heavy-metal heterostructures. *Phys. Rev. B* **97,** 014417. doi:10.1103/PhysRevB.97.014417 (1 Jan. 2018).

46. Hoogeboom, G. R., Aqeel, A., Kuschel, T., Palstra, T. T. M. & van Wees, B. J. Negative spin Hall magnetoresistance of Pt on the bulk easy-plane antiferromagnet NiO. *Applied Physics Letters* **111,** 052409. doi:10.1063/1.4997588. eprint: https://doi.org/10.1063/1.4997588 (2017).

47. Han, J. H., Song, C., Li, F., Wang, Y. Y., Wang, G. Y., Yang, Q. H. & Pan, F. Antiferromagnet-controlled spin current transport in $SrMnO_3$/Pt hybrids. *Phys. Rev. B* **90,** 144431. doi:10.1103/PhysRevB.90.144431 (14 Oct. 2014).

48. Hanle, W. Über magnetische Beeinflussung der polarisation der Resonanzfluoreszenz. *Zeitschrift für Physik* **30,** 93–105 (1924).

49. Dyakonov, M. I. Magnetoresistance due to Edge Spin Accumulation. *Phys. Rev. Lett.* **99,** 126601. doi:10.1103/PhysRevLett.99.126601 (12 Sept. 2007).

50. Vélez, S., Golovach, V. N., Bedoya-Pinto, A., Isasa, M., Sagasta, E., Abadia, M., Rogero, C., Hueso, L. E., Bergeret, F. S. & Casanova, F. Hanle Magnetoresistance in Thin Metal Films with Strong Spin-Orbit Coupling. *Physical Review Letters* **116,** 016603. doi:10.1103/physrevlett.116.016603 (Jan. 2016).

51. Wu, H., Zhang, X., Wan, C. H., Tao, B. S., Huang, L., Kong, W. J. & Han, X. F. Hanle magnetoresistance: The role of edge spin accumulation and interfacial spin current. *Phys. Rev. B* **94,** 174407. doi:10.1103/PhysRevB.94.174407 (17 Nov. 2016).

52. Uchida, K., Takahashi, S., Harii, K., Ieda, J., Koshibae, W., Ando, K., Maekawa, S. & Saitoh, E. Observation of the spin Seebeck effect. *Nature* **455,** 778–781. doi:10.1038/nature07321 (Oct. 2008).

53. Uchida, K., Xiao, J., Adachi, H., Ohe, J., Takahashi, S., Ieda, J., Ota, T., Kajiwara, Y., Umezawa, H., Kawai, H., Bauer, G. E. W., Maekawa, S. & Saitoh, E. Spin Seebeck insulator. *Nature Materials* **9,** 894–897. doi:10.1038/nmat2856 (Sept. 2010).

54. Princep, A. J., Ewings, R. A., Ward, S., Tóth, S., Dubs, C., Prabhakaran, D. & Boothroyd, A. T. The full magnon spectrum of yttrium iron garnet. *npj Quantum Materials* **2.** doi:10.1038/s41535-017-0067-y (Nov. 2017).

55. Rose, G. *De novis quibusdam fossilibus, quae in montibus uraliis inveniuntur* PhD thesis (Berlin, 1839).

56. Malinkiewicz, O., Yella, A., Lee, Y. H., Espallargas, G. M., Graetzel, M., Nazeeruddin, M. K. & Bolink, H. J. Perovskite solar cells employing organic charge-transport layers. *Nature Photonics* **8,** 128–132. doi:10.1038/nphoton.2013.341 (Dec. 2013).

57. Lin, Q., Armin, A., Nagiri, R. C. R., Burn, P. L. & Meredith, P. Electro-optics of perovskite solar cells. *Nature Photonics* **9,** 106–112. doi:10.1038/nphoton.2014.284 (Dec. 2014).

58. Murphy, D. W., Sunshine, S., van Dover, R. B., Cava, R. J., Batlogg, B., Zahurak, S. M. & Schneemeyer, L. F. New superconducting cuprate perovskites. *Phys. Rev. Lett.* **58,** 1888–1890. doi:10.1103/PhysRevLett.58.1888 (18 May 1987).

59. Burns, G. & Scott, B. A. Lattice Modes in Ferroelectric Perovskites: $PbTiO_3$. *Phys. Rev. B* **7,** 3088–3101. doi:10.1103/PhysRevB.7.3088 (7 Apr. 1973).

60. Fiebig, M., Lottermoser, T., Meier, D. & Trassin, M. The evolution of multiferroics. *Nature Reviews Materials* **1.** doi:10.1038/natrevmats.2016.46 (July 2016).

61. Goldschmidt, V. M. Die Gesetze der Krystallochemie. *Naturwissenschaften* **14,** 477–485 (1926).

62. Momma, K. & Izumi, F. VESTA3 for three-dimensional visualization of crystal, volumetric and morphology data. *Journal of Applied Crystallography* **44,** 1272–1276. doi:10.1107/S0021889811038970 (Dec. 2011).

63. Mix, C. & Jakob, G. Multiferroic and structural properties of $BiFeO_3$ close to the strain induced phase transition on different substrates. *Journal of Applied Physics* **113,** 17D907. doi:10.1063/1.4795216 (May 2013).

64. Reeve, R. M., Mix, C., König, M., Foerster, M., Jakob, G. & Kläui, M. Magnetic domain structure of $La_{0.7}Sr_{0.3}MnO_3$ thin-films probed at variable temperature with scanning electron microscopy with polarization analysis. *Applied Physics Letters* **102,** 122407. doi:10.1063/1.4798538 (Mar. 2013).

65. Mix, C., Finizio, S., Buzzi, M., Kronast, F., Nolting, F., Jakob, G. & Kläui, M. Direct observation of temperature dependent magnetic domain structure of the multiferroic $La_{0.66}Sr_{0.34}MnO_3/BiFeO_3$ bilayer system by x-ray linear dichroism- and x-ray magnetic circular dichroism-photoemission electron microscopy. *Journal of Applied Physics* **115,** 193901. doi:10.1063/1.4876300 (May 2014).

66. Mix, C., Finizio, S., Kläui, M. & Jakob, G. Conductance control at the $LaAlO_3/SrTiO_3$-interface by a multiferroic $BiFeO_3$ ad-layer. *Applied Physics Letters* **104,** 262903. doi:10.1063/1.4886405 (June 2014).

67. Euler, C., Holuj, P., Talkenberger, A. & Jakob, G. Magnetic field dependent thermal conductance in $La_{0.67}Sr_{0.33}MnO_3$. *Journal of Magnetism and Magnetic Materials* **381,** 188–193. doi:10.1016/j.jmmm.2014.12.083 (May 2015).

68. Vafaee, M., Finizio, S., Deniz, H., Hesse, D., Zabel, H., Jakob, G. & Kläui, M. The effect of interface roughness on exchange bias in $La_{0.7}Sr_{0.3}MnO_3$-$BiFeO_3$ heterostructures. *Applied Physics Letters* **108,** 072401. doi:10.1063/1.4941795 (Feb. 2016).

69. Geller, S. Crystal Structure of Gadolinium Orthoferrite, $GdFeO_3$. *The Journal of Chemical Physics* **24,** 1236–1239. doi:10.1063/1.1742746 (June 1956).

70. Gilleo, M. A. Magnetic Properties of a Gadolinium Orthoferrite, $GdFeO_3$, Crystal. *The Journal of Chemical Physics* **24,** 1239–1243. doi:10.1063/1.1742747 (June 1956).

71. White, R. L. Review of Recent Work on the Magnetic and Spectroscopic Properties of the Rare-Earth Orthoferrites. *Journal of Applied Physics* **40,** 1061–1069. doi:10.1063/1.1657530 (Mar. 1969).

72. Leake, J., Shirane, G. & Remeika, J. The magnetic structure of thulium orthoferrite, $TmFeO_3$. *Solid State Communications* **6,** 15–17. doi:10.1016/0038-1098(68)90327-x (Jan. 1968).

73. Treves, D. Magnetic Studies of Some Orthoferrites. *Physical Review* **125,** 1843–1853. doi:10.1103/physrev.125.1843 (Mar. 1962).

74. Eibschütz, M., Shtrikman, S. & Treves, D. Mössbauer Studies of $Fe^{57}$ in Orthoferrites. *Physical Review* **156,** 562–577. doi:10.1103/physrev.156.562 (Apr. 1967).

75. Bertaut, E. in *Spin Arrangements and Crystal Structure, Domains, and Micromagnetics* 149–209 (Elsevier, 1963). doi:10.1016/b978-0-12-575303-6.50011-7.

76. Marezio, M., Remeika, J. P. & Dernier, P. D. The crystal chemistry of the rare earth orthoferrites. *Acta Crystallographica Section B Structural Crystallography and Crystal Chemistry* **26,** 2008–2022. doi:10.1107/s0567740870005319 (Dec. 1970).

77. Saito, K., Sato, A., Bhattacharjee, A. & Sorai, M. High-precision detection of the heat-capacity anomaly due to spin reorientation in $TmFeO_3$ and $HoFeO_3$. *Solid State Communications* **120,** 129–132. doi:10.1016/s0038-1098(01)00359-3 (Oct. 2001).

78. Blum, N., Freeman, A. J., Shaner, J. W. & Grodzins, L. Mössbauer Studies of Spin Flop in Antiferromagnetic Hematite. *Journal of Applied Physics* **36,** 1169–1170. doi:10.1063/1.1714153 (1965).

79. Jacobs, I. S. Spin-Flopping in $MnF_2$ by High Magnetic Fields. *Journal of Applied Physics* **32,** S61–S62. doi:10.1063/1.2000500 (Mar. 1961).

80. Belov, K., Zvezdin, A. & Kadometseva, A. Rare-earth orthoferrites, symmetry and non-Heisenberg exchange. *Physics Reviews* **9,** 117 (1987).

81. LeCraw, R. C., Wolfe, R., Gyorgy, E. M., Hagedorn, F. B., Hensel, J. C. & Remeika, J. P. Microwave Absorption near the Reorientation Temperature in Rare Earth Orthoferrites. *Journal of Applied Physics* **39,** 1019–1020. doi:10.1063/1.1656152 (Feb. 1968).

82. Schmool, D., Keller, N., Guyot, M., Krishnan, R. & Tessier, M. Evidence of very high coercive fields in orthoferrite phases of PLD grown thin films. *Journal of Magnetism and Magnetic Materials* **195,** 291–298. doi:10.1016/s0304-8853(99)00102-x (May 1999).

83. Schmool, D. S., Keller, N., Guyot, M., Krishnan, R. & Tessier, M. Magnetic and magneto-optic properties of orthoferrite thin films grown by pulsed-laser deposition. *Journal of Applied Physics* **86,** 5712–5717. doi:10.1063/1.371583 (Nov. 1999).

84. Jin, L., He, Y., Zhang, D., Zhang, H., Wei, M. & Zhong, Z. Near-ultraviolet photodetector based on hexagonal $TmFeO_3$ ferroelectric semiconductor thin film with photovoltaic and pyroelectric effects. *APL Materials* **7,** 121105. doi:10.1063/1.5128702. eprint: https://doi.org/10.1063/1.5128702 (2019).

85. Han, H., Kim, D., Chae, S., Park, J., Nam, S. Y., Choi, M., Yong, K., Kim, H. J., Son, J. & Jang, H. M. Switchable ferroelectric photovoltaic effects in epitaxial h-$RFeO_3$ thin films. *Nanoscale* **10,** 13261–13269. doi:10.1039/c7nr08666k (2018).

86. Shannon, R. D. Revised effective ionic radii and systematic studies of interatomic distances in halides and chalcogenides. *Acta Crystallographica Section A* **32,** 751–767. doi:10.1107/s0567739476001551 (Sept. 1976).

87. Xu, X. & Wang, W. Multiferroic hexagonal ferrites (h-$RFeO_3$, R = Y, Dy-Lu): a brief experimental review. *Modern Physics Letters B* **28,** 1430008. doi:10.1142/s0217984914300087 (Aug. 2014).

88. Yakel Jnr, H. L., Koehler, W. C., Bertaut, E. F. & Forrat, E. F. On the crystal structure of the manganese (III) trioxides of the heavy lanthanides and yttrium. *Acta Crystallographica* **16,** 957–962. doi:10.1107/S0365110X63002589 (Oct. 1963).

89. Yamaguchi, O., Takemura, H., Yamashita, M. & Hayashida, A. Formation of Yttrium Iron Oxides Derived from Alkoxides. *Journal of The Electrochemical Society* **138,** 1492–1494. doi:10.1149/1.2085813 (May 1991).

90. Akbashev, A. R., Semisalova, A. S., Perov, N. S. & Kaul, A. R. Weak ferromagnetism in hexagonal orthoferrites $RFeO_3$ (R=Lu, Er-Tb). *Applied Physics Letters* **99,** 122502. doi:10.1063/1.3643043 (Sept. 2011).

91. Das, H., Wysocki, A. L., Geng, Y., Wu, W. & Fennie, C. J. Bulk magnetoelectricity in the hexagonal manganites and ferrites. *Nature Communications* **5.** doi:10.1038/ncomms3998 (Jan. 2014).

92. Aken, B. B. V., Palstra, T. T., Filippetti, A. & Spaldin, N. A. The origin of ferroelectricity in magnetoelectric $YMnO_3$. *Nature Materials* **3,** 164–170. doi:10.1038/nmat1080 (Feb. 2004).

93. Ye, M. & Vanderbilt, D. Magnetic charges and magnetoelectricity in hexagonal rare-earth manganites and ferrites. *Phys. Rev. B* **92,** 035107. doi:10.1103/PhysRevB.92.035107 (3 July 2015).

94. Spaldin, N. A. & Ramesh, R. Advances in magnetoelectric multiferroics. *Nature Materials* **18,** 203–212. doi:10.1038/s41563-018-0275-2 (Feb. 2019).

95. Bonnet, M., Delapalme, A., Fuess, H. & Thomas, M. Refinement of the structure of yttrium iron garnet (YIG). A case of severe extinction and absorption. *Acta Crystallographica Section B Structural Crystallography and Crystal Chemistry* **31,** 2233–2240. doi:10.1107/s0567740875007315 (Sept. 1975).

96. Sawada, H. Electron Density Study of Garnets: $Z_3Ga_5O_{12}$; Z = Nd, Sm, Gd, Tb. *Journal of Solid State Chemistry* **132,** 300–307. doi:10.1006/jssc.1997.7462 (Sept. 1997).

97. Geller, S., Williams, H. J. & Sherwood, R. C. Magnetic and Crystallographic Study of Neodymium-Substituted Yttrium and Gadolinium Iron Garnets. *Phys. Rev.* **123,** 1692–1699. doi:10.1103/PhysRev.123.1692 (5 Sept. 1961).

98. Wigen, P., McMichael, R. & Jayaprakash, C. Route to chaos in the magnetic garnets. *Journal of Magnetism and Magnetic Materials* **84,** 237–246. ISSN: 0304-8853. doi:https://doi.org/10.1016/0304-8853(90)90101-U (1990).

99. Cherepanov, V., Kolokolov, I. & L'vov, V. The saga of YIG: Spectra, thermodynamics, interaction and relaxation of magnons in a complex magnet. *Physics Reports* **229,** 81–144. doi:10.1016/0370-1573(93)90107-o (July 1993).

100. Gilleo, M. A. & Geller, S. Magnetic and Crystallographic Properties of Substituted Yttrium-Iron Garnet, $3Y_2O_3{\cdot}xM_2O_3{\cdot}(5\text{-}x)Fe_2O_3$. *Phys. Rev.* **110,** 73–78. doi:10.1103/PhysRev.110.73 (1 Apr. 1958).

101. Shinagawa, K., Sato, H., Saito, T. & Tsushima, T. Charge transfer transitions in yttrium iron garnet. *Journal of Magnetism and Magnetic Materials* **104-107,** 443–444. doi:10.1016/0304-8853(92)90871-k (Feb. 1992).

102. Pauthenet, R. Spontaneous Magnetization of Some Garnet Ferrites and the Aluminum Substituted Garnet Ferrites. *Journal of Applied Physics* **29,** 253–255. doi:10.1063/1.1723094 (Mar. 1958).

103. Cramer, J., Guo, E.-J., Geprägs, S., Kehlberger, A., Ivanov, Y. P., Ganzhorn, K., Coletta, F. D., Althammer, M., Huebl, H., Gross, R., Kosel, J., Kläui, M. & Goennenwein, S. T. B. Magnon Mode Selective Spin Transport in Compensated Ferrimagnets. *Nano Letters* **17,** 3334–3340. doi:10.1021/acs.nanolett.6b04522 (May 2017).

104. Braun, W. *Applied RHEED: reflection high-energy electron diffraction during crystal growth* (Springer Science & Business Media, 1999).

105. Delmdahl, R. & Pätzel, R. Pulsed laser deposition - UV laser sources and applications. *Applied Physics A* **93,** 611–615. doi:10.1007/s00339-008-4716-7 (June 2008).

106. Becker, S. *Magnetische Austauschkopplung in oxidischen Heterostrukturen* MA thesis (University of Mainz, Apr. 2017).

107. Wong, K., Hau, S., Chan, P., Leung, L., Choy, C. & Wong, H. XeCl excimer laser interaction with partially stabilized zirconia target. *Journal of materials science letters* **10,** 801–803 (1991).

108. Selinder, T. I., Larsson, G., Helmersson, U., Olsson, P., Sundgren, J.-E. & Rudner, S. Target presputtering effects on stoichiometry and deposition rate of Y-Ba-Cu-O thin films grown by dc magnetron sputtering. *Applied Physics Letters* **52,** 1907–1909. doi:10.1063/1.99740 (May 1988).

109. Birkholz, M. *Principles of X-ray Diffraction* 1–40. ISBN: 9783527607594. doi:https://doi.org/10.1002/3527607595.ch1. eprint: https://onlinelibrary.wiley.com/doi/pdf/10.1002/3527607595.ch1 (John Wiley and Sons, Ltd, 2005).

110. Vilanova Vidal, E., Schneider, H. & Jakob, G. Influence of disorder on anomalous Hall effect for Heusler compounds. *Phys. Rev. B* **83,** 174410. doi:10.1103/PhysRevB.83.174410 (17 May 2011).

111. Patterson, A. L. The Scherrer Formula for X-Ray Particle Size Determination. *Phys. Rev.* **56,** 978–982. doi:10.1103/PhysRev.56.978 (10 Nov. 1939).

112. Ying, A. J., Murray, C. E. & Noyan, I. C. A rigorous comparison of X-ray diffraction thickness measurement techniques using silicon-on-insulator thin films. *Journal of Applied Crystallography* **42,** 401–410. doi:10.1107/S0021889809006888 (June 2009).

113. Kiessig, H. Interferenz von Röntgenstrahlen an dünnen Schichten. *Annalen der Physik* **402,** 769–788. doi:https://doi.org/10.1002/andp.19314020702. eprint: https://onlinelibrary.wiley.com/doi/pdf/10.1002/andp.19314020702 (1931).

114. Chesca, B., Kleiner, R. & Koelle, D. *The SQUID Handbook* ISBN: 9783527603640. doi:https://doi.org/10.1002/3527603646.ch2. eprint: https://onlinelibrary.wiley.com/doi/pdf/10.1002/3527603646.ch2 (John Wiley and Sons, Ltd, 2004).

115. Buchner, M., Höfler, K., Henne, B., Ney, V. & Ney, A. Tutorial: Basic principles, limits of detection, and pitfalls of highly sensitive SQUID magnetometry for nanomagnetism and spintronics. *Journal of Applied Physics* **124,** 161101. doi:10.1063/1.5045299 (Oct. 2018).

116. Finizio, S., Foerster, M., Buzzi, M., Krüger, B., Jourdan, M., Vaz, C. A. F., Hockel, J., Miyawaki, T., Tkach, A., Valencia, S., Kronast, F., Carman, G. P., Nolting, F. & Kläui, M. Magnetic Anisotropy Engineering in Thin Film Ni Nanostructures by Magnetoelastic Coupling. *Phys. Rev. Applied* **1,** 021001. doi:10.1103/PhysRevApplied.1.021001 (2 Mar. 2014).

117. Tkach, A., Kehlberger, A., Büttner, F., Jakob, G., Eisebitt, S. & Kläui, M. Electric field modification of magnetotransport in Ni thin films on (011) PMN-PT piezosubstrates. *Applied Physics Letters* **106,** 062404. doi:10.1063/1.4907775 (Feb. 2015).

118. Zhao, P., Bao, M., Bur, A., Hockel, J. L., Wong, K., Mohanchandra, K. P., Lynch, C. S. & Carman, G. P. Domain engineered switchable strain states in ferroelectric (011) $[Pb(Mg_{1/3}Nb_{2/3})O_3]_{(1-x)}$-$[PbTiO_3]_x$ (PMN-PT, $x \approx 0.32$) single crystals. *Journal of Applied Physics* **109,** 124101. doi:10.1063/1.3595670 (June 2011).

119. Boldrin, D., Johnson, F., Thompson, R., Mihai, A. P., Zou, B., Zemen, J., Griffiths, J., Gubeljak, P., Ormandy, K. L., Manuel, P., Khalyavin, D. D., Ouladdiaf, B., Qureshi, N., Petrov, P., Branford, W. & Cohen, L. F. The Biaxial Strain Dependence of Magnetic Order in Spin Frustrated $Mn_3NiN$ Thin Films. *Advanced Functional Materials* **29,** 1902502. doi:10.1002/adfm.201902502 (Aug. 2019).

120. Leon, A. O., Cahaya, A. B. & Bauer, G. E. W. Voltage Control of Rare-Earth Magnetic Moments at the Magnetic-Insulator–Metal Interface. *Phys. Rev. Lett.* **120,** 027201. doi:10.1103/PhysRevLett.120.027201 (2 Jan. 2018).

121. Yu, W., Lan, J., Wu, R. & Xiao, J. Magnetic Snell's law and spin-wave fiber with Dzyaloshinskii-Moriya interaction. *Phys. Rev. B* **94,** 140410. doi:10.1103/PhysRevB.94.140410 (14 Oct. 2016).

122. Kehlberger, A., Ritzmann, U., Hinzke, D., Guo, E.-J., Cramer, J., Jakob, G., Onbasli, M. C., Kim, D. H., Ross, C. A., Jungfleisch, M. B., Hillebrands, B., Nowak, U. & Kläui, M. Length Scale of the Spin Seebeck Effect. *Phys. Rev. Lett.* **115,** 096602. doi:10.1103/PhysRevLett.115.096602 (9 Aug. 2015).

123. Guo, E.-J., Cramer, J., Kehlberger, A., Ferguson, C. A., MacLaren, D. A., Jakob, G. & Kläui, M. Influence of Thickness and Interface on the Low-Temperature Enhancement of the Spin Seebeck Effect in YIG Films. *Phys. Rev. X* **6,** 031012. doi:10.1103/PhysRevX.6.031012 (3 July 2016).

124. Onbasli, M. C., Kehlberger, A., Kim, D. H., Jakob, G., Kläui, M., Chumak, A. V., Hillebrands, B. & Ross, C. A. Pulsed laser deposition of epitaxial yttrium iron garnet films with low Gilbert damping and bulk-like magnetization. *APL Materials* **2,** 106102. doi:10.1063/1.4896936 (2014).

125. Komar, P. & Jakob, G. CADEM: calculate X-ray diffraction of epitaxial multilayers. *Journal of Applied Crystallography* **50,** 288–292. doi:10.1107/S1600576716018379 (Feb. 2017).

126. Ganzhorn, K., Wimmer, T., Cramer, J., Schlitz, R., Geprägs, S., Jakob, G., Gross, R., Huebl, H., Kläui, M. & Goennenwein, S. T. B. Temperature dependence of the non-local spin Seebeck effect in YIG/Pt nanostructures. *AIP Advances* **7,** 085102. doi:10.1063/1.4986848 (2017).

127. Sparks, M. *Ferromagnetic-relaxation theory* (McGraw-Hill, 1964).

128. Hauser, C., Richter, T., Homonnay, N., Eisenschmidt, C., Qaid, M., Deniz, H., Hesse, D., Sawicki, M., Ebbinghaus, S. G. & Schmidt, G. Yttrium Iron Garnet Thin Films with Very Low Damping Obtained by Recrystallization of Amorphous Material. *Scientific Reports* **6.** doi:10.1038/srep20827 (Feb. 2016).

129. Bayaraa, T., Xu, C., Campbell, D. & Bellaiche, L. Tuning magnetization compensation and Curie temperatures in epitaxial rare earth iron garnet films. *Phys. Rev. B* **100,** 214412. doi:10.1103/PhysRevB.100.214412 (21 Dec. 2019).

130. Nagahama, T., Mibu, K. & Shinjo, T. The magnetization process and magnetoresistance of exchange-spring bilayer systems. *Journal of Physics D: Applied Physics* **31,** 43–49. doi:10.1088/0022-3727/31/1/007 (Jan. 1998).

131. Mibu, K., Nagahama, T., Shinjo, T. & Ono, T. Magnetoresistance of Bloch-wall-type magnetic structures induced in NiFe/CoSm exchange-spring bilayers. *Phys. Rev. B* **58,** 6442–6446. doi:10.1103/PhysRevB.58.6442 (10 Sept. 1998).

132. Gomez-Perez, J. M., Vélez, S., McKenzie-Sell, L., Amado, M., Herrero-Martín, J., López-López, J., Blanco-Canosa, S., Hueso, L. E., Chuvilin, A., Robinson, J. W. A. & Casanova, F. Synthetic Antiferromagnetic Coupling Between Ultrathin Insulating Garnets. *Phys. Rev. Applied* **10,** 044046. doi:10.1103/PhysRevApplied.10.044046 (4 Oct. 2018).

133. Li, S., Shen, K. & Xia, K. Magnon hybridization in ferrimagnetic heterostructures. *Phys. Rev. B* **102,** 224413. doi:10.1103/PhysRevB.102.224413 (22 Dec. 2020).

134. Guo, J., Cheng, L., Ren, Z., Zhang, W., Lin, X., Jin, Z., Cao, S., Sheng, Z. & Ma, G. Magnetic field tuning of spin resonance in $TmFeO_3$ single crystal probed with THz transient. *Journal of Physics: Condensed Matter* **32,** 185401. doi:10.1088/1361-648x/ab6d0f (Feb. 2020).

135. Shapiro, S. M., Axe, J. D. & Remeika, J. P. Neutron-scattering studies of spin waves in rare-earth orthoferrites. *Phys. Rev. B* **10,** 2014–2021. doi:10.1103/PhysRevB.10.2014 (5 Sept. 1974).

136. Cinader, G. Effect of Antisymmetric Exchange Interaction on the Magnetization and Resonance in Antiferromagnets. *Physical Review* **155,** 453–457. doi:10.1103/physrev.155.453 (Mar. 1967).

137. Bazaliy, Y. B., Tsymbal, L. T., Kakazei, G. N., Izotov, A. I. & Wigen, P. E. Spin-reorientation in $ErFeO_3$: Zero-field transitions, three-dimensional phase diagram, and anisotropy of erbium magnetism. *Phys. Rev. B* **69,** 104429. doi:10.1103/PhysRevB.69.104429 (10 Mar. 2004).

138. Tsymbal, L. T., Kakazei, G. N. & Bazaliy, Y. B. Single-domain-wall states in millimeter-scale samples of $ErFeO_3$. *Phys. Rev. B* **79,** 092414. doi:10.1103/PhysRevB.79.092414 (9 Mar. 2009).

139. Bazaliy, Y. B. & Tsymbal, L. T. Triangular hysteresis loops in the spin-rotation region of orthoferrites. *Low Temperature Physics* **36,** 798–801. doi:10.1063/1.3499246 (Aug. 2010).

140. Rossol, F. C. Temperature Dependence of Magnetic Domain Structure and Wall Energy in Single-Crystal Thulium Orthoferrite. *Journal of Applied Physics* **39,** 5263–5267. doi:10.1063/1.1655950 (Oct. 1968).

141. Szymczak, R. & Balbashov, A. The temperature dependence of domain wall energy in $TmFeO_3$. *Physica B+C* **125,** 40–44. doi:10.1016/0378-4363(84)90015-9 (July 1984).

142. Treves, D. Studies on Orthoferrites at the Weizmann Institute of Science. *Journal of Applied Physics* **36,** 1033–1039. doi:10.1063/1.1714088 (Mar. 1965).

143. Kuroda, C., Miyadai, T., Naemura, A., Niizeki, N. & Takata, H. Magnetic Torque Curves for a Single Crystal of Thulium Orthoferrite ($TmFeO_3$). *Phys. Rev.* **122,** 446–447. doi:10.1103/PhysRev.122.446 (2 Apr. 1961).

144. Durbin, G. W., Johnson, C. E. & Thomas, M. F. Direct observation of field-induced spin reorientation in $YFeO_3$ by the Mössbauer effect. *Journal of Physics C: Solid State Physics* **8,** 3051–3057. doi:10.1088/0022-3719/8/18/024 (Sept. 1975).

145. Walling, J. C. & White, R. L. Study of magnetic interactions in $HoFeO_3$. *Phys. Rev. B* **10,** 4748–4759. doi:10.1103/PhysRevB.10.4748 (11 Dec. 1974).

146. Hoogeboom, G. R., Kuschel, T., Bauer, G. E. W., Mostovoy, M. V., Kimel, A. V. & van Wees, B. J. Magnetic order of $Dy^{3+}$ and $Fe^{3+}$ moments in antiferromagnetic $DyFeO_3$ probed by spin Hall magnetoresistance and spin Seebeck effect. *Phys. Rev. B* **103,** 134406. doi:10.1103/PhysRevB.103.134406 (13 Apr. 2021).

147. Bossak, A. A., Graboy, I. E., Gorbenko, O. Y., Kaul, A. R., Kartavtseva, M. S., Svetchnikov, V. L. & Zandbergen, H. W. XRD and HREM Studies of Epitaxially Stabilized Hexagonal Orthoferrites $RFeO_3$ (R = Eu-Lu). *Chemistry of Materials* **16,** 1751–1755. doi:10.1021/cm0353660 (May 2004).

148. Morrish, A. H. *Canted Antiferromagnetism: Hemati* eng. ISBN: 9810220073 (World Scientific Publishing Company, 1995).

149. Dionne, G. F. & Tumelty, P. F. Molecular-field coefficients of $Tm_3Fe_5O_{12}$. *Journal of Applied Physics* **50,** 8257–8258. doi:10.1063/1.325931 (Dec. 1979).

150. Walz, F. The Verwey transition - a topical review. *Journal of Physics: Condensed Matter* **14,** R285–R340. doi:10.1088/0953-8984/14/12/203 (Mar. 2002).

151. Özdemir, Ö., Dunlop, D. J. & Moskowitz, B. M. Changes in remanence, coercivity and domain state at low temperature in magnetite. *Earth and Planetary Science Letters* **194,** 343–358. doi:10.1016/s0012-821x(01)00562-3 (Jan. 2002).

152. Barbier, A., Belkhou, R., Ohresser, P., Gautier-Soyer, M., Bezencenet, O., Mulazzi, M., Guittet, M.-J. & Moussy, J.-B. Electronic and crystalline structure, morphology, and magnetism of nanometric $Fe_2O_3$ layers deposited on Pt(111) by atomic-oxygen-assisted molecular beam epitaxy. *Phys. Rev. B* **72,** 245423. doi:10.1103/PhysRevB.72.245423 (24 Dec. 2005).

153. Bezencenet, O., Bonamy, D., Belkhou, R., Ohresser, P. & Barbier, A. Origin and Tailoring of the Antiferromagnetic Domain Structure in $\alpha$-$Fe_2O_3$ Thin Films Unraveled by Statistical Analysis of Dichroic Spectromicroscopy (X-Ray Photoemission Electron Microscopy) Images. *Phys. Rev. Lett.* **106,** 107201. doi:10.1103/PhysRevLett.106.107201 (10 Mar. 2011).

154. Dutta, P., Manivannan, A., Seehra, M. S., Shah, N. & Huffman, G. P. Magnetic properties of nearly defect-free maghemite nanocrystals. *Phys. Rev. B* **70,** 174428. doi:10.1103/PhysRevB.70.174428 (17 Nov. 2004).

155. Staub, U., Rettig, L., Bothschafter, E. M., Windsor, Y. W., Ramakrishnan, M., Avula, S. R. V., Dreiser, J., Piamonteze, C., Scagnoli, V., Mukherjee, S., Niedermayer, C., Medarde, M. & Pomjakushina, E. Interplay of Fe and Tm moments through the spin-reorientation transition in $TmFeO_3$. *Phys. Rev. B* **96,** 174408. doi:10.1103/PhysRevB.96.174408 (17 Nov. 2017).

156. *Magnetic microscopy of nanostructures* 2005th ed. en (eds Hopster, H. & Oepen, H. P.) (Springer, Berlin, Germany, Sept. 2004).

157. Czekaj, S., Nolting, F., Heyderman, L. J., Willmott, P. R. & van der Laan, G. Sign dependence of the x-ray magnetic linear dichroism on the antiferromagnetic spin axis in $LaFeO_3$ thin films. *Phys. Rev. B* **73,** 020401. doi:10.1103/PhysRevB.73.020401 (2 Jan. 2006).

158. Vlietstra, N., Shan, J., Castel, V., van Wees, B. J. & Ben Youssef, J. Spin-Hall magnetoresistance in platinum on yttrium iron garnet: Dependence on platinum thickness and in-plane/out-of-plane magnetization. *Phys. Rev. B* **87,** 184421. doi:10.1103/PhysRevB.87.184421 (18 May 2013).

159. Aqeel, A., Vlietstra, N., Roy, A., Mostovoy, M., van Wees, B. J. & Palstra, T. T. M. Electrical detection of spiral spin structures in Pt—$Cu_2OSeO_3$ heterostructures. *Phys. Rev. B* **94,** 134418. doi:10.1103/PhysRevB.94.134418 (13 Oct. 2016).

160. Lu, Y. M., Choi, Y., Ortega, C. M., Cheng, X. M., Cai, J. W., Huang, S. Y., Sun, L. & Chien, C. L. Pt Magnetic Polarization on $Y_3Fe_5O_{12}$ and Magnetotransport Characteristics. *Phys. Rev. Lett.* **110,** 147207. doi:10.1103/PhysRevLett.110.147207 (14 Apr. 2013).

161. Lang, L., Zhou, S. & Qiu, X. Surface magnetization thermal fluctuation driven anomalous behaviour of ordinary Hall effect in Pt/YIG. *Journal of Physics D: Applied Physics* **52,** 085001. doi:10.1088/1361-6463/aaf6c3 (Dec. 2018).

162. Fischer, J., Althammer, M., Vlietstra, N., Huebl, H., Goennenwein, S. T., Gross, R., Geprägs, S. & Opel, M. Large Spin Hall Magnetoresistance in Antiferromagnetic $\alpha$-$Fe_2O_3$/Pt Heterostructures. *Phys. Rev. Applied* **13,** 014019. doi:10.1103/PhysRevApplied.13.014019 (1 Jan. 2020).

163. Ross, A., Lebrun, R., Ulloa, C., Grave, D. A., Kay, A., Baldrati, L., Kronast, F., Valencia, S., Rothschild, A. & Kläui, M. Structural sensitivity of the spin Hall magnetoresistance in antiferromagnetic thin films. *Phys. Rev. B* **102,** 094415. doi:10.1103/PhysRevB.102.094415 (9 Sept. 2020).

164. Herrmann, G. Resonance and high frequency susceptibility in canted antiferromagnetic substances. *Journal of Physics and Chemistry of Solids* **24,** 597–606. doi:10.1016/s0022-3697(63)80001-3 (May 1963).

165. Niimi, Y., Wei, D., Idzuchi, H., Wakamura, T., Kato, T. & Otani, Y. Experimental Verification of Comparability between Spin-Orbit and Spin-Diffusion Lengths. *Phys. Rev. Lett.* **110,** 016805. doi:10.1103/PhysRevLett.110.016805 (1 Jan. 2013).

166. Uecker, R., Velickov, B., Klimm, D., Bertram, R., Bernhagen, M., Rabe, M., Albrecht, M., Fornari, R. & Schlom, D. Properties of rare-earth scandate single crystals (Re=Nd-Dy). *Journal of Crystal Growth* **310,** 2649–2658. doi:10.1016/j.jcrysgro.2008.01.019 (May 2008).

167. Bercha, D. M., Rushchanskii, K. Z., Sznajder, M., Matkovskii, A. & Potera, P. Elementary energy bands in ab initio calculations of the $YAlO_3$ and SbSI crystal band structure. *Phys. Rev. B* **66,** 195203. doi:10.1103/PhysRevB.66.195203 (19 Nov. 2002).

168. Derks, C., Kuepper, K., Raekers, M., Postnikov, A. V., Uecker, R., Yang, W. L. & Neumann, M. Band-gap variation in $R\mathrm{Sc}O_3$ ($R$=Pr, Nd, Sm, Eu, Gd, Tb, and Dy): X-ray absorption and O $K$-edge x-ray emission spectroscopies. *Phys. Rev. B* **86,** 155124. doi:10.1103/PhysRevB.86.155124 (15 Oct. 2012).

169. Afanas'ev, V. V., Stesmans, A., Zhao, C., Caymax, M., Heeg, T., Schubert, J., Jia, Y., Schlom, D. G. & Lucovsky, G. Band alignment between (100) Si and complex rare earth/transition metal oxides. *Applied Physics Letters* **85,** 5917–5919. doi:10.1063/1.1829781 (Dec. 2004).

170. Dumont, Y., Vedpathak, M., Keller, N., Tessier, M., Tromson-Carli, A. & Guyot, M. Evidence of hetero-epitaxy of Sm-orthoferrite on MgO(001) substrates by the pulsed laser deposition technique. *Journal of Crystal Growth* **244,** 274–280. ISSN: 0022-0248. doi:https://doi.org/10.1016/S0022-0248(02)01654-8 (2002).

171. Galinski, H., Ryll, T., Elser, P., Rupp, J. L. M., Bieberle-Hütter, A. & Gauckler, L. J. Agglomeration of Pt thin films on dielectric substrates. *Phys. Rev. B* **82,** 235415. doi:10.1103/PhysRevB.82.235415 (23 Dec. 2010).

172. Yamaguchi, T. Theory of spin reorientation in rare-earth orthochromites and orthoferrites. *Journal of Physics and Chemistry of Solids* **35,** 479–500. doi:10.1016/s0022-3697(74)80003-x (Jan. 1974).

173. Koshizuka, N. & Hayashi, K. Raman Scattering from Magnon Excitations in $R\mathrm{Fe}O_3$. *Journal of the Physical Society of Japan* **57,** 4418–4428. doi:10.1143/jpsj.57.4418 (Dec. 1988).

174. Hahn, S. E., Podlesnyak, A. A., Ehlers, G., Granroth, G. E., Fishman, R. S., Kolesnikov, A. I., Pomjakushina, E. & Conder, K. Inelastic neutron scattering studies of $YFeO_3$. *Phys. Rev. B* **89,** 014420. doi:10.1103/PhysRevB.89.014420 (1 Jan. 2014).

175. Li, X., Bamba, M., Yuan, N., Zhang, Q., Zhao, Y., Xiang, M., Xu, K., Jin, Z., Ren, W., Ma, G., Cao, S., Turchinovich, D. & Kono, J. Observation of Dicke cooperativity in magnetic interactions. *Science* **361,** 794–797. doi:10.1126/science.aat5162 (Aug. 2018).

176. Jacobs, I. S., Burne, H. F. & Levinson, L. M. Field-Induced Spin Reorientation in $YFeO_3$ and $YCrO_3$. *Journal of Applied Physics* **42,** 1631–1632. doi:10.1063/1.1660372 (Mar. 1971).

177. Prelorendjo, L. A., Johnson, C. E., Thomas, M. F. & Wanklyn, B. M. A Mossbauer study of spin reorientation in $ErFeO_3$. *Journal of Physics C: Solid State Physics* **15,** 3199–3208. doi:10.1088/0022-3719/15/14/024 (May 1982).

178. Prelorendjo, L. A., Johnson, C. E., Thomas, M. F. & Wanklyn, B. M. Spin reorientation transitions in $DyFeO_3$ induced by magnetic fields. *Journal of Physics C: Solid State Physics* **13,** 2567–2578. doi:10.1088/0022-3719/13/13/012 (May 1980).

179. Gorodetsky, G., Sharon, B. & Shtrikman, S. Magnetic Properties of an Antiferromagnetic Orthoferrite. *Journal of Applied Physics* **39,** 1371–1372. doi:10.1063/1.1656309. eprint: https://doi.org/10.1063/1.1656309 (1968).

180. Johnson, C., Prelorendjo, L. & Thomas, M. Field induced spin reorientation in orthoferrites $DyFeO_3$, $HoFeO_3$ and $ErFeO_3$. *Journal of Magnetism and Magnetic Materials* **15-18,** 557–558. ISSN: 0304-8853. doi:https://doi.org/10.1016/0304-8853(80)90662-9 (1980).

181. Durbin, G. W., Johnson, C. E., Prelorendjo, L. A. & Thomas, M. F. Spin reorientation in rare earth orthoferrites. *Le Journal de Physique Colloques* **37,** C6–621–C6–624. doi:10.1051/jphyscol:19766129 (Dec. 1976).

182. Durbin, G. W., Johnson, C. E. & Thomas, M. F. Temperature dependence of field-induced spin reorientation in GdFeO3. *Journal of Physics C: Solid State Physics* **10,** 1975–1978. doi:10.1088/0022-3719/10/11/031 (June 1977).

183. Mohammed, M. H., Cheng, Z. X., Cao, S., Rule, K. C., Richardson, C., Edwards, A., Studer, A. J. & Horvat, J. Non-zero spontaneous magnetic moment along crystalline b-axis for rare earth orthoferrites. *Journal of Applied Physics* **127,** 113906. doi:10.1063/1.5115518. eprint: https://doi.org/10.1063/1.5115518 (2020).

184. Chowdhury, U., Goswami, S., Roy, A., Rajput, S., Mall, A. K., Gupta, R., Kaushik, S. D., Siruguri, V., Saravanakumar, S., Israel, S., Saravanan, R., Senyshyn, A., Chatterji, T., Scott, J. F., Garg, A. & Bhattacharya, D. Origin of ferroelectricity in orthorhombic $LuFeO_3$. *Phys. Rev. B* **100,** 195116. doi:10.1103/PhysRevB.100.195116 (19 Nov. 2019).

185. Sudandararaj, A. T. S., Kumar, G. S., Dhivya, M., Eithiraj, R. & Banu, I. S. Spin reorientation transition in nanoscale multiferroic $PrFeO_3$ and its band structure calculation. *Journal of Alloys and Compounds* **817,** 152747. doi:10.1016/j.jallcom.2019.152747 (Mar. 2020).

186. Lee, J.-H., Jeong, Y. K., Park, J. H., Oak, M.-A., Jang, H. M., Son, J. Y. & Scott, J. F. Spin-Canting-Induced Improper Ferroelectricity and Spontaneous Magnetization Reversal in $SmFeO_3$. *Phys. Rev. Lett.* **107,** 117201. doi:10.1103/PhysRevLett.107.117201 (11 Sept. 2011).

187. Peyrard, J. & Sivardiere, J. Chaleurs specifiques a basse temperature de quelques orthoferrites de terres rares. *Solid State Communications* **7,** 605–609. ISSN: 0038-1098. doi:https://doi.org/10.1016/0038-1098(69)90627-9 (1969).

188. Nikitin, S. E., Wu, L. S., Sefat, A. S., Shaykhutdinov, K. A., Lu, Z., Meng, S., Pomjakushina, E. V., Conder, K., Ehlers, G., Lumsden, M. D., Kolesnikov, A. I., Barilo, S., Guretskii, S. A., Inosov, D. S. & Podlesnyak, A. Decoupled spin dynamics in the rare-earth orthoferrite $YbFeO_3$: Evolution of magnetic excitations through the spin-reorientation transition. *Phys. Rev. B* **98,** 064424. doi:10.1103/PhysRevB.98.064424 (6 Aug. 2018).

189. Zhou, J.-S., Marshall, L. G., Li, Z.-Y., Li, X. & He, J.-M. Weak ferromagnetism in perovskite oxides. *Phys. Rev. B* **102,** 104420. doi:10.1103/PhysRevB.102.104420 (10 Sept. 2020).

190. Gorodetsky, G. & Lüthi, B. Sound-Wave—Soft-Mode Interaction near Displacive Phase Transitions: Spin Reorientation in $ErFeO_3$. *Phys. Rev. B* **2,** 3688–3698. doi:10.1103/PhysRevB.2.3688 (9 Nov. 1970).

191. Levinson, L. M., Luban, M. & Shtrikman, S. Microscopic Model for Reorientation of the Easy Axis of Magnetization. *Phys. Rev.* **187,** 715–722. doi:10.1103/PhysRev.187.715 (2 Nov. 1969).

192. Ganzhorn, K., Barker, J., Schlitz, R., Piot, B. A., Ollefs, K., Guillou, F., Wilhelm, F., Rogalev, A., Opel, M., Althammer, M., Geprägs, S., Huebl, H., Gross, R., Bauer, G. E. W. & Goennenwein, S. T. B. Spin Hall magnetoresistance in a canted ferrimagnet. *Phys. Rev. B* **94,** 094401. doi:10.1103/PhysRevB.94.094401 (9 Sept. 2016).

193. Antel, W. J., Schwickert, M. M., Lin, T., O'Brien, W. L. & Harp, G. R. Induced ferromagnetism and anisotropy of Pt layers in Fe/Pt(001) multilayers. *Phys. Rev. B* **60,** 12933–12940. doi:10.1103/PhysRevB.60.12933 (18 Nov. 1999).

194. Goennenwein, S. T. B., Schlitz, R., Pernpeintner, M., Ganzhorn, K., Althammer, M., Gross, R. & Huebl, H. Non-local magnetoresistance in YIG/Pt nanostructures. *Applied Physics Letters* **107,** 172405. doi:10.1063/1.4935074. eprint: https://doi.org/10.1063/1.4935074 (2015).

195. Kim, T. H., Grüenberg, P., Han, S. H. & Cho, B. K. Field-driven dynamics and time-resolved measurement of Dzyaloshinskii-Moriya torque in canted antiferromagnet $YFeO_3$. *Scientific Reports* **7.** doi:10.1038/s41598-017-04883-3 (July 2017).

196. Šmejkal, L., González-Hernández, R., Jungwirth, T. & Sinova, J. Crystal time-reversal symmetry breaking and spontaneous Hall effect in collinear antiferromagnets. *Science Advances* **6,** eaaz8809. doi:10.1126/sciadv.aaz8809 (June 2020).

197. Babu, K. R., Lingam, C. B., Auluck, S., Tewari, S. P. & Vaitheeswaran, G. Structural, thermodynamic and optical properties of $MgF_2$ studied from first-principles theory. *Journal of Solid State Chemistry* **184,** 343–350. doi:10.1016/j.jssc.2010.11.025 (Feb. 2011).

198. Baur, W. H. Rutile-type compounds. V. Refinement of $MnO_2$ and $MgF_2$. *Acta Crystallographica Section B: Structural Crystallography and Crystal Chemistry* **32,** 2200–2204 (1976).

199. Francisco, E., Recio, J. M., Blanco, M. A., Pendás, A. M. & Costales, A. Quantum-Mechanical Study of Thermodynamic and Bonding Properties of $MgF_2$. *The Journal of Physical Chemistry A* **102,** 1595–1601. doi:10.1021/jp972516j (Feb. 1998).

200. Diebold, U. The surface science of titanium dioxide. *Surface Science Reports* **48,** 53–229. doi:10.1016/s0167-5729(02)00100-0 (Jan. 2003).

201. Burdett, J. K., Hughbanks, T., Miller, G. J., Richardson Jr, J. W. & Smith, J. V. Structural-electronic relationships in inorganic solids: powder neutron diffraction studies of the rutile and anatase polymorphs of titanium dioxide at 15 and 295 K. *Journal of the American Chemical Society* **109,** 3639–3646 (1987).

202. GRANT, F. A. Properties of Rutile (Titanium Dioxide). *Reviews of Modern Physics* **31,** 646–674. doi:10.1103/revmodphys.31.646 (July 1959).

203. Schäfer, H., Schneidereit, G. & Gerhardt, W. Zur Chemie der Platinmetalle. $RuO_2$ Chemischer Transport, Eigenschaften, thermischer Zerfall. *Zeitschrift für anorganische und allgemeine Chemie* **319,** 327–336. doi:10.1002/zaac.19633190514 (Jan. 1963).

204. Over, H. Surface Chemistry of Ruthenium Dioxide in Heterogeneous Catalysis and Electrocatalysis: From Fundamental to Applied Research. *Chemical Reviews* **112,** 3356–3426. doi:10.1021/cr200247n (Mar. 2012).

205. Boman, C.-E. Refinement of the crystal structure of ruthenium dioxide. *Acta Chem. Scand* **24,** 116–122 (1970).

206. Berlijn, T., Snijders, P. C., Delaire, O., Zhou, H.-D., Maier, T. A., Cao, H.-B., Chi, S.-X., Matsuda, M., Wang, Y., Koehler, M. R., Kent, P. R. C. & Weitering, H. H. Itinerant Antiferromagnetism in $RuO_2$. *Physical Review Letters* **118.** doi:10.1103/physrevlett.118.077201 (Feb. 2017).

207. Zhu, Z. H., Strempfer, J., Rao, R. R., Occhialini, C. A., Pelliciari, J., Choi, Y., Kawaguchi, T., You, H., Mitchell, J. F., Shao-Horn, Y. & Comin, R. Anomalous Antiferromagnetism in Metallic $RuO_2$ Determined by Resonant X-ray Scattering. *Phys. Rev. Lett.* **122,** 017202. doi:10.1103/PhysRevLett.122.017202 (1 Jan. 2019).

208. Stoerzinger, K. A., Qiao, L., Biegalski, M. D. & Shao-Horn, Y. Orientation-Dependent Oxygen Evolution Activities of Rutile $IrO_2$ and $RuO_2$. *The Journal of Physical Chemistry Letters* **5,** 1636–1641. doi:10.1021/jz500610u (Apr. 2014).

209. Jia, Q. X., Wu, X. D., Foltyn, S. R., Findikoglu, A. T., Tiwari, P., Zheng, J. P. & Jow, T. R. Heteroepitaxial growth of highly conductive metal oxide $RuO_2$ thin films by pulsed laser deposition. *Applied Physics Letters* **67,** 1677–1679. doi:10.1063/1.115054 (Sept. 1995).

210. Jia, Q. X., Wu, X. D., Song, G. & Foltyn, S. R. Role of substrates for heteroepitaxial growth of low room-temperature resistivity $RuO_2$ thin films deposited by pulsed laser deposition. *Journal of Vacuum Science & Technology A* **14,** 1107–1110. doi:10.1116/1.580277 (1996).

211. Kutsuzawa, D., Oka, D. & Fukumura, T. Thickness Effects on Crystal Growth and Metal-Insulator Transition in Rutile-Type $RuO_2$ (100) Thin Films. *physica status solidi (b)* **257,** 2000188. doi:10.1002/pssb.202000188 (June 2020).

212. Jia, Q. X., Song, S. G., Wu, X. D., Cho, J. H., Foltyn, S. R., Findikoglu, A. T. & Smith, J. L. Epitaxial growth of highly conductive $RuO_2$ thin films on (100) Si. *Applied Physics Letters* **68,** 1069–1071. doi:10.1063/1.115715 (Feb. 1996).

213. Patil, U., Kulkarni, S., Jamadade, V. & Lokhande, C. Chemically synthesized hydrous $RuO_2$ thin films for supercapacitor application. *Journal of Alloys and Compounds* **509,** 1677–1682. doi:10.1016/j.jallcom.2010.09.133 (Feb. 2011).

214. Butkute, R., Lisauskas, V. & Vengalis, B. High-quality conductive $I_2O_3$(Sn) and $RuO_2$ layers grown by magnetron sputtering. *Surface and Coatings Technology* **100-101,** 305–308. doi:10.1016/s0257-8972(97)00638-5 (Mar. 1998).

215. Fröhlich, K., Machajdík, D., Cambel, V., Kostič, I. & Pignard, S. Epitaxial growth of low-resistivity $RuO_2$ films on oriented $Al_2O_3$ substrate. *Journal of Crystal Growth* **235,** 377–383. doi:10.1016/s0022-0248(01)01907-8 (Feb. 2002).

216. Kim, Y., Gao, Y. & Chambers, S. Core-level X-ray photoelectron spectra and X-ray photoelectron diffraction of $RuO_2$ (110) grown by molecular beam epitaxy on $TiO_2$ (110). *Applied Surface Science* **120,** 250–260. doi:10.1016/s0169-4332(97)00233-x (Dec. 1997).

217. Rizzi, G., Magrin, A. & Granozzi, G. Preparation of epitaxial ultrathin $RuO_2$-$TiO_2$ (110) films by decomposition of $Ru_3(CO)_{12}$. *Surface Science* **443,** 277–286. doi:10.1016/s0039-6028(99)01026-2 (Dec. 1999).

218. Martín, V. S., Palazón, J. M., Rodríguez, C. M., Nevill, C. R. & Hutchinson, D. K. *Ruthenium(VIII) Oxide* Sept. 2013. doi:10.1002/047084289x.rr009.pub3.

219. Glassford, K. M. & Chelikowsky, J. R. Electronic and structural properties of $RuO_2$. *Phys. Rev. B* **47,** 1732–1741. doi:10.1103/PhysRevB.47.1732 (4 Jan. 1993).

220. Ryden, W. D., Lawson, A. W. & Sartain, C. C. Electrical Transport Properties of $IrO_2$ and $RuO_2$. *Phys. Rev. B* **1,** 1494–1500. doi:10.1103/PhysRevB.1.1494 (4 Feb. 1970).

221. Tsujimoto, Y., Matsushita, Y., Yu, S., Yamaura, K. & Uchikoshi, T. Size dependence of structural, magnetic, and electrical properties in corundum-type $Ti_2O_3$ nanoparticles showing insulator-metal transition. *Journal of Asian Ceramic Societies* **3,** 325–333. doi:10.1016/j.jascer.2015.06.007 (Sept. 2015).

222. Kitada, A., Hasegawa, G., Kobayashi, Y., Kanamori, K., Nakanishi, K. & Kageyama, H. Selective Preparation of Macroporous Monoliths of Conductive Titanium Oxides $Ti_nO_{2n-1}$ ($n = 2, 3, 4, 6$). *Journal of the American Chemical Society* **134,** 10894–10898. doi:10.1021/ja302083n (June 2012).

223. Da-Ming, S., Zhao-Qi, S., Ai-Xia, L. & Zhi-Yuan, X. Oxidation behaviour of $MgF_2$ in Ag-$MgF_2$ cermet. *Vacuum* **55,** 39–44. doi:10.1016/s0042-207x(99)00121-9 (Oct. 1999).

224. Kadivar, E. & Mozafari, Z. Investigation of the High Temperature Oxidation Behavior of $MgF_2$ in Air Atmosphere. *Oxidation of Metals* **94,** 179–189. doi:10.1007/s11085-020-09993-4 (Aug. 2020).

225. Lin, J. J., Huang, S. M., Lin, Y. H., Lee, T. C., Liu, H., Zhang, X. X., Chen, R. S. & Huang, Y. S. Low temperature electrical transport properties of $RuO_2$ and $IrO_2$ single crystals. *Journal of Physics: Condensed Matter* **16,** 8035–8041. doi:10.1088/0953-8984/16/45/025 (Oct. 2004).

226. Fletcher, J. M., Gardner, W. E., Greenfield, B. F., Holdoway, M. J. & Rand, M. H. Magnetic and other studies of ruthenium dioxide and its hydrate. *Journal of the Chemical Society A: Inorganic, Physical, Theoretical,* 653. doi:10.1039/j19680000653 (1968).

227. Feng, Z., Zhou, X., Šmejkal, L., Wu, L., Zhu, Z., Guo, H., González-Hernández, R., Wang, X., Yan, H., Qin, P., Zhang, X., Wu, H., Chen, H., Xia, Z., Jiang, C., Coey, M., Sinova, J., Jungwirth, T. & Liu, Z. *Observation of the Anomalous Hall Effect in a Collinear Antiferromagnet* 2021. arXiv: 2002.08712 [cond-mat.mtrl-sci].

# Acknowledgements

Aus Datenschutzgründen entfernt / Removed due to data privacy

# Curriculum vitae

Aus Datenschutzgründen entfernt / Removed due to data privacy

# Eidesstattliche Erklärung

Hiermit erkläre ich an Eides statt, dass ich meine Dissertation selbständig und ohne fremde Hilfe verfasst und keine anderen als die von mir angegebenen Quellen und Hilfsmittel zur Erstellung meiner Dissertation verwendet habe. Die Arbeit ist in vorliegender oder ähnlicher Form bei keiner anderen Prüfungsbehörde zur Erlangung eines Doktorgrades eingereicht worden.

Mainz, den

Sven Becker